Reconstructing Local Redox Conditions, Mineral Precipitation Processes and Nutrient Availability in Seawater During Deposition of the Transvaal Supergroup, South Africa

Thesis presented for the degree of

Doctor of Philosophy

in the Department of Geological Sciences

University of Cape Town

Presented by

Ansahmbom Yong Nke

July 2024

Supervisor: Dr Rosalie Tostevin

Co-supervisor: Prof Harilaos Tsikos

Declaration

I, ANSAHMBOM YONG NKE, hereby declare that:

i. the work on which this thesis is based is my original work (except where acknowledgements indicate otherwise) and that neither the whole work nor any part of it has been, is being, or is to be submitted for another degree in this or any other university. I authorise the University to reproduce for the purpose of research either the whole or any portion of the contents in any manner whatsoever.

ii. this thesis is my own unaided work, both in concept and execution, and that apart from the normal guidance from my supervisor, I have received no assistance.

Date: 31 July, 2024

I confirm that I have been granted permission by the University of Cape Town's Doctoral Degrees Board to include the following publication(s) in my PhD thesis, and where co-authorships are involved, my co-authors have agreed that I may include the publication(s):

1. **Nke et al.**, "A Seawater Origin for Greenalite in Iron Formation of the Transvaal Supergroup", *Earth and Planetary Science Letters*. 2024 July Vol. 643, 118917.*

Signature: Signed by candidate Date: 31 July, 2024

Student Name: ANSAHMBOM YONG NKE Student Number: NKXANS001

Contents

Reconstructing Local Redox Conditions, Mineral Precipitation Processes and Nutrient Availability in Seawater During Deposition of the Transvaal Supergroup, South Africa i

List of figures v

List of tables vi

List of abbreviations vii

Abstract viii

Chapter 1 1

Introduction 1

1.1. Opening statement 2

1.2. A review of Earth surface conditions during the Precambrian 2

1.3. Marine sediments 7

1.4. Rare Earth Elements as a Geochemical Proxy 13

1.5. Geological setting – Transvaal Supergroup 18

1.6. Thesis structure 23

Chapter 2 25

Searching for Local Oxygen Generation in Microbial Carbonates of the Campbellrand Subgroup, Transvaal Supergroup 25

2.1. Introduction 26

2.2. Stratigraphic setting and sample selection 28

2.3. Methods 29

2.4. Mineralogy and petrography 33

2.5. Trace and REE geochemistry of microbial carbonates 43

2.6. Discussion 49

2.7. Conclusion 58

Chapter 3 59

Identification of Greenalite and New Methodology for Isolating its Trace Element Signal 59

3.1. Introduction 60

3.2. Stratigraphic setting 61

3.3. Sample selection and preparation 62

3.4. Characterisation of greenalite 63

3.5. Assessing the greenalite data 74

3.6. Conclusion 75

Chapter 4 77

A Seawater Origin for Greenalite in Iron Formation of the Transvaal Supergroup 77
4.1. Introduction 78
4.2. Rare earth element characteristics of greenalite 79
4.3. Discussion 84
4.4. Conclusion 90
Chapter 5 91
Metal Concentrations in Paleoproterozoic Seawater 91
5.1. Introduction 92
5.2. Calculating the trace metal concentration in seawater 93
5.3. Metal abundance in Paleoproterozoic greenalite 98
5.4. An archive of shallow marine conditions 99
5.5. An emerging picture from geology and biology 99
5.6. Conclusion 102
Chapter 6 104
Conclusions and Outlook 104
6.1. Introduction 105
6.2. Integrative synthesis of findings 105
6.3. Broader geological context 108
6.4. Future directions and implications 109
6.5. Concluding thoughts 109
References 111
Supplementary Data 128
Acknowledgments 129

List of figures

Figure 1. 1 | Changes of oxygen concentrations in Earth's atmosphere 4
Figure 1. 2 | A summary of the current model of evolution of ocean redox 6
Figure 1. 3 | PAAS-normalized REE + Y patterns 15
Figure 1. 4 | A simplified map distribution of the Transvaal Supergroup 19

Figure 2. 1 | Griqualand West basin outcrops and Log of the Gasesa drill core 28
Figure 2. 2 | Hand samples and photomicrographs of microbialites 34
Figure 2. 3 | Mineral phases identified in microbial carbonates 36
Figure 2. 4 | Plots of averaged REY from ICP-MS analyses 43
Figure 2. 5 | Box plots comparing key parameters 45
Figure 2. 6 | $(Ce/Ce^*)_{SN}$ vs. $(Pr/Pr^*)_{SN}$ and REY patterns of four samples 48
Figure 2. 7 | Bivariate plots evaluating REE data 51
Figure 2. 8 | REE trends for screened carbonate and BIF data 54
Figure 2. 9 | Overview of recalculated $(Ce/Ce^*)_{SN}$ values 55

Figure 3. 1 | Regional setting of the Griqualand West basin 62
Figure 3. 2 | Representative bulk rock XRD pattern showing greenalite 64
Figure 3. 3 | Cross-section view of micro-banded IF 65
Figure 3. 4 | Images of samples used in this study from the Kuruman IF 66
Figure 3. 5 | SEM-BSE micrographs of LA ICP-MS craters 68
Figure 3. 6 | Microprobe and LA ICP-MS major element data for greenalite 69
Figure 3. 7 | Cross plots of major elements in greenalite 71
Figure 3. 8 | SEM-BSE image of larger siderite grains 75

Figure 4. 1 | LA ICP-MS REY data from the ~2.46 Ga greenalite 80
Figure 4. 2 | REY data for the greenalite vs. chert 84
Figure 4. 3 | Comparison between greenalite and average bulk rock from IF 86
Figure 4. 4 | Mixing model between modern seawater and hydrothermal fluids 88
Figure 4. 5 | Modelled relationship between Fe^{2+} activity and pH 90

Figure 5. 1 | Cross plots of unadjusted metal abundance in greenalite 98
Figure 5. 2 | Metal concentrations in greenalite along with partition coefficients (K'_D) 99
Figure 5. 3 | Comparison of my estimate for the metal concentration in Paleoproterozoic seawater with quantitative estimates from other geological archives or models. 101

List of tables

Table 2. 1 | Sedimentary and textural characteristics of microbial carbonates 30
Table 2. 2 | Averaged major and trace element data from ICP-MS analyses 39
Table 2. 3 | Averaged REY data from ICP-MS analyses 41

Table 3. 1 | Commonly observed minerals in iron formations 61
Table 3. 2 | EMPA major element data for IF greenalite 70
Table 3. 3 | Major element concentrations of greenalite measured by LA ICP-MS. 72

Table 4. 1 | LA ICP-MS data, diagnostic REY ratios and anomalies for greenalite 82
Table 4. 2 | Average and standard deviation of key REY anomalies 87

Table 5. 1 | Raw LA ICP-MS trace metal concentration from natural greenalite 95
Table 5. 2 | Trace metal concentrations in Paleoproterozoic seawater 97
Table 5. 3 | Summary of trace metal content in ~2.46 Ga greenalite 98

List of abbreviations

GENERAL

BIF	Banded iron formation
GOE	Great Oxidation Event
PAL	Present-day atmospheric levels
REE	Rare earth element
ROI	Region of interest
MIF-S	Mass independent fractionation of sulphur isotopes
PAAS	Post-Archean Australian Shale
NMH	Non microbial horizon (in microbial carbonates)
MH	Microbial horizon (in microbial carbonates)
ppm	Parts per million
ppb	Parts ber billion
Ma	Million years ago
Ga	Billion years ago

ANALYTICAL TECHNIQUES AND INSTRUMENTS

SEM	Scanning electron microscopy
BSE	Backscatter electron
LA ICP-MS	Laser ablation inductively coupled plasma-mass spectrometry
ICP-AES	Inductively coupled plasma-atomic emission spectrometry
XRD	X-ray diffraction
XRF	X-ray flourescence spectrometry
EMPA	Electron microprobe analyser

Abstract

Iron formations (IF) and carbonate rocks serve as geochemical archives, which can be used to reconstruct marine environments in the Archean and Proterozoic Eons. The chemistry of ancient oceans influenced iron redox states and primary mineral precipitation, affecting the cycling of other trace elements and nutrients. While carbonate minerals are commonly used as geochemical archives, reconstructions using IF have proved more challenging, with many studies analysing bulk powders. However, reconstructing ancient conditions is challenging due to post-depositional alteration, fine-grained mineral composition, and complex mineralogy. Recent studies highlight greenalite, an Fe(II)-silicate mineral, as a primary phase in IF and a potential proxy for ancient seawater chemistry. This study combines geochemical reconstructions from carbonate rocks with mineral-specific data from greenalite.

The Transvaal Supergroup in South Africa spans the Great Oxidation Event (GOE), and provides an ideal setting for studying ancient marine chemistry due to its exceptional preservation across a range of facies. This study aims to uncover early ocean conditions by investigating carbonate and IF sequences from across a shelf environment using laser ablation inductively coupled plasma-mass spectrometry. Specifically, it explores Archean oxygen oases by studying redox-sensitive rare earth element (REE) data from contorted microbial laminae and adjacent carbonate cement from microbial carbonates, alongside a new compilation of existing data to explore the implications for pre-GOE molecular oxygen availability. A novel methodology that involves cutting along bedding planes to maximize exposure of fine-grained primary seawater phases like greenalite, combined with MATLAB code to isolate greenalite data from the enclosing chert, is used to extract accurate trace metal and REE content from primary precipitates. The trace metal content from Paleoproterozoic greenalite is then used to predict Paleoproterozoic ocean metal content.

The findings from this study show that the microbial carbonates from the Campbellrand Subgroup exhibit seawater-like post-Archean Australian Shale patterns, characterized by heavy REE enrichment, small positive Eu and La anomalies, super-chondritic Y/Ho ratios, but lack Ce anomalies, indicating deposition in anoxic marine conditions. These results provide no evidence for an oxygen oasis in the Transvaal basin. However, Fe-speciation data from these carbonates show evidence for pre-GOE free molecular oxygen. This suggests that one of the proxy records is not recording primary conditions, or that cyanobacteria were producing oxygen, but it was either being consumed by aerobic processes or the environmental conditions might be too fine-scaled to be recorded by the laser ablation technique.

Greenalite from the Paleoproterozoic Kuruman Formation shows heavy REE enrichment, small positive Eu anomalies, super-chondritic Y/Ho ratios, and low total REE, consistent with formation in a shelf environment. While greenalite precipitation in vent settings is possible, significant formation likely occurred on the shelf, potentially triggered by the presence of minor Fe^{3+}, local pH increases, or warmer temperatures. High resolution data from the greenalite in this study provide quantitative constraints on marine metal concentrations in an ~2.46 Ga shelf environment, revealing drastically different patterns compared to today. Specifically, Zn and V were scarce, Ni levels were similar, Co was enriched, and Mn was highly abundant. These patterns align with thermodynamic models and other geological archives, suggesting significant impacts on early microbial evolution. This supports phylogenomic and proteomic data indicating early microbes' preference for Mn and Co over Zn. This research highlights greenalite's value as a paleo-archive and lays the groundwork for exploring the Archean and Late Proterozoic Eons to reconstruct metal concentrations across various settings and geological epochs.

Chapter 1

Introduction

1.1. Opening statement

The characteristics of marine chemical sediments can provide a snapshot of conditions on Earth in the geological past. Iron- and silica-rich sedimentary deposits, termed iron formations, are particularly significant because they were abundant deposits in the Archean Eon and Paleoproterozoic Era, and serve as the primary source of iron ore for the global steel industry. They are radically different to sedimentary rocks that form today, indicating that seawater chemistry has evolved over geological time. Low oxygen levels in the Archean Eon and Paleoproterozoic Era would have impacted the redox state of iron and other trace metals, and the primary minerals that precipitated out of seawater. Mineral preciptiation, in turn, would have influenced the cycling of other trace elements and nutrients.

This thesis aims to describe and interpret the conditions in early oceans during sediment deposition, focusing on the mineralogy of marine precipitates and their chemical composition. By clarifying which chemical precipitates formed directly from seawater, this study seeks to enhance our understanding of early Earth's ocean chemistry and biology, the locations of iron precipitation, as well as metal availability in ancient oceans. Investigating Earth's ancient conditions is complex, requiring reliable proxies and a thorough understanding of their mechanisms. This study employs the redox properties of rare earth elements and trace metals, commonly used to explore ancient ocean chemistry. Additionally, this study offers an integrated geochemical assessment of marine sedimentary deposits within South African basins, utilizing both new and existing geochemical data to improve our understanding of the availability and distribution of free molecular oxygen (O_2) in the ancient ocean. The following sections of this chapter review the relevant literature, addressing key issues related to the formation of marine sediments.

1.2. A review of Earth surface conditions during the Precambrian

1.2.1. Oxygen evolution

Geochemical studies have a long tradition of exploring the oxygenation history of the atmosphere and oceans using redox-sensitive elements and isotopic systems. While the broad patterns of atmospheric and oceanic oxygenation are relatively well established, many details about the ocean's oxygenation and the processes driving major changes in the atmosphere-ocean system's oxidation state remain unclear. Multiple studies have confirmed that during the Archean Eon and Early Paleoproterozoic Era, from 4 to 2.4 billion years ago (Ga), both the atmosphere and oceans were predominantly anoxic (e.g., Farquhar et al., 2000; Poulton & Canfield, 2011), with potential exceptions being oxygen "whiffs" (e.g., Anbar et al., 2007) and isolated "oases" in shallow ocean waters (e.g., Olson et al., 2013; Riding et al., 2014). Prior to the emergence of photosynthetic, oxygen-producing bacteria like cyanobacteria, free

O_2 in the Earth's atmosphere was less than 10^{-5} of present atmospheric levels (PAL) (Farquhar et al., 2000; Pavlov & Kasting, 2002). It is hypothesized that O_2 concentrations in the atmosphere reached appreciable proportions between 2.4 and 2.1 Ga (Bekker et al., 2004; Canfield, 2005), termed the Great Oxidation Event (GOE; Fig. 1.1) (Holland, 2002). This is based on the mass-independent fractionation of sulphur isotopes (MIF-S), a distinctive process of isotope fractionation during which the amount of isotope separation is not proportional to the difference in isotopic masses, in sulphides and sulphates (Farquhar et al., 2000). MIF-S signatures are generated and preserved exclusively in conditions where atmospheric oxygen levels are lower than 10^{-5} of PAL (Pavlov & Kasting, 2002). These signatures are absent from sedimentary rocks formed after *ca.* 2.4–2.3 Ga (Farquhar et al., 2000; Gumsley et al., 2017; Guo et al., 2009; Luo et al., 2016).

The GOE coincides approximately with the first of the great "Snowball Earth" glaciations (Evans et al., 1997). It is worth noting that the Earth's oxygenation may have been protracted, rather than just a single event, leading to suggestions that the GOE should be renamed the Great Oxidation Period (Bekker et al., 2004; Guo et al., 2009; Holland, 2002; Lyons et al., 2014). Some studies suggest that there was an initial, more significant increase in oxygen levels, lasting a few hundred million years and coinciding with the Lomagundi Event, a positive carbon isotope excursion, before they dropped to lower levels (Planavsky et al., 2012) (Fig. 1.1). While there is broad consensus that oxygen levels remained low throughout the Proterozoic Eon, studies that attempt to quantify this have produced mixed results. While chromium isotopes suggest oxygen levels remained <0.1% PAL (Crowe et al., 2013), other studies suggest oxygen levels reached 10% PAL (Planavsky et al., 2014) (Fig. 1.1).

While there is broad consensus on the timing of the GOE, the onset of oxygenic photosynthesis in the Precambrian oceans is hotly debated (Anbar & Rouxel, 2007; Canfield, 2005; Rasmussen et al., 2008), with the proposed ages varying between *ca.* 3.8 Ga (Rosing & Frei, 2004) and 2.35 Ga (Kirschvink & Kopp, 2008). Evidence for oxygen oases in Neoarchean shallow-marine carbonate successions up to hundreds of millions of years before the GOE is based on iron isotopes (Czaja et al., 2012; Dauphas et al., 2004), chromium isotopes (Crowe et al., 2013), molybdenum isotopes (Planavsky et al., 2014; Voegelin et al., 2010), and cerium anomalies (Riding et al., 2014). To reconcile this with evidence for an anoxic atmosphere, it has been suggested that O_2 was being produced in ancient oceans during oxygenic photosynthesis and was simultaneously being consumed in reactions with reducing agents such as carbon, hydrogen, iron, and sulphur supplied by hydrothermal vents (Catling et al., 2001; Claire et al., 2006; Zahnle et al., 2013). If this scenario is true, then the GOE resulted from the balance between O_2 and reducing agents shifting in favour of O_2 accumulation (Catling et al., 2001; Claire et

al., 2006; Eroglu et al., 2017; Olson et al., 2013; Zahnle et al., 2013). Other researchers have argued, instead, that oxygenic photosynthesis began at the same time as the GOE (French et al., 2015; Kirschvink & Kopp, 2008; Ward et al., 2016). The whiff concept suggests that oxygen was produced in the Archean oceans but promptly released into the atmosphere. This idea is mainly supported by rhenium and molybdenum isotope data from shales (Anbar et al., 2007; Kendall et al., 2010; Reinhard et al., 2009). However, this model for pre-GOE oxygenation remains controversial (Anbar et al., 2023; Slotznick et al., 2022).

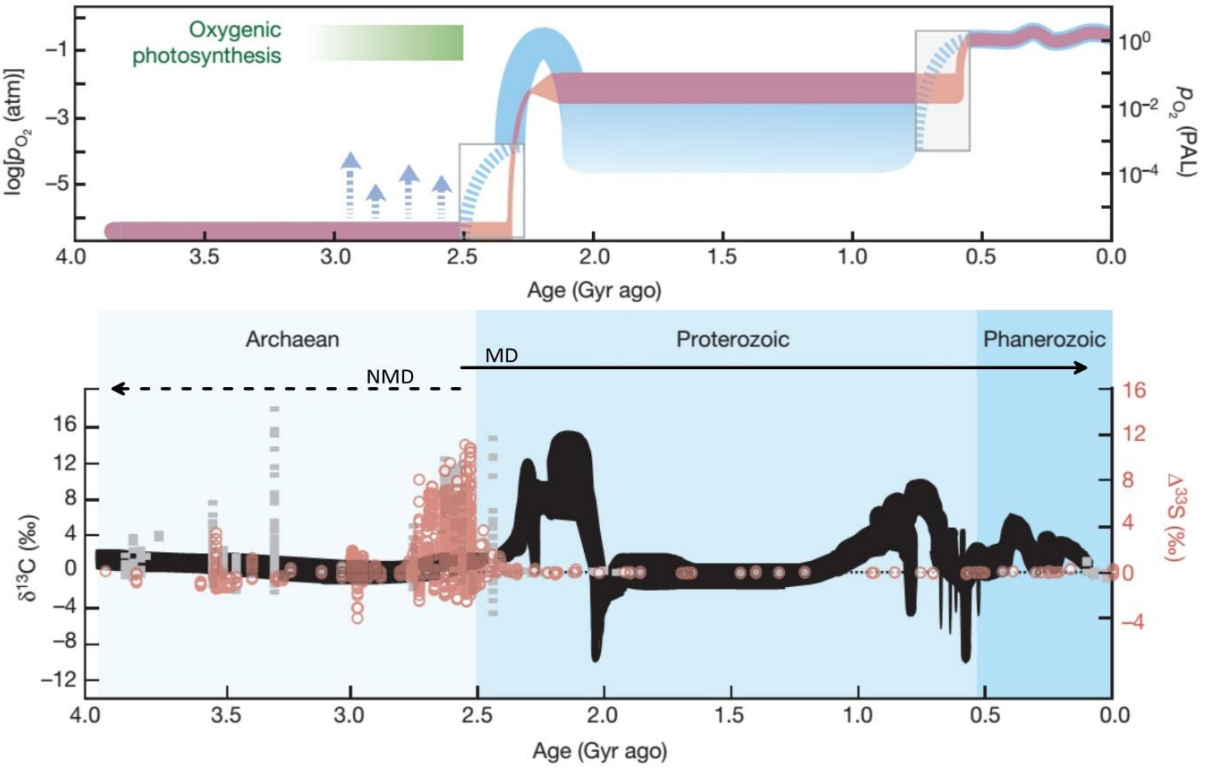

Figure 1. 1 | Changes of oxygen concentrations in Earth's atmosphere (top) and a representation of sulphur (red and grey) and carbon (black) isotope record (bottom) through time (after Lyons et al., 2014). Top: the faded red pattern highlights the popular 'two-step' evolution of Earth's oxygenation history, the blue pattern highlights the newly suggested stepwise model, the blue dashed arrows indicate possible whiffs of oxygen before the GOE and the green band highlights the (uncertain) period for the start of oxygenic photosynthesis. **Bottom:** the grey speckles indicate sulphur data obtained through secondary ion mass spectrometry (SIMS), while the red circles indicate sulphur data obtained through either laser or micro-drilling. The black arrows indicate the ages from which mass-independent-fractionation (NMD) fractionation (left) and mass-dependent (MD) fractionation (right) of sulphur have been recorded.

1.2.2. Seawater chemistry and ocean redox evolution

Significant oxygenation in the deep ocean did not occur immediately at the onset of the GOE but approximately two billion years later when atmospheric oxygen levels rose to ~100% PAL (Fig. 1.1)

(Krause et al., 2018). Throughout the Archean and Proterozoic Eons, the oceans were largely anoxic, though the type of anoxia (ferruginous or sulfidic) varied over time and space (Fig. 1.2). This anoxic nature likely influenced the evolution of other essential elements (Anbar, 2008). Early on, it was suggested that in addition to being oxygen-poor, the deep ancient ocean was sulphide-rich (euxinia) (Canfield, 1998). Evidence supporting euxinic conditions was found in 2.7–2.5 Ga shales from the Hamersley Group, Western Australia (Reinhard et al., 2009; Scott et al., 2011). However, the combination of factors needed to sustain these H_2S-rich conditions has not been identified (Boyle et al., 2013; Reinhard et al., 2013; Scott et al., 2008). Since micronutrients like molybdenum are easily removed in euxinic conditions, the Proterozoic oceans would have been molybdenum-deficient (Anbar & Knoll, 2002). However, although molybdenum shortages were found in the mid-Proterozoic ocean (Scott et al., 2008), molybdenum isotope data did not support widespread euxinia (Arnold et al., 2004). The flux of organic matter significantly influences oceanic redox conditions (Johnston et al., 2010; Poulton et al., 2010; Reinhard et al., 2009). Local organic matter flux in the ancient ocean was variable and likely limited euxinic conditions to midpoints of the water column on basin margins (Fig. 1.2a–c) (Reinhard et al., 2009). Evidence has been provided to support spatially restricted euxinic conditions (Li et al., 2010; Poulton & Canfield, 2011; Poulton et al., 2010).

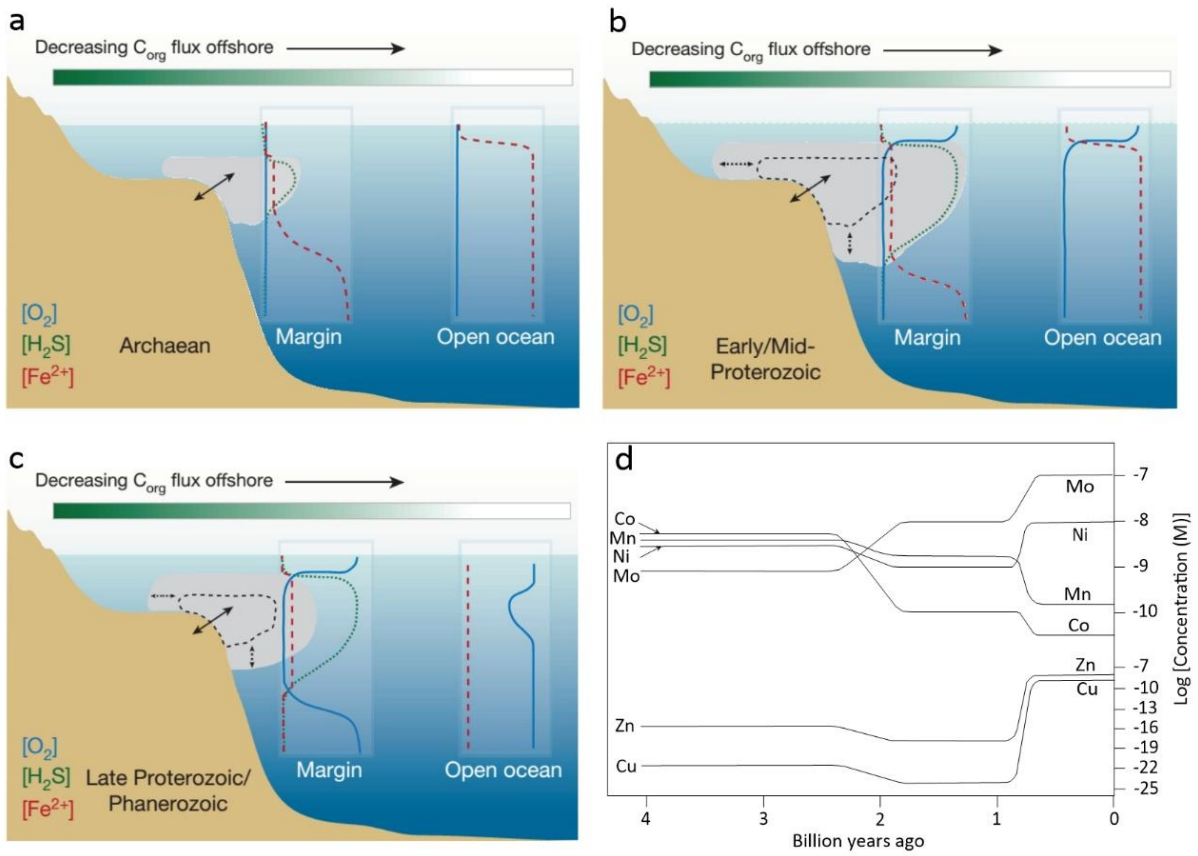

(Caption on the next page)

Figure 1. 2 | A summary of the current model of evolution of ocean redox structure (after Anbar, 2008; Lyons et al., 2014). Relative relationships between oxygen, sulphides, and iron in: **(a).** Archean oceans; **(b).** Eearly/mid-Proterozoic oceans; **(c).** Late Proterozoic/Phanerozoic oceans; Left and right inserts: the blue curves represent average O_2 profiles, the green curves represent H_2S profiles, and the red curves represent Fe^{2+} profiles. The colour bar is the general offshore decrease in local organic carbon (C_{org}) fluxes and its impact on the redox profile of the water column. Double-headed arrows denote expected expansion and contraction of sulphidic and/or ferruginous conditions (grey shading) along the productive and correspondingly reducing ocean margins. It is also important to note that small amounts of oxygen were probably present, locally and perhaps transiently, in the Archean atmosphere and shallow ocean (a), perhaps as local oxygen oases for the latter (Schopf & Klein, 1992). **(d).** Approximate changes in ocean metal concentrations through time.

More recent geochemical studies indicate that iron-rich (ferruginous) conditions were widespread in ancient ocean basins and possibly persisted into the Cambrian (Canfield et al., 2008; Planavsky et al., 2011; Poulton et al., 2010; Reinhard et al., 2013). This is supported by redox-sensitive trace element data (Och & Shields-Zhou, 2012; Partin et al., 2013; Reinhard et al., 2013; Robbins et al., 2016; Sahoo et al., 2016). The form of anoxia is crucial because it could have led to the limitation of nutrients, such as phosphate and trace metals. Euxinic basins experience intense recycling of phosphorus, while ferruginous conditions might scavenge phosphorus through sorption on iron-oxide particles (Schobben et al., 2020).

pH is a crucial parameter in seawater chemistry because it influences the saturation state of carbonate minerals (such as biogenic calcium carbonates) (Feely et al., 2009), the stability of primary authigenic and crustal minerals (Palandri & Kharaka, 2004), and the solubility, speciation, and sorption behavior of both bioessential nutrients (e.g., Fe and Zn) and proxies for Earth's surface oxidation states (e.g., Mo, Cr, and U) (Lyons et al., 2014). Early research on seawater pH values as a function of atmospheric partial pressure of CO_2 (pCO_2) provided a wide range of values (Grotzinger & Kasting, 1993; Walker, 1983). Some researchers proposed that the ancient ocean was alkaline (Kempe & Degens, 1985), acidic (Macleod et al., 1994), or neutral (Sleep & Zahnle, 2001). More recently, it has been suggested that seawater pH values increased from ~6.5–7.0 in the early Archean ocean to ~7.5–9.0 in the Phanerozoic Eon with decreasing atmospheric pCO_2 (Halevy & Bachan, 2017). Limited variability observed in calcium isotope ($\delta^{44}Ca$) data from Archean–Paleoproterozoic evaporitic sedimentary carbonates were attributed to a high ratio of calcium to carbonate alkalinity (ALK = $HCO_3^- + 2CO_3^{2-}$) in ancient seawater (Blättler et al., 2017). This suggests that the ancient oceans might not have been characterized by large amounts of dissolved carbonate species, as previously suggested by the proposed "soda ocean" (HCO_3^- > Ca^{2+}) model (Grotzinger & Kasting, 1993; Kempe & Degens, 1985).

Low sulphate (SO_4^{2-}) concentrations, estimated to be less than 80 µmol.L^{-1}, have been proposed for the Archean oceans (Habicht et al., 2002; Jamieson et al., 2013). The levels of phosphorus during the Archean Eon were suggested to have been low due to sorption onto iron oxide minerals and formation of ferrous phosphate minerals (Bjerrum & Canfield, 2002; Derry, 2015; Jones et al., 2015). However, recent findings of abundant apatite nanoparticles in banded iron formations from the Archean Hamersley Group, Western Australia (Muhling et al., 2023), and high solubility of Fe(II)-phosphate minerals (Brady et al., 2022), indicate that phosphorous concentrations were much higher than previously predicted. Phosphorus on early Earth came from weathering of various sources, including phosphate minerals, silicate minerals, reactive phases from dust and meteorites (Walton et al., 2023), and from the alteration of basalt under submarine anoxic conditions (Syverson et al., 2021; Rasmussen et al., 2024).

The distribution of bioessential metals in marine environments has changed over time, as inferred from the chemical characteristics of marine precipitates. Some of these changes are more pronounced than others (Anbar, 2008; Anbar & Knoll, 2002; Robbins et al., 2016; Severmann & Anbar, 2009). For example, the abundance of iron in the geologic record has shifted significantly, with most iron deposits forming before 1.8 Ga. In contrast, changes in the abundance of transitional metals have been more subtle (Fig. 1.2d). These shifts in metal abundance may be linked to changes in ocean redox chemistry over time (Anbar, 2008). The history of bioessential elements suggests at least two notable changes (Fig. 1.2d; Anbar et al., 2007). However, these conclusions are mainly based on geochemical concepts and few experimental predictions (Dupont et al., 2010; Robbins et al., 2013; Saito et al., 2003; Scott et al., 2013; Williams & Da Silva, 2003) to determine actual metal concentrations in ancient oceans, as they cannot be sampled directly. Therefore, the metal abundances in ancient seawater remain unclear.

1.3. Marine sediments

Marine sediments typically fall into three main categories: detrital, biogenic, and metalliferous. Detrital sediments originate from external sources, such as terrigenous (land-derived) and volcanic materials. In contrast, biogenic sediments form from biological activity, while metalliferous sediments arise from metals sourced mainly from hydrothermal vents and mid-ocean ridges (Dunlea et al., 2018). Typically, marine sediments are a mix of these components rather than pure forms of any one type (Dunlea et al., 2018). The characteristics of sediments are initially shaped by their formation environments. However, post-depositional processes, including "diagenetic" and "authigenic"

processes, further modify them. Diagenetic processes involve changes that occur after deposition, whereas authigenic processes include the in situ formation of minerals by replacing precursor minerals or through direct precipitation from seawater (Berner, 1980; Kastner, 1999; Piper & Heath, 1989).

Precambrian sediment types include shales, carbonate deposits, iron formations, and manganese formations, among other rock types. The deposition and characteristics of sedimentary rocks during the Archean Eon were influenced by the evolving crustal conditions, the composition of the early atmosphere and oceans, and the environment of sediment precipitation (Eriksson et al., 1994; Eriksson, 1995; Lowe, 1994). Despite undergoing extensive diagenesis, these ancient marine sediments remain invaluable for reconstructing the environmental and chemical history of early Earth.

1.3.1. Shale

Shale is the most prevalent type of sedimentary rock and consists of very fine-grained minerals. It typically forms in low-energy environments such as deep marine settings, but can also develop in shallow seas, river floodplains, and playas (Blatt et al., 2006). The composition of shale can vary widely, with differing levels of silt, clay, organic matter, oxides, and calcareous content. Archean shales are primarily composed of aluminosilicates, which mostly came from volcanic and terrigenous sources (Hofmann et al., 2003). Terrigenous sediments are produced through the weathering of upper crustal rocks exposed at the Earth's surface (McLennan & Taylor, 1991). Consequently, Archean shales often contain high concentrations of aluminum (Al) and titanium (Ti), along with other elements such as potassium (K), sodium (Na), and rubidium (Rb).

1.3.2. Manganese formations

Manganese deposition occurs through redox-controlled processes in modern environments, predominantly in deep-sea areas (Hein et al., 1997; Nicholson, 1992; Roy, 1992). Hydrothermal vents contribute significantly to the ocean's manganese content, with dispersion from vent sites influenced by flow rate, temperature, and residence time in seawater. Sedimentary iron-manganese crusts form on volcanic substrates through hydrogenous deposition in mid-water column oxygen-minimum zones, while abyssal iron-manganese nodules derive from both basin water and pore water metal supplies (Roy, 1992). Biological activity also influences manganese deposition, with stratified basins like the Black Sea serving as models for ancient manganese deposition during sea-level highstands and transgressive-regressive cycles. Under anoxic conditions, manganese-rich carbonate can form through early diagenetic reactions (Roy, 1992).

During the Early Archean Eon, manganese deposits were sparse, with manganese enrichment observed in Archean carbonate rocks (Veizer et al., 1982) and locally in iron formations (Gole & Klein, 1981), but not reaching economically viable levels (Roy, 2000). Despite similar geological conditions in other regions, significant manganese deposits were found only in specific locations, such as India and Brazil (Roy, 2000). A notable shift occurred in the Late Archean Eon when manganese mineralization began to develop more extensively, albeit in limited regions. The early Paleoproterozoic Era saw a significant increase in manganese deposits, particularly the Kalahari manganese field in South Africa, representing the largest known manganese accumulation on land (Beukes, 1986). This evolution reflects the interplay of multiple factors driving changes in the geological and geochemical landscape during the Archean Eon, with manganese-rich layers providing valuable insights into ancient oceanic redox conditions.

1.3.3. Carbonate successions

Carbonates, often classified as biogenic sediments, originate from the processes of production, preservation, and subsequent diagenetic transformation of minerals initially created by living organisms. In ancient geological settings, these carbonates typically formed in calm, sheltered environments such as platforms, leeward slopes of these platforms, or shallow epeiric seas (Eriksson, 1995; Schopf et al., 1983). The formation of carbonates is intricately linked to the behavior of CO_2 in the fluid environment, which has a direct impact on pH through various chemical reactions (Eriksson et al., 1998). During the Late Archean Eon, a significant phase of carbonate platform development began, indicating a substantial fixation of CO_2 (Altermann & Nelson, 1998).

The key processes influencing carbonate dynamics include carbonate dissolution and precipitation. Carbonate dissolution occurs when CO_2 reacts with water and calcium carbonate, resulting in the formation of calcium ions and bicarbonate ions ($CO_2 + H_2O + CaCO_3 \rightarrow Ca^{2+} + 2HCO_3^-$) (Walter & Burton, 1990). This reaction is driven by the addition of CO_2 from organic matter decomposition, which decreases carbonate ion activity and leads to dissolution. Conversely, carbonate precipitation happens when calcium ions and bicarbonate ions recombine to form calcium carbonate, releasing CO_2 and water in the process ($Ca^{2+} + 2HCO_3^- \rightarrow CaCO_3 + CO_2 + H_2O$) (Claypool & Kaplan, 1974; Ritger et al., 1987). This process can be stimulated by CO_2 degassing due to a drop in pressure or by microbial CO_2 reduction in anoxic sediments. Hence, the behavior of CO_2 is crucial in driving both carbonate dissolution and precipitation.

Archean carbonates, which are predominantly found as calcite/aragonite ($CaCO_3$) and dolomite ($CaMgCO_3$), are notably characterized by herringbone calcite and abundant stromatolites, such as roll-up structures, indicating their formation in the photic zone (Buick, 1992; Schopf et al., 1983; Sumner, 1997; Sumner & Grotzinger, 2004). These Archean carbonates are primarily authigenic (Ritger et al., 1987; Webb & Kamber, 2000). As a result, they retain characteristics of ancient seawater conditions, making them valuable proxies for studying past marine environments..

1.3.4. Iron formations

Iron formations (IF) are unique sedimentary rocks formed as chemical precipitates in marine environments, characterized by ≥ 15 wt.% iron typically associated with chert (Gross, 1980; James, 1954; Klein, 2005). Throughout this study, the term "iron formation" is used to refer generally to iron-rich sedimentary rocks, whereas "banded iron formation" is used to denote distinctly microbanded IFs. Most IFs were deposited in the Precambrian, with the earliest known examples dating back to 3.8 Ga in the Isua Greenstone Belt, West Greenland (Moorbath et al., 1973). The most well-preserved iron formations date to around 2.5 Ga, particularly evidenced by deposits in the Transvaal Supergroup, South Africa, and the Hamersley Group, Western Australia (Bekker et al., 2010; Beukes & Gutzmer, 2008; Simonson et al., 2003; Trendall, 2002). After ~2.5 Ga, IF deposition declined significantly but there was a peak around 1.9–1.8 Ga (Klein, 2005) and again during the Snowball Earth events, *ca*. 720 to 635 Ma (Klein & Beukes, 1993; Rooney et al., 2015; Swanson-Hysell et al., 2010).

Given their presence during significant changes in ocean chemistry and the biosphere, the mechanisms of IF deposition likely evolved over time (Bekker et al., 2010). Extensive research has been conducted on the genesis of IF, but this study specifically focuses on the primary mineralogy of IF and the geochemical composition of the primary phase. Understanding these aspects is crucial for predicting the environmental conditions and geochemical processes that prevailed in the Precambrian oceans during the formation of these ancient sedimentary rocks.

1.3.4.1. Depositional models of iron formations

Given the economic importance of IF, they have been at the centre of many studies (Bau & Dulski, 1996; Bekker et al., 2010; Konhauser et al., 2002, 2017; Planavsky et al., 2010, 2011, 2014; Rasmussen et al., 2015, 2017, 2021). However, aspects of their genesis remain poorly understood. The formation of large iron deposits suggests that iron was transported as aqueous Fe^{2+}, since Fe^{3+} is insoluble in the presence of even trace amounts of oxygen (< 1 µM) at neutral pH. Isley (1995) was the first to suggest that the iron required for IF genesis came from deep marine systems, and was transported to shallow

marine levels as Fe^{2+}. The primary minerals in IF and the mechanism by which they were deposited remains controversial (Bekker et al., 2010; Beukes & Gutzmer, 2008; Klein, 2005; Rasmussen et al., 2021; Simonson et al., 2003; Trendall, 2002).

Since iron-bearing minerals in IF are commonly ferric (Fe^{3+}-bearing), the prevailing models for IF genesis propose redox processes involving oxidation of Fe^{2+} to Fe^{3+}, followed by precipitation of ferric oxyhydroxides that get converted after deposition to the iron-rich minerals which make up IF. This model is referred to as the "ferric model" from this point forth. Oxidation of Fe^{2+} is associated with an iron isotope fractionation, consistent with positive $\delta^{56}Fe$ signals as recorded in the magnetite of IF (Beard & Johnson, 2004; Johnson & Beard, 2006; Johnson et al., 2008b). In the ferric model, Fe^{2+} can be oxidized in oxygen-free environments through biological processes such as CO_2 fixation by photoautotrophic bacteria in sunlight (Crowe et al., 2008; Konhauser et al., 2002; Widdel et al., 1993), or abiotic photo-oxidation by sunlight. Alternatively, Fe^{2+} can be oxidized in the presence of O_2 produced during photosynthesis by oxygen-generating cyanobacteria, which also reside in the photic zone (Beukes, 1992; Beukes & Gutzmer, 2008; Klein & Beukes, 1989). This suggests that the oxidation of Fe^{2+} is directly or indirectly linked to biological processes and sunlight. However, Fe^{2+} oxidation can also happen below the photic zone by chemolithoautotrophs in dark, anoxic waters, though this process is slower (Konhauser et al., 2002). Experiments have shown that in Archean-like anoxic seawater, ferrous iron rapidly oxidizes after forming ferrous hydroxide (Dodd et al., 2022). This hydroxide decomposes into elemental iron, which then reacts with water at room temperature to form ferric iron and hydrogen gas. The ferric iron can subsequently develop into green rust, a mixed iron phase that transforms into mixed-valence iron minerals.The presence of ferrous and mixed-valence iron minerals in IFs, such as magnetite, hematite, and siderite, is explained by secondary reduction of ferric oxide/hydroxide precipitates on the seafloor and during early diagenesis. This reduction could occur through reactions with abundant Fe^{2+} or with organic carbon, supported by light carbon isotope signatures in IF (Johnson et al., 2008b; Tice & Lowe, 2004). However, there is recent evidence that light C isotope signatures can also be generated abiotically at high precipitation rates (Jiang et al., 2022).

More recently, a new model has been proposed, where the primary IF minerals were ferrous (Fe^{2+}), including Fe(II)-silicates and Fe(II)-carbonates (Johnson et al., 2018; Rasmussen et al., 2013, 2014, 2015, 2017, 2018; Tosca et al., 2016). In contrast to the ferric model, there are no redox processes involved in this model and the Fe(II)-silicate and -carbonate phases precipitated abiotically once critical supersaturation was attained. Iron silicates have previously been identified in IF, but for a long

time they were considered secondary minerals (Beukes & Gutzmer, 2008; Fischer & Knoll, 2009; Klein, 2005). However, a large body of recent work has reexamined IF using high resolution imaging, and uncovered widespread greenalite minerals with petrographic evidence for an early origin. For example, greenalite commonly pre-dates shrinkage structures in chert (Rasmussen et al., 2013, 2014). This model, referred to as the "ferrous model" from this point forth, proposes that ferric minerals in IF are products of post-depositional oxidative processes. While some primary iron-rich minerals are preserved by the enclosing chert, ferric minerals form through fluid-mediated oxidative weathering of iron-rich precursor phases. Evidence for this includes observations of hematite minerals increasing in abundance near faults and fluid flow pathways and following micro-fractures (Rasmussen et al., 2014).

It is well established that IF have experienced early and late diagenesis, fluid flow, and metamorphism over their multibillion-year existence, and therefore, many—if not all—minerals present in IF are attributed to diagenesis and later alteration (Bekker et al., 2014; Beukes, 1984; Klein, 2005; Pufahl & Hiatt, 2012; Simonson et al., 2003). Identifying the original precipitate(s) of IF has therefore been a critical question pertinent to understanding what IF represent and record with respect to ancient seawater chemistry and early life. While it is impossible to pinpoint the precursor phases that originally formed in the water column, it is possible to determine the first stable crystalline minerals that formed under Archean ocean conditions and were preservable in the rock record—which will be called the primary mineral(s).

1.3.4.2. Depositional settings of iron formations and their characteristics

The depositional models and settings of IF have changed through time, from the Archean Eon through the Paleoproterozoic to the Neoproterozoic Eras, and reflect diverse paleo-environmental changes on Earth through time (Bekker et al., 2010; Beukes, 1992; Klein, 2005). Archean IFs, dating back to the Eoarchean Era (3.8–2.3 Ga), formed under a fully anoxic atmosphere (Farquhar et al., 2007) and are often associated with volcanic-sedimentary sequences (Bekker et al., 2010; Klein, 2005). Examples include sedimentary successions in the Canadian greenstone belts, the Yilgarn Block and the Hamersley Group in Western Australia, the Itabira Group BIF in Brazil, the Transvaal supergroup BIF in South Africa, which formed under similar atmospheric conditions. These formations, known as Algoma-type deposits, feature alternating bands of ferric and ferrous minerals and chert, indicating deposition in deepwater basins with minimal detrital material (Beukes & Gutzmer, 2008; Krapež et al., 2003; Trendall, 2002). Their depositional settings are complex due to diagenesis and metamorphism, but they likely formed in closed to semi-closed basins with significant hydrothermal activity (Bekker et al., 2010).

In contrast, Paleoproterozoic IFs (*ca*. 1.90–1.85 Ga), referred to as Superior-type deposits, formed under a weakly oxygenated atmosphere and typically exhibit granular textures (Klein, 2005). Examples include those of the Lake Superior region, and the Frere Formation in Western Ausralia. These formations are typically associated with black shales, carbonates, and arenites, and are found in well-preserved sequences outside greenstone belts (Beukes & Gutzmer, 2008; Klein, 2005). They exhibit structures like ripple marks and cross-bedding, suggesting deposition in shallow-water, high-energy environments near continental shelves (Gross, 1980; Morris, 1993). The ferric model has been used to explain their formation, with Fe^{2+}-rich waters reaching oxygenated zones, leading to the precipitation of ferrihydrite and lateral variations in mineralogical assemblages (Beukes & Gutzmer, 2008; Klein, 2005).

Neoproterozoic IFs (*ca*. 0.8–0.6 Ga) appeared almost two billion years after the GOE and are associated with glacial diamictites. Unlike earlier formations, these deposits are characterized by Fe-oxide phases with positive Eu anomalies (Beukes, 1992; Klein & Beukes, 1993). They formed during the Cryogenian Snowball Earth period when complete ice cover created reducing, stagnant conditions. It was previously suggested that interglacial periods led to the exposure of water masses to an oxygenated atmosphere, causing iron oxidation and IF deposition alongside diamictites (Klein & Beukes, 1993). However, recent studies suggest that these formations may have been deposited below ice shelves through an ice pump mechanism, mixing cold, oxygenated glacial fluid with ferruginous seawater, rather than drastic environmental changes from glacial retreat (Lechte & Wallace, 2016; Lechte et al., 2018).

1.4. Rare Earth Elements as a Geochemical Proxy

The redox properties of rare earth elements, including their concentrations, distribution patterns, and elemental anomalies, provide valuable insights into Earth's history. These properties help elucidate the geochemical characteristics of authigenic components (Bolhar et al., 2004; Dauphas et al., 2007) and the sources and characteristics of the precipitating waters (Bau & Dulski, 1999; Chen et al., 2006; Douville et al., 1999; Kamber & Webb, 2001; Zhao & Zheng, 2017). Additionally, they offer insights into marine redox environments (Bolhar & Van Kranendonk, 2007; Byrne & Sholkovitz, 1996; German & Elderfield, 1990; Ling et al., 2013) and the formation mechanisms of rocks and minerals (Himmler et al., 2010).

Rare earth elements in seawater are typically low in concentration and can be incorporated into authigenic components (Rasmussen et al., 1998), such as carbonates (Kamber & Webb, 2001; Meyer

et al., 2012), phosphates (Chen et al., 2015; Shields & Webb, 2004), banded IFs (Bolhar et al., 2005; Gourcerol et al., 2015), and cherts (Zhao et al., 2016). These components act as geochemical archives of the ancient marine environments from which they precipitated, providing essential information on the depositional settings (Guo et al., 2007; Kamber & Webb, 2001; Robbins et al., 2016). Reconstructing past environments relies on accurately interpreting the geochemical characteristics of these proxies, which requires ensuring the primary signals are preserved. Various depositional phases, including carbonates and primary phase(s) from banded IFs, show significant potential for this purpose.

1.4.1. Rare earth element systematics

The 15 rare earth elements (REE), or the lanthanides series, are often analysed alonside yttrium (Y). In order of increasing atomic number, the lanthanides include lanthanum (La), cerium (Ce), praseodymium (Pr), neodymium (Nd), promethium (Pm), samarium (Sm), europium (Eu), gadolinium (Gd), terbium (Tb), dysprosium (Dy), holmium (Ho), erbium (Er), thulium (Tm), ytterbium (Yb), and lutetium (Lu). Traditionally, the REEs are grouped into light rare earth elements (LREEs; La, Ce, Pr, Nd, and Ho), medium rare earth elements (MREEs; Sm, Eu, Gd, Tb, and Dy), and heavy rare earth elements (HREEs; Er, Tm, and Yb) (Chen et al., 2015). In general, the REEs form trivalent cations, but in some circumstances, Ce can also form tetravalent cations, and Eu can form divalent cations. As each new electron is added across the series, they enter the 4*f* orbital, but because they are located inside the outer three valence electrons, they do not directly participate in bonding. The outer or valence electrons for the lanthananides ($5d6s^2$) are the same as for Y ($4d5s^2$). Thus, the REEs have very similar behaviour to one another across the series. The ionic radius of Y is similar to that of Ho and thus tends to have coherent geochemical characteristics with the REEs. As the atomic number increases from La to Lu, there is an accompanying increase in nuclear charge, which results from the progressive filling of the 4*f* electron orbital. This causes the effective ionic radius of the trivalent ions to decrease gradually from La^{3+} to Lu^{3+} (Elderfield & Greaves, 1982; Haynes, 2016).

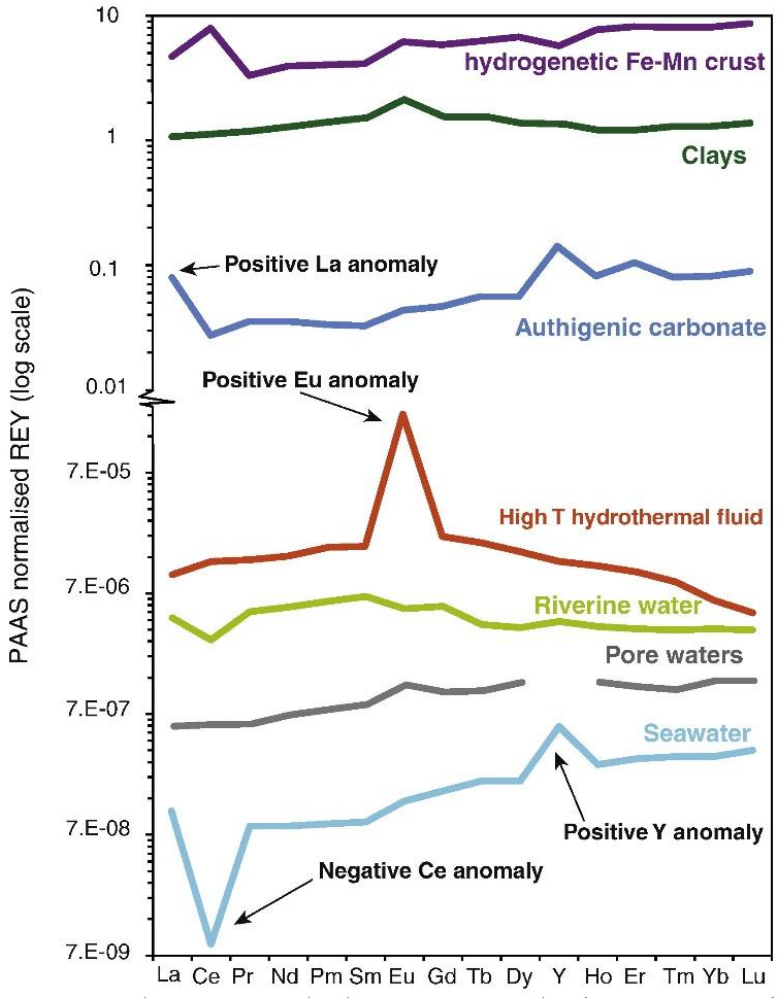

Figure 1. 3 | Post-Archean Australian Shale-normalized REE + Y patterns for different mineral phases and marine environments, emphasizing elements that show deviations from the typical trend (from Tostevin et al., 2016). While some patterns, like those for seawater, are broadly consistent, others, such as those for pore waters, exhibit significant local variations.

The main source of REEs to the ocean is terrigenous dissolved REEs from surface fluxes, with supplementary sources including hydrothermal activity, glacial activity, aeolian dust, and magmatic rocks (Dubinin, 2004). The abundances of REEs are additionally controlled by solution-particle interaction which are in turn controlled by factors such as seawater salinity, redox state, and water depths (Elderfield, 1988). Although the REEs generally have coherent chemical characteristics, some are unique. This anomalous behavior can be quantified by comparing the element's normalized concentration to the neighbouring elements. Differences in the abundances of lanthanides with odd versus even atomic numbers create a spike-like pattern in unnormalized REE plots. In sedimentary rocks, REE concentrations are typically normalized to Post-Archean Australian Shale (PAAS) to remove the spike pattern, but for other rock types, they may be normalized to chondrites (CHUR), mid-ocean ridge basalts (MORB), or other standards. They are normalized by taking the REE's concentration ratio

between the sample and the appropriate standard (e.g., Pourmand et al., 2012; Taylor & McLennan, 1985). The anomaly shown by an element is generally represented as REE_n/REE_n^* = $2[REE]_n/([REE]_{n-1} + [REE]_{n+1})$, where REE_n is the REE concentration normalized to the appropriate standard. The symbol * indicates the expected average normalized concentration of the REE, based on its neighbouring elements in the periodic sequence, and n refers to the atomic number. However, in cases where the neighbouring elements are themselves potentially anomalous, or where there is only one adjacent element, anomalies can be quantified graphically or by making use of other non-adjacent elements (Bau & Dulski, 1996; Lawrence et al., 2006). The unique chemical character of selected REEs introduces deviations from the normalized slope (Fig. 1.3). To identify seawater REE signatures from ancient ocean proxies, it is necessary to understand these processes in the modern ocean.

The PAAS-normalized concentrations of REEs in modern seawater display a predictable pattern (Fig. 1.3), which is characterized by:

(1) A relative enrichment of HREEs compared to LREEs and MREEs. This enrichment is due to the preferential adsorption of LREEs onto particle surfaces, which is linked to the increased complexation of carbonate ions with decreasing atomic radii (Byrne & Kim, 1990; Cantrell & Byrne, 1987; Sholkovitz et al., 1994). As carbonate ion complexation intensifies in HREEs, the amount of free REE available for adsorption onto particles decreases, resulting in higher total concentrations of HREEs in seawater (Lee & Byrne, 1993). The PAAS-normalized Yb/Nd ratio is used to measure this enrichment, with values greater than 1 indicating enrichment of HREEs.

(2) A negative Ce anomaly. In seawater with sufficient oxygen levels, Ce^{3+} is oxidized to Ce^{4+} and subsequently removed from the water column through adsorption onto mineral surfaces (Elderfield, 1988). This oxidation process leads to redox-stratified seawater, which can be observed in authigenic minerals formed in oxygen-rich environments (Webb & Kamber, 2000). The redox process primarily occurs on the surfaces of Mn^{4+}-oxyhydroxides/oxides, where Ce^{4+} is effectively immobilized (Takahashi et al., 2002). This relationship is often seen as positive Ce anomalies in Fe/Mn oxyhydroxide phases due to Ce oxidation and scavenging, while authigenic phases from seawater typically exhibit negative Ce anomalies (Pattan et al., 2005; Piper & Bau, 2013). While similar oxidation can occur on Fe^{3+} oxyhydroxide/oxide surfaces (Bau, 1999; Bau & Koschinsky, 2009), the evidence is less definitive compared to Mn-oxyhydroxides/oxides (Loges et al., 2012). Conversely, positive Ce anomalies in authigenic

carbonates can arise under conditions where oxygen levels are sufficient to oxidize Ce^{3+} in surface waters, but become limited in deeper, redox-stratified sections of the water column (Tostevin et al., 2016). As oxidized particles descend into lower oxygen zones, they are reduced, releasing Ce^{3+} and causing an anomalous enrichment at depth, which is then incorporated into precipitating carbonates (Planavsky et al., 2010; Tostevin et al., 2016). Various methods have been proposed for quantifying Ce anomalies (Bau & Dulski, 1996; Bolhar et al., 2004; Lawrence et al., 2006), with the following geometric formula from Lawrence et al. (2006) being used in this study to quantify the Ce anomaly.

$$Ce_{SN}/Ce^{*}_{SN} = \frac{[Ce]_{SN}}{([Pr]_{SN})^2/\,[Nd]_{SN}}$$

(3) A positive La anomaly. This positive La anomaly in PAAS-normalized REE patterns isn't always distinctly visible due to the common depletion of the neighboring Ce. This anomalous behavior of La is linked to its relatively high stability in solution, which may be attributed to the lack of inner 4*f* electrons (De Baar et al., 1991). Given that the Ce is commonly depleted, the anomaly is most accurately determined by extrapolating from the concentrations of Pr and Nd. The La anomaly in this study is calculated using the formula below proposed by Lawrence et al. (2006).

$$La_{SN}/La^{*}_{SN} = \frac{[La]_{SN}}{([Pr]_{SN})^3/\,([Nd]_{SN})^2}$$

(4) A small positive Gd anomaly (De Baar et al., 1985a), although negative anomalies have also been reported. This Gd anomaly is attributed to the variable surface complexation properties and solution stabilities of Gd (Kim et al., 1991). It is suggested that the stability of Gd in solution is influenced by its half-filled 4*f* electron orbital (De Baar et al., 1985b; Kim et al., 1991). The enrichment of Gd in seawater is linked to its ability to form low stability complexes, limiting its removal from solution (Lee & Byrne, 1993). The Gd anomaly is quantified by extrapolating from Tb and Sm, using the formula below provided by Lawrence et al. (2006).

$$Gd_{SN}/Gd^{*}_{SN} = \frac{[Gd]_{SN}}{(([Tb]_{SN})^2.[Sm]_{SN})^{1/3}}$$

(5) A significant positive Y anomaly. Ho and Y share an identical ionic radius and both occur in the trivalent oxidation state (Shannon, 1976), resulting in similar chemical behaviors in the modern ocean and comparable nutrient-like concentration profiles (Bolhar et al., 2004). The Y/Ho ratio in seawater is typically higher than in shales and chondrites and decreases with depth (Byrne & Lee, 1993; Høgdahl et al., 1968; Nozaki et al., 1997). This variation is likely due to differences in the complexation behavior or higher solubility of Y compared to Ho-

phosphates, or it may result from fractionation during the weathering of continental materials (Bau, 1999). It has been suggested that scavenging by particulate matter (Nozaki et al., 1997; Zhang et al., 1994) or preferential incorporation into Fe-oxyhydroxides (Bau, 1999) could cause the decoupling of Y from Ho. An Y/Ho ratio of > 36 is used to assess the preservation of seawater patterns.

(6) A small positive Eu anomaly. Modern seawater generally lacks a Eu anomaly, but it is a common feature in well-mixed Archean and Paleoproterozoic seawater (Bau & Dulski, 1996; Bau et al., 1995; Bolhar et al., 2004). Eu enrichment in hydrothermal fluids is due to Eu's unique behavior; in reducing and slightly acidic solutions above ~200 °C, Eu exists mainly as Eu^{2+}. Unlike its trivalent counterparts, Eu^{2+} remains in the dissolved phase during water-rock interactions, leading to a positive Eu anomaly in high-temperature hydrothermal fluids, not seen in low-temperature systems (Bau et al., 1995). In this study, this anomaly is quantified using the formula provided by Lawrence et al. (2006).

$$Eu_{SN}/Eu^{*}_{SN} = \frac{([Eu])_{SN}}{(([Sm]_{SN})^{2}.[Tb]_{SN})^{1/3}}$$

Several features make REEs and yttrium (REY) particularly valuable for reconstructing ancient paleoredox conditions. REY appear to be relatively robust to alteration relative to other proxy systems, and the quality of preservation can be checked using internal benchmarks. For ancient sediments to be considered reliable archives of ancient marine settings, their PAAS-normalized REY patterns should display a seawater-like signature (Fig. 1.3). In summary, typical features of these profiles include a positive Y anomaly, HREE over LREE enrichment, a low total REE concentration, and an La anomaly. Such patterns indicate that authigenic minerals formed under marine conditions and retained the primary signals, suggesting minimal secondary alteration and thereby enhancing the reliability of other geochemical data (Bolhar & Van Kranendonk, 2007; Frimmel, 2010). In primary REY patterns, the Ce anomaly can provide information about the local redox conditions.

1.5. Geological setting – Transvaal Supergroup

The Archean-Paleoproterozoic Transvaal Supergroup on the Kaapvaal Craton in South Africa presents an outstanding sedimentary and stratigraphic record, ideal for examining changes in ocean chemistry over time (Fig. 1.4). The lithological units of the Transvaal Supergroup were deposited around the time of the GOE (Bekker et al., 2001; Gumsley et al., 2017; Guo et al., 2009; Senger et al., 2023). This supergroup contains some of the most well-preserved and laterally extensive sedimentary sequences globally (Beukes & Gutzmer, 2008), having only experienced sub-greenschist metamorphism (Miyano

& Beukes, 1984). The ~2.66–2.24 Ga Transvaal Supergroup (Fischer et al., 2009; Gumsley et al., 2017; Senger et al., 2023) comprises a mix of siliciclastic-carbonate ramps that transition upwards into broad carbonate platforms, followed by deep subtidal banded IFs with associated manganese deposits, and glacial deposits (Beukes, 1986; Beukes & Gutzmer, 2008; Schröder et al., 2006). This sequence is preserved in two primary basins in South Africa: the western Griqualand West basin (Northern Cape province) and the eastern Transvaal basin (Gauteng and Northwest provinces) (Fig. 1.4; Eriksson et al., 1995). Although this study focuses primarily on the Griqualand West basin, it also incorporates data from the Transvaal basin.

The Griqualand West basin has a stratigraphic depth exceeding 2 km, consisting of the Ghaap and Postmasburg Groups (Fig. 1.4; Beukes, 1986). These groups are stratigraphically equivalent to the Chuniespoort and Pretoria Groups, respectively, in the Transvaal basin (Fig. 1.4). The Ghaap Group includes the Schmidtsdrif, Campbellrand, Asbesheuwels, and Koegas Subgroups, while the Postmasburg Group consists of the Magkanyene and Ongeluk Formations, along with the Voëlwater Subgroup (see sections 1.5.1 and 1.5.2 below for description). The original sedimentary sequence of the Transvaal Supergroup has been well established but may appear disturbed in tectonically affected areas (Beukes, 1986; Knoll & Beukes, 2009; Schröder et al., 2006).

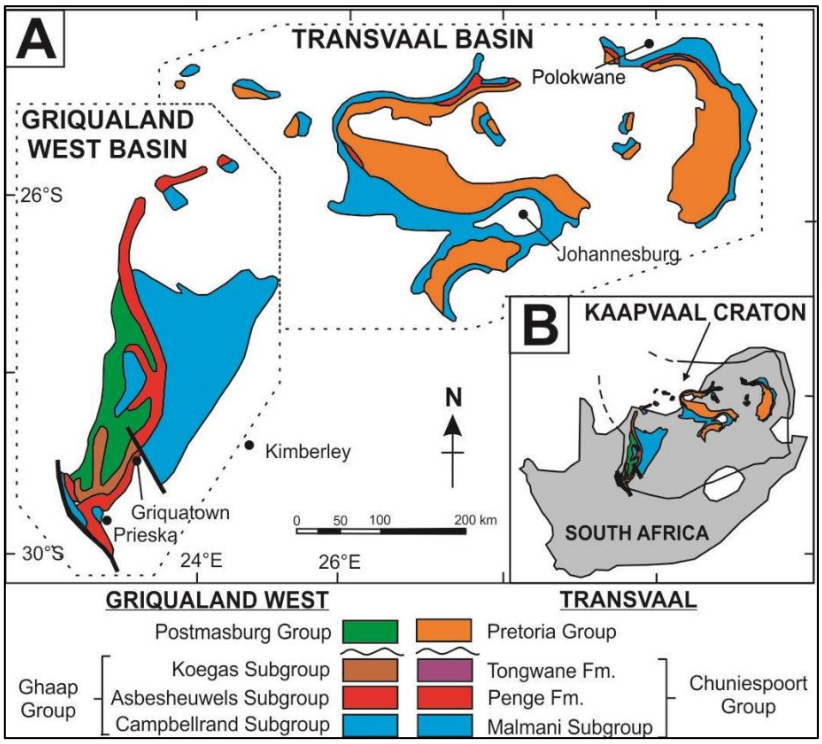

Figure 1. 4 | A simplified map illustrating the distribution of the Transvaal Supergroup in South Africa: (A). The locations of Griqualand West and Transvaal basins; **(B).** The position of the Kaapvaal Craton within South Africa, where the basins are situated (from Warke, 2017). Fm. = Formation.

1.5.1. The Ghaap Group

~2.66–2.64 Ga Schmidtsdrif Subgroup

The Schmidtsdrif Subgroup, occuring at the base of the Transvaal Supergroup in the Griqualand West basin, consists of siliciclastic-carbonate ramp successions dating back to approximately 2.66–2.64 Ga (Fischer et al., 2009). The subgroup's thickness ranges from 10 to 250 m and includes three distinct formations (Eriksson et al., 2006). These formations, from bottom to top, are the Vryburg Formation, characterized by subtidal and tidal flat sandstones; the Boomplaas Formation, made up of shallow-water oolitic and stromatolitic carbonates; and the Lokammona Formation, consisting of deeper-water siliciclastic mudstones. The geological record of the Schmidtsdrif Subgroup indicates a cratonic flooding event and the development of a mixed siliciclastic-carbonate slope (Eriksson et al., 2006). The basal Vryburg Formation in the Griqualand West basin correlates stratigraphically with the basal Black Reef Formation of the Transvaal basin (Beukes et al., 2019).

~2.55–2.52 Ga Campbellrand Subgroup

The Campbellrand Subgroup in the Griqualand West basin, equivalent to the Malmani Subgroup in the Transvaal basin (e.g., Beukes et al., 2019), was deposited between 2552 ± 11 and 2521 ± 3 Ma (Fig. 1.4; Barton et al., 1994; Sumner & Bowring, 1996). The Campbellrand subgroup consists of a thick sequence of carbonate successions, deposited in two main domains: a shallow subtidal platform domain and a deeper basinal domain (Beukes, 1980). The shallow subtidal platform sequence is up to 1900 m thick and consists of oolitic and stromatolitic carbonate rocks. This platform gradually transitions into the basinal domain, which reaches up to 650 m in thickness and comprises microbialitic and laminated carbonates interbedded with siliciclastic mudstone (Beukes, 1987; Sumner & Grotzinger, 2004).

The lithostratigraphic units that make up these domains are named differently. In the basinal domain, the Campbellrand Subgroup includes the basal Monteville Formation, characterized by dolostones with some siliciclastic mudstones and thin microbialite beds. It is overlain by the Nauga Formation, characterized by microbialites and slope dolostones, with an increasing dolostone content and fewer stromatolites towards the top. The basinal domain is topped by the Klein Naute Formation, made up of significant chert nodules, diagenetic pyrite, and siliciclastic mudstone (Beukes, 1980, 1987). In the shelf domain, the sequence begins with the Monteville Formation at the base, followed by the Reivilo, Fairfield, Klipfonteinheuwel, Papkuil, Klippan, and Kogelbeen Formations, which are equivalent to the

Nauga Formation of the basinal domain. The shelf domain is capped by the Gamohaan Formation (Beukes, 1980, 1987).

~2.48–2.46 Ga Asbestos Hills Subgroup

The Asbestos Hills Subgroup, also known as the Ashbeshewels Subgroup, conformably overlies the Campbellrand Subgroup in the Griqualand West basin (Fig. 1.4). It primarily consists of up to 1,000 m of IF and banded chert (Beukes, 1984). The Asbestos Hills Subgroup includes both the Kuruman Formation (KIF) and the Griquatown Formation (GIF). The KIF is equivalent to the Penge Formation in the Transvaal Basin (Beukes et al., 2019). The KIF, deposited approximately around 2480 ± 6 and 2460 ± 10 Ma (Lantink et al., 2019; Pickard, 2003; Zeh et al., 2020), forms the base of the Asbestos Hills Subgroup. The KIF is characterized by rhythmically banded iron formations (BIF), indicating deposition in an open-shelf environment below the wave base (Beukes, 1984; Beukes & Klein, 1990). This formation includes the Groenwater Member at the base, dominated by Fe carbonate and Fe oxide phases, followed by the chert-poor, Fe silicate- and Fe carbonate-rich BIF of the Riries Member, and capped by the Fe carbonate-rich, clastic-textured IF of the Ouplaas Member (Beukes, 1984).

The KIF transitions upwards to the shallower-water, clastic-textured IFs of the GIF (Beukes, 1984; Beukes & Klein, 1990). The GIF consists of the basal Daniëlskuil Member, characterized by Fe silicate- and Fe carbonate-rich IF interbedded with grainstones. This is overlain by the Skietfontein Member, consisting of Fe silicate lutite-BIF. Above this is the Middelwater Member, composed of Fe silicate-rich IF, and capped by the Pietersberg Member, also consisting of Fe silicate-rich IF (Beukes, 1984; Beukes & Klein, 1990).

~2.46–2.45 Ga Koegas Subgroup

The Koegas Subgroup comformably overlies the Asbestos Hills Subgroup and occurs at the top of the Ghaap Group (Fig. 1.4). It consists of IFs, minor carbonate deposits, and immature siliciclastics, representing a transition from distal chemical precipitation to proximal clastic sedimentation, indicative of a transition from open-shelf to deltaic settings (Beukes, 1983; Schröder et al., 2011; Warke et al., 2020). The depositional age of the Koegas Subgroup has been recently constrained to around 2456.6 ± 7 and 2451.5 ± 2.5 Ma (Senger et al., 2023).

The Koegas Subgroup consists of several lithostratigraphic units. In summary, the Pannetjie Formation occurs at the base. This formation features an upward-coarsening sequence, transitioning from mudstone to sandstone. Above this lies the Doradale Formation, which is characterized by BIF and Fe

carbonate-rich granular IFs. The sequence continues upward into the Kwakwas Formation, consisting of Fe silicate-rich mudstones. Overlying the Kwakwas Formation is the Naragas Formation, which is predominantly siliciclastic. This is followed by the Heynskop Formation, marked by iron-rich lithologies with coarser siliciclastics becoming more prominent towards the top of the formation. The Koegas Subgroup is capped by the Rooinekke and Nelani Formations. These formations are dominated by Fe oxide-rich and Fe silicate-rich BIF and include stromatolitic carbonate sequences (Beukes, 1983; Beukes & Gutzmer, 2008; Nel, 2013; Schier et al., 2018; Schröder et al., 2011).

1.5.2. The Postmasburg Group

~2.44–2.42 Ga Magkanyene Formation

The Makganyene Formation unconformably overlies the Koegas Subgroup and is located at the base of the Postmasburg Group in the Griqualand West basin (Fig. 1.4). This formation primarily consists of glacial diamictites interbedded with minor siltstones and sandstones (Beukes, 1986; Eriksson et al., 2006). The glacial diamictites are believed to have been deposited at low latitude during a Snowball Earth glacial event (Evans et al., 1997; Kirschvink et al., 2000; Polteau et al., 2006) that occurred shortly after the GOE (Gumsley et al., 2017). While the deposition of the Makganyene Formation was previously dated to around 2436 ± 14 Ma (Moore et al., 2012), more recent data suggests a depositional age of 2423.1 ± 1 Ma (Senger et al., 2023).

~2.42 Ga Ongeluk Formation

The Ongeluk Formation, part of the Postmasburg Group in the Griqualand West basin, has no equivalent in the Transvaal basin (Gumsley et al., 2017; Moore et al., 2012; Senger et al., 2023). It consists of a 300–900 m-thick volcanic succession that generally conformably overlies, and occasionally interfingers with, the Makganyene Formation (Cornell et al., 1996; Eriksson et al., 1995; Warke, 2017). This succession is made up of tholeiitic basaltic andesites, featuring hyaloclastites, pillow lavas, and massive flows, suggesting subaqueous extrusion (Cornell et al., 1996). The Ongeluk Formation has been reliably dated to 2424 ± 32 Ma (Gumsley et al., 2017).

~2.41–2.39 Ga Voëlwater Subgroup

The uppermost succession of the Transvaal Supergroup in the Griqualand West basin is represented by the Mooidraai Formation, which comprises banded iron-rich carbonates indicative of a shallow-marine platform (Kunzmann et al., 2014). These carbonates have been dated to 2394 ± 23 and 2392 ± 26 Ma (Bau et al., 1999; Fairey et al., 2013). The Mooidraai Formation conformably overlies the 2413 ± 15 Ma Hotazel Formation (Gutzmer & Beukes, 1998), and together they form the Voëlwater

Subgroup. The Hotazel Formation consists of 100–150 m thick chemical sediments, characterized by four BIF units interbedded with three distinct manganese ore beds (Beukes et al., 2016; Tsikos et al., 2010; Tsikos & Moore, 1997). Transitional hematite lutite, or fine-grained cherty IFs, form the contact between the manganese beds and BIF, with thicknesses ranging from a few decimeters to several meters (Gutzmer & Beukes, 1996a; Tsikos et al., 2003, 2010). The chemical marine sediments of the Hotazel Formation were likely deposited in a mid-ocean ridge or back-arc setting (Cornell & Schütte, 1995; Schneiderhan et al., 2006) through diagenetic organic matter oxidation and Fe/Mn reduction (Johnson et al., 2013; Maynard, 2010; Nealson & Myers, 1992) or primary aerobic oxidation of Mn(II) to Mn(III) (Mhlanga et al., 2023; Tsikos et al., 2010).

1.6. Thesis structure

The following chapters are included in the rest of this thesis.

Chapter 2: Searching for Local Oxygen Generation in Microbial Carbonates of the Campbellrand Subgroup, Transvaal Supergroup. This chapter provides a stratigraphic description of microbial carbonate samples used in this thesis to investigate the presence of pre-GOE oxygen oases in the Transvaal Supegroup. It then discusses the mineralogical composition and presents the geochemical data from various regions of interest within these samples. The implications of these findings for the onset of oxygenic photosynthesis are explored in conjunction with a new compilation of published data for the Transvaal Supergroup.

Chapter 3: Identification of Greenalite and New Methodology for Isolating its Trace Element Signal (PUBLICATION). This chapter contextualizes the samples selected for analyses of the primary depositional environment of BIF within their stratigraphic framework. It details the analytical techniques used to identify and analyse greenalite, introduces a novel method to extract optimal signals from greenalite laths, and describes additional post-processing techniques to isolate the greenalite signal.

Chapter 4: A Seawater Origin for Greenalite in Iron Formation of the Transvaal Supergroup (PUBLICATION). This chapter, based on the main findings from my paper recently published by Earth and Planetary Science Letters, describes and interprets the rare earth element composition of greenalite. It discusses the implications for the depositional environment of the Transvaal Supergroup BIF and ancient seawater chemistry.

Chapter 5: Metal Concentrations in Paleoproterozoic Seawater. This chapter uses the trace metal composition measured from the Paleoproterozoic natural greenalite described in chapters 3 and 4 above, to predict metal concentrations in Precambrian oceans and discusses the implications for geology and biology.

Chapter 6: Conclusions and Outlook. This chapter summarizes the findings of my research, placing them within the broader context of current efforts in geochemistry and geobiology.

Chapter 2

Searching for Local Oxygen Generation in Microbial Carbonates of the Campbellrand Subgroup, Transvaal Supergroup

2.1. Introduction

The absence of MIF-S in sedimentary minerals deposited after 2.4 Ga is strong evidence for the GOE (Farquhar et al., 2000; Pavlov & Kasting, 2002). However, some geochemical data suggest that small amounts of free oxygen may have existed locally in seawater—either as brief accumulations in the atmosphere (whiffs) or isolated pockets dissolved in seawater (oxygen oases)—hundreds of millions of years before the atmosphere became fully oxygenated (Anbar et al., 2007; Olson et al., 2013; Ossa et al., 2018; Planavsky et al., 2014; Riding et al., 2014; Voegelin et al., 2010). For example, Mo concentrations measured from shales and carbonates of the Ghaap Group, Transvaal Supergroup, South Africa, along with rapidly fluctuating and strongly fractionated δ^{98}Mo values, suggest the presence of free O_2 between 2.6 and 2.5 Ga (Eroglu et al., 2015; Voegelin et al., 2010; Wille et al., 2007). Coupled Fe and Mo isotopes from the Ghaap Group (Czaja et al., 2012), as well as enrichment in redox-sensitive Mo and Re in the Mount McRae shale, Hamersley Basin, Western Australia, have also been interpreted as evidence for whiffs of atmospheric oxygen before the GOE (Anbar et al., 2007). Negative Ce anomalies from 2.8 Ga shallow-marine limestones of Steep Rock Lake, Canada (Riding et al., 2014), provide local evidence for the accumulation of oxygen in shallow marine settings. Frei et al. (2009) later provided Cr-isotope evidence from deep-water BIF, indicating fluctuations in Archean atmospheric oxygen levels. If free oxygen was being produced in the ocean before the GOE, then it must have been consumed before it could leak into the atmosphere. One potential sink is the oxidation of aqueous Fe^{2+} and Mn^{2+} to Fe(III)-, Mn(III)-, and Mn(IV)-bearing minerals, which has been suggested to be consistent with the widespread occurrence of oxide minerals in Archean BIF and Mn-rich rocks (Canfield, 2005; Holland, 2006).

Models for pre-GOE oxygen oases in seawater suggest an early origin for oxygenic photosynthesis, and by extension, the evolution of cyanobacteria. However, some geochemical models suggest that the evolution of oxygenic photosynthesis would trigger rapid atmospheric oxidation, and suggest it developed much later, immediately preceding the GOE (Ward et al., 2016). Recently, some of the geochemical evidence for pre-GOE oxygen has been questioned. For example, Slotznick et al. (2022) discovered that previously reported signatures from trace metals and sulfur isotopes from the Mount McRae Shales, used to argue for pre-GOE oxygenation, are not consistent across longer stratigraphic sections. They concluded that metal enrichment may have originated from Mo-enriched volcanic glass, rather than from seawater reservoirs as previously assumed (but see Anbar et al. (2023) for a rebuttal). In addition, recent high resolution imaging techniques of Archean rocks suggest that many of the oxide minerals in IF are products of late-stage oxidation, and that the primary minerals were in fact Fe(II)-silicates and Fe(II)-carbonates (Rasmussen et al., 2021). Therefore, the timing of the rise of

oxygenic photosynthesis, and by extension, the history of marine oxygenation and the depositional mechanism for Archean sediments, remains controversial.

If there were pockets of free oxygen in the Archean ocean, reconstructing their distribution and extent would help constrain the role of oxygen in the generation of Fe- and Mn-rich marine sediments. Such reconstructions can be achieved by studying the trace and rare earth element plus yttrium (REY) signatures of Archean carbonate rocks. Microbial carbonates, in particular, are a good target because they were generated by microbial mats, whose modern counterparts contain cyanobacteria (Buick, 1992; Wilmeth et al., 2019). Therefore, if oxygenic cyanobacteria were present before the GOE, we would expect signals of oxygenation in these facies. In addition, carbonates usually form in ramp environments, in relatively shallow waters, and can provide local information to complement deeper water, outer ramp sediments such as BIF. The shallow-water carbonates of the ~2.55 Ga Campbellrand Subgroup, Transvaal Supergroup, South Africa contain a range of microbialite fabrics, and are overlain by Asbestos Hills Subgroup BIF (Fig. 2.1), making them suitable for this study. The first step in utilizing microbial carbonates for geochemical analysis is to ensure that they are low in non-carbonate components, such as clastic, volcanic, or diagenetic fragments, which may contaminate the signal. Once the integrity of the samples is confirmed, PAAS-normalized REY patterns can provide valuable insights into marine redox conditions during deposition (Kamber & Webb, 2001).

This chapter presents analyses of representative drill core and outcrop samples from the Campbellrand Subgroup, confirming their mineralogy and microfabric textures, and reports their trace element chemistry. Further analyses of REY in microbial horizons (MHs), where oxygen-producing cyanobacteria would most likely be found, as well as in adjacent non-microbial horizons (NMHs), are conducted. The Ce anomaly is used to search for a direct link between microbial mats and oxygen generation. The objective is to track pre-GOE marine redox conditions in the Transvaal Supergroup, South Africa. To achieve this, new data is examined and the results are compared with previous studies that examined Archean carbonates and BIF from the Transvaal Supergroup. All REY anomalies and ratios were recalculated using geometric methods and the REY trends were reassessed to ensure consistency across the datasets. Only data that strictly meets certain criteria were included in the interpreted dataset. This comparative approach allows integration of results from this study with existing knowledge and discussion of the local redox conditions in an ancient marine setting in the run up to the GOE.

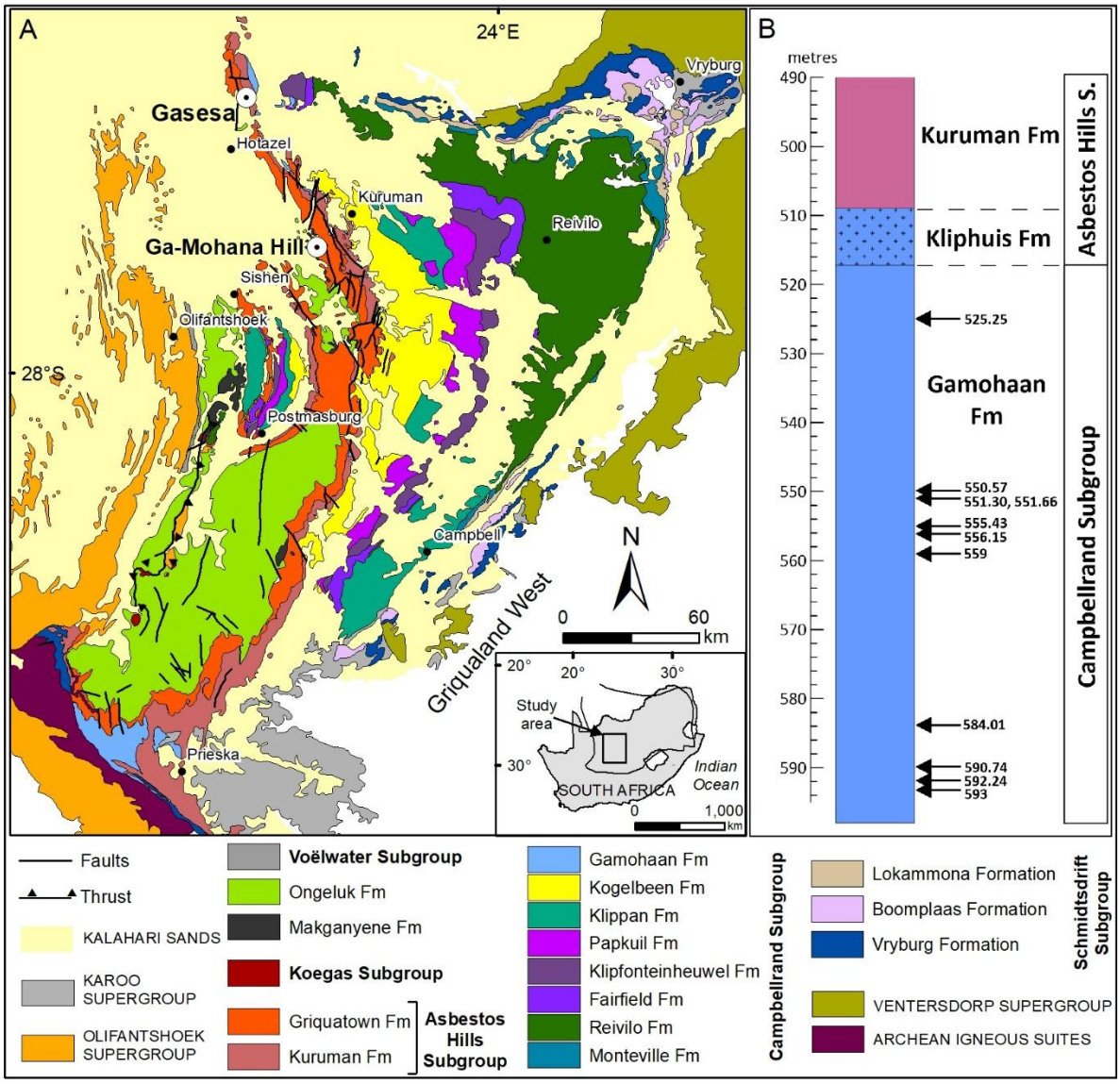

Figure 2. 1 | (A). Distribution of the Griqualand West basin outcrops, Transvaal Supergroup, South Africa, showing the locations of the Gasesa drill core and Ga-Mohana Hill sampled for this sudy; **(B)**. Log section of the Gasesa drill core used in this study, with an expanded view to accurately represent sample collection depths from the Gamohaan Formation.

2.2. Stratigraphic setting and sample selection

The top-most carbonate successions of the Campbellrand Subgroup in the shelf domain of the Griqualand West basin are the Kogelbeen and Gamohaan Formations (Fig. 2.1). The Kogelbeen Formation is about 300 m thick and consists of limestone, dolomite, and chert, with oolites, microbialites, and laminates, along with doleritic intrusions. This formation is thought to represent shallow subtidal to intertidal environments, with organic-rich and fenestral sediments indicating a lagoonal setting (Beukes, 1980). The overlying Gamohaan Formation, about 110 m thick, contains microfossils interpreted as Neoarchean cyanobacteria (Butterfield, 2015; Schirrmeister et al., 2016;

Wright & Altermann, 2000). It is characterized by organic-rich layers, dolomitic intercalations, and fenestral limestones, indicating a deeper, oxygen-poor basinal environment (Sumner, 1997). The lower part of the formation displays ripple-marked sandy dolomites and repetitive layers of coarse-grained carbonate rocks and microbialites, indicating energetic shallow-water conditions. The middle and upper parts are characterized by an abundance of pyrite nodules.

Samples representing the Kogelbeen and Gamohaan Formations were collected as outcrop samples from Ga-Mohana Hill (also referred to as Kuruman Kop in some literature) (Fig. 2.1A) and from the Gasesa drill core (Fig. 2.1B). While outcrop samples are more laterally extensive and can be placed into a wider context, drill core samples are also important, because they are likely to have better preserved fabrics.

The lithotype succession intersected by the Gasesa drill core represents typical sequences of the Transvaal Supergroup. From bottom to top, it includes: 70 m of the Gamohaan Formation, which contains organic-rich microbial limestones, dolomites, and thin shale beds; 200 m of the Kuruman Formation; and the upper 180 m of partially weathered Griquatown Formation. The occurrence of hematite cherts in the Kliphuis Formation (Beukes, 1984) marks the transition from the Gamohaan Formation to the chemical-sedimentary Kuruman Formation, and the transition from the Kuruman to the Griquatown Formation is gradational.

2.3. Methods

Samples were described (see section 2.4) and collected from key locations at Ga-Mohana Hill and the Gasesa drill core, where microbial textures were observed (Fig. 2.1). Specifically, samples from the Kogelbeen and Gamohaan Formations were taken from Ga-Mohana Hill, while the Gasesa drill core provided samples solely from the Gamohaan Formation. The best-preserved samples were selected for detailed mineralogical and geochemical analyses.

2.3.1. Sample preparation

Samples were cut into pieces of approximately 1 cm by 2 cm using a diamond circular saw. These pieces were then mounted in epoxy resin and polished to achieve a flat topography, and adjacent slices were used to prepare thin sections. The remaining off-cuts were powdered for further mineralogical and geochemical analyses. The off-cuts were crushed in a jaw crusher before being pulverized on a SIEBTECHNIK disk swing mill with a tungsten carbide steel mill set and rings at the Department of Geological Sciences at the University of Cape Town (UCT), South Africa. The mineralogy

was identified using optical microscopy, X-ray diffraction and scanning electron microscope analyses. The carbonate-bound trace element and REY concentrations were determined using both solution and laser ablation inductively coupled plasma-mass spectrometry (ICP-MS), with more abundant elements analysed using solution inductively coupled plasma-atomic emission spectrometry (ICP-AES). Measurements were taken from specific regions of interest (ROIs) within 22 samples (Table 2.1).

Table 2. 1 | Details of sedimentary and textural characteristics of microbial carbonate samples, and the types of analyses (solution ICP-MS/AES and in situ laser ablation ICP-MS) performed on selected ROIs.

Sample ID	Sample characteristics	LA ICP-MS	ICP-MS & ICP-AES
Drill core samples			
525.25	Microbial limestone with roll-up structures: They are typically dark grey carbonate rocks comprising microbial mats, characterized by 1 to 5 mm-thick layers of partially degraded filaments, which typically surround coarse-grained (5–30 µm) white calcite cement.	15 spots	Not used
550.57		5 spots	
551.3		13 spots	
551.66		15 spots	
556.15		10 spots	
559		12 spots	
584.01		10 spots	
590.74		10 spots	
592.24		5 spots	
593		15 spots	
Outcrop samples			
GC-23-1	Microbial limestone with roll-up structures: Dark grey carbonates, consisting of microbial mats. They are characterized by 1 to 5 mm-thick layers of partially degraded filaments, surrounding coarse-grained (5–30 µm) white calcite cement, though the cement may appear slightly altered.	20 spots	Not used
GC-23-22		20 spots	Not used
GCC01		Not used	1 horizon
GCC03		Not used	1 horizon
GCC04		10 spots	3 horizons
GCC09		10 spots	5 horizons
GCC12		10 spots	Not used
GCC06A	Microbial dolomite with cuspate stromatolite: Dark brown cement with cuspate shaped-assemblages comprising vertical pillars, concave drapes, and crescent-shaped calcite lenses, often stacked and surrounded by contorted microbial mats.	Not used	1 horizon
GCC06B-2		10 spots	1 horizon
GCC06B-1		7 spots	Not used
GCC11		10 spots	Not used
GCC10	Dark brown dolomite cement with distinctive spheruliti (herringbone) calcite aggregates.	Not used	4 horizons

2.3.2. Mineralogical analyses

2.3.2.1. Optical microscopy

Thin sections were examined under a petrographic microscope in transmitted and reflected polarized light to identify the textures and phases present in the microbial carbonate samples. The optical images of the microbial carbonate were captured using a Zeiss Axio Scope A1 imaging light microscope in the Department of Geological Sciences at UCT. This microscope has a 100 W halogen illumination that is stabilized for both reflected and transmitted light microscopy, resulting in high intensity and sharp images.

2.3.2.2. X-ray diffraction (XRD) analyses

The identification of very fine-grained phases present in bulk rock powdered samples was performed using a Bruker AXS D8 Advanced X-ray diffractometer with a Co-anode and K radiation in the Department of Chemical Engineering at UCT. The X-ray diffractometer was set to a generator voltage of 35 kV and a current of 40 mA, with 2θ values ranging from 5° to 120°. Data were collected in 0.031° 2θ step sizes, with the counting time set to 1 s for bulk powders. PANalytical X'Pert HighScore Plus software and the PANalytical Inorganic Crystal Structure Database (ICSD) were used for background stripping, indexing of diffraction peaks, and mineral identification.

2.3.2.3. Scanning electron microscopy (SEM)

Epoxy mounts were studied with back-scattered electron (BSE) imaging using a Nova NanoSEM in the Department of Chemical Engineering at UCT. The samples were observed and imaged at a 5.5 mm working distance and 20 kV accelerating voltage. In this work, BSE images were used to determine the morphology of minerals, while energy dispersive X-ray spectrometry (EDS) using the INCA (Integrated Calibration and Application Tool) software from Oxford Instruments provided information on their major element chemistry. Minerals were identified by comparing their EDS spectra with published data. For SEM-EDS analysis, most microbial carbonate samples were not carbon coated to ensure accurate carbon readings.

2.3.3. Geochemical analyses

Powders were micro-drilled from selected calcite-dominated microbial and non-microbial horizons adjacent to blocks used for thin section preparation. The powders were then digested using the sequential extraction method of Tostevin et al. (2016). In summary, 25 mg of powder was transferred into a 15 ml Greiner tube, and 5 mg of the sample (20%) was dissolved by adding 0.45 ml of 1% (0.2 M) nitric acid (HNO_3). The resulting solution was then shaken and allowed to react for an hour, and

then centrifuged at 4000 rpm for 10 minutes. The supernate was extracted and discarded. Next, 0.9 ml of 0.2 M HNO_3 was added to the dried-down sample to dissolve a further 10 mg of $CaCO_3$ (40%). The resulting solution was centrifuged and the supernate was removed, filtered (0.2 µm), transferred to a clean centrifuge tube and then dried down. Trace and major element concentrations in micro-drilled and acid digested samples were measured using an Agilent 7500cx inductively coupled plasma-mass spectrometer and a Horoba JY Ultima inductively coupled plasma-atomic emission spectrometer, respectively, at University College London, United Kingdom. To prepare the samples for analysis, 10 ml of 2% HNO_3 was added and the samples were dissolved over 24 hours with intermittent shaking, followed by centrifugation at 4000 rpm for 10 minutes. Accuracy and precision were determined from internal standards (Suppl. Table S1a).

Polished epoxy mounts were prepared to expose microbial and non-microbial horizons that could easily be targeted using a laser beam. These polished mounts were analysed in situ using a ThermoFischer Scientific Element 2 magnetic sector inductively coupled plasma-mass spetrometer and a Lambda Physik excimer laser (193 nm) with GeoLas optics at Utrecht University, Netherlands. The trace element analysis used 60–120 µm laser spot size, 10 Hz frequency, 10 J/cm^2 energy density, and the NIST612 synthetic glass as the primary calibration reference material. The synthetic basaltic glass BCR2G was used as the secondary standard. Each analysis includes 60–70 s background measurement and 45 s sample signal measurement. Raw isotope data were reduced using the "Trace Elements IS" data reduction scheme, using Iolite version 3.71 (Paton et al., 2011). In Iolite, baseline correction was applied using my defined time intervals to adjust the values for each isotope across the entire session. The standard values for BCR-2G and NIST612 were sourced from the GeoREM database (Jochum et al., 2005). For trace elements with concentrations greater than 0.05 ppm, NIST612 typically demonstrates an accuracy within ± 7% and an analytical precision of ± 2% (1 RSD). In contrast, BCR-2G shows accuracy within ± 25% and the same analytical precision of ± 10% (1 RSD) (Suppl. Table S1b).

Measured REY concentrations were normalized to PAAS (Pourmand et al., 2012) and are denoted as REY_{SN}. Promethium (Pm) does not occur in nature, so values were interpolated based on neighbouring elements. Furthermore, anomalies of REY_{SN} were calculated using geometric methods (Lawrence et al., 2006), as described in section 1.4.1. These methods were combined with binary plots of $(Ce/Ce^*)_{SN}$ vs. $(Pr/Pr^*)_{SN}$ (Bau & Dulski, 1996) to accurately determine the presence or absence of anomalies. (Kamber et al., 2014) suggested this combination to mitigate errors and biases inherent in each method, providing a more accurate assessment of Ce anomalies. Screening steps identified samples

that might produce false redox signals or deviate from seawater REY trends by checking for HREE enrichment over LREE depletion, positive Y, Eu, and La anomalies, Y/Ho ratios greater than 36, low total REE, and overall smooth REY trends (e.g., Tostevin et al., 2016). To further ensure the accuracy of calculated Ce anomalies, $(Ce/Ce^*)_{SN}$ was considered significant if it was less than 0.9 (negative anomaly) or greater than 1.3 (positive anomaly). Averaged major and trace element data are reported in Table 2.2, while averaged REY data are reported in Table 2.3. The complete dataset is presented in supplementary Tables S2 and S3.

2.4. Mineralogy and petrography

The Gamohaan and Kogelbeen Formation sediments exposed at Ga-Mohana Hill are predominantly microbialitic limestones, with evident dolomitization. The dominant microbialites in the study area are stromatolites with distinct morphologies, including contorted and cuspate-fenestrate forms (Fig. 2.2). Other sedimentary structures identified include calcite mosaics, dolomitization, antiformal structures, and collapse and solution breccia. The stratigraphy and sedeimentary structures at Ga-Mohana Hill have been well documented in previous studies (Gandin & Wright, 2007; Gandin et al., 2005; Sumner, 1997; Wright & Altermann, 2000). In this chapter, I focus on the fabrics relevant to this study, specifically the contorted microbial laminae (MHs) that form microbial mats, which potentially hosted oxygen-producing cyanobacteria, and the interstitial non-microbial horizons (NMHs), which include cements.

In the Gasesa drill core, microbialitic limestones of the Gamohaan Formation comprise MHs characterized by roll-up structures and crumpled mats, interlayered with non-microbial calcite horizons. At varying intervals, the microbialites alternate with shale beds ranging in thickness from 1 to 10 cm. In some layers, abundant nodular pyrite is preferentially associated with MHs and shale beds (Fig. 2.2). The diameter of pyrite nodules in the Gamohaan Formation microbialites ranges from a few millimeters to several centimeters and is commonly deformed into ovoid shapes.

2.4.1. Non-microbial horizons (NMHs)

The NMHs in outcrop samples are composed mainly of calcite, with some occurrences of dolomite. The dolomite fabric makes up less than 10% of the lithostratigraphic units at Ga-Mohana Hill. It typically appears as dark, rusty, organic-rich submicron cements in hand samples and also as a replacement phase (Fig. 2.2b and d). Two distinct textural forms of calcite aggregates were observed.

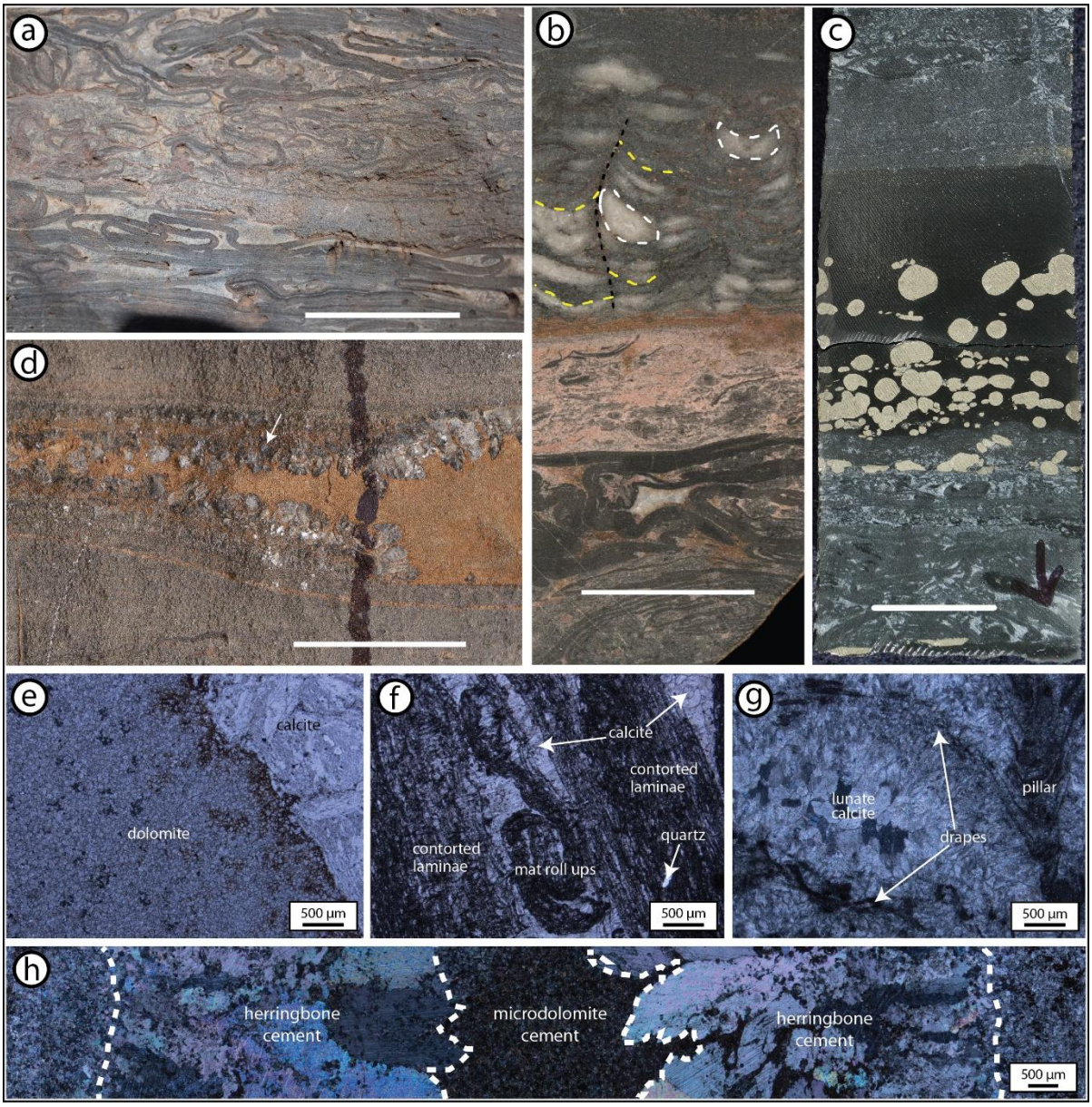

Figure 2. 2 | Hand samples and photomicrographs of microbialites of the Gamohaan Formation: **(a)**. Profile view of contorted microbial laminae with non-microbial cements; **(b)**. Layered cuspate-fenestrate stromatolite with microdolomite cement and contorted microbial laminae, showing pillar (black dotted line), drape structure (yellow dotted line), and nodular lunate calcite cement (white dotted line); **(c)**. Drill core sample of microbialites interlayered with a black shale bed containing a band of disseminated pyrite nodules; **(d)**. Spherulitic (herringbone) calcite aggregates surrounding dolomite cement; **(e)**. PPL photomicrograph showing large calcite aggregates adjacent to dolomite cement; **(f)**. Plane-polarized light photomicrograph of contorted microbial laminae with calcite infillings; **(g)**. Cross-polarized light photomicrograph of cuspate-fenestrate stromatolite textures, highlighting main fabric elements; **(h)**. Cross-polarized light image showing microdolomite cement flanked by herringbone (spheurilitic) calcite and microbial fabric. White scale bar = 2 cm.

The first form consists of coarse (50–100 µm) grained, white calcite crystals. These aggregates generally dominate the NMHs that occupy the spaces between the contorted microbial mats (Fig.

2.2a–c). The aggregates may be lunate (Fig. 2.2b) or may take the shape of the void spaces between the contorted mats (Fig. 2.2a–c). Nucleation of this form seems to be inhibited in microbialite laminae, which instead consist of submicron (<20 μm) calcite infillings. The second form, which is rare, consists of spherulitic calcite aggregates that appear shiny on the outcrop. These form layers that enclose and appear to intrude the adjacent laminated microbial structures (Fig. 2.2d). Spherulitic calcite aggregates are characterized by elongated-lenticular, crenulated crystals whose long axes are perpendicular to the banding in the support structures. This calcite aggregate typically has a darker coloration.

Petrographically, the dolomite fabric is fabric-destructive. Dolomite is characterized by fine-sized, subhedral to euhedral crystals with a relatively unimodal crystal size distribution (50 to 250 μm) (Fig. 2.2e and h). Under plane-polarized light, dolomite exhibits cloudy, inclusion-rich cores and clear-rimmed crystals (Fig. 2.2e) and displays sharp extinction under crossed polars. The calcite crystals that represent the most abundant form show undulose extinction along their long axis in plane-polarized light. However, spherulitic calcite ranges from 1–5 mm in length and 500 μm to 1 mm in width, showing complex extinction; one part of the crystal exhibits undulose extinction while the other part shows unit extinction (Fig. 2.2h).

2.4.2. Microbial horizons (MHs)

The most abundant microbial fabrics in the Gamohaan Formation consist of thin, regular layers or bundles of partially degraded organic filaments forming a microbial mat, with less frequent microsparitic and granular laminae (Fig. 2.2). Preserved micrite (1–4 μm calcite grains) is lacking or rarely found as a thin lining of organic filaments. Wavy or plane layers are commonly found in association with the deformed beds consisting of lenticular or contorted laminar shreds and/or rolled up ribbons (Fig. 2.2a) enclosed in calcite spar (5–30 μm). The contortions generally range from the microscale up to a few centimetres in length, and are 1–8 mm thick.

Another type of microbial fabric encountered in the Gamohaan Formation is cuspate stromalite. The cuspate stromatolites, which are commonly associated with contorted mats, are characterized by three main fabric elements: (i) a vertical pillar, (ii) sub-horizontal drape structures, which are commonly concave upwards, and (iii) calcite lenses representing lunate void-filings (Fig. 2.2b). The cuspate morphologies in Fig. 2.2b occur as columns of concave-up, void-filled calcite cement stacked upward, bounded by contorted MH in limestone.

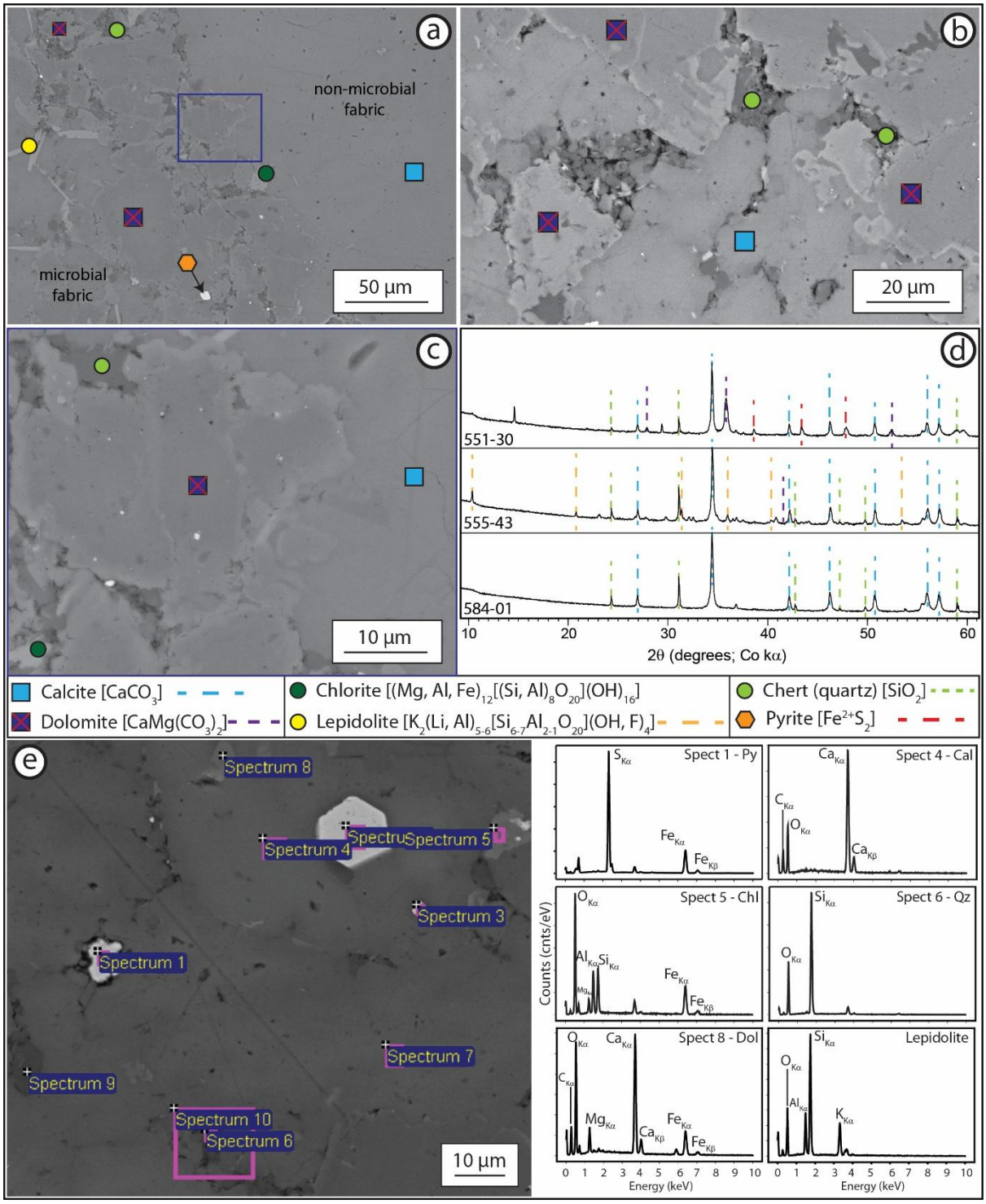

Figure 2. 3 | Mineral phases identified in the microbial carbonates of the Campbellrand Subgroup: **(a–c)**. SEM-BSE view of nanoparticles forming the microbial fabric in drill core samples; **(d)**. Selected XRD spectra of microbial carbonate samples from the Gasesa drill core, showing all mineral phases present; **(e)**. SEM-BSE image along with results of SEM-EDS analyses, highlighting the spectra of identified minerals. Py = pyrite; Cal = calcite; Chl = chlorite; Qz = quartz; Dol = dolomite.

Under the microscope, MHs and NMHs can be easily distinguished. In transmitted light, MHs (support, drape, and contorted laminae) consist mostly of finely crystalline (10–50 μm), planar to non-planar, Fe-rich dolomite crystals (Fig. 2.2f). The contorted laminae are characterized by bands dominated by Fe-rich dolomite (30–40 μm). These bands, which make up the MHs, show porosity filled with finer, equigranular calcite (10–30 μm) compared to the coarser calcite grains (50–100 μm) found between the contorted microbial mats (Fig. 2.2f). The contorted bands are thicker than the drape structures, which are 10–100 μm thick (Fig. 2.2g). In the contorted laminae horizons of the drill core samples, Fe-rich dolomite and calcite are sometimes associated with small, equant, cubic or nodular pyrite crystals, which are absent in outcrop samples from Ga-Mohana Hill (Fig. 2.2). SEM-EDS, SEM-BSE, and XRD analyses of the MHs revealed several minerals: quartz, dolomite, calcite, pyrite, apatite, and Fe-oxide, as well as fibers and sheets of clay minerals (Fig. 2.3).

Calcite [$CaCO_3$]

SEM-EDS analyses reveal that this phase is composed largely of Ca (24.4 to 32.4%), along with C and O. The phase also contains minor amounts of Fe (0.4 to 1.2%) and Mn (0 to 0.7%), indicating a calcite mineralogy (Fig. 2.3a–e). The crystal sizes vary from 50 to 100 μm (Fig. 2.3a–c). The presence of this phase is further confirmed by matching and overlapping XRD peaks with rhombohedral calcite from the ICSD database.

Dolomite [$CaMg(CO_3)_2$]

Crystals with high Mg (>5%) and Ca content, identified by SEM-EDS, were interpreted as dolomite. These crystals, with low Mn (0.9–1.5%) and high Fe (2.1–6.6%), indicate an Fe-rich dolomite mineralogy (Fig. 2.3e; right panel). Typically 10-30 μm in length, they can reach up to 50 μm (Fig. 2.3). Based on Mg:Fe ratios, two generations of Fe-rich dolomite are identified. The first generation, termed low-Fe dolomite, contains Ca (18.0-20.0%), Mg (7.4–12.0%), and lower Fe (2.1–3.3%), often forming the core (Fig. 2.3b, c). The second generation, termed high-Fe dolomite, appears brighter in SEM-BSE images (Fig. 2.3b) and has Ca (15.8–17.0%), Mg (6.8–8.9%), and higher Fe (3.5–6.3%), sometimes forming rims around the first generation (Fig. 2.3b).

Quartz [SiO_2]

SEM-BSE and SEM-EDS analyses reveal a phase composed largely of Si (29.5 to 32.7%) and up to 56.7% O (Fig. 2.3e; right panel), which is interpreted to be quartz. There are two generations of quartz. The first generation, which appears to be the oldest, is interstitial to calcite and/or low-Fe dolomite and is systematically associated with Fe-Al-Mg silicate fibers (Fig. 2.3b). This generation of quartz measures

up to 20 µm in length and up to 10 µm across. The second generation of quartz is smaller, typically less than 10 µm in length and about 5 µm across. This generation is mostly "clean" and appears to replace the high-Fe dolomite (Fig. 2.3c).

Clay minerals

Sheets of clay minerals are observed within the MHs. SEM-EDS chemical analyses show that one of these minerals is composed of Fe (16.7–25.0%), Al (7.2–9.7%), Mg (2.7–3.7%), and Si (8.6–11.1%), along with a large amount of O, which can reach up to 50% (Fig. 2.3e; Spect 5). These Fe-Al-Mg silicate sheets are likely chlorite [$(Mg, Al, Fe)_{12}[(Si, Al)_8O_{20}](OH)_{16}$], as XRD analyses indicate the presence of chlorite (Fig. 2.3d). They are mostly interstitial to calcite crystals and are found in close proximity to other clay fibers and quartz within the microbial fabric, as well as on calcite crystal surfaces (Fig. 2.3a, c). These sheets are abundant in drill core samples, commonly measuring 15 µm in length, occasionally up to 20 µm, and 15 to 20 µm across. They are absent in outcrop samples.

Another clay mineral within the microbial fabric primarily consists of Si (20.5 to 28.6%), K (8.8 to 12.1%), and Al (6.8 to 8.8%), with minor Ca peaks, as shown by EDS spectra (Fig. 2.3e; bottom right). This K-Al silicate, likely lepidolite [$K_2(Li, Al)_{5-6}[Si_{6-7}Al_{2-1}O_{20}](OH, F)_4$]], also present in XRD (Fig. 2.3d), typically measures 5 to 10 µm in length, occasionally reaching up to 20 µm, and 5 to 10 µm across (Fig. 2.3a). In outcrop samples, this phase is enriched in Mg, as seen from SEM-EDS spectra (Fig. 2.3e; bottom right).

Fe-rich phases [Fe_xO_y and FeS_2]

Fe-oxide, potentially hematite, is present in outcrop samples but absent in drill core samples. SEM-EDS analyses show it is mainly composed of Fe (26.0–46.9%) and O, likely as a secondary oxidation product. Pyrite is abundant only in the microbial fabric of microbial carbonates within drill core samples and is not found in outcrop samples. This phase is primarily composed of S (29.6–42.2%) and Fe (22.2–34.4%), as identified by SEM-EDS (Fig. 2.3e). The crystals are cubic, mostly ranging between 5 and 40 µm (Fig. 2.3a, e), with some up to 1 cm observed in drill core samples.

Apatite [$Ca_5(PO_4)_3(OH, F, Cl)$]

Apatite occurs as a submicron accessory phase in the microbial carbonate samples from Ga-Mohana Hill. SEM-EDS analyses reveal that it is primarily composed of Ca (22.16–29.48%) and P (12.54–15.52%), with minor amounts of Si and Al, and O up to 54.45%.

Table 2. 2 | Averaged major and trace element data from laser ablation ICP-MS and solution ICP-MS/-AES analyses of Transvaal Supergroup microbial carbonate samples. All concentrations are in ppm.

Sample ID	Horizon	Mg	Al	Si	Mn	Fe	Ti	Zr	Th
525.25	MC[a]	11872	1610	7177	5401	8958	62	3.6	0.371
525.3	C[a]	1927	149	322	4434	4192	1	0.2	0.020
550.57	C[a]	1905	BLD	222	5848	6875	BLD	0.3	0.114
550.57	MC[a]	131050	7960	53700	26630	158450	616	39.4	2.745
551.3	C[a]	1567	14	411	5806	6339	2	0.8	0.015
551.3	MC[a]	58201	7733	42414	15066	96409	380	15.6	1.457
551.66	C[a]	1640	1	270	5763	6750	1	0.3	0.004
551.66	MC[a]	14353	8437	30594	7292	25876	232	13.5	1.277
555.43	MC[a]	13505	43500	105000	6935	24965	1107	32.3	2.395
556.15	C[a]	2181	1	261	6720	7560	1	0.4	0.049
556.15	MC[a]	25452	4035	10816	9694	29379	67	4.0	0.301
559	C[a]	3155	BLD	261	6850	12850	5	1.2	0.001
559	MC[a]	5291	16698	24119	5418	15371	184	18.1	1.111
584.01	C[a]	2095	1	289	7515	3906	1	0.2	0.002
584.01	MC[a]	3473	2072	51420	6905	4111	89	3.4	0.242
590.74	C[a]	4695	7	251	12280	4430	3	0.3	0.009
590.74	MC[a]	4526	2693	11480	11944	4974	192	4.1	0.346
592.24	C[a]	4120	BLD	197	12930	4210	BLD	0.2	0.005
592.24	MC[a]	3947	2517	10170	12433	5230	61	5.7	0.348
593	C[a]	2328	15	295	8766	4315	1	1.5	0.043
593	MC[a]	25685	4115	15115	12101	12884	95	6.4	0.540

[a]:laser ablation ICP-MS analysis; [b]:solution ICP-MS/-AES analysis; MC = Calcite-dominated microbial horizon; C = Interstitial calcite cement; MD = Dolomite-dominated microbial horizon; D = Interstitial dolomite; BLD = below limit of detection.

Table 2.2 (continued)

Sample ID	Horizon	Mg	Al	Si	Mn	Fe	Ti	Zr	Th
GC-23-1	C [a]	2623	3	294	11039	4490	1	2.1	0.003
GC-23-1	MC [a]	2161	4239	12617	9648	3905	228	6.2	0.551
GC-23-2	C [a]	3406	3	262	7800	2620	BLD	1.0	0.001
GC-23-2	MC [a]	2609	2202	6477	9011	3382	75	4.3	0.324
GCC04	C [a]	5767	3	355	10338	4626	1	0.3	0.033
GCC04	MC [a]	4329	1866	6486	10094	5568	80	2.4	0.294
GCC06B-2	C [a]	1756	BLD	265	7163	1226	2	1.3	0.002
GCC06B-2	MC [a]	28620	1641	5705	12283	7143	60	4.2	0.322
GCC06B-1	D [a]	89580	7310	26116	15754	17688	263	12.0	0.810
GCC06B-1	MD [a]	191680	3074	16474	26746	22744	92	6.5	0.518
GCC09	C [a]	1030	10	279	7493	1911	1	0.9	0.001
GCC09	MC [a]	1717	4354	16944	7923	5732	186	8.5	0.438
GCC11	D [a]	43208	14020	59980	9932	32480	940	20.5	1.781
GCC11	MD [a]	5734	4094	16034	6534	2493	168	5.1	0.549
GCC12	C [a]	1821	4	228	8667	3357	BLD	5.0	0.010
GCC12	MC [a]	1752	1668	5894	8582	3232	59	4.5	0.262
GCC01	C [b]	N/A	0.010	N/A		0.6	N/A		
GCC03	MC [b]		0.004			2.3			
GCC04	C [b]		0.016			4.4			
GCC04	MC [b]		0.004			1.9			
GCC06A	C [b]		0.030			4.3			
GCC06B-2	MC [b]		0.235			15.3			
GCC09	C [b]		0.003			1.4			
GCC09	MC [b]		0.008			2.2			
GCC10	C [b]		0.006			3.7			
GCC10	D [b]		0.027			7.9			

[a]:laser ablation ICP-MS analysis; [b]:solution ICP-MS/-AES analysis; MC = Calcite-dominated microbial horizon; C = Interstitial calcite cement; MD = Dolomite-dominated microbial horizon; D = Interstitial dolomite; BLD = below limit of detection.

Table 2. 3 | Averaged REY data from laser ablation ICP-MS and solution ICP-MS/-AES analyses, including key ratios, for microbial carbonate samples from the Transvaal Supergroup.

Sample ID	Horizon	La	Ce	Pr	Nd	Sm	Eu	Gd	Tb	Dy	Y	Ho	Er	Tm	Yb	Lu	Ce/Ce*	La/La*	Y/Ho	Eu/Eu*	ΣREE	Yb/Nd
525.25	MC[a]	4.36	5.88	0.66	2.66	0.50	0.16	0.56	0.08	0.62	7.29	0.15	0.50	0.07	0.48	0.09	1.14	1.85	48.65	1.62	16.76	2.21
525.3	C[a]	3.87	4.41	0.51	2.08	0.39	0.11	0.53	0.08	0.62	8.95	0.16	0.57	0.09	0.62	0.12	1.11	2.14	54.76	1.32	14.16	3.71
550.57	C[a]	2.79	2.54	0.26	1.05	0.16	0.05	0.24	0.03	0.24	4.79	0.07	0.25	0.04	0.21	0.04	1.21	2.86	72.30	1.53	7.96	2.46
550.57	MC[a]	20.47	30.30	3.51	13.72	2.59	0.62	2.27	0.30	1.92	16.1	0.38	1.09	0.15	0.80	0.13	1.06	1.50	42.72	1.41	78.22	0.73
551.3	C[a]	4.39	6.11	0.58	2.52	0.43	0.18	0.49	0.08	0.60	8.59	0.17	0.60	0.09	0.65	0.12	1.41	2.36	50.99	2.06	17.01	3.18
551.3	MC[a]	6.13	10.84	1.05	4.15	0.72	0.18	0.59	0.09	0.60	5.47	0.13	0.40	0.06	0.40	0.06	1.27	1.53	40.78	1.41	25.42	1.21
551.66	C[a]	2.07	2.91	0.28	0.98	0.17	0.06	0.18	0.02	0.18	2.74	0.05	0.15	0.03	0.16	0.03	1.11	1.47	57.42	1.97	7.26	2.03
551.66	MC[a]	5.76	10.77	1.12	4.17	0.73	0.18	0.64	0.09	0.58	4.42	0.12	0.36	0.05	0.36	0.05	1.12	1.20	36.27	1.38	25.00	1.06
555.43	MC[a]	19.95	36.25	3.65	12.40	2.15	0.53	1.76	0.25	1.61	9.69	0.33	0.98	0.15	1.02	0.17	1.06	1.07	29.06	1.46	81.20	1.02
556.15	C[a]	5.98	7.22	0.76	2.85	0.45	0.16	0.47	0.07	0.52	7.84	0.14	0.44	0.07	0.48	0.09	1.11	1.86	58.07	1.92	19.68	2.08
556.15	MC[a]	6.44	9.18	0.92	3.46	0.57	0.19	0.54	0.08	0.54	6.55	0.13	0.40	0.06	0.38	0.07	1.17	1.66	51.87	1.90	22.94	1.36
559	C[a]	0.73	0.90	0.10	0.47	0.09	0.03	0.11	0.02	0.12	1.17	0.03	0.07	0.01	0.06	0.01	1.23	2.43	37.49	1.62	2.76	1.60
559	MC[a]	8.34	13.73	1.66	7.21	1.36	0.42	1.16	0.16	1.08	8.66	0.24	0.69	0.09	0.64	0.10	1.12	1.58	36.77	1.83	36.89	1.10
584.01	C[a]	2.38	2.25	0.22	0.90	0.13	0.04	0.23	0.03	0.22	6.43	0.06	0.21	0.03	0.19	0.03	1.29	2.97	100.8	1.43	6.92	2.63
584.01	MC[a]	3.82	4.43	0.44	1.90	0.31	0.12	0.49	0.07	0.55	12.2	0.15	0.51	0.08	0.48	0.09	1.36	2.72	79.88	1.76	13.43	3.16
590.74	C[a]	0.84	0.91	0.11	0.39	0.07	0.02	0.06	0.01	0.06	1.67	0.02	0.06	5E-03	0.03	0.01	0.89	1.54	91.92	1.74	2.59	1.07
590.74	MC[a]	4.57	5.58	0.66	2.60	0.45	0.20	0.49	0.07	0.51	8.61	0.13	0.44	0.06	0.39	0.07	1.04	1.80	64.73	2.34	16.22	1.86
592.24	C[a]	0.59	0.82	0.10	0.35	0.04	BLD	0.07	0.01	0.02	0.60	0.01	0.02	0.01	0.02	BLD	0.95	1.35	108.5			0.77
592.24	MC[a]	3.81	5.82	0.65	2.74	0.50	0.12	0.46	0.07	0.46	4.51	0.10	0.30	0.04	0.27	0.04	1.20	1.80	43.37	1.36	15.37	1.21
593	C[a]	2.61	3.46	0.37	1.50	0.24	0.06	0.25	0.03	0.23	3.31	0.05	0.17	0.02	0.16	0.03	1.19	1.96	62.86	1.42	9.20	1.32
593	MC[a]	2.36	3.67	0.42	1.74	0.31	0.09	0.30	0.04	0.29	3.44	0.07	0.20	0.03	0.18	0.03	1.11	1.58	51.94	1.58	9.72	1.28

[a]:laser ablation ICP-MS analysis; [b]: solution ICP-MS/-AES analyses; MC = Calcite-dominated microbial horizon; C = Interstitial calcite cement; MD = Dolomite-dominated microbial horizon; D = Interstitial dolomite; BLD = below limit of detection. Except for Y/Ho and ΣREE, all ratios are PAAS-normalized ratios.

Table 2.3 (continued)

Sample ID	Horizon	La	Ce	Pr	Nd	Sm	Eu	Gd	Tb	Dy	Y	Ho	Er	Tm	Yb	Lu	Ce/Ce*	La/La*	Y/Ho	Eu/Eu*	ΣREE	Yb/Nd
GC-23-1	C[a]	1.154	1.247	0.147	0.585	0.093	0.034	0.105	0.015	0.103	2.081	0.027	0.091	0.012	0.077	0.014	1.06	2.10	77	1.91	3.70	1.63
GC-23-1	MC[a]	2.990	4.183	0.482	1.845	0.330	0.092	0.329	0.045	0.316	4.518	0.077	0.251	0.036	0.230	0.039	1.04	1.53	59	1.56	11.24	1.55
GC-23-2	C[a]	0.379	0.400	0.045	0.160	0.029	BLD	0.048	0.005	0.031	0.540	0.006	0.021	0.003	0.013	0.003	0.98	1.77	89	1.14		1.02
GC-23-2	MC[a]	1.791	2.247	0.259	1.029	0.178	0.059	0.198	0.027	0.190	3.021	0.046	0.145	0.019	0.133	0.021	1.08	1.85	65	1.77	6.34	1.60
GCC04	C[a]	0.767	0.960	0.104	0.437	0.068	0.026	0.079	0.011	0.075	1.497	0.019	0.091	0.009	0.057	0.010	1.22	2.21	78	2.04	2.71	1.62
GCC04	MC[a]	1.358	2.087	0.223	0.877	0.158	0.042	0.129	0.017	0.125	1.754	0.030	0.093	0.014	0.076	0.014	1.16	1.60	59	1.59	5.24	1.08
GCC06B-2	C[a]	1.309	1.788	0.178	0.661	0.097	0.040	0.133	0.012	0.091	1.960	0.023	0.072	0.011	0.062	0.012	1.16	1.70	85	2.43	4.49	1.15
GCC06B-2	MC[a]	2.772	4.105	0.423	1.656	0.290	0.065	0.313	0.039	0.300	4.648	0.074	0.237	0.034	0.227	0.035	1.19	1.70	63	1.26	10.57	1.69
GCC06B-1	D[a]	2.946	4.628	0.491	1.908	0.339	0.067	0.335	0.048	0.335	4.370	0.078	0.260	0.033	0.210	0.032	1.14	1.52	56	1.09	11.71	1.37
GCC06B-1	MD[a]	6.040	10.958	1.152	4.372	0.784	0.157	0.733	0.106	0.705	7.592	0.144	0.468	0.064	0.414	0.065	1.13	1.27	53	1.13	26.16	1.17
GCC09	C[a]	0.797	1.012	0.104	0.416	0.057	0.018	0.067	0.009	0.063	1.203	0.017	0.058	0.008	0.050	0.008	1.22	2.08	72	1.67	2.68	1.48
GCC09	MC[a]	2.447	4.372	0.458	1.944	0.327	0.092	0.302	0.039	0.258	2.676	0.058	0.162	0.022	0.140	0.022	1.27	1.63	46	1.64	10.64	0.89
GCC11	D[a]	4.442	9.238	1.251	5.140	1.083	0.254	0.888	0.112	0.682	4.426	0.132	0.367	0.053	0.358	0.050	0.95	1.01	34	1.44	24.05	0.86
GCC11	MD[a]	4.487	8.338	0.904	3.466	0.588	0.150	0.485	0.060	0.389	2.785	0.073	0.214	0.031	0.223	0.035	1.11	1.23	38	1.57	19.44	0.80
GCC12	C[a]	1.358	1.729	0.155	0.660	0.109	0.044	0.137	0.015	0.111	2.022	0.031	0.099	0.011	0.074	0.014	1.48	2.65	65	2.24	4.55	1.40
GCC12	MC[a]	2.119	3.195	0.316	1.198	0.214	0.062	0.204	0.028	0.210	3.325	0.053	0.170	0.024	0.155	0.028	1.20	1.63	63	1.65	7.98	1.61
GCC01	C[b]	2E-03	1E-03	1E-04	5E-04	6E-05	2E-05	8E-05	8E-06	5E-05	1E-03	1E-05	4E-05	5E-06	2E-05	4E-06	1.17	3.42	94	1.48	4E-03	0.68
GCC03	MC[b]	2E-04	1E-04	1E-05	3E-05	4E-06	1E-06	1E-05	1E-06	5E-06	2E-04	1E-06	6E-06	5E-07	3E-06	5E-07	1.28	3.70	200	1.09	4E-04	1.02
GCC04	C[b]	1E-03	1E-03	1E-04	4E-04	5E-05	1E-05	6E-05	7E-06	5E-05	1E-03	1E-05	4E-05	6E-06	4E-05	6E-06	1.27	2.62	104	1.51	3E-03	1.25
GCC04	MC[b]	2E-04	9E-05	6E-06	2E-05	2E-06	1E-06	BLD	2E-07	2E-06	2E-04	1E-06	3E-06	3E-07	2E-06	3E-07	1.44	4.75	155	3.10	3E-03	1.18
GCC06A	C[b]	8E-04	9E-04	9E-05	3E-04	5E-05	1E-05	6E-05	9E-06	7E-05	2E-03	2E-05	6E-05	9E-06	6E-05	1E-05	1.17	2.20	95	1.51	2E-03	2.10
GCC06B-2	MC[b]	1E-03	1E-03	1E-04	4E-04	5E-05	1E-05	8E-05	1E-05	6E-05	1E-03	2E-05	5E-05	6E-06	3E-05	6E-06	1.34	2.60	85	1.11	4E-03	1.01
GCC09	C[b]	2E-04	1E-04	9E-06	3E-05	3E-06	1E-06	BLD	BLD	4E-06	2E-04	1E-06	4E-06	5E-07	4E-06	5E-07	1.39	3.74	150	2.86	4E-04	1.53
GCC09	MC[b]	1E-03	1E-03	8E-05	3E-04	3E-05	1E-05	5E-05	7E-06	4E-05	1E-03	1E-05	4E-05	5E-06	3E-05	5E-06	1.36	3.17	98	1.66	3E-03	1.13
GCC10	C[b]	1E-03	9E-04	9E-05	3E-04	4E-05	7E-06	7E-05	7E-06	4E-05	1E-03	1E-05	4E-05	4E-06	2E-05	3E-06	1.33	3.53	110	0.90	3E-03	0.81
GCC10	D[b]	1E-03	1E-03	1E-04	4E-04	5E-05	1E-05	1E-04	1E-05	7E-05	2E-03	2E-05	6E-05	6E-06	3E-05	5E-06	1.08	3.18	113	1.20	3E-03	0.83

[a]:laser ablation ICP-MS analysis; [b]: solution ICP-MS/-AES analyses; MC = Calcite-dominated microbial horizon; C = Interstitial calcite cement; MD = Dolomite-dominated microbial horizon; D = Interstitial dolomite; BLD = below limit of detection. Except for Y/Ho and ΣREE, all ratios are PAAS-normalized ratios.

2.5. Trace and REE geochemistry of microbial carbonates

Laser ablation (LA) and solution ICP-MS trace and REY analyses were conducted on 22 samples, focusing on ROIs such as calcite aggregates (white and spherulitic) and microdolomite cement in the NMHs, as well as cuspate stromatolite and contorted laminae in the MHs. The MHs are predominantly calcite- or dolomite-dominated. Solution ICP-MS analyses were performed on 16 microdrilled laminae from seven samples (), while LA ICP-MS analyses were conducted on 195 spots from 18 samples (Tables 2.1 and S2). Samples selected for the interpretation of seawater chemistry were chosen based on their purity (>80% $CaCO_3$), with trace and major element concentrations summarized in Table 2.2 and REY characteristics shown in Table 2.3 and Figs. 2.4–2.6. Data from multiple spot analyses within the same ROI on each sample were averaged to generate REY plots (Fig. 2.4). The complete dataset from all analysed spots is provided in suppl. Tables S2 and S3. In the following sections, the results from the analyzed ROIs will be presented in three distinct ways: (i) as a comparison between the analytical methods described above, (ii) as a comparison between the dominant mineral phases, calcite and dolomite, and (iii) as "bulk" analysis, calculated as the total contributions from both MHs and NMHS across all samples.

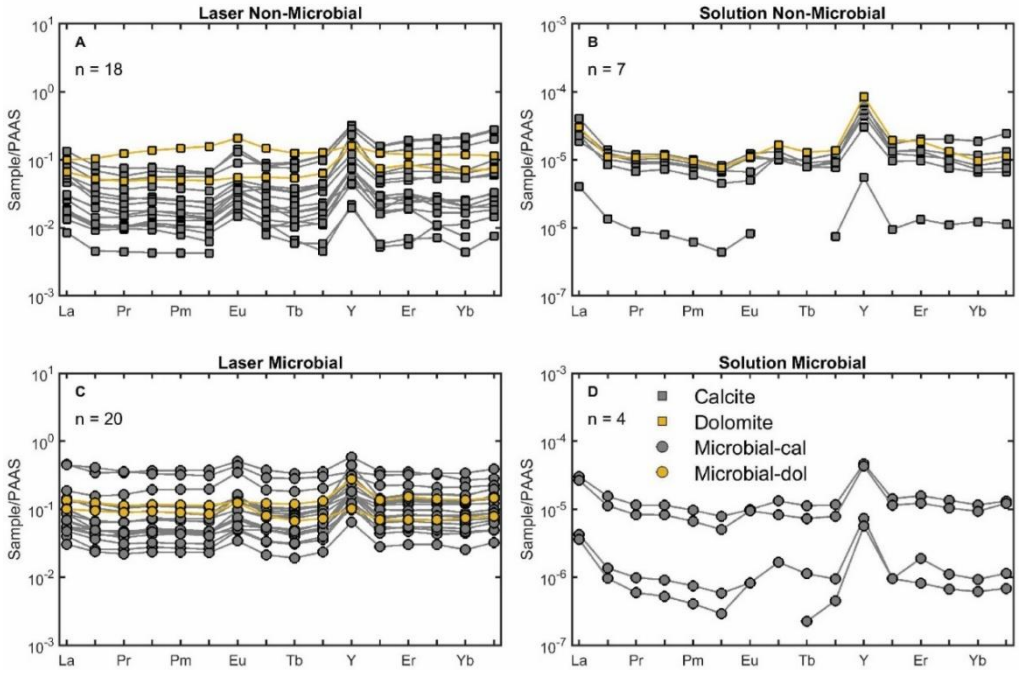

Figure 2. 4 | Plots of averaged REY from solution and laser ablation ICP-MS analyses. Samples were first grouped by the method of analysis and then further by the type of horizon, as described in section 2.4: **(A & B)**. Non-microbial horizons, composed of calcite and dolomite; **(C & D)**. Microbial horizons, composed of calcite-dominated, dolomite-dominated, and cuspate microbialites. n = number of ROIs plotted, with each one representing an average of 5–10 spot analyses.

2.5.1. Geochemical characteristics by analytical method: LA vs. solution ICP-MS

Laser ablation analyses from all horizons reveal total REE contents ranging from >0.02 to 92.21 ppm (mean = 13.4 ± 24.8) (suppl. Table S2). The $(La/La^*)_{SN}$ values typically range from 0.9 to 6.9 (suppl. Table S2) (mean = 1.9 ± 2.8), while $(Eu/Eu^*)_{SN}$ values mostly range from 1.0 to 2.6 (mean = 1.6 ± 0.4), with one outlier at 9.05 (suppl. Table S2; Fig. 2.5A). Y/Ho ratios are mostly between 32 and 128, with three outliers between 150 and 210 (suppl. Table S2; Fig. 2.5A). The REY pattern shows significant HREE enrichment, with $(Yb/Nd)_{SN}$ values ranging from 1 to 6 (suppl. Table S2; Fig. 2.5A). Laser ablation analyses also reveal that several elements show considerable variability. Silicon concentrations vary between 0.02 and 23.3 wt.%, Mg between 0.07 and 20.2 wt.%, Fe from 0.1 to 19.6 wt.%, Ti from 0.3 to 1190 ppm, and Al from 0.9 ppm to 2.3 wt.%. Manganese concentrations are high, ranging between 0.4 to 2.8 wt.%. Zr ranges between 0.02 and 42.5 ppm (suppl. Table S2).

Samples analysed via solution ICP-MS analyses from all horizons show significantly lower total REE contents compared to samples analysed via LA, ranging from 0.3 to 3.9 ppb (mean = 2.3 ± 1.3) (suppl. Table S3). The $(La/La^*)_{SN}$ values are higher than LA analysis, typically ranging from 2.2 to 5.5 (mean = 3.4 ± 0.8) (suppl. Table S3). The $(Eu/Eu^*)_{SN}$ values are similar to those from LA analyses, ranging from 0.9 to 4.3 (mean = 1.8 ± 1.0) (suppl. Table S3). Y/Ho ratios are significantly higher, typically between 76 and 200 (mean = 120 ± 34) (suppl. Table S3; Fig. 2.5B). The REY pattern is HREE-enriched, with $(Yb/Nd)_{SN}$ values mainly ranging from 1 to 2.1 (mean = 1.1 ± 0.4) (suppl. Table S3). Solution analyses indicate very low and consistent concentrations of Al and Fe, with Al ranging from 4 to 30 ppb and Fe from 0.6 to 4.9 ppm (suppl. Table S3).

Notably high Y/Ho ratios are observed in both solution and LA analyses, consistently in samples with very low total REE content where most elements approach the detection limit. These elevated ratios likely arise as an artefact of Y and Ho nearing the detection limit. Solution ICP-MS data reveal lower detrital concentrations (e.g., Al and Fe) relative to LA ICP-MS data, which is expected since the digestion methods used in this study aimed to eliminate as much detrital material as possible, leaving behind a purer signal. Therefore, observations from LA ICP-MS analyses can be compared with solution data to determine their accuracy.

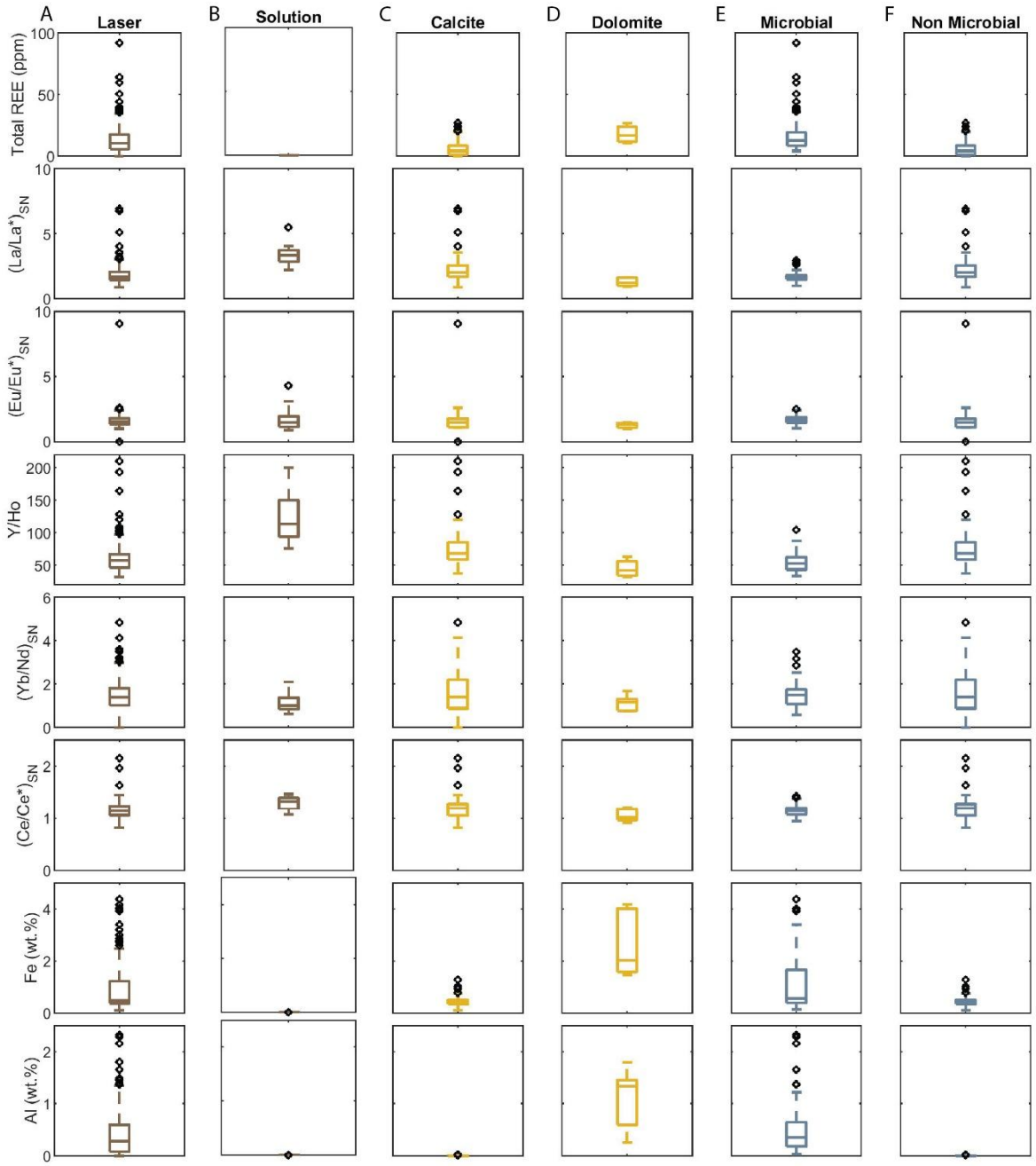

Figure 2. 5 | Box plots comparing key parameters for REE, trace, and major element data from samples of the Campbellrand Subgroup, Transvaal Supergroup, by various groupings. All concentrations are in ppm, except for Fe and Al. The suffix "$_{SN}$" denotes PAAS-normalized values. **A & B**: Comparison of laser ablation (n = 195) and solution analyses (n = 16) for the same samples. **C & D**: comparison of data by mineralogy: calcite and dolomite. **E & F**: Comparison of data from calcite-dominated microbial and non-microbial horizons, excluding the dolomite data. Only laser ablation data are shown in C–F.

2.5.2. Geochemical characteristics by dominant mineralogy: calcite vs. dolomite

In the ROIs within the NMHs, calcite and dolomite aggregates exhibit distinct geochemical signatures. Here, the focus is on the LA data, given that the number of analyses via LA ICP-MS (n = 195) are

significantly higher than the solution ICP-MS data (n = 16). Calcite aggregates have total REE contents ranging from >0.02 to 26.4 ppm (mean = 5.9 ± 34.6 ppm) (suppl. Table S2). The $(La/La^*)_{SN}$ values in calcite typically range from 0.9 to 6.9 (mean = 2.2 ± 4.3), while $(Eu/Eu^*)_{SN}$ values range from 1.1 to 2.6 (mean = 1.6 ± 0.4) (suppl. Table S2). Y/Ho ratios generally fall between 37 and 210 (mean = 77 ± 31) (suppl. Table S2; Fig. 2.5C). The REY pattern is HREE-enriched, with $(Yb/Nd)_{SN}$ values ranging from 0.1 to 6.0 (mean = 1.8 ± 1.0) (suppl. Table S2). Elemental concentrations in calcite aggregates are mostly consistent, with Si ranging from 197 to 661 ppm, Mn between 0.4 and 1.3 wt.%, Fe from 0.1 to 1.3 wt.%, Mg from 0.07 to 0.7 wt.%, Ti from 0.27 to 5.2 ppm, and Zr between 0.02 to 10.7 ppm. Aluminium concentrations range mostly from 0.9 to 23.3 ppm, with two outliers at 93.1 and 204 ppm (suppl. Table S2; Fig. 2.5C).

In contrast, LA ICP-MS data from dolomite aggregates show higher total REE contents, ranging from 10.8 to 26.9 ppm (mean = 17.9 ± 6.4 ppm) (suppl. Table S2). The $(La/La^*)_{SN}$ values in dolomite aggregates are lower, ranging between 0.9 and 1.7 (mean = 1.3 ± 0.3) (suppl. Table S2). The $(Eu/Eu^*)_{SN}$ values are slightly lower, ranging from 1.0 to 1.5 (mean = 1.3 ± 0.2) (suppl. Table S2). Y/Ho ratios range from 32 to 63 (mean = 45 ± 11.8), being lower and less variable in comparison to calcite aggregates (suppl. Table S2; Fig. 2.5D). The REY pattern in dolomite is flat to slightly HREE-depleted, with $(Yb/Nd)_{SN}$ values from 0.8 to 1.7 (mean = 1.1 ± 0.3) (Fig. 2.5D). Silicon and Fe concentrations in dolomite aggregates are higher, ranging from 0.9 to 6.7 wt.% and 1.5 to 4.2 wt.%, respectively, while Mn contents (0.8 to 1.8 wt.%) are similar, in comparison to calcite aggregates. Titanium, Zr and Al concentrations are also higher, ranging from 96 to 1120 ppm, and 6.6 to 27 ppm, and 0.2 to 1.8 wt.%, respectively. Magnesium concentrations are expectedly higher, ranging between 3.7 and 9.8 wt.% (suppl. Table S2).

The solution ICP-MS data closely mirrors the LA data, showing higher $(La/La^*)_{SN}$, $(Eu/Eu^*)_{SN}$, Y/Ho, and $(Yb/Nd)_{SN}$ ratios. These variations reflect the distinct mineralogical and geochemical characteristics of calcite and dolomite. Elemental concentrations in calcite aggregates typically appear lower than those in dolomite aggregates, with some elements nearing their detection limits, contributing to the highly variable Y/Ho values observed in calcite. Dolomite is often considered a secondary product of calcite in many environments. The data from both solution and LA ICP-MS analyses suggest that dolomite does not retain seawater characteristics, as indicated by the flat REY patterns (Yb/Nd ~ 1).

2.5.3. Geochemical characteristics by horizons: microbial vs. non microbial

Calcite-dominated MHs, characterized by contorted laminae and cuspate morphologies, have total REE contents from LA ICP-MS analyses ranging from 4.12 to 92.21 ppm (mean = 17.7 ± 14.2) (suppl. Table S2). The $(La/La^*)_{SN}$ values range from 1.0 to 3.0 (mean = 1.7 ± 0.4), and $(Eu/Eu^*)_{SN}$ values are between 1.0 and 2.5 (mean = 1.7 ± 0.4) (suppl. Table S2). Y/Ho ratios generally range from 33 to 104 (mean = 54 ± 13.4), with higher values noted in solution analyses (suppl. Table S2; Fig. 2.5E). The REY pattern shows moderate HREE enrichment, with $(Yb/Nd)_{SN}$ values ranging from 0.6 to 3.5 (mean = 1.5 ± 0.6) (suppl. Table S2; Fig. 2.5E). Silicon and Al concentrations in MHs vary widely, from 0.02 to 23.3 wt.% for Si (mean = 1.9 ± 2.6 wt. %), and from 0.02 to 2.3 wt.% for Al (mean = 0.5 ± 0.4 wt.%). Manganese ranges from 0.4 to 2.7 wt.% (mean = 1.0 ± 0.5 wt.%), Fe from 0.1 to 19.6 wt.% (mean = 2.1 ± 3.7 wt.%), Mg from 0.1 to 13.2 wt.% (mean = 1.7 ± 2.9 wt.%), Ti from 1.8 to 1190 ppm (mean = 159.7 ± 187.1 ppm), and Zr from 0.1 to 42.5 ppm (mean = 8.0 ± 7.9 ppm) (suppl. Table S2).

In contrast, NMHs, characterized by calcite aggregates, have lower total REE contents, ranging from >0.02 to 26.9 ppm (mean = 5.9 ± 34.6 ppm) (suppl. Table S2). Calcite NMHs exhibit higher $(La/La^*)_{SN}$ values, mostly between 0.6 and 6.9 (mean = 2.2 ± 4.3) (suppl. Table S2; Fig. 2.5F). The $(Eu/Eu^*)_{SN}$ values in calcite NMHs are similar, ranging from 1.1 to 2.6 (mean = 1.6 ± 0.4) (Fig. 2.5F). Y/Ho and $(Yb/Nd)_{SN}$ ratios in NMHs are also similar to those in MHs, ranging from 37 to 210 (mean = 77 ± 30.6) and 0.1 to 6.0 (mean = 1.8 ± 1.0), respectively (Fig. 2.5F). The NMHs show lower concentrations of Si (0.02 to 0.06 wt.%; mean = 0.03 ± 1.6 wt.%), Mg (0.07 to 0.7 wt.%; mean = 0.2 ± 0.8), Al (0.9 to 204 ppm; mean = 159.7 ± 187.1 ppm), Fe (0.1 to 1.3 wt.%; mean = 0.4 ± 0.6), Zr (0.02 to 10.7 ppm; mean = 1.0 ± 11.8), and Ti (0.3 to 5.2 ppm; mean = 1.3 ± 33.1) compared to MHs. Conversely, NMHs show similar Mn concentrations (0.4 to 1.3 wt.%; mean = 0.8 ± 0.3) (suppl. Table S2).

The variability in Si and Al concentrations between the MHs and the NMHs can be attributed to the range in grain sizes of the chert and clay minerals within the MHs, indicating that varying amounts of chert and clays were incorporated during the LA analyses. This variability highlights the distinct mineralogy of the MHs and its impact on elemental composition. The different mineralogy, which may reflect changes in the primary depositional environment and chemistry, results in a different weighted mean signal.

The relationships between MHs and NMHs, based on solution ICP-MS data, differ significantly from those observed using LA ICP-MS data. Both MHs and NMHs exhibit similar trace and REE characteristics in solution ICP-MS analyses, as reflected in the small ranges shown in the boxplots in

the solution column above. According to solution ICP-MS data, the Al and Fe concentrations in MHs (0.003 to 0.235 ppm; mean = 0.04 ± 0.09 and 1.3 to 15.3 ppm; mean = 4.3 ± 4.9, respectively) and NMHs (0.003 to 0.03 ppm; mean = 0.02 ± 0.009 and 0.6 to 4.9 ppm; mean = 3.0 ± 1.6, respectively) are similar (suppl. Table S3). The total REE content, as determined by solution ICP-MS, is similar in both MHs and NMHs, ranging from 0.4 to 3.9 ppb (mean = 2.5 ± 1.1 ppb) in MHs and from 0.3 to 3.6 ppb (mean = 1.7 ± 1.4 ppb) in NMHs (suppl. Table S3). The $(La/La^*)_{SN}$ ratios are also similar between NMHs (2.2 to 4.0; mean = 3.2 ± 0.6) and MHs (2.6 to 5.5; mean = 3.7 ± 0.9). The $(Eu/Eu^*)_{SN}$ ratios are similar between the two horizons, ranging from 0.9 to 2.9 (mean = 1.5 ± 0.7) in NMHs and from 1.1 to 4.3 (mean = 2.2 ± 1.2) in MHs. The Y/Ho ratios range from 83 to 150 (mean = 111 ± 24.6) in NMHs and from 76 to 200 (mean = 132 ± 43.2) in MHs. The $(Yb/Nd)_{SN}$ ratios range from 0.6 to 2.1 (mean = 1.2 ± 0.5) in NMHs and from 0.9 to 1.5 (mean = 1.2 ± 0.2) in MHs. These observations reveal that the REE patterns in MHs and NMHs start to converge, which is expected given that the sequential digestion eliminates detrital content that would influence the REE characteristics if not excluded.

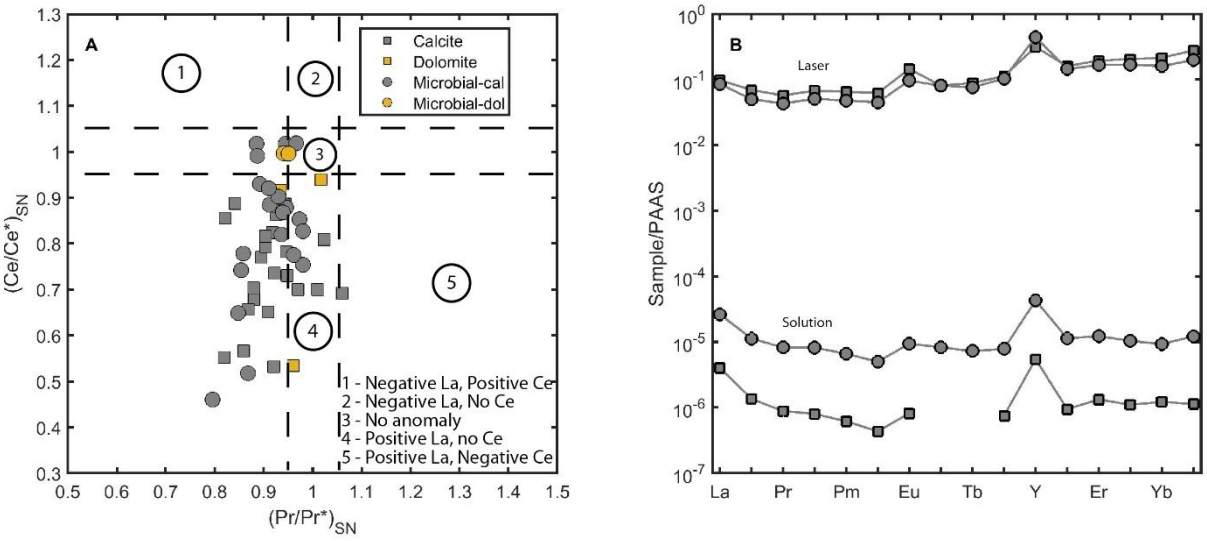

Figure 2. 6 | (A). $(Ce/Ce^*)_{SN}$ vs. $(Pr/Pr^*)_{SN}$ calculated from averaged laser ablation and solution ICP-MS analyses of non-microbial and microbial horizons, using the linear method, to graphically identify true Ce anomalies. The threshold values used are as specified by Bau and Dulski (1996). The bottom left quadrant is not labelled by the original authors. Groups are the same as in Fig. 2.4. $_{SN}$: PAAS-normalized; **(B)**. REY patterns of the four samples showing true positive Ce anomalies.

2.5.4. Ce anomalies and their distribution

Solution ICP-MS analyses reveal a small range of $(Ce/Ce^*)_{SN}$ values, ranging mainly from 1.1 to 1.5, with the exception of a single analysis (suppl. Table S3; Fig. 2.5). In MHs, solution analyses yield $(Ce/Ce^*)_{SN}$ values between 1.3 and 1.5 (mean = 1.4 ± 0.06). Notably, only sample GCC09 meets the seawater signal criteria—HREE enrichment over LREE, Y/Ho > 36, positive Eu and La anomalies, and

low total REE—and has a $(Ce/Ce^*)_{SN}$ value of 1.4. However, it does not fall within the positive Ce anomaly quadrant of the graph proposed by Bau and Dulski (1996) to identify true Ce anomalies (Fig. 2.6A). Consequently, this is not considered a convincing positive anomaly. In NMHs, $(Ce/Ce^*)_{SN}$ values from solution analyses vary from 1.2 to 1.4 (suppl. Table S3), but only sample GCC09, with a $(Ce/Ce^*)_{SN}$ value of 1.4, has an REY trend consistent with a seawater signal. All other samples with $(Ce/Ce^*)_{SN}$ values > 1.3 do not show seawater REY characteristics, indicating these Ce anomalies are artefacts.

Laser ablation analyses reveal $(Ce/Ce^*)_{SN}$ values ranging from 0.7 to 2.2 (mean = 1.2 ± 0.2) (suppl. Table S2; Fig. 2.5). $(Ce/Ce^*)_{SN}$ values in dolomite NMH and MH range from 0.9 to 1.2, indicating no Ce anomalies. In microbial calcite, values span from 0.9 to 1.4 (mean = 1.2 ± 0.1). Among the four samples with $(Ce/Ce^*)_{SN}$ > 1.3, only sample 584.01 meets seawater criteria (Fig. 2.6B). Non-microbial calcite exhibits $(Ce/Ce^*)_{SN}$ values from 0.7 to 2.2 (mean = 1.2 ± 0.2), with three analyses having values of 0.7 and 0.8, and thirteen analyses between 1.4 and 2.2. Of these, only sample 551.3 consistently shows $(Ce/Ce^*)_{SN}$ values > 1.3 and meets seawater criteria, but it does not fall within the positive Ce anomaly quadrant of the graph proposed by Bau and Dulski (1996) to identify true Ce anomalies (Fig. 2.6A).

2.6. Discussion

2.6.1. Evaluation of analytical contamination and post-depositional alteration

One major challenge in utilizing PAAS-normalized REY compositions of ancient microbial carbonates for paleoenvironmental studies lies in identifying potential contamination from other phases such as oxides, organic compounds, silicates, sulfides, clays, and phosphates. This contamination can occur during post-depositional processes like diagenesis and metamorphism, or be incorporated during analytical procedures such as laser ablation and acid dissolution. Silicates and clays, for instance, have significantly higher REE contents compared to carbonates, and even minimal exchange of REE between these minerals, or incorporation of minor amounts of these phases during analysis, can obscure the original carbonate depositional signature (Nothdurft et al., 2004).

To track detrital contamination in carbonate REY contents, Al, Th, and Zr are commonly used due to their higher concentrations in average shale compared to marine carbonates (Nothdurft et al., 2004; Webb & Kamber, 2000). The diagrams in Fig. 2.7A–C reveal statistically insignificant correlations between Zr, Th, and Al vs. total REE in the calcite NMHs ($r_{C(Zr)}$ = -0.04, $r_{C(Th)}$ = 0.20, and $r_{C(Al)}$ = 0.49), which suggest that they are not contaminated by terrigenous components. The same correlations are statistically significant in both dolomite NMHs ($r_{D(Zr)}$ = 0.76, $r_{D(Th)}$ = 0.90, and $r_{D(Al)}$ = 0.69) and calcite MHs ($r_{MC(Zr)}$ = 0.80, $r_{MC(Th)}$ = 0.80, and $r_{MC(Al)}$ = 0.58, respectively). Among these three elements, only Al

is above detection in the solution ICP-MS dataset, showing a correlation with total REE similar to that observed in the LA dataset for both the calcite NMH ($r_{C(Al)}$ = 0.43) and the calcite MH ($r_{MC(Al)}$ = 0.62).

The positive correlations between Zr, Th, and Al vs. total REE in the calcite MHs could be a reflection of their mineral composition. Petrographic analyses show that MHs contain multiple non-carbonate phases, possibly authigenic, while NMHs are primarily mono-mineralic, consisting mainly of calcite or dolomite. This may be because microbial carbonates form alongside the mineralization of organic material, which can provide a sticky surface for clay adhesion (e.g., Trichet & Defarge, 1995). The LA technique, involving in situ ablation, captures a mix of REY characteristics due to the laser beam incorporating various mineral phases within the MHs, such as REY-rich clays, resulting in higher REY concentrations compared to solution ICP-MS analyses (section 2.5). Even in regions dominated by a single mineral, LA analyses show significant variations across different ROIs. This could be due to micro-scale heterogeneities within the mineral phases themselves or the presence of trace amounts of other minerals that are not easily detectable through petrographic analysis alone. These factors collectively contribute to higher and more variable REY concentrations observed in LA ICP-MS data. Positive correlations between Zr, Th, and Al vs. total REE in the dolomite NMHs suggest that dolomitization, often regarded as a secondary process, modifies REE patterns as primary limestone transforms into dolomite (Banner et al., 1988), which could explain the positive correlations between Zr, Th, and Al vs. total REE in the dolomite NMHs.

Iron and manganese oxides/oxyhydroxides could also contaminate carbonate REY data, but the lack of correlation between total REE and Fe/Mn in calcite NMH (Fig. 2.7D) rules out their impact. However, a significant correlation in calcite MHs ($r_{MC(Fe/Mn)}$ = 0.77; Fig. 2.7D) suggests possible contamination in this horizon. The Ce/Ce* ratios in this study are not influenced by Fe and Mn oxyhydroxides, given the lack of correlations between Fe/Mn and Ce/Ce* in all horizons (Fig. 2.7E). To further investigate post-depositional alterations, particularly in Ce/Ce*, parameters proposed by Shields and Stille (2001) were used (Figs. 2.7 F–H). Post-depositional increases in Ce/Ce*, shown by increasing total REE and MREE and decreasing $(Dy/Sm)_{SN}$ ratios, would also result in negative Eu anomalies. Weak correlations between these parameters in both calcite MHs and NMHs suggest minimal post-depositional alteration of Ce/Ce*. Phosphate contamination is typically indicated by convex MREE to HREE-enriched patterns (Baldwin et al., 2011), but the REY patterns in this study are not convex (Fig. 2.4), ruling out phosphate contamination. These findings indicate that the calcite NMHs have insignificant shale contamination and minimal post-depositional alteration, making them the most reliable archives of ambient seawater paleoredox conditions.

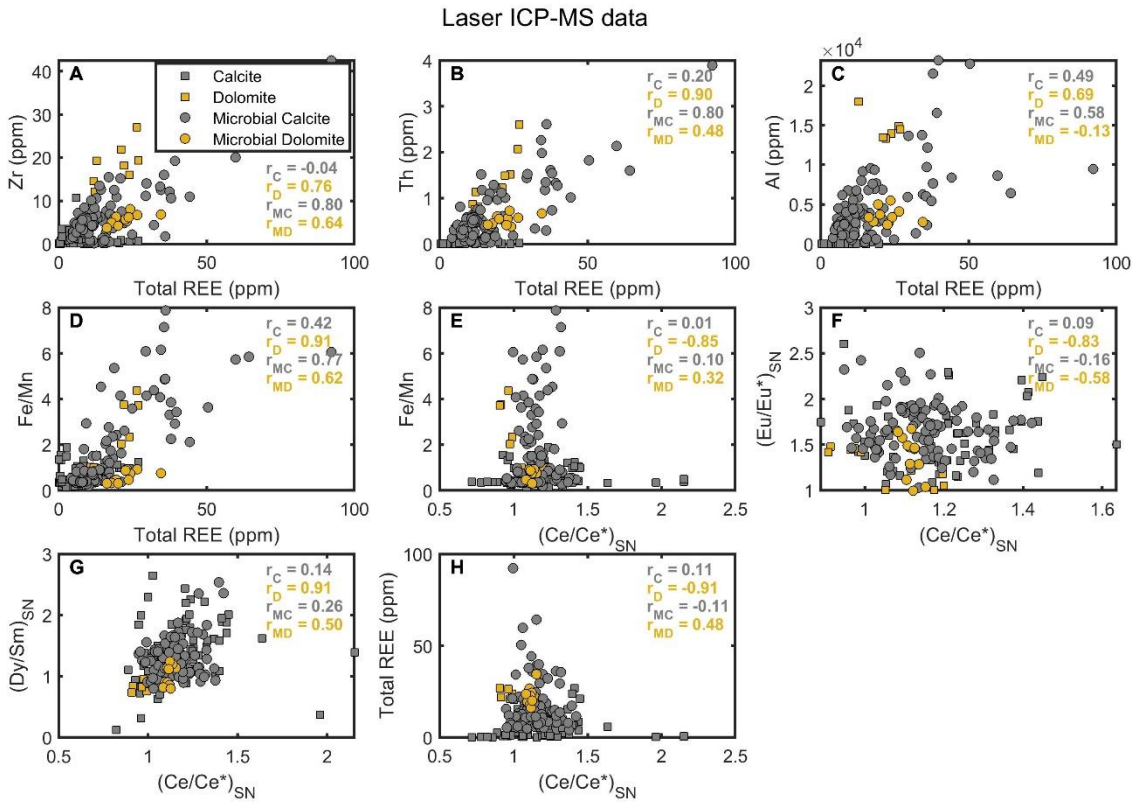

Figure 2. 7 | Bivariate plots evaluating REE data from laser ablation ICP-MS analyses of the Campbellrand Subgroup are presented for: detrital contamination **(A–E)**; and post-depositional (hydrothermal or diagenetic) alteration **(F–H)**. The correlation coefficients shown are calculated according to the following horizons: calcite NMH (r_C), dolomite NMH (r_D), calcite MH (r_{MC}), and dolomite (r_{MD}).

2.6.2. Comments on methodology

2.6.2.1. Laser ablation vs. solution ICP-MS

Laser ablation and solution ICP-MS analyses are well-established techniques for analyzing trace elements and REY in various sample types, including carbonates (Strnad et al., 2009; Tostevin et al., 2016; Zhang et al., 2015). The data obtained in this study using these two methods highlight clear differences, offering insights into the strengths and limitations of each. As discussed above, total REE from LA analyses are higher and more variable. In contrast, solution ICP-MS analyses yield more consistent results. This latter method involves the sequential digestion of microdrilled horizons, effectively isolating the carbonate signal and excluding non-carbonate phases. Consequently, the REY patterns obtained from solution analyses represent a more pure carbonate endmember signal with lower total REY content and less variability. Isolating the pure carbonate component minimizes the impact of non-carbonate phases and provides a clearer picture of the primary geochemical signals.

Despite the differences in total REE between the two methods, both produce seawater REY patterns, making both datasets valuable for understanding ancient seawater chemistry. While LA ICP-MS is useful for capturing the full spectrum of elemental variability within complex samples, it introduces challenges in interpreting data due to its sensitivity to heterogeneity. On the other hand, solution ICP-MS provides a more purified and consistent analysis of the carbonate component, ideal for studies focused on primary geochemical signatures. Therefore, the choice between LA and solution ICP-MS analyses should be guided by the specific research objectives and the nature of the samples being studied. In this study, inferences made from the LA data are compared with data from solution analyses where applicable.

2.6.2.2. Dolomite vs. Calcite

The REY characteristics of calcite and dolomite aggregates in this study reveal distinct differences, highlighting the unique mineralogical properties and formation processes of these phases. Understanding these differences is crucial for reconstructing paleoenvironmental conditions and diagenetic histories. Both LA and solution ICP-MS data from calcite horizons generally meet the criteria for a seawater signal, including HREE enrichment over LREE, Y/Ho ratios greater than 36, positive La anomalies, and low total REE concentrations. These characteristics suggest that calcite retains geochemical signatures indicative of its original marine depositional environment. The observed high variability in elemental concentrations and REY patterns of calcite may indicate a higher susceptibility to diagenetic alteration and analytical contamination compared to other phases like dolomite. However, the importance of calcite in paleoredox studies is further strengthened by the fact that even after diagenetic modifications, it preserves a primary REY signal (Webb et al., 2009).

In contrast, dolomite aggregates analysed using both LA and solution ICP-MS analyses do not exhibit seawater-like REY characteristics. The REY pattern in dolomite is characterized by a flat to slightly HREE-depleted profile, with $(Yb/Nd)_{SN}$ values around 1. Dolomite that forms through alteration by seawater-derived fluids retains the REE characteristics of the initial limestone (Zhao & Jones, 2013), while dolomite formed by fluids from a source(s) significantly different from seawater will display REE features distinct from those of the original limestone (Nothdurft et al., 2004). To obtain seawater-like characteristics from dolomite, making it a suitable archive for Ce anomalies, an appropriate digestion method is required (Tostevin et al., 2016). However, in this study, the same analytical procedure was used for both calcite and dolomite, meaning our dolomite data are not optimized. This finding is consistent with previous studies that highlight the complexities of interpreting REY patterns in dolomitized samples (Tostevin et al., 2016). These results suggest that while solution ICP-MS analyses can be optimized to retrieve useful data from dolomite, LA ICP-MS is not ideal for analyzing dolomite.

2.6.3. Synthesis of REY data from the Transvaal Supergroup

2.6.3.1. The shallow-water carbonate record

To compare with the full carbonate geochemical record from the Transvaal Supergroup, a database of literature REY data was compiled, meticulously screened, and Ce/Ce* values were recalculated using the geometric method of Lawrence et al. (2006) and refined further following Tostevin et al. (2016) (section 2.3.3). The screened data are presented in Figs. 2.8 and 2.9. The REY characteristics observed in our study samples align closely with those found in the majority of Archean carbonates from the Transvaal Supergroup (Eroglu et al., 2015, 2017; Hickman-Lewis et al., 2020; Kamber & Webb, 2001, 2020; Kamber et al., 2014; Schier et al., 2018; Voegelin et al., 2010; Warke et al., 2019). Archean stromatolites from the Transvaal Supergroup show minimal variability in Ce/Ce*, with few exceptions. Rare earth element studies of the Monteville and Boomplass Formations produced seawater-like signals with Ce/Ce* values ranging from 1.00 to 1.27 (Voegelin et al., 2010). A combined REE study of the Oaktree and Monte Christo Formations (Malmani Supergroup, Traansvaal basin) and the Reivilo Formation (Campbellrand Supergroup, Griqualand West basin) produced Ce/Ce* values of 0.93 to 1.15 (Eroglu et al., 2017). Microbial carbonates from the Kogelbeen and Gamohaan Formations are characterized by PAAS-normalized seawater REE patterns and produce Ce/Ce* values of 1.0–1.08 and 0.97–1.11, respectively (Kamber & Webb, 2001). High resolution analyses of cuspate stromatolites from the ~2.52 Ga Upper Nauga Formation revealed a complex paragenetic evolution, suggesting that trace metal distributions in microbial carbonates cannot be conclusively linked to specific metabolic pathways (Warke et al., 2019). However, the dolomitized stromatolitic structures from this formation produced marine PAAS-normalized REE patterns with Ce/Ce* ratios between 0.99 and 1.02. The platform dolomites of the Tongwane Formation exhibit marine REY patterns with Ce/Ce* ranging from 0.94 to 1.30 (Warke et al., 2018). Studies of detritus-free stromatolitic limestone successions from the Rooinekke Formation produced Ce/Ce* ratios of 0.94 to 1.12 (Schier et al., 2018). Banded iron-rich carbonates of the ~2.39 Ga Moodraai Formation exhibit seawater REE patterns with Ce/Ce* values ranging from 0.88 to 1.05 (Figs. 2.8 and 2.9) (Tsikos et al., 2001).

Carbonate-bound data from the Klipputs Formation, Koegas Subgroup produced PAAS-normalized seawater-like REE patterns with positive Ce anomalies (Warke et al., 2020). This was interpreted as evidence for a redox-stratified basin where Ce^{3+} oxidation occurred in oxygen-rich surface waters, while lower oxygen levels in deeper waters led to Ce^{4+} reduction. Five samples with seawater-like REY characteristics, after screening, maintained Ce/Ce* values of 1.43–2.24, suggesting "true" positive Ce anomalies (Fig. 2.9). However, this small sample size does not support widespread Ce redox cycling.

Furthermore, Schier et al. (2018) detected no Ce anomalies from the same formation (Ce/Ce* = 0.97–1.04). The interpretation of Ce anomalies in the Transvaal Supergroup carbonates consistently points to anoxic marine conditions.

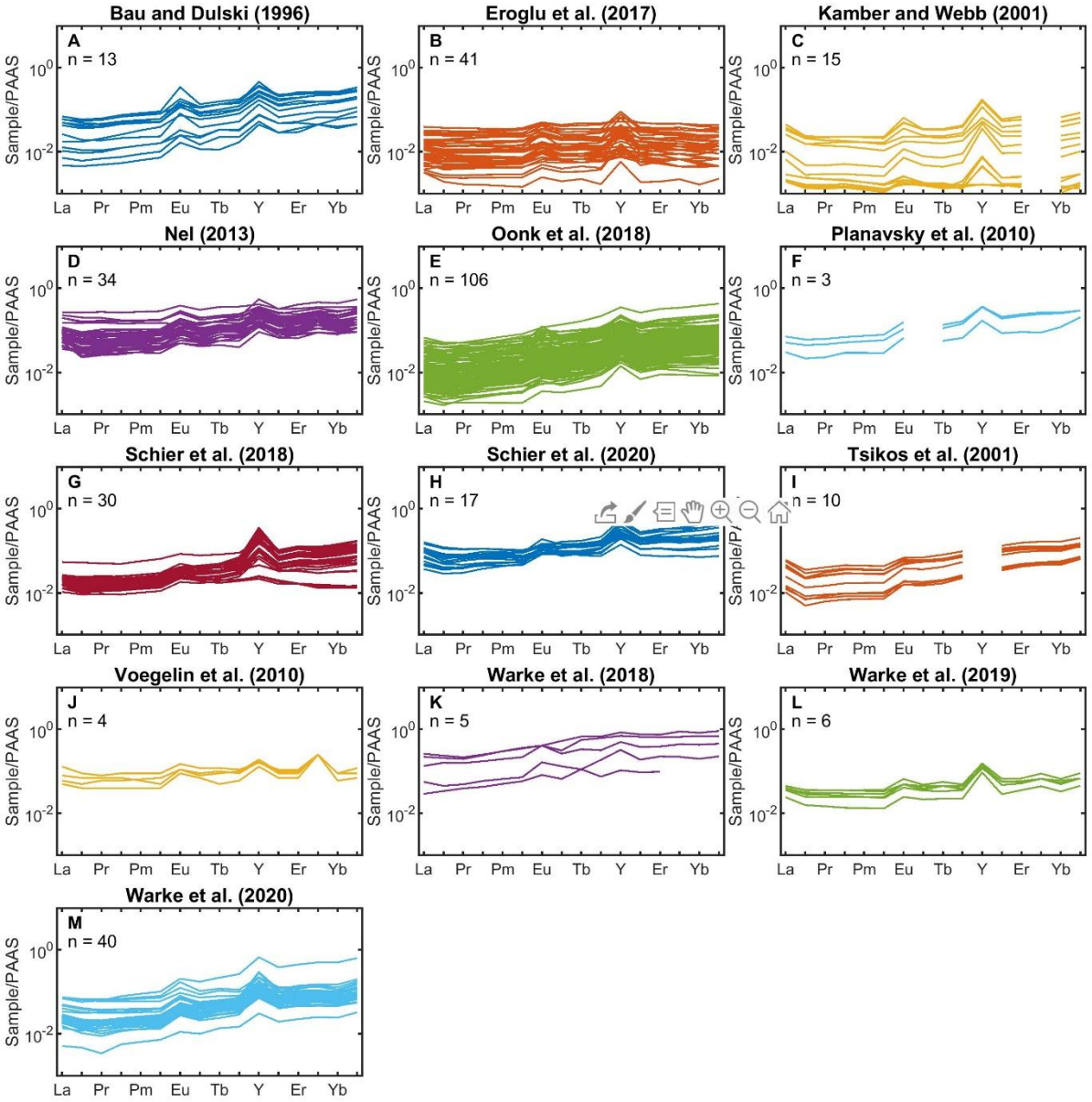

Figure 2. 8 | REE trends for screened carbonate and banded iron formation data from various formations of the Transvaal Supergroup, based on literature values: **(A).** Kuruman Formation; **(B).** Reivilo Formation; **(C).** Gamohaan & Kogelbeen Formations; **(D).** Nelani, Rooinekke, & Doradale Formations; **(E).** Griquatown and Kuruman Formations; **(F).** Kuruman Formation; **(G).** Rooinekke & Klipput Formations; **(H).** Hotazel Formation; **(I).** Moodraai Formation; **(J).** Campbellrand Subgroup; **(K).** Tongwane Formation; **(L).** Upper Nauga Formation; **(M).** Klipput Formation. n = number of analyses producing convincing seawater-like trends after screening.

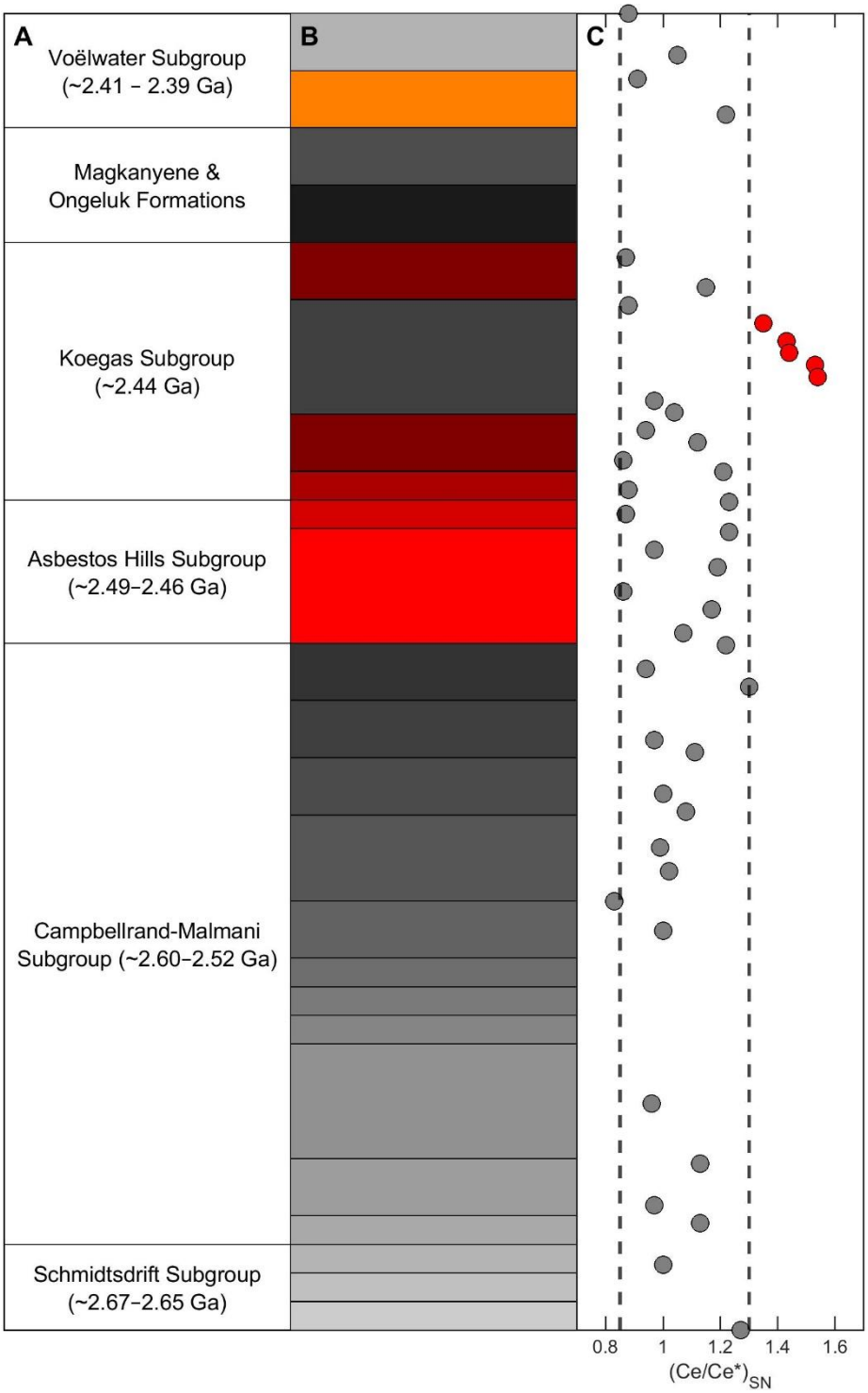

Figure 2. 9 | Overview of recalculated $(Ce/Ce^*)_{SN}$ values from the data presented in Figure 2.8: **(A).** Subgroup division of the Griqualand West and Transvaal basins; **(B).** Formations within the subgroups – Grey represents carbonate successions, Red indicates BIF successions, Black denotes diamictites, and Orange signifies interbedded Mn- and Fe-rich successions; **(C).** $(Ce/Ce^*)_{SN}$ values recalculated using the geometric method described by Lawrence et al. (2006). Dotted lines distinguish between negative anomalies (left), positive anomalies (right), and no anomalies (middle).

2.6.3.2. The inner ramp record

Rare earth element studies on deep-water Fe- and Mn-rich sediments of the Transvaal Supergroup reveal consistent patterns indicative of anoxic conditions during deposition. Analyses of BIF from the Kuruman Formation show seawater-like REE trends with Ce/Ce* values ranging from 0.97–1.17 (Bau & Dulski, 1996) and 1.07–1.22 (Planavsky et al., 2010). Carbonate fraction-specific REE patterns from the Kuruman and Griquatown Formations display positive slopes with Ce/Ce* values of 0.86–1.17 and 0.87-1.23, respectively, suggesting variable depositional conditions and redox states (Oonk et al., 2018). A combined study of the Doradale, Rooinekke, and Nelani iron formations from the Koegas Subgroup shows Ce/Ce* values of 0.88–1.23, 0.86–1.21, and 0.87–1.15, respectively (Nel, 2013). BIF interbedded with Mn-rich sediments in the Hotazel Formation exhibit seawater REE patterns with Ce/Ce* values between 0.91 and 1.22 (Schier et al., 2020). These findings consistently show a lack of Ce anomalies, implying low oxygen levels during the deposition of Transvaal Supergroup deep-water sediments.

2.6.4. What does the data tell us about marine redox conditions before GOE

Despite the proposed availability of pre-GOE free molecular oxygen (Anbar et al., 2007; Holland, 2002), the data discussed here suggest anoxic conditions dominated the shallow marine Campbellrand-Malmani carbonate platform, including in microbial mat communities, where oxygen generation would likely have been centered. The REY characteristics of BIF from the Transvaal Supergroup also suggest anoxic outer ramp conditions up to ~2.4 Ga.

Geochemical evidence for pre-GOE oxygen can be divided into two categories: evidence for local oxygen oases in shallow seawater and evidence for a substantial build-up of free oxygen in the ocean which escapes to the atmosphere enabling oxidative weathering on land and the release of redox-sensitive metals into the ocean (the whiff model) (Kamber et al., 2014). A major implication of the whiff idea, notably the release of Mo from terrestrial sulfide weathering long before the GOE (Anbar et al., 2007; Wille et al., 2007), is that the oxidation of Earth's atmosphere was a complex and reversible process rather than a unidirectional progression. The REY systematics of shallow-water microbial carbonates are not sensitive to oxidative weathering on land, and cannot be used to evaluate the whiff model, characterized by intermittent oxygenation of the Neoarchaean atmosphere.

Instead, Ce anomaly is more suitable to study the oxygen oases hypothesis. Local oxygen build-up is distinct from oxygen production, which has been inferred from various indicators such as Neoarchaean C-isotope fractionation (Grassineau et al., 2002), stromatolite diversity (Buick, 1992;

Wilks & Nisbet, 1988), and cyanobacterial mats (Noffke et al., 2008). Evidence for buildup of dissolved free oxygen in shallow marine environments was presented by Zerkle et al. (2012) through Fe-speciation data, mainly from some shallow water microbial carbonates of the Boomplaas and Lokammona Formations. These carbonates showed low ratios of highly reactive to total Fe, suggesting oxygenation. However, neither solution ICP-MS of the same formations (Voegelin et al., 2010) nor the petrographically guided LA and solution ICP-MS data of similar microbial carbonates (this study; Kamber & Webb, 2001) showed significant Ce anomalies.

The absence of a siginificant Ce anomaly in Archaean-Paleoproterozoic stromatolites suggests that either shallow seawater was not sufficiently oxygenated to oxidize Ce^{3+} to Ce^{4+}, or that this process was kinetically inhibited, or both. Given that the oxidation of Ce^{3+} is facilitated by Mn/Fe-oxyhydroxides, the lack of a Ce anomaly could suggest the absence of these oxyhydroxides. Recent studies suggest that Fe(II)-bearing silicates were the principal primary precipitates and that Fe-hydroxides in BIF are early diagenetic phases (Rasmussen et al., 2021), which could suggest oxyhroxides were scarce. This interpretation aligns with the broader understanding of Archean environments, which were predominantly anoxic with only limited and localized occurrences of low oxygen levels.

2.6.5. Implications for biology and mineralogy

Layering in microbial carbonates forms through sediment trapping as well as in-situ mineralization on microbial mats, influenced by phototrophs and heterotrophs in both marine and freshwater settings (Grotzinger & Knoll, 1999; Power et al., 2011). Microorganisms facilitate carbonate precipitation via metabolic pathways such as photosynthesis, ureolysis, ammonification, denitrification, sulfate reduction, anaerobic sulfide oxidation, and methane oxidation, all of which increase pH or dissolved inorganic carbon by, for example, amino acid metabolism, or hydrolysis (De Muynck et al., 2013; Knoll, 2003). Denitrification typically occurs where nitrate and organic carbon are present and oxygen is limited (DeJong et al., 2010). Sulfate-reducing bacteria reduce sulfate to sulfide while oxidizing organic carbon to bicarbonate, thereby increasing pH and the saturation state (Baumgartner et al., 2006).

Microbial carbonates of the Campbellrand Supergroup exhibit PAAS-normalized REY patterns lacking negative Ce anomalies. One key consideration is whether Ce anomalies are recording ambient conditions from surrounding water through trapping and binding, or if they are capturing in situ conditions via induced precipitation. The microbialies likely formed in situ through biological mineralization. In which case, it is possible that oxygen production was occurring in the mats but

limited to micron scale horizons, which were spatially separated from the locus of carbonate precipitation (Sumner et al., 2015). It is possible that localized environmental processes are not easily detected through broader-scale analyses, even at the ~40 micron scale afforded by laser ablation techniques. Alternatively, it is possible that cyanobacteria were producing oxygen in the mats, but it was consumed by aerobic respiration at comparable rates, preventing environmental build-up. Regardless, our data suggest that if oxygen production was occurring at the micro-scale, it is not captured by carbonate precipitation. An alternative explanation is that oxygenic cyanobacteria had not evolved at this point in time, and the microbial communities were anaerobic.

Furthermore, substantial Ce anomalies are notably rare until the mid-Paleozoic Era (Wallace et al., 2017). This scarcity of anomalies in earlier records might suggest that the Ce proxy may not have been sensitive enough to detect redox cycling until oxygen levels in the environment were significantly higher. Therefore, the current Ce anomaly records may underestimate the complexity of early redox conditions. While there may have been localized oases of oxygen production, the limited evidence in the Ce record suggests that these occurrences were not widespread or substantial enough to leave a significant imprint. Thus, we can hypothesize the existence of such oases but must acknowledge the scant evidence supporting this in the Ce anomaly record. This discussion underscores the need for more sensitive proxies and finer-scale analyses to better understand early oxygen production and redox conditions.

2.7. Conclusion

My analysis of well-preserved MHs and NMHs in microbial carbonates from the Gamohaan and Kogelbeen Formations in the Transvaal Supergroup shows primary seawater REY patterns, implying primary depositional signals were preserved, but no negative Ce anomalies. This similarity to other carbonate and IF data from the Transvaal Supergroup suggests deposition in predominantly anoxic conditions, although pre-GOE oxygen oases cannot be ruled out. The scarcity of geochemical data supporting oxygenation, even in shallow facies with clear evidence for microbial mats, is consistent with hypotheses that suggest oxygenic photosynthesis evolved relatively late in Earth history, coincident with the GOE, and that Archean oceans were fully anoxic. This, in turn, suggests that the protolith sediments for IF likely included ferrous minerals such as siderite and greenalite, although other models propose deposition of Fe^{3+} oxyhydroxides by anoxygenic photosynthesizers (photoferrotrophs) in an anoxic ocean.

Chapter 3

Identification of Greenalite and New Methodology for Isolating its Trace Element Signal

3.1. Introduction

Iron formations, specifically BIF, are typically composed of alternating Fe- and silica- rich layers. BIFs are polymineralic, and mostly fine-grained (<10 μm), which can make sedimentological and mineralogical descriptions challenging. Some minerals identified in BIF are shown in Table 3.1. There is considerable debate around the primary mineralogy of IF (e.g., Klein, 2005; Rasmussen et al., 2013), and identifying mineral paragenesis is essential before interpreting any associated trace element or isotope records. While many of these phases can be distinguished relatively easily, Fe-silicates present a unique challenge due to their physical and geochemical similarities. Recent studies using high resolution imaging suggest that the Fe(II)-silicate, greenalite, is a primary phase in BIF (Rasmussen et al., 2021). Accurate identification of greenalite is therefore crucial for subsequent mineral-specific geochemical analyses and interpretations, especially in studies that aim to understand the depositional environment of BIF.

This chapter aims to address two key issues related to the study of greenalite. Misidentification of greenalite with other Fe-silicates can lead to erroneous geochemical interpretations. In this chapter, I make use of approriate identification methods, drawing from the latest research and techniques to distinguish greenalite from other Fe-silicates. Secondly, greenalites fine-grained nature poses significant challenges for conventional geochemical analysis methods. Traditional techniques often fall short in accurately extracting and measuring trace and REY concentrations from such fine-grained minerals. To overcome these limitations, this chapter introduces a novel approach specifically designed for fine-grained greenalite. This new method enhances the accuracy and reliability of geochemical data extraction.

The Transvaal Supergroup provides an ideal context for this study due to its well-preserved BIF sequences. The Gasesa drill core samples offer a comprehensive representation of the Kuruman and Griquatown Formations, enabling a thorough examination of greenalite within this sequence. The identification process and subsequent geochemical analyses presented in this chapter form the foundation for understanding greenalites role and formation within the broader geological context of the Transvaal Supergroup. This chapter is crucial as it lays the groundwork for the subsequent geochemical analyses, ensuring clarity and avoiding redundancy. By focusing on the identification and methodological advancements in studying greenalite, this chapter provides the essential framework needed to interpret data reported in the following chapters.

Table 3. 1 | Commonly observed minerals in iron formations, with specified mineral groups and oxidation states of Fe- and Mn- phases.

Mineral name	Mineral formula	Group	Fe/Mn Oxidation state
Hematite	$Fe_2^{3+}O_3$	Oxide	Oxidized
Ilmenite	$Fe^{2+}TiO_3$	Oxide	Reduced
Magnetite	$Fe^{2+}Fe_2^{3+}O_4$	Oxide	Mixed
Ankerite	$Ca(Fe^{2+}, Mg, Mn^{2+})(CO_3)_2$	Carbonate	Reduced
Calcite	$CaCO_3$	Carbonate	N/A
Dolomite	$CaMg(CO_3)_2$	Carbonate	N/A
Siderite	$Fe^{2+}CO_3$	Carbonate	Reduced
Chert (quartz)	SiO_2	Silicate	N/A
Greenalite	$(Fe^{2+}, Fe^{3+})_{2-3}Si_2O_5(OH)_4$	Silicate	Mixed
Minnesotaite	$(\mathrm{Fe}^{2+}, \mathrm{Mg})_3Si_4O_{10}(OH)_2$	Silicate	Reduced
Riebeckite	$Na_2[(Fe^{2+}, Mg)_3\mathrm{Fe}_2^{3+}]Si_8O_{22}(OH)_2$	Silicate	Mixed
Serpentine	$Mg_6Si_4O_{10}(OH)_8$	Silicate	N/A
Stilpnomelane	$K(Fe^{2+}, Mg, Fe^{3+})_8(Si, Al)_{12}(O, OH)_{27}$	Silicate	Mixed
Zircon	$ZrSiO_4$	Silicate	N/A
Pyrite	$Fe^{2+}S_2$	Sulphide	Reduced
Sphalerite	$(Zn, Fe^{2+})S$	Sulphide	Reduced
Apatite	$Ca_5(PO_4)_3(OH, F, Cl)$	Phosphate	N/A
Monazite	$(Ce, La, Nd, Th)PO_4$	Phosphate	N/A

3.2. Stratigraphic setting

The *ca*. 2.66–2.39 Ga Transvaal Supergroup, situated within the Griqualand West and Transvaal basins on the Kaapvaal Craton (Fig. 3.1A), spans an area of around 250 000 km^2. The supergroup comprises diverse lithological assemblages of IF, carbonates, and siliciclastic sediments (Beukes & Klein, 1990), and has only experienced sub-greenschist facies metamorphism, making it suitable for paleodepositional investigations (Miyano & Beukes, 1984). The Asbestos Hills Subgroup (~2.48 to 2.46 Ga; Lantink et al., 2019; Pickard, 2003; Zeh et al., 2020), which includes the Kuruman and Griquatown Formations (Fig. 3.1B), hosts the main IF deposits within the Transvaal Supergroup, with the Kuruman banded IF showing rhythmic micro-banding. Sedimentary characteristics suggest that the Kuruman Formation was deposited in an open-shelf environment below wave base, while the granular Griquatown Formation was deposited in a shallower marine environment (Beukes & Klein, 1990).

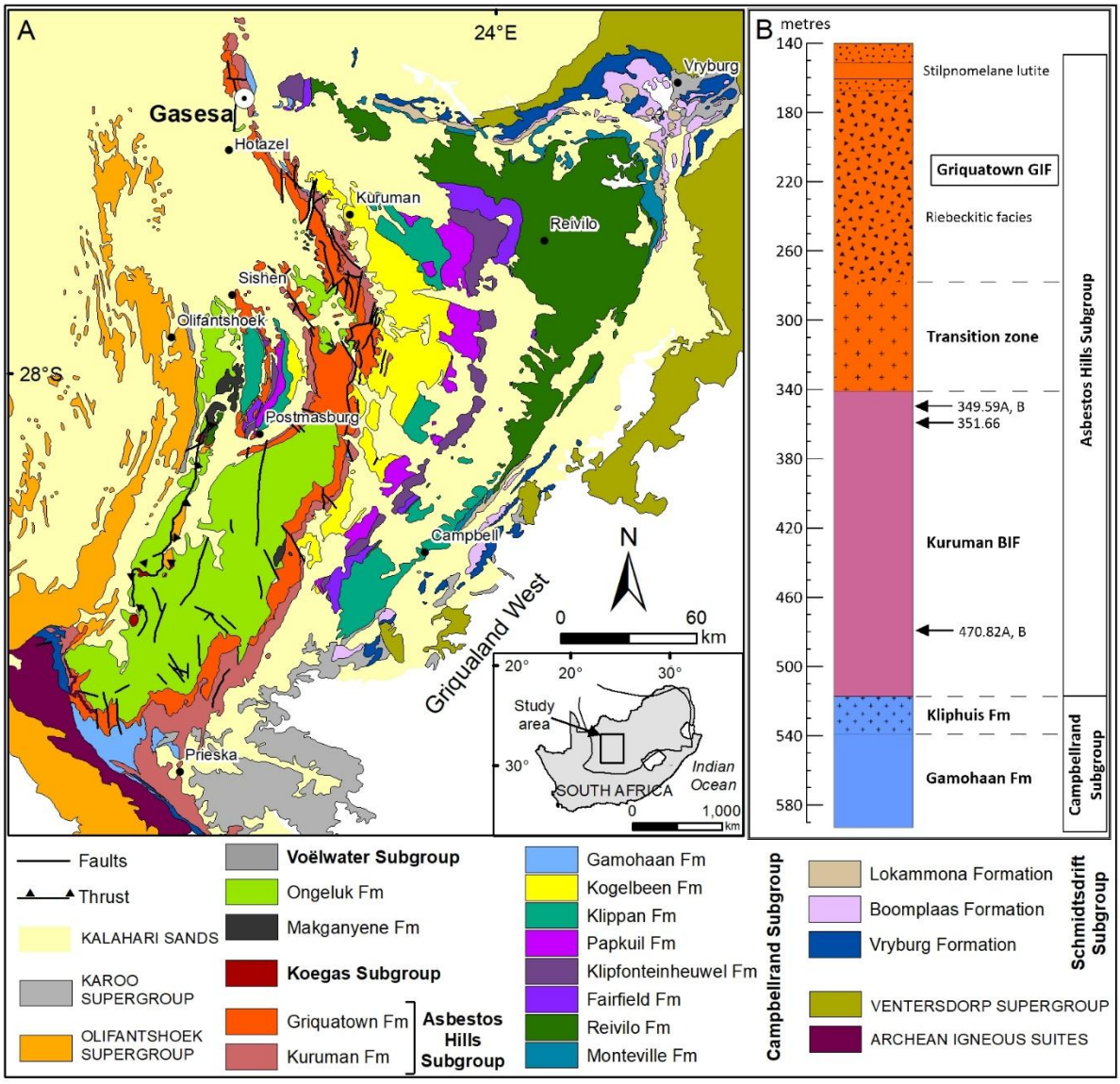

Figure 3. 1 | (A). Regional setting of the Griqualand West basin, Transvaal Supergroup, showing the location of the Gasesa drill hole. Modified from the 1:250 000 Geological Map of South Africa, Council for Geosciences, 2019; **(B).** Log of the Gasesa drill core. Arrows indicate the positions of samples in this study. Fm = Formation; BIF = banded iron formation; GIF = granular iron formation.

3.3. Sample selection and preparation

The three greenalite samples used for this study (349.59A and B; 351.66) were collected from drill core Gasesa (Fig. 3.1B). Greenalite, a very fine-grained mineral, generally occurs in low abundances, making it difficult to identify in samples. However, it imparts a distinctive dusty pale green coloration to chert layers. To locate and isolate greenalite, pale green chert laminae within the Kuruman Formation were targeted, as they had a high likelihood of containing greenalite. The targeted chert layers were extracted over short intervals (<1 cm). The presence of greenalite was initially confirmed using bulk rock powder XRD analyses at depths of 349.59 m and 351.66 m (Fig. 3.1B). Subsequently,

adequate samples were prepared to further confirm the identity of greenalite and to measure major, trace, and REY.

Obtaining greenalite-specific data is challenging due to its very fine grain size, low abundance, and intergrowths with other minerals. To address this, samples were cut parallel to greenalite-rich micro-bands, maximizing the density of exposed greenalite within a pure chert matrix. Additionally, extra chert samples (470.82A & B; Fig. 3.1B) were prepared to use as a reference in assessing the data measured from greenalite. The identity of greenalite was further confirmed through petrography, electron probe microanalysis, and SEM-EDS analysis. Trace and REY concentrations were measured using LA ICP-MS. A methodology was developed in MATLAB® R2019a to quantify the proportion of greenalite versus chert in the analysis area and to extract the REY pattern of the greenalite endmember.

3.4. Characterisation of greenalite

3.4.1. X-ray diffraction (XRD)

Powder samples were prepared using off-cuts from thin-sectioned samples, which were crushed in a jaw crusher and then pulverized in a SIEBTECHNIK disk swing mill with a tungsten carbide steel mill set and rings at the Department of Geological Sciences, UCT. The identity of greenalite and other fine-grained phases in the powdered sample was determined using a Bruker AXS D8 Advanced XRD with a Co-anode and K radiation (Guggenheim et al., 1982) at the Chemical Engineering Department, UCT. The XRD operated at a generator voltage of 35 kV and a current of 40 mA, covering 2θ values from 5° to 120°. Data were collected in 0.031° 2θ step sizes with a counting time of 1 s for bulk powders. For background stripping, indexing of diffraction peaks, and mineral identification, the PANalytical X'Pert HighScore Plus software and the PANalytical ICSD database were used. A peak at 14.35° 2θ, with a d-spacing of 7.12 Å, is characteristic of greenalite (Fig. 3.2).

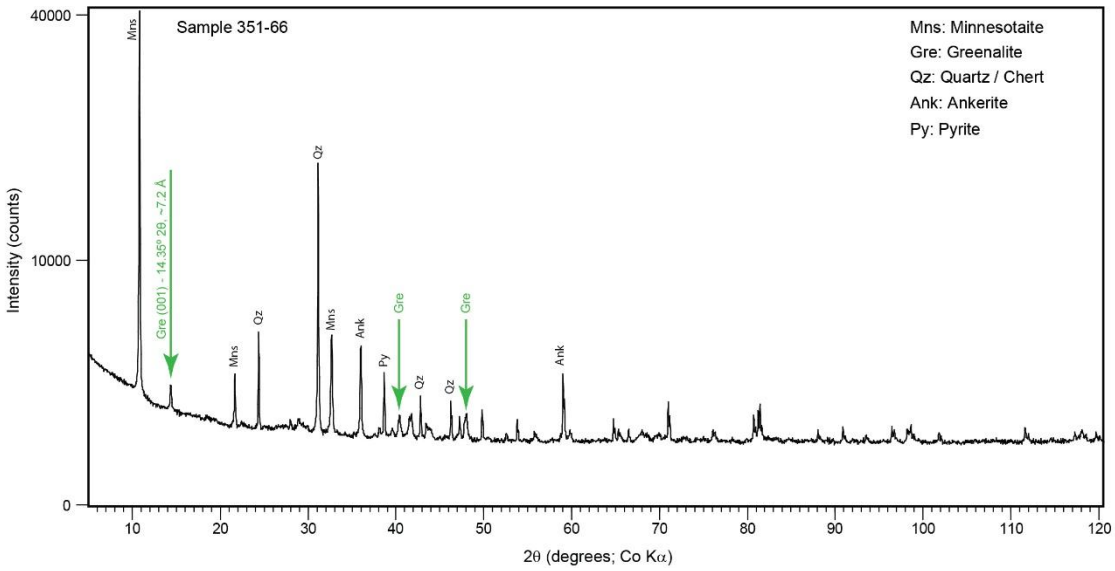

Figure 3. 2 | Representative bulk rock XRD pattern with greenalite peaks highlighted in green (7Å phase) and other phases shown in black.

3.4.2. Scanning electron microscopy (SEM)

Samples where greenalite was identified were then prepared as thin sections, which were used to identify larger grains. However, greenalite is below the resolution of optical microscopy, so samples were cut from these sections and mounted in epoxy resin for SEM and BSE imaging using a Nova NanoSEM at the Chemical Engineering Department, UCT, to enable the analysis of textural relationships and mineral paragenesis (Fig. 3.3). The SEM was fitted with an Oxford Instruments XMax EDS, which was used for quantitative and qualitative chemical analysis of mineral grains using AZtec software from Oxford Instruments. The samples were observed and imaged at a 5.5 mm working distance and 20 kV accelerating voltage. SEM-EDS was used to generate a cross-sectional view across several micro-bands to illustrate the mineral compositions of bands in BIF (Fig. 3.3).

BSE images were used to ascertain the morphological properties of minerals, while SEM-EDS provided information on their major element chemistry. Greenalite and minnesotaite have similar chemical compositions, but the former has a higher Fe/Si ratio and contains less Mg, reflected by its brighter appearance in SEM-BSE images (Figs. 3.3 and 3.4). SEM-EDS analyses can differentiate greenalite $[(Fe^{2+}, Fe^{3+})_{2-3}Si_2O_5(OH)_4]$ from minnesotaite $[(\mathrm{Fe}^{2+}, \mathrm{Mg})_3Si_4O_{10}(OH)_2]$, both in terms of morphology and chemical composition. For example, submicron grains with EDS spectra that show major O, Si and Fe, and minor Mg peaks, but no Al, Na or K peaks, were interpreted to be greenalite (Fig. 3.4 H – K; Muhling and Rasmussen, 2020). Other common Fe-silicates can be excluded because they are associated with additional peaks, for example, stilpnomelane exhibits a K peak and riebeckite

displays a Na peak. Morphologically, minnesotaite occurs as larger (5–20 µm long and 2–5 µm wide) 'bow-tie shaped' needles while greenalite laths are smaller (micron-scale) and occur as aggregates.

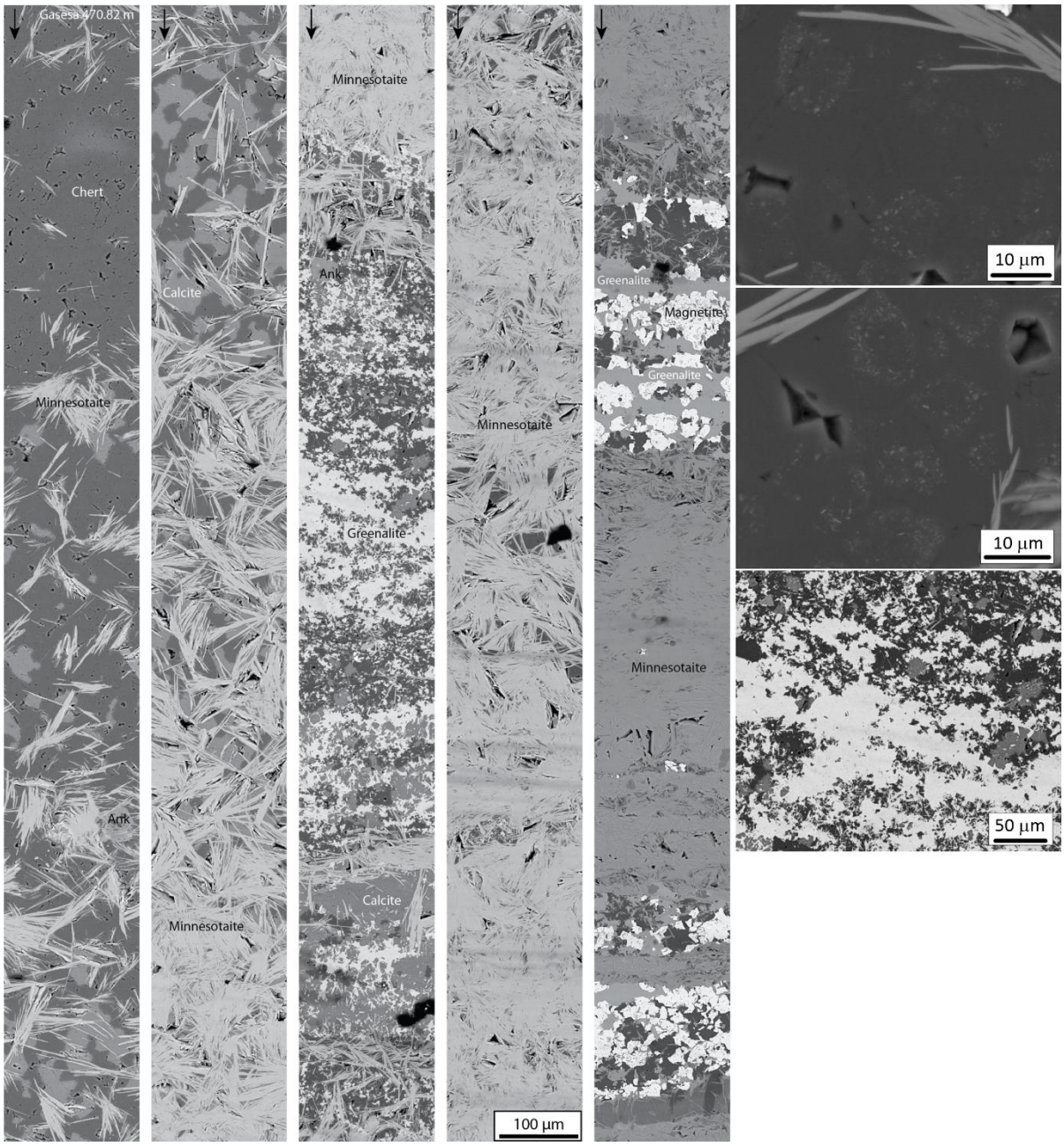

Figure 3. 3 | Cross-section view of micro-banded IF from the Transvaal Supergroup, South Africa. Stitched SEM-BSE image revealing micro-bands alternating between chert-, calcite-, ankerite-, Greenalite-, minnesotaite- and magnetite-rich layers, with abundant minnesotaite. Hexagonal structures formed by randomly oriented flakes of greenalite in chert are also shown. Each panel was imaged using unique settings, resulting in differences in brightness across panels for the same mineral.

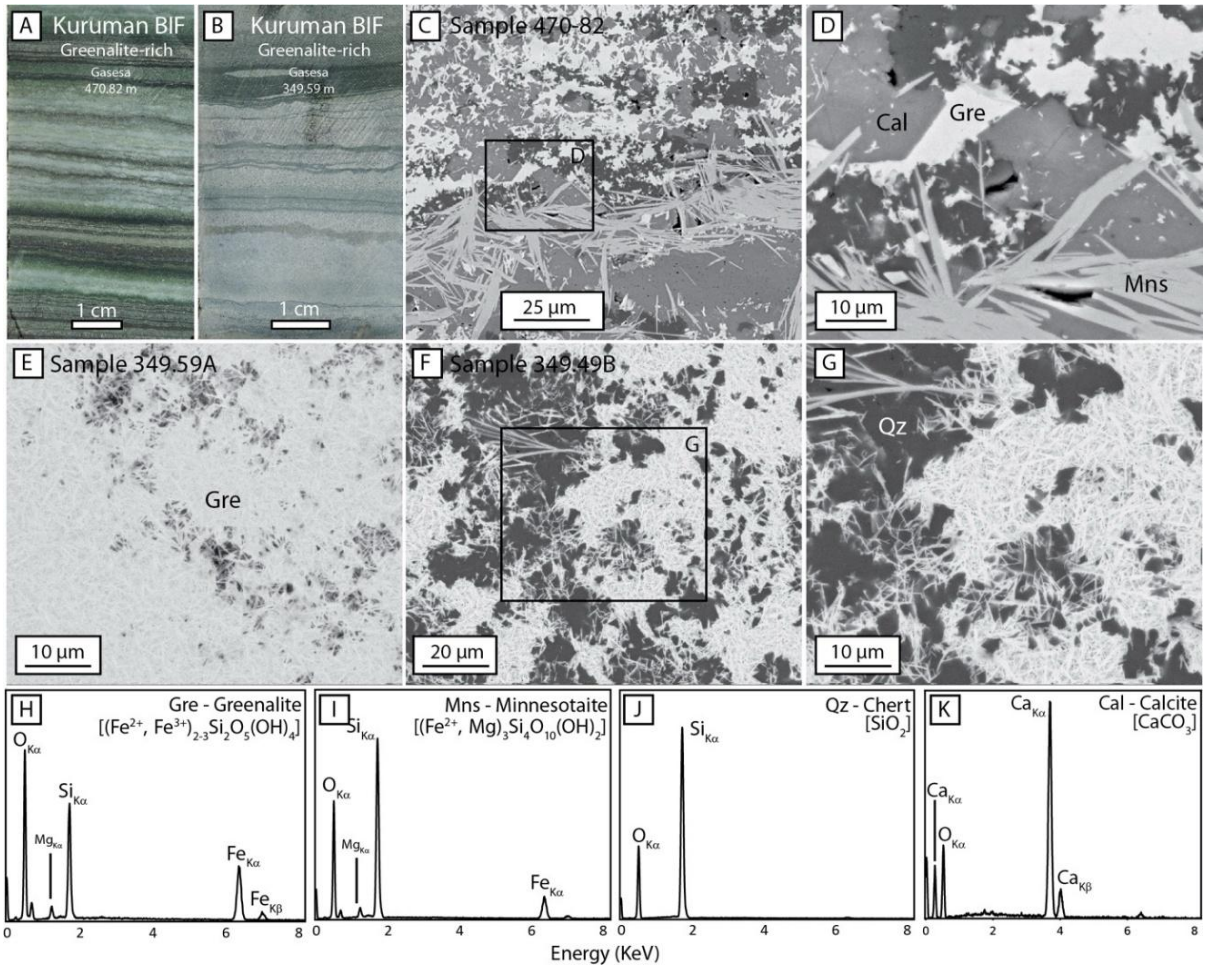

Figure 3. 4 | Images of samples used in this study from the Kuruman IF, Transvaal Supergroup. **A & B:** Drill core photos of greenalite-rich banded IF. **C & D:** BSE images of greenalite, minnesotaite, chert and calcite cut perpendicular to lamination. **E - G:** BSE images of samples cut parallel to a greenalite-chert laminae. These samples maximise exposure of the greenalite laths, which are suspended in chert and were used for LA ICP-MS analysis. **H - K:** SEM-EDS spectra differentiating greenalite (Gre), minnesotaite (Mns), chert (Qz) and calcite (Cal).

Internal lamination in very thinly laminated chert (typical laminae <1 mm thick) is commonly defined by greenalite (Fig. 3.4A–D). Greenalite is extremely fine-grained, occurring as laths, <1 µm in width and ~2–7 µm in length, which form dense aggregates, which may represent clusters of nanoparticles that formed in the water column (Rasmussen et al., 2013). The most common greenalite assemblages are chert-calcite-minnesotaite-greenalite, chert-minnesotaite-greenalite, chert-greenalite, and occasionally chert-greenalite-siderite (Fig. 3.3). In the chert-calcite-minnesotaite-greenalite assemblage, greenalite is cross-cut by calcite, which is in turn crosscut by minnesotaite, suggesting that these grains did not form in equilibrium, and that greenalite was the earliest forming phase (Fig. 3.4 C-D). Experimental work indicates that the primary phase precipitated from seawater was an amorphous Fe(II)-silicate gel, which crystallized to greenalite during heating and burial (Hinz et al.,

2021; Tosca et al., 2016; Tostevin & Ahmed, 2023). Since there is no direct evidence for this intermediate phase in the rock record, greenalite is referred to throughout this thesis.

3.4.3. Laser Ablation ICP-MS

Due to the complex mineralogy of banded IF, trace element concentrations determined via dissolution ICP-MS on bulk rocks or micro-drilled horizons integrate multiple phases. Given the high abundance of REY in other phases, such as apatite and siderite, incorporation of even small volumes can skew the average REY trends (Alibert, 2016; Oonk et al., 2018). Laser ablation ICP-MS allows a much smaller region to be targeted in isolation (40–120 µm), but the generally very fine grain size, low abundance, and fine-grained intergrowths of greenalite with other minerals make it challenging to obtain greenalite-specific trace element concentrations. To address this, samples were selected where greenalite is suspended in a pure chert matrix, to the exclusion of other minerals and these samples were cut parallel to micro-bands to expose the highest possible density of greenalite (Fig. 3.4E–G). Epoxy mounts were then used for major and trace element analysis via LA ICP-MS.

In situ mineral-specific REY data were obtained by spot analysis using a 193 nm wavelength COMPex 102 ArF excimer laser ablation system (Lambda Physik) connected to an Element 2 sector field inductively coupled plasma-mass spectrometer (Thermo Scientific) at Utrecht University, Netherlands. The mass spectrometer was operated in low-resolution mode. LA ICP-MS was performed with an energy density of 10 J/cm^2 and a pulse repetition rate of 10 Hz. Each analysis includes 60–70 s background measurement and 45 s sample signal measurement. The spot size (120 µm) was optimized to ensure that REY values were above the detection limit. The ablation area was maximized, resulting in signal homogenization across a significant number of greenalite grains (Fig. 3.5). This approach was taken to enhance the material ablation rate, ultimately leading to improved detection limits (sub-ppb), accuracy, and precision (suppl. Table S1c). The raw isotope data underwent reduction using a standardized trace element data reduction scheme in Iolite version 3.71 (Paton et al., 2011). ^{29}Si was used as an internal standard for greenalite, assuming 36.49 wt.%, a value constrained by microprobe analysis. Calibration was performed against NIST SRM 612, with results for secondary USGS standard BCR-2G typically within 0.5% of published reference values taken from the GeoReM database (Jochum et al., 2005). Major elements (Fe, Mg, Si, Ca), trace metals (V, Zn, Co, Ni, Mn), and the REY were analysed. The REY data is presented in chapter 4, while the trace metals data is presented in chapter 5.

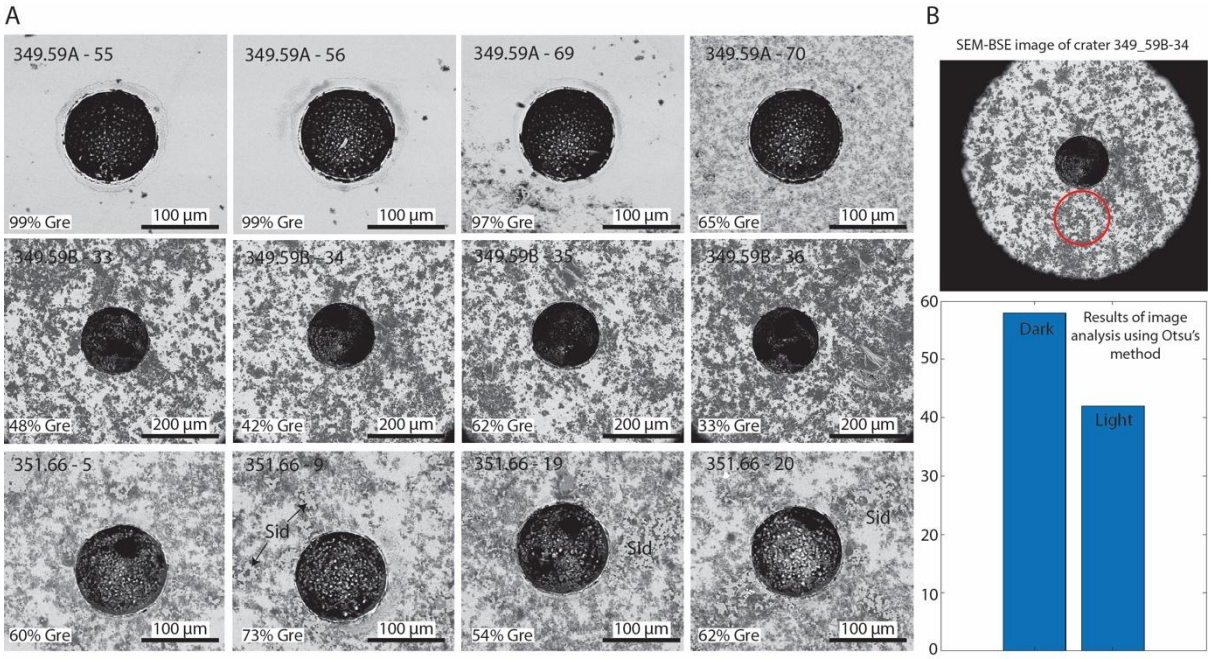

Figure 3. 5 | A: SEM-BSE micrographs of selected craters from in situ LA ICP-MS analyses on aggregates of greenalite laths, Transvaal Supergroup, South Africa, with 120 µm spot analyses. Greenalite appears white whereas chert is grey, and there are variable proportions of chert in each region. **B:** SEM-BSE image of a laser ablation crater showing a selected region (red circle) used to estimate the chert-to-greenalite proportion, alongside a histogram depicting the estimated proportion of greenalite (bright) to chert (dark) in the analysed area.

3.4.4. Electron probe microanalysis (EPMA)

Further confirmation of the mineralogy was achieved with the aid of electron probe microanalysis (EPMA) at Utretch University (Fig. 3.6). The samples used for LA ICP-MS analyses were repolished and carbon coated to ensure optimal electrical conductivity for electron probe microanalysis. To confirm the identity of the targeted Fe-silicate phases, analysed spots were carefully chosen in proximity to laser ablation craters. The major element composition was determined using wavelength dispersive spectroscopy on the 5-spectrometer JEOL JXA-8530F Hyperprobe Electron Probe Micro-Analyser at Utretch University. The operational parameters include a 20 nA beam current and a 20 kV accelerating voltage. A defocused beam with a 10 µm diameter was used during EMPA analyses to capture the compositions of Fe-silicate phases. Calibration to natural mineral standards was performed, and the counting times for all elements were 20 seconds on peak and 10 seconds on background. The results of the EPMA analyses are presented in Table 3.2. EMPA analyses provided further confirmation of the identity of our targeted Fe-silicate phases, revealing Si concentrations ranging from 15.0 to 18.4 wt.%, total Fe content ranging from 34.5 to 37.3 wt.%, characteristics consistent with greenalite (Fig. 3.6;

Gole, 1980; Jolliffe, 1935). Importantly, our findings demonstrate that these silicates are distinct from minnesotaite and other common Fe-silicates, despite potential geochemical similarities (Fig. 3.6).

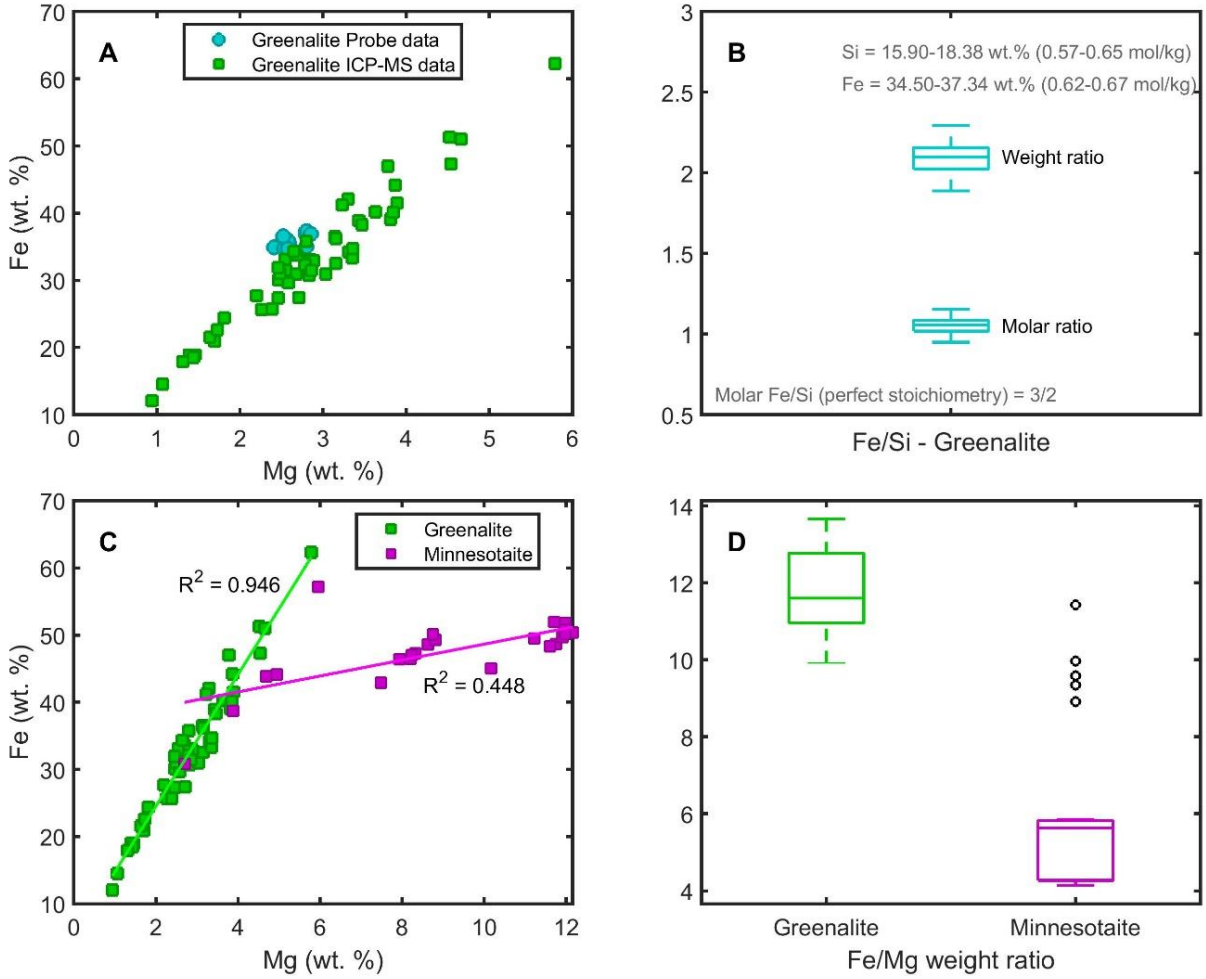

Figure 3. 6 | Microprobe and LA ICP-MS major element data for greenalite in micro-banded IFs, Transvaal Supergroup, South Africa: **(A).** Correlation between LA ICP-MS and microprobe data. Both techniques yield comparable outcomes, with microprobe data exhibiting enhanced precision owing to its smaller beam size; **(B).** Fe/Si weight and molar ratios assessment to confirm the identity of greenalite based on microprobe data; **C & D.** Distinguishing between our identified greenalite versus minnesotaite using LA ICP-MS data.

Table 3. 2 | EMPA major element data for IF greenalite of the Transvaal Supergroup. A 10 µm spot size was used for all analyses. All oxide and elemental data are reported in wt. %, while calculated molecular data for Si and Fe, denoted by [a], are reported in molkg^{-1}.

Analysis	SiO_2	Si	TiO_2	Al_2O_3	FeO	Fe	MgO	CaO	Na_2O	K_2O	P_2O_5	Si[a]	Fe[a]	Fe/Si	Calc. % water
351.66_1A	36.92	17.26	0.04	0.96	45.75	35.56	4.24	0.04	-0.01	0.20	-0.03	0.61	0.64	1.04	11.87
351.66_1B	35.65	16.66	0.06	0.88	46.19	35.90	4.27	0.10	0.03	0.19	-0.01	0.59	0.64	1.08	12.64
351.66_1C	36.64	17.12	0.03	0.94	45.89	35.67	4.28	0.05	0.02	0.19	-0.02	0.61	0.64	1.05	12.00
351.66_1D	36.48	17.05	0.06	0.92	46.02	35.77	4.21	0.05	0.04	0.20	0.01	0.61	0.64	1.06	12.00
351.66_1E	36.47	17.05	0.04	0.83	46.07	35.81	4.26	0.04	0.05	0.19	-0.01	0.61	0.64	1.06	12.07
351.66_1E 2	36.13	16.89	0.06	0.94	45.73	35.54	4.18	0.05	0.03	0.21	-0.02	0.60	0.64	1.06	12.70
351.66_1F	37.29	17.43	0.04	1.14	45.14	35.09	4.28	0.05	0.03	0.25	-0.02	0.62	0.63	1.01	11.81
351.66_1F 2	34.01	15.90	0.04	1.08	45.03	35.00	4.64	0.20	0.04	0.23	-0.01	0.57	0.63	1.11	14.74
351.66_2A	37.64	17.59	0.05	1.06	45.05	35.02	4.22	0.06	0.00	0.26	-0.01	0.63	0.63	1.00	11.67
351.66_2A 2	38.94	18.20	0.04	0.86	44.95	34.94	4.00	0.05	0.02	0.17	-0.03	0.65	0.63	0.97	10.98
351.66_2B	36.71	17.16	0.04	0.85	46.46	36.11	4.24	0.04	0.01	0.19	0.00	0.61	0.65	1.06	11.47
351.66_2C	36.11	16.88	0.04	0.87	46.82	36.39	4.18	0.05	0.03	0.17	-0.02	0.60	0.65	1.08	11.74
351.66_2C	36.02	16.84	0.03	0.85	46.24	35.94	4.23	0.04	0.23	0.17	-0.01	0.60	0.64	1.07	12.18
351.66_2C 2	35.72	16.69	0.06	0.97	45.41	35.30	4.25	0.08	0.11	0.18	-0.02	0.59	0.63	1.06	13.24
351.66_2D	36.87	17.23	0.03	1.11	45.17	35.11	4.24	0.06	0.35	0.25	0.00	0.61	0.63	1.02	11.92
351.66_2E	36.82	17.21	0.03	1.11	44.83	34.85	4.23	0.07	0.10	0.25	-0.01	0.61	0.62	1.02	12.57
351.66_2E 2	36.92	17.26	0.07	0.98	44.86	34.87	4.27	0.09	0.16	0.22	-0.04	0.61	0.62	1.02	12.47
351.66_2F	36.64	17.13	0.05	1.17	44.79	34.82	4.22	0.08	0.23	0.27	0.01	0.61	0.62	1.02	12.53
351.66_2G	36.95	17.27	0.03	1.17	44.76	34.80	4.20	0.07	0.13	0.28	0.01	0.61	0.62	1.01	12.41
351.66_2G 2	36.34	16.99	0.03	0.83	46.38	36.05	4.23	0.04	0.14	0.17	-0.01	0.60	0.65	1.07	11.84
351.66_2H	37.25	17.41	0.06	1.01	45.52	35.38	4.30	0.05	0.07	0.24	-0.01	0.62	0.63	1.02	11.52
351.66_2I	36.75	17.18	0.02	1.00	46.07	35.81	4.28	0.05	0.08	0.19	0.00	0.61	0.64	1.05	11.56
351.66_2I 2	36.27	16.95	0.06	0.82	47.04	36.57	4.18	0.04	0.04	0.15	-0.02	0.60	0.65	1.08	11.43
349.59A_1A	35.09	16.40	0.02	0.59	47.95	37.27	4.63	0.04	0.00	0.01	-0.02	0.58	0.67	1.14	11.70
349.59A_1B	35.25	16.48	0.01	0.57	47.42	36.86	4.63	0.02	0.01	0.01	-0.04	0.59	0.66	1.13	12.12
349.59A_1B 2	34.82	16.27	0.02	0.64	48.04	37.34	4.65	0.04	-0.01	0.00	-0.02	0.58	0.67	1.15	11.82
349.59A_2B	35.02	16.37	0.03	0.61	47.51	36.93	4.73	0.05	0.00	0.02	-0.01	0.58	0.66	1.13	12.03
349.59A_2C	39.33	18.38	0.01	0.47	44.64	34.70	4.27	0.03	0.00	0.01	0.01	0.65	0.62	0.95	11.23

3.4.5. Isolating the greenalite signal

For each of the three samples, every laser crater represents an independent analysis of a unique group of greenalite laths within a single layer. Targeted laser craters contained both greenalite and chert, but a customized code written in MATLAB® R2019a (Mathworks Inc., Natick, MA, USA) was used to independently estimate the proportion of greenalite-to-chert around each laser ablation hole. The SEM-BSE images of laser ablation craters were used to identify regions that provided an accurate representation of mineral proportions (Fig. 3.5). The code involved image pre-processing, including isolating ROIs and smoothing the image. Selection of ROIs was based on the laser analysis spot size and the distribution of minerals closest to the spot. I employed Otsu's method (Otsu, 1979) to automatically determine a global threshold for distinguishing chert and greenalite (dark and bright, respectively). This threshold was applied to segment the image into greenalite and chert, enabling the calculation of the proportions for each phase in the selected area (Fig. 3.5B). Colors, specifically white and grey, served as proxies for mineralogy in line with the greyscale nature of SEM-BSE images. It assumed a homogeneous average texture on a scale of 10–100 µm, and therefore the region around the crater is representative of the ablated area. The majority of the spots contained >50% greenalite (Table 3.3).

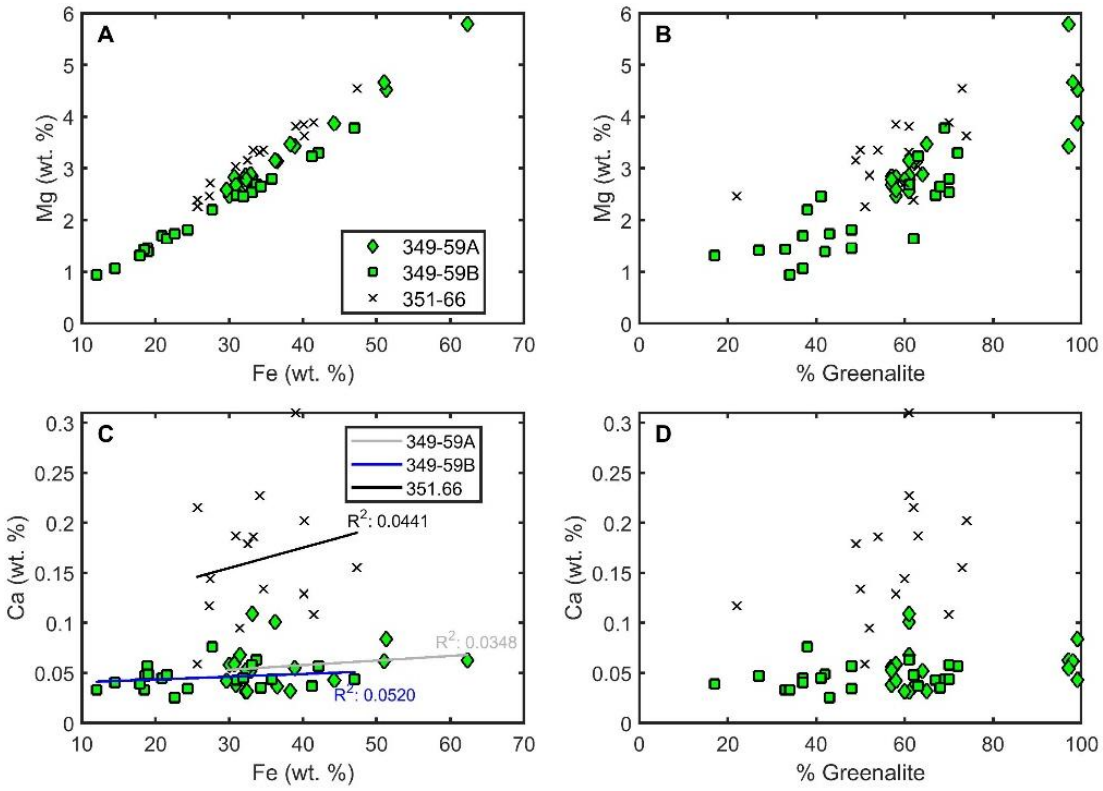

Figure 3. 7 | Cross plots of major elements in greenalite from LA ICP-MS analyses: **A & B**: % Greenalite and Fe vs. Mg showing Fe and Mg are hosted in greenalite. **C & D**: Ca vs. Fe and % Greenalite showing that Fe is not hosted in the calcite phase, and Ca is not hosted in greenalite, in sample 351.66.

Table 3. 3 | Major element concentrations of greenalite measured by LA ICP-MS and percentage of greenalite determined using a custom MATLAB script. All element concentrations are in ppm.

Analysis	Phase	Mg	Al	Ca	Fe	% Chert	% Greenalite
470-82A-83	Chert	1430	210	1280	17600	N/A	
470-82A-85	Chert	626	60	830	6100		
470-82A-86	Chert	2490	108	BLD	30900		
470-82A-91	Chert	1230	79	910	15510		
470-82A-92	Chert	13600	494	1090	162000		
470-82A-93	Chert	2290	99	680	24800		
470-82A-94	Chert	560	82	1110	7300		
470-82B-5	Chert	10580	444	1440	107200		
470-82B-9	Chert	3120	149	1330	29600		
349-59A-55	Greenalite	45200	4190	840	513000	1	99
349-59A-56	Greenalite	38700	3090	431	442000	1	99
349-59A-58	Greenalite	25540	1273	680	314700	39	61
349-59A-59	Greenalite	24660	1072	582	300400	42	58
349-59A-62	Greenalite	57900	6500	626	623000	3	97
349-59A-63	Greenalite	46600	4530	616	510000	2	98
349-59A-64	Greenalite	31400	1870	365	365000	38	62
349-59A-65	Greenalite	31500	1271	1010	362100	39	61
349-59A-66	Greenalite	27830	1231	1090	331100	39	61
349-59A-69	Greenalite	34300	2190	550	389000	3	97
349-59A-70	Greenalite	34700	2360	320	383000	35	65
349-59A-71	Greenalite	28490	1329	560	330600	43	57
349-59A-72	Greenalite	28300	1294	590	307000	42	58
349-59A-73	Greenalite	28580	1614	312	322400	39	61
349-59A-76	Greenalite	28890	1552	520	329100	36	64
349-59A-77	Greenalite	27850	1353	318	324100	40	60
349-59A-78	Greenalite	26780	1287	381	309000	43	57
349-59A-79	Greenalite	27810	1256	530	323000	43	57
349-59A-80	Greenalite	25830	1089	421	296400	42	58

BDL = below limit of detection

Table 3. 3 (Continued)

Analysis	Phase	Mg	Al	Ca	Fe	% Chert	% Greenalite
349-59B-26	Greenalite	26850	912	631	337100	39	61
349-59B-27	Greenalite	21990	809	760	276900	62	38
349-59B-28	Greenalite	24800	841	430	310000	33	67
349-59B-29	Greenalite	14160	512	470	186000	73	27
349-59B-30	Greenalite	16970	654	448	209000	63	37
349-59B-33	Greenalite	14600	554	570	189100	52	48
349-59B-34	Greenalite	13950	522	488	190200	58	42
349-59B-35	Greenalite	16390	632	480	215600	38	62
349-59B-36	Greenalite	14380	557	332	185000	67	33
349-59B-37	Greenalite	13120	534	390	179200	83	17
349-59B-38	Greenalite	9430	354	331	120400	66	34
349-59B-40	Greenalite	33000	1204	570	421000	28	72
349-59B-41	Greenalite	37800	1363	438	470000	31	69
349-59B-42	Greenalite	25400	872	582	331000	30	70
349-59B-43	Greenalite	28000	973	440	358000	30	70
349-59B-44	Greenalite	32320	1368	370	412000	37	63
349-59B-47	Greenalite	10670	425	404	145000	63	37
349-59B-48	Greenalite	24590	959	450	319000	59	41
349-59B-49	Greenalite	18100	693	346	244000	52	48
349-59B-50	Greenalite	17300	643	254	226000	57	43
349-59B-51	Greenalite	26490	943	354	343000	32	68
351-66-5	Greenalite	27100	3340	1442	274200	40	60
351-66-6	Greenalite	36300	5030	2020	402200	26	74
351-66-7	Greenalite	24590	3270	1170	273400	78	22
351-66-8	Greenalite	30330	3170	1870	309300	37	63
351-66-9	Greenalite	45400	6730	1550	473000	27	73
351-66-12	Greenalite	38910	6710	1083	415000	30	70
351-66-13	Greenalite	31520	3620	1790	325100	51	49
351-66-14	Greenalite	22590	3610	589	256800	49	51
351-66-15	Greenalite	33100	4785	2270	342000	39	61
351-66-16	Greenalite	28600	4355	949	314700	48	52
351-66-19	Greenalite	33510	3540	1860	333000	46	54
351-66-20	Greenalite	23900	3450	2150	257000	38	62
351-66-21	Greenalite	38120	5340	3100	390700	39	61
351-66-22	Greenalite	33590	5340	1340	346900	50	50
351-66-23	Greenalite	38460	6680	1290	401400	42	58

3.5. Assessing the greenalite data

Magnesium content in greenalite, analysed via LA ICP-MS, ranges from 1.0 to 4.8 wt.%, except for two outliers at 5.25 and 5.94 wt.% (Fig. 3.7; Table 3.3) while EMPA analyses show more consistent values of 2.4–2.9 wt.% Mg (Figs. 3.6 & 3.7; Table 3.2). Iron content in greenalite ranges from 11 to 60% in LA ICP-MS, with a more consistent range of values via EMPA from 34.5 to 37.3 wt% Fe. There are positive correlations between Mg, Fe, and % greenalite (Fig. 3.7), suggesting that Mg and Fe are both hosted in greenalite. The observed variability in these elements via LA ICP-MS is due to the variable proportion of greenalite laths in each spot analysis (Fig. 3.5; Table 3.3), implying the maximum Mg content is representative of the greenalite endmember. However, the maximum Fe and Mg content analysed via LA ICP-MS exceeds the Fe and Mg content of greenalite via EMPA, which cannot result from chert dilution. This discrepancy likely arises because ICP-MS is optimized for trace element analysis, and the accuracy of major elements can be poor. However, the relative trends are accurate, and this is supported by the close correlation between the Fe and Mg content and the % greenalite determined independently from Otsu's method.

While recent experimental work has shown that synthetic Fe(II)-silicate nanoparticles contain little Mg (Hinz et al., 2021), and this is consistent with quantitative transmission electron microscopy-EDS analysis of natural greenalite nanoparticles in chert, the EMPA data in this study aligns with previous work on coarser grained natural greenalite, which can contain up to 4 wt.% Mg (Gole, 1980; Jolliffe, 1935). The observed variation in Mg content across these studies may reflect differences in the primary fluid chemistry of the depositional environments, variation in K'_D depending on the depositional mechanism, or subsequent enrichment processes. It is difficult to quantify the partitioning of Mg into greenalite under realistic Mg concentrations (~30–50 mmol.kg^{-1}) because the proportional change in Mg concentration during greenalite precipitation would be too small to detect.

SEM-BSE images of sample 351.66 show the presence of fine-grained siderite (Figs. 3.5 & 3.8). While efforts were made to avoid it, there is a possibility that fine siderite grains may have been inadvertently included in the LA ICP-MS analysis in this sample, and geochemical data support this, showing higher Ca content (Fig. 3.7C). This is consistent with previous work which demonstrated that siderite and ankerite host REY in the Kuruman and Griquatown Formations (Oonk et al., 2018). However, there is no correlation between Ca and either % greenalite or Fe content (Fig. 3.7C & D), so the major control on Ca appears to be siderite. In contrast, there is no evidence for siderite or any other phases in samples 349-59A and 349-59; they only contain greenalite and chert. Samples 349-59A and 349-59B were obtained from the same drill core depth, but their exposed surfaces show

variations in the proportion of chert to greenalite (Table 3.3). As a result, the trace and REY data from greenalite-rich craters are dominated by greenalite. The large range of Fe and Mg, content reflects the proportion of greenalite in each spot, rather than geochemical variation between greenalite grains.

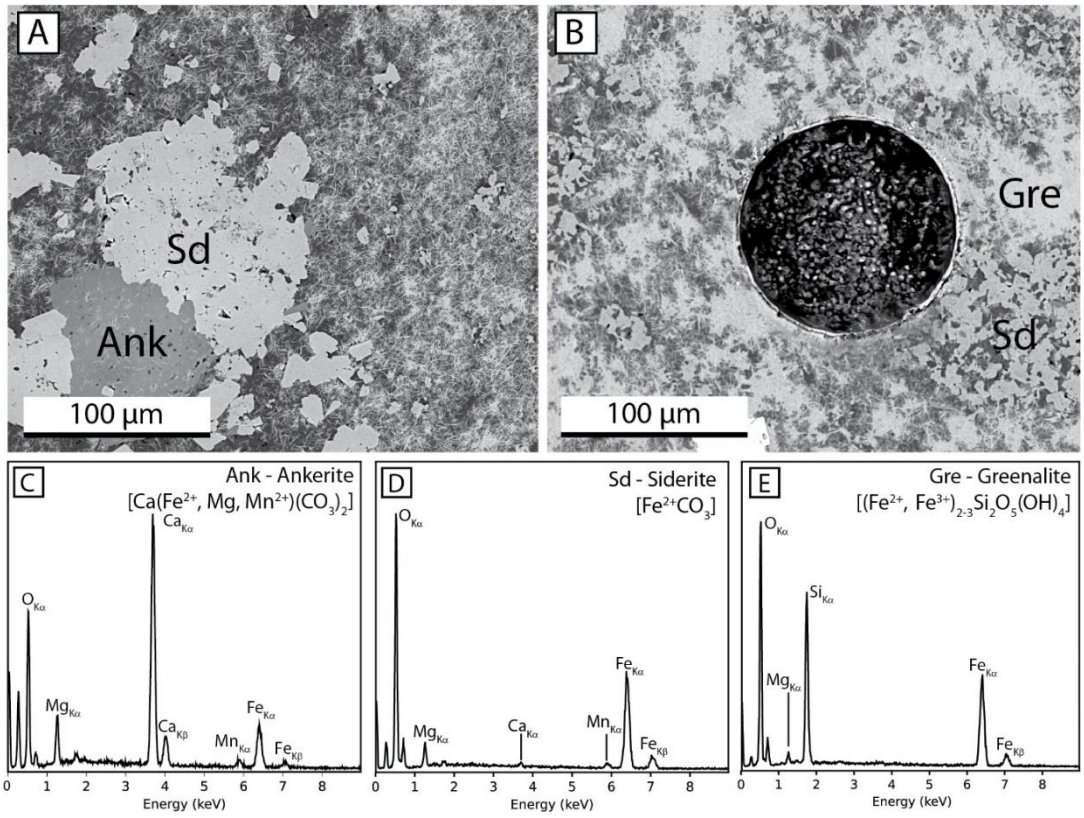

Figure 3. 8 | (A). SEM-BSE image of sample 351-66 showing an example of a larger siderite (Sd) grain that was avoided during LA ICP-MS analysis, as well as smaller grains that may have been incorporated into the ablation craters; **(B).** SEM-BSE image of a laser ablation crater in a region that contains fine grained siderite. **C–E**. EDS spectra for ankerite (Ank), siderite (Sd) and greenalite (Gre).

3.6. Conclusion

This new methodology offers a refined approach to deconvolve geochemical signals from greenalite and the surrounding chert. It proves most effective when only two minerals are present, necessitating a pre-screening for siderite or other phases.

There are some limitations to this approach, primarily the estimation of greenalite proportion, as the area targeted for measuring mineral proportions isn't always the exact area analyzed. Accurately pre-marking these targeted spots is challenging. Additionally, the technique depends on differentiating minerals with significant differences in atomic weights to be distinguishable in SEM and subsequently by the MATLAB code.

Despite these challenges, this method has broader applicability and can be accurately used for similar issues in other rocks containing tiny minerals below the laser's spot size. The novel approach detailed in this chapter not only enhances the accuracy and reliability of geochemical data extraction but also lays the groundwork for subsequent geochemical analyses, ensuring clarity and avoiding redundancy. This advancement is crucial for understanding greenalite's role and formation within the broader geological context of the Transvaal Supergroup, providing a robust framework for interpreting the data reported in the following chapters.

Chapter 4

A Seawater Origin for Greenalite in Iron Formation of the Transvaal Supergroup

4.1. Introduction

Iron formation are abundant in Archean and Paleoproterozoic rocks, but their origin remains enigmatic. They are typically characterized by a diverse mineralogy and include both Fe(II)- and Fe(III)-bearing minerals (Klein, 2005). Biological or abiotic redox processes may have played an important role in the generation of ferric minerals in banded IF (Johnson et al., 2008a). Conventional models proposing the genesis of IF emphasize poorly crystalline ferrihydrite ($Fe(OH)_3$), which persists as fine-grained "dusty" hematite, as a central component of the depositional model (Konhauser et al., 2017; Sun et al., 2015). Green rust, a mixed-valence Fe(II)-Fe(III) hydroxide, has also been proposed as an important primary phase (Halevy et al., 2017). In this model, Fe(II)-bearing minerals formed during anoxic diagenesis, fuelled by the degradation of organic carbon.

Emerging models challenge this view by proposing that Fe(II)-bearing minerals were the principal primary precipitates (Rasmussen et al., 2021). This model is supported by high resolution imaging that has revealed abundant primary Fe(II)-silicate minerals such as greenalite in IF (Johnson et al., 2018; Rasmussen et al., 2015, 2017). Some proponents have even argued that all hematite in IF is a product of late-stage alteration by oxygen-bearing fluids (Rasmussen et al., 2014). This perspective raises a number of possibilities, such as the complete absence of O_2 before the GOE around 2.43 Ga (Gumsley et al., 2017), which would have far-reaching consequences for the timing of the origin of cyanobacteria and the interpretation of geochemical proxy records. However, current evidence for these two depositional models is mixed, and it is possible that ferric minerals contributed to primary IF (Sun et al., 2015). Nevertheless, geological evidence underscores the importance of greenalite as a primary phase in these rocks (Rasmussen et al., 2021).

The key question arises: what triggered the precipitation of greenalite? One possibility is that greenalite precipitated in a shallow-water shelf environment. Several triggers for greenalite precipitation have been proposed, such as small increases in pH (Rasmussen et al., 2017; Tosca et al., 2016). However, greenalite precipitation at ambient temperature requires pH >7.5, and models predict that the average pH in Archean oceans was 6.7–7.0 (Krissansen-Totton et al., 2018). Recent work has shown that the presence of small amounts of Fe^{3+} could have facilitated the precipitation of well-ordered greenalite at the lower pH of 6.5–7 (Hinz et al., 2021). Another pathway for greenalite precipitation on the shelf is the aging of green rust (Halevy et al., 2017). An alternative model proposes that greenalite formed as hot hydrothermal fluids mixed with anoxic, sulphate-free seawater in and around vents, and was subsequently transported laterally and re-deposited on the shelf (Tosca & Tutolo, 2023). This is supported by experiments that show Fe(II)-silicate solubility decreases with

temperature, which when extrapolated to the T-pH combinations typically found in vent systems, suggest rapid precipitation (Tostevin & Ahmed, 2023). The lateral transport of greenalite in plumes may have been aided by its relatively low density (Tosca & Tutolo, 2023). This hydrothermal model aligns with some chemical and sedimentological indicators from IF, such as low organic carbon content (Konhauser et al., 2017), and prominent Eu/Eu* anomalies in bulk IF (Bau & Dulski, 1996).

One pathway to distinguish between these models for greenalite precipitation is using the relative abundance of REY in primary greenalite, because hydrothermal fluids and seawater have distinct PAAS-normalized REY patterns. Here, I present new mineral-specific REY data from natural greenalite in micro-banded IF from the Transvaal Supergroup, South Africa. The REY data was collected using LA ICP-MS and the detailed methodology used is described in chapter 3. Additionally, I conducted a comparative analysis of key features in the REY patterns with those of bulk rock IF, limestone and other mineral-specific data from the Transvaal Supergroup, as well as the seawater and hydrothermal fluid endmembers to determine the origin of greenalite.

The interpretations presented in this chapter build upon foundational work by Rasmussen et al. (2013, 2014, 2019), which provided compelling evidence through high-resolution microscopy that greenalite is a primary precipitate in iron formations. This chapter is focused specifically on using the chemical properties of greenalite to determine its precipitation environment, operating on the assumptions that greenalite is indeed a primary phase, and there is an absence of REY fractionation between sweater and greenalite. However, if the greenalite analyzed here were instead a diagenetic phase, several key implications would arise. For example, the REY data may exhibit chemical characteristics that instead reflect the environment of diagenesis, or they could represent of REY fractionation. These considerations are acknowledged and would warrant a re-evaluation of certain conclusions if further evidence were to indicate a diagenetic origin for greenalite in these samples.

4.2. Rare earth element characteristics of greenalite

All REY patterns were normalized to PAAS using the values of Pourmand et al. (2012). Promethium (Pm) does not occur in nature, so values were interpolated based on neighbouring elements. Anomalies such as $(La/La^*)_{SN}$, $(Ce/Ce^*)_{SN}$, and $(Eu/Eu^*)_{SN}$, as well as Y/Ho and total REE (∑REE) were calculated using formulas recommended by Lawrence et al. (2006). There are positive correlations between Fe content, ∑REE, and % greenalite (Fig. 4.1)—determined using Otsu's method—indicating that greenalite is the primary host for these elements. While chert dilution reduces ∑REE, it does not

affect the overall REY pattern. The observed variation in Fe and REY reflects differences in the proportion of greenalite rather than intrinsic geochemical differences between greenalite grains.

The PAAS-normalized REY trends for greenalite (samples 349-59A and 349-59B) are highly consistent and indicate HREE enrichment (Yb_{SN}/Nd_{SN} = 4–21) with super-chondritic Y/Ho ratios (37.5 ± 2.0) and low ∑REE (1.4–13.1 ppm) (Table 4.1; Fig. 4.1). They have positive $(Eu/Eu^*)_{SN}$ (= 1.41 ± 0.19) and lack significant positive or negative Ce anomalies (Ce_{SN}/Ce_{SN}^* = 1.15 ± 0.18) or La anomalies (La_{SN}/La_{SN}^* = 1.19 ± 0.34) (Table 4.1). The overall REY patterns for sample 351-66 are similar, despite the presence of minor siderite (see section 3.5), consistent with evidence that greenalite is the dominant phase and the host for the majority of REE (Fig. 4.1). However, the REY patterns in sample 351-66 are associated with slightly higher $(Eu/Eu^*)_{SN}$ (1.65 ± 0.18) and $(La/La^*)_{SN}$ (1.57 ± 0.29) (Table 4.1). Most of the analyzed craters contained >50% greenalite (Fig. 4.1E–F; Table 3.3). We also analyzed the REY concentrations in greenalite-free chert (<5% Fe-silicate), which were associated with lower ∑REE (0.67–1.28 ppm; Fig. 4.2; Table 4.1). As a consequence, much of the chert data, including Eu, were below the detection limit, resulting in an incomplete REY pattern (Fig. 4.2). As such, the chert REY signal has little impact on the weighted-average REY pattern or the calculated Eu anomaly, but when the chert component exceeded 40% of the ablated crater, the drop in REE content can introduce some artefacts into the REY patterns. However, the REY patterns for greenalite-rich craters (<40% chert) are highly consistent (Fig. 4.1A – C).

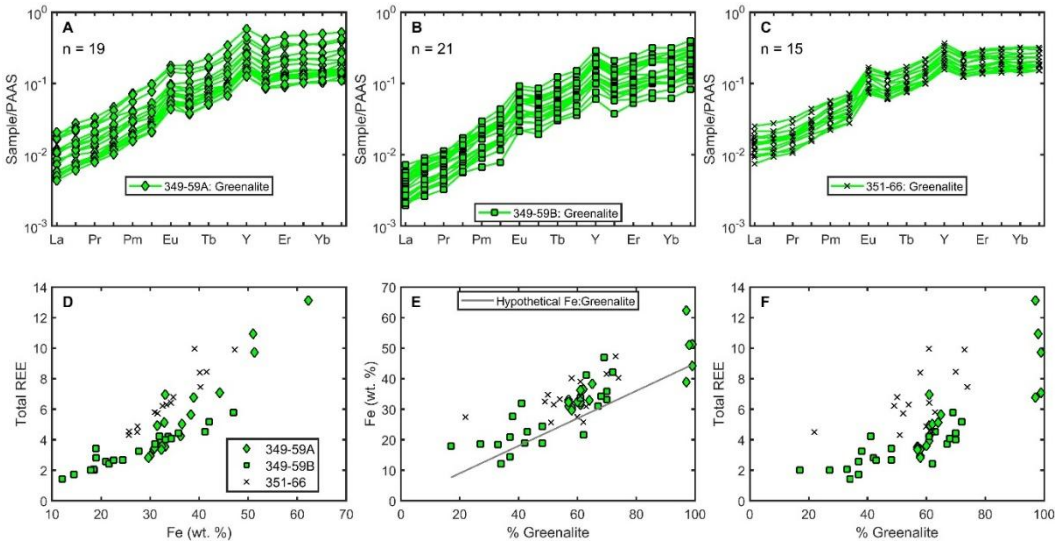

Figure 4. 1 | LA ICP-MS REY data from the ~2.46 Ga Kuruman IF, Transvaal Supergroup: **(A–C).** PAAS-normalised REY patterns from analysis of greenalite for three samples. The only other phase present in samples 349-59A and 349-59B was chert. Sample 351-66 contained greenalite, chert and minor siderite. **(D)**: cross-plot of ∑REE vs. wt. % Fe, determined by LA ICP-MS; **(E–F).** wt. % Fe and ∑REE, determined by LA ICP-MS, vs. the % greenalite determined by Otsu's method. The black line (y = 0.45x) is the hypothetical Fe content of diluted greenalite. Fe

content is overestimated by LA ICP-MS (see supplementary discussion and comparison with EMPA data). In general, analyses with lower ∑REE represent ablation craters that contained a greater proportion of chert.

Table 4. 1 | LA ICP-MS data, diagnostic REY ratios and anomalies related to the lanthanide tetrad effect for IF greenalite (samples 349-59A, B & 351-66) and chert (samples 470-82A, B) of the Kuruman Formation, Transvaal Supergroup.

Analysis	La	Ce	Pr	Nd	Sm	Eu	Gd	Tb	Dy	Y	Ho	Er	Tm	Yb	Lu	Ce/Ce*	La/La*	Y/Ho	Eu/Eu*	ΣREE	Yb/Nd
470-82A-83	0.021	0.045	BLD	BLD	BLD	BLD	0.013	0.011	0.018	0.254	BLD	0.014	BLD	0.040	BLD					0.16	
470-82A-85	0.010	0.020	BLD	0.014	BLD	BLD	BLD	BLD	0.009	0.340	0.006	BLD	BLD	BLD	0.028			54.84		0.09	
470-82A-86	0.042	0.049	0.008	0.015	BLD	BLD	BLD	BLD	0.009	0.281	BLD	0.021	0.005	0.022	BLD	0.40	0.36			0.17	18.17
470-82A-91	0.041	0.072	0.011	0.033	BLD	BLD	BLD	BLD	BLD	0.316	0.011	0.009	BLD	0.040	0.007	0.59	0.54	28.99		0.22	15.02
470-82A-92	0.062	0.133	0.014	0.082	BLD	BLD	BLD	BLD	0.038	0.576	0.015	0.040	0.008	0.022	0.015	1.84	2.79	38.66		0.43	3.32
470-82A-93	0.032	0.033	BLD	BLD	0.012	BLD	0.046	0.005	BLD	0.225	0.005	0.004	BLD	0.011	BLD			41.67		0.15	
470-82A-94	0.063	0.073	0.010	0.066	BLD	BLD	BLD	BLD	0.009	0.320	0.005	0.004	BLD	0.025	BLD	1.48	4.49	60.38		0.26	4.69
470-82B-5	0.224	0.335	0.064	0.290	0.066	BLD	BLD	0.019	0.090	1.150	0.022	0.047	0.007	0.096	0.020	0.74	1.21	52.27		1.28	4.10
470-82B-9	0.053	0.105	0.015	0.012	BLD	BLD	BLD	0.001	0.019	0.288	0.001	0.005	BLD	0.003	0.011	0.18	0.04	480.00		0.22	3.10
349-59A-55	0.730	1.890	0.277	1.270	0.528	0.175	0.830	0.147	1.190	10.900	0.289	1.020	0.163	1.050	0.171	0.98	0.93	37.72	1.37	9.73	10.24
349-59A-56	0.457	1.280	0.194	0.980	0.357	0.118	0.627	0.108	0.930	8.460	0.236	0.743	0.121	0.803	0.129	1.04	1.01	35.85	1.31	7.08	10.15
349-59A-58	0.530	1.170	0.163	0.870	0.227	0.092	0.339	0.057	0.460	4.220	0.114	0.405	0.052	0.393	0.061	1.20	1.56	37.02	1.76	4.93	5.60
349-59A-59	0.222	0.588	0.090	0.429	0.142	0.064	0.224	0.045	0.364	3.430	0.090	0.275	0.046	0.309	0.055	0.97	0.94	38.20	1.75	2.94	8.92
349-59A-62	0.821	2.420	0.335	1.730	0.678	0.215	1.100	0.202	1.820	15.910	0.441	1.415	0.215	1.500	0.229	1.17	1.10	36.08	1.27	13.12	10.74
349-59A-63	0.756	2.100	0.275	1.570	0.670	0.196	0.960	0.157	1.360	12.200	0.320	1.130	0.155	1.110	0.185	1.36	1.51	38.13	1.32	10.94	8.76
349-59A-64	0.344	0.990	0.132	0.669	0.270	0.090	0.405	0.082	0.619	6.000	0.155	0.558	0.086	0.542	0.089	1.19	1.13	38.71	1.32	5.03	10.04
349-59A-65	0.385	0.882	0.110	0.558	0.197	0.070	0.302	0.064	0.526	4.550	0.132	0.423	0.071	0.444	0.082	1.27	1.52	34.47	1.35	4.25	9.86
349-59A-66	0.920	1.970	0.262	1.270	0.332	0.094	0.485	0.076	0.492	4.700	0.119	0.401	0.059	0.417	0.062	1.14	1.39	39.50	1.29	6.96	4.07
349-59A-69	0.510	1.420	0.211	0.990	0.364	0.112	0.517	0.098	0.810	7.240	0.180	0.668	0.100	0.667	0.117	0.99	0.90	40.22	1.30	6.76	8.35
349-59A-70	0.324	1.024	0.144	0.800	0.300	0.113	0.461	0.092	0.717	6.960	0.200	0.633	0.099	0.641	0.093	1.24	1.17	34.80	1.48	5.64	9.93
349-59A-71	0.262	0.689	0.097	0.508	0.176	0.066	0.273	0.054	0.408	4.200	0.110	0.364	0.058	0.408	0.067	1.16	1.25	38.36	1.48	3.54	9.95
349-59A-72	0.232	0.639	0.098	0.451	0.147	0.061	0.284	0.053	0.427	4.280	0.115	0.361	0.059	0.389	0.060	0.94	0.84	37.22	1.49	3.38	10.69
349-59A-73	0.255	0.698	0.093	0.554	0.201	0.081	0.375	0.063	0.488	4.710	0.116	0.433	0.068	0.446	0.066	1.39	1.62	40.74	1.57	3.94	9.97
349-59A-76	0.480	1.260	0.165	0.730	0.269	0.090	0.371	0.068	0.510	5.160	0.133	0.454	0.071	0.460	0.070	1.06	0.96	38.80	1.46	5.13	7.81
349-59A-77	0.215	0.637	0.084	0.495	0.172	0.061	0.327	0.061	0.485	4.410	0.113	0.398	0.062	0.427	0.061	1.40	1.50	38.96	1.28	3.60	10.69
349-59A-78	0.209	0.614	0.093	0.466	0.184	0.070	0.319	0.057	0.477	4.050	0.104	0.379	0.059	0.363	0.058	1.03	0.95	38.83	1.48	3.45	9.65
349-59A-79	0.226	0.631	0.084	0.430	0.173	0.062	0.309	0.051	0.413	4.080	0.106	0.357	0.054	0.396	0.063	1.20	1.19	38.64	1.44	3.35	11.41
349-59A-80	0.194	0.532	0.079	0.381	0.143	0.053	0.230	0.046	0.359	3.450	0.093	0.296	0.046	0.329	0.048	1.01	0.95	37.18	1.43	2.83	10.70

BLD = below limit of dectection. Except for Y/Ho and ΣREE, all ratios are PAAS-normalized ratios.

Table 4. 1 (continued)

Analysis	La	Ce	Pr	Nd	Sm	Eu	Gd	Tb	Dy	Y	Ho	Er	Tm	Yb	Lu	Ce/Ce*	La/La*	Y/Ho	Eu/Eu*	ΣPEE	Yb/Nd
349-59B-26	0.171	0.536	0.089	0.470	0.188	0.087	0.394	0.072	0.606	5.480	0.143	0.539	0.097	0.694	0.129	1.00	0.91	38.32	1.60	4.22	18.30
349-59B-27	0.149	0.495	0.077	0.374	0.176	0.066	0.276	0.053	0.430	3.930	0.109	0.408	0.061	0.496	0.087	0.98	0.77	35.92	1.49	3.26	16.43
349-59B-29	0.089	0.281	0.040	0.231	0.103	0.035	0.166	0.039	0.340	2.670	0.076	0.213	0.045	0.300	0.052	1.27	1.25	35.13	1.18	2.01	16.09
349-59B-30	0.122	0.350	0.061	0.272	0.109	0.051	0.229	0.047	0.349	3.400	0.099	0.346	0.054	0.402	0.080	0.80	0.67	34.34	1.52	2.57	18.31
349-59B-33	0.320	0.770	0.099	0.470	0.184	0.037	0.259	0.047	0.369	3.320	0.094	0.283	0.052	0.375	0.069	1.16	1.23	35.32	0.87	3.43	9.89
349-59B-34	0.197	0.580	0.086	0.450	0.146	0.054	0.205	0.036	0.325	2.890	0.074	0.246	0.045	0.306	0.052	1.10	1.06	39.32	1.62	2.80	8.43
349-59B-35	0.109	0.336	0.051	0.274	0.114	0.043	0.199	0.041	0.364	3.080	0.086	0.303	0.051	0.399	0.064	1.13	1.07	35.81	1.38	2.43	18.04
349-59B-38	0.095	0.231	0.033	0.208	0.054	0.027	0.117	0.027	0.190	1.630	0.040	0.162	0.028	0.187	0.036	1.39	1.94	41.27	1.46	1.43	11.14
349-59B-40	0.212	0.656	0.103	0.648	0.249	0.101	0.460	0.088	0.723	6.450	0.175	0.660	0.115	0.819	0.147	1.25	1.37	36.86	1.47	5.16	15.66
349-59B-41	0.256	0.796	0.115	0.555	0.302	0.112	0.518	0.110	0.802	7.910	0.223	0.738	0.143	0.950	0.175	1.04	0.87	35.47	1.32	5.80	21.21
349-59B-42	0.193	0.543	0.078	0.475	0.175	0.073	0.357	0.073	0.561	5.190	0.147	0.511	0.088	0.614	0.114	1.34	1.56	35.31	1.37	4.00	16.02
349-59B-43	0.230	0.690	0.103	0.500	0.207	0.071	0.386	0.072	0.593	5.620	0.157	0.539	0.103	0.673	0.122	1.02	0.89	35.80	1.26	4.45	16.68
349-59B-44	0.210	0.631	0.098	0.501	0.190	0.089	0.363	0.070	0.585	6.080	0.163	0.575	0.102	0.796	0.135	1.03	0.94	37.30	1.66	4.51	19.69
349-59B-47	0.094	0.294	0.044	0.214	0.102	0.026	0.143	0.029	0.213	2.048	0.060	0.186	0.033	0.248	0.047	1.01	0.84	33.91	1.05	1.73	14.36
349-59B-48	0.252	0.730	0.087	0.590	0.196	0.070	0.349	0.069	0.483	4.910	0.139	0.426	0.089	0.650	0.091	1.78	2.24	35.32	1.30	4.22	13.65
349-59B-49	0.119	0.340	0.057	0.315	0.116	0.043	0.247	0.041	0.361	3.500	0.088	0.327	0.061	0.498	0.064	1.03	1.07	39.77	1.34	2.68	19.59
351-66-6	0.766	1.538	0.187	1.060	0.404	0.149	0.611	0.116	0.848	7.290	0.202	0.668	0.107	0.698	0.102	1.46	2.22	36.09	1.50	7.46	8.16
351-66-7	0.413	0.909	0.128	0.590	0.230	0.101	0.374	0.070	0.527	4.740	0.129	0.431	0.067	0.465	0.067	1.02	1.16	36.74	1.74	4.50	9.77
351-66-8	0.678	1.320	0.173	0.884	0.278	0.108	0.414	0.078	0.597	5.150	0.143	0.461	0.081	0.503	0.080	1.22	1.72	36.01	1.60	5.80	7.05
351-66-9	0.950	1.890	0.279	1.480	0.494	0.204	0.830	0.152	1.175	9.910	0.276	0.913	0.142	0.967	0.140	1.12	1.61	35.91	1.62	9.89	8.10
351-66-12	0.617	1.467	0.199	1.128	0.456	0.190	0.790	0.139	1.140	9.060	0.260	0.869	0.136	0.921	0.132	1.31	1.68	34.85	1.64	8.44	10.12
351-66-13	0.657	1.400	0.185	0.900	0.350	0.102	0.489	0.088	0.691	5.770	0.157	0.522	0.088	0.510	0.082	1.15	1.42	36.75	1.27	6.22	7.02
351-66-14	0.331	0.822	0.108	0.619	0.190	0.091	0.357	0.068	0.596	4.730	0.133	0.436	0.071	0.419	0.067	1.36	1.70	35.56	1.72	4.31	8.39
351-66-15	0.648	1.370	0.187	0.875	0.347	0.150	0.502	0.099	0.740	6.380	0.176	0.567	0.090	0.594	0.090	1.07	1.28	36.25	1.76	6.43	8.41
351-66-16	0.507	1.139	0.161	0.782	0.270	0.121	0.455	0.085	0.740	5.750	0.181	0.520	0.095	0.573	0.090	1.07	1.25	31.77	1.74	5.72	9.08
351-66-19	0.820	1.478	0.184	0.964	0.242	0.126	0.449	0.083	0.584	5.240	0.152	0.511	0.073	0.548	0.080	1.32	2.06	34.47	1.93	6.29	7.04
351-66-20	0.440	0.945	0.115	0.578	0.242	0.093	0.382	0.066	0.531	4.290	0.131	0.420	0.064	0.459	0.066	1.29	1.63	32.75	1.61	4.53	9.84
351-66-21	1.121	2.430	0.326	1.640	0.485	0.169	0.723	0.122	0.975	8.100	0.235	0.739	0.111	0.778	0.117	1.17	1.47	34.47	1.52	9.97	5.88

BLD = below limit of dectection. Except for Y/Ho and ΣREE, all ratios are PAAS-normalized ratios.

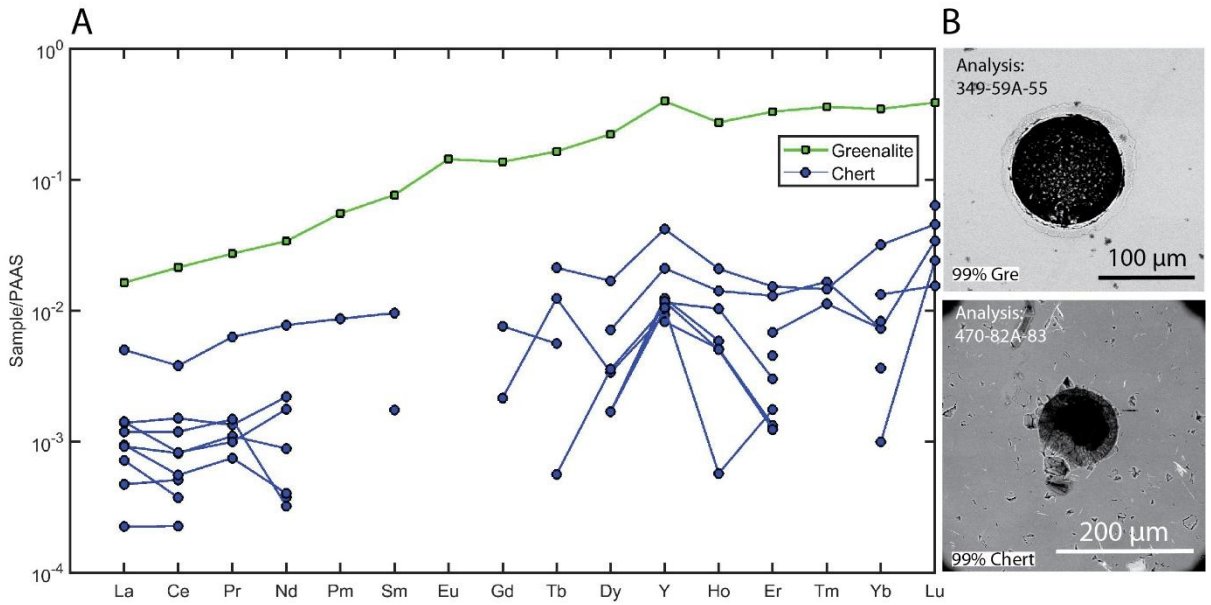

Figure 4. 2 | (A). REY data for the greenalite endmember (>99% Greenalite) and greenalite-free chert (<1% Fe). **(B)**. Laser ablation crater for greenalite endmember (top) and a representative crater for the chert endmember (bottom), showing the homogeneous mineralogy.

4.3. Discussion

4.3.1. A seawater origin for greenalite

In modern, well-oxygenated seawater, the typical REY distribution pattern includes a negative Ce anomaly, HREE enrichment, large positive Y anomalies, small positive La and Gd anomalies and no Eu/Eu* anomaly (Bau et al., 1995). Progressive enrichment in REE across the series is driven by increasing carbonate complexation at higher atomic number and is characteristic of seawater. While there is minor variation in seawater REE patterns driven by water mass mixing, and significant variation in Ce/Ce* in response to local redox conditions, the general shape and features are present globally and are distinct from other fluid sources. Furthermore, the non-redox sensitive aspects of seawater REE patterns are thought to have been conservative over Earth history (Shields & Webb, 2004). In contrast, hydrothermal fluids generally contain higher ∑REE and have a distinct REY pattern, with a flat or even LREE enriched shape and a large positive Eu anomaly (e.g., Eu/Eu* = 25) (Bau & Dulski, 1999). Hydrothermal systems occur in diverse settings, including mid-ocean ridges, deep faults on continental margins, and brine systems in sedimentary basins, and due to differences in temperature and host rock, the fluids exhibit variable pH and chemical composition (Tivey, 2007). Some diversity is therefore expected in the REE composition of hydrothermal fluids, both geographically and over geological time. One distinct feature that is commonly present in hydrothermal fluids is the large Eu anomaly, because the highly reducing, high temperature conditions in hydrothermal fluids can drive the reduction of Eu^{3+} to Eu^{2+} (Bau & Dulski, 1999).

The data from this study show that greenalite is a significant host for REY. Greenalite is assumed to preserve primary geochemical signals for several reasons. Firstly, stratigraphic relationships here and in a range of other Archean and Paleoproterozoic sediments suggest it was the earliest forming phase (Rasmussen et al., 2021). Secondly, greenalite is commonly encased in early diagenetic chert, which provides protection from alteration during burial (Rasmussen & Muhling, 2021). The location of the REY in the primary Fe(II)-silicate gel is not known, but if they are surface bound, they could be susceptible to re-equilibration during transport and settling over a period of weeks–months. This is less likely if the REY are structurally incorporated, as has been demonstrated for several other metals in Fe(II)-silicate (a precursor to greenalite; Tostevin & Ahmed, 2023). Uniform partition coefficients (K'_D) are are assumed for all REY, and while this is broadly true for other authigenic minerals, such as carbonates (Webb & Kamber, 2000), REY partitioning behaviour has not been explicitly tested for greenalite.

The most comparable data to ours come from Muhling et al. (2023), who analysed chert samples from a range of depositional settings that span 3.46 – 2.45 Ga. In the majority of samples, greenalite was present in low abundance (10 – 20%). Many of their samples also contained apatite (1%), fine-grained siderite, and in some cases, fine-grained hematite. These minerals can be important hosts for REE so inclusion of small amounts can skew average REY signals (Alibert, 2016; Muhling et al., 2023; Oonk et al., 2018). However, their results from the 2.483 Ga Colonial chert of the Mt McRae shale are greenalite-rich (Mitchell2-418 = 28% Fe; Fig. 4.3), and although the Ca content is high, the strong correlation between REE and Fe suggests greenalite is dominating the average REY signal. The REY pattern for this sample is comparable to our data (Fig. 4.3), with HREE enrichment (Yb/Nd = 9.94), ∑REE = 5.9 ppm, high Y/Ho ratios (48), small Eu anomalies (2.4), and no Ce anomalies (1.2). In contrast to our data, their results from the Colonial chert samples show a positive La anomaly (La/La* = 1.9) (Muhling et al., 2023). These largely comparable trends suggest a similar depositional environment across two different continental cratons. Interestingly, cherts from the Marble Bar Chert, which formed in a volcanic exhalative setting, show a distinct REY signal with LREE enrichment and larger Eu anomalies. This suggests that chemical sediments may capture distinct REY trends during formation in vent proximal settings, although variability exists across samples from different locations. By extension, chemical sediments formed in or around vent systems, which were subsequently transported to vent-distal shelf settings, would be expected to carry a similar signal, but this is not what we observe in greenalite from the Kuruman Formation.

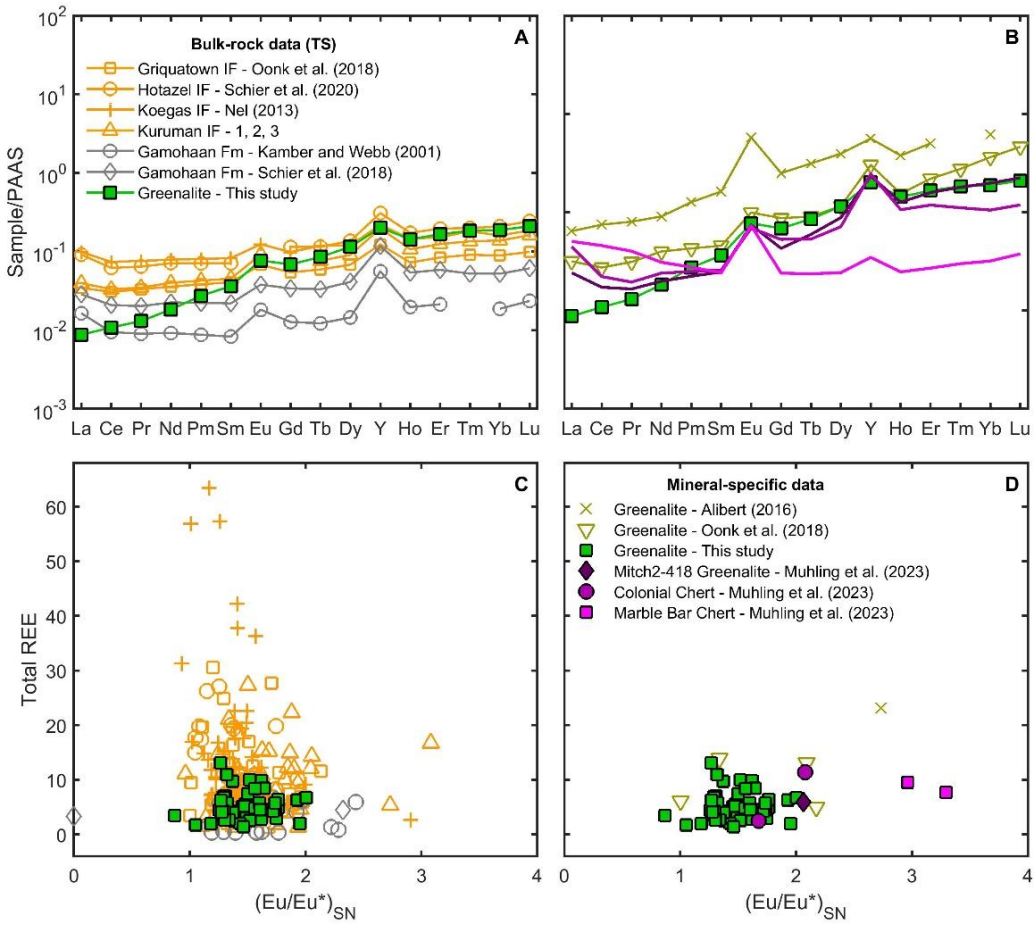

Figure 4. 3 | A and C: Comparison between greenalite (this study) and average bulk rock from IF (orange) and carbonate rocks (grey) in the Transvaal Supergroup (TS). References for Kuruman IF: 1 - Bau and Dulski (1996), 2 - Planavsky et al. (2010), 3 - Oonk et al. (2018). **B and D:** Comparison between greenalite (this study) and other mineral-specific data from the TS as well as chert and greenalite from Australian pre-GOE successions (Muhling et al., 2023). The average greenalite data is calculated from the analyses with >90 % greenalite in the ablation area. **A and B:** Comparison of REY patterns using average data for each study. **C & D:** Comparison of $(Eu/Eu^*)_{SN}$ and ∑REE for the same samples, demonstrating that greenalite overlaps with the other phases. All data points from each study are plotted.

The REY pattern of greenalite shows HREE enrichment and includes a positive Eu anomaly (mean = 1.41), but this is small compared with hydrothermal fluids. Furthermore, the overall patterns and Eu/Eu* overlap with data from bulk IF, which represent an integrated REY pattern from multiple minerals with diverse origins (Fig. 4.3). None of these minerals are proposed to have formed in hydrothermal vents, but rather on the seafloor or during early diagenesis. More significantly, the REY patterns from greenalite in this study are similar to microbial carbonate rocks from the Transvaal Supergroup, showing a similar range for many key features such as ∑REE, Ce/Ce*, Eu/Eu*, and Yb/Nd (Table 4.2). These minerals must have precipitated in shelf environments and are thought to preserve primary REY signals, so should capture the important features of marine REY at this time (Fig. 4.3B;

Kamber & Webb, 2001; Warke et al., 2020). While REY patterns from greenalite share many of the key features of bulk IF and carbonate rocks, HREE/LREE enrichment is more pronounced in greenalite (Table 4.2). This could be because REE partition coefficients during carbonate precipitation gradually decrease across the series, resulting in relatively higher incorporation of the LREE, and dampening the magnitude of HREE enrichment relative to seawater (Webb & Kamber, 2000).

Table 4. 2 | Average and standard deviation of key REY anomalies in LA-ICP-MS data from the three greenalite samples in this study compared with averages for microbial carbonates of the Gamohaan Formation (Kamber and Webb, 2001) and bulk powders from the Kuruman Formation (Bau and Dulski, 1996) ($_{SN}$: Post-Archean Australian Shale - normalized).

Sample	∑REE	$(Eu/Eu^*)_{SN}$	$(Ce/Ce^*)_{SN}$	$(La/La^*)_{SN}$	Y/Ho	$(Yb/Nd)_{SN}$
349-59A	5.6 ± 0.8	1.4 ± 0.1	1.1 ± 0.1	1.2 ± 0.3	38.0 ± 1.7	9.3 ± 1.8
349-59B	3.3 ± 0.4	1.4 ± 0.2	1.2 ± 0.2	1.2 ± 0.4	37.1 ± 2.3	16.0 ± 3.3
351-66	6.6 ± 0.4	1.7 ± 0.2	1.2 ± 0.1	1.6 ± 0.3	35.2 ± 1.7	8.3 ± 1.2
BIF	8.7 ± 5.3	1.9 ± 0.5	1.1 ± 0.1	1.5 ± 0.2	44.8 ± 4.9	4.6 ± 1.0
Microbial carbonates	4.1 ± 2.0	2.0 ± 0.4	1.1 ± 0.1	2.0 ± 0.3	77.0 ± 13.9	2.2 ± 0.5

The presence of positive Eu/Eu* anomalies in a wide range of minerals in Archean and Paleoproterozoic sedimentary rocks suggests that, in contrast to modern seawater, small positive Eu/Eu* anomalies were a ubiquitous feature of well-mixed seawater (e.g., Bau & Dulski, 1999; Kamber & Webb, 2001). This may be because hydrothermal fluxes are estimated to have been up to three times higher than the modern day, at 1014 Kg yr^{-1}, which may have resulted in higher hydrothermal contributions to the marine REY inventory. In addition, the anoxic nature of seawater may have transported Fe and REY from hydrothermal fluids over long distances as dilute plumes, imparting a hydrothermal overprint on shelf waters. We conclude that small positive Eu anomalies in greenalite, which have been interpreted to indicate a hydrothermal origin (Bau & Dulski, 1996; Tosca & Tutolo, 2023), are in fact consistent with a shelf origin. If greenalite precipitated directly as hot, hydrothermal fluids mixed with seawater in and around vent systems, we would expect to see a distinct REY signal with higher ∑REE, a flatter profile, larger $(Eu/Eu^*)_{SN}$ and LREE enrichment compared to other phases. We calculated the REY pattern anticipated under these conditions at a range of relevant mixing ratios (from 2:1 to 10:1 by mass; Tosca & Tutolo, 2023). Due to the considerably higher REY concentration in vent fluids, the solid retains the characteristic features of vent fluids (Fig. 4.4). Instead, our REY data support a seawater origin for greenalite and models that invoke precipitation on the shelf. To reproduce the Eu/Eu* observed in greenalite, a dilution factor of 100000:1 is required (Fig. 4.4). At this level of dilution, the fluids would be at ambient temperature and pH.

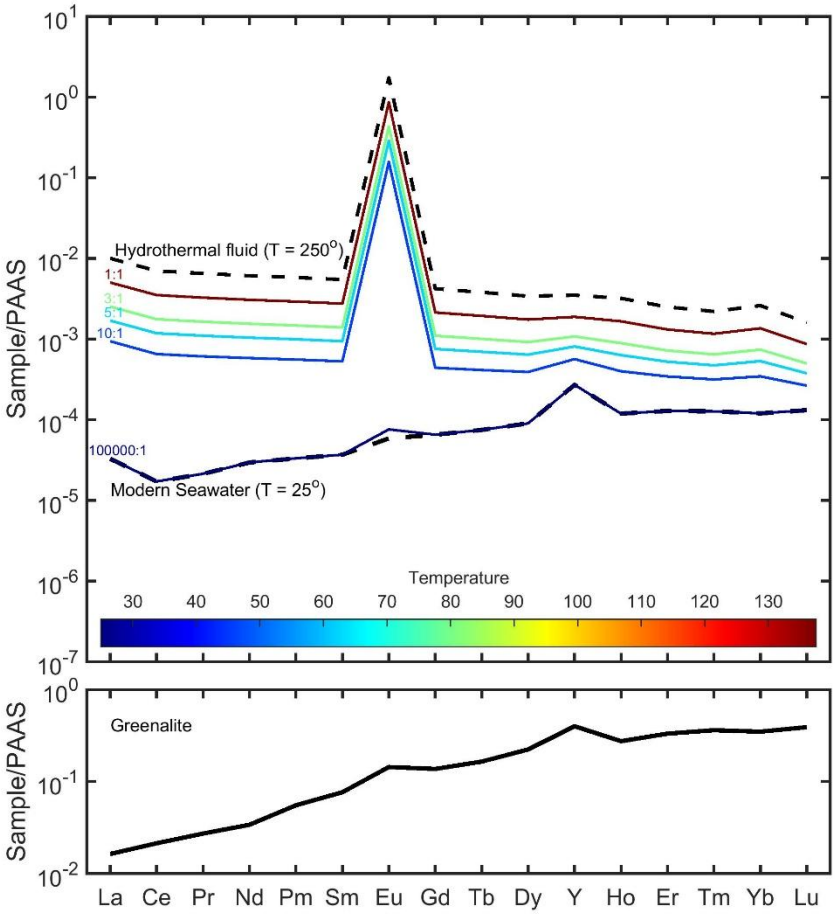

Figure 4. 4 | Mixing between modern seawater (Alibo & Nozaki, 1999), with negative Ce/Ce* removed, and hydrothermal fluids (Bau & Dulski, 1999) at ratios anticipated in and around hydrothermal vent systems (Tosca & Tutolo, 2023) still produces a flat REY pattern dominated by a large Eu anomaly. To produce a REY pattern similar to greenalite, with an Eu/Eu* of 1.5, a mixing ratio of 100000:1 is required.

4.3.2. Redox conditions, pH and temperature in Paleoproterozoic shelf environments

If greenalite was forming on the shelf, then how was its precipitation triggered? Our REY data do not contain any positive or negative Ce anomalies. This indicates that greenalite formation occurred under anoxic conditions, which is to be expected in an Fe(II)-bearing mineral. However, experimental work has shown that greenalite precipitation occurs more rapidly in the presence of small amounts of Fe^{3+} (Hinz et al., 2021). Furthermore, natural greenalite commonly contains some Fe(III) in its structure, which has been interpreted to represent Fe^{3+} in ancient seawater (10 – 20%; Johnson et al., 2018). If this Fe(III) is primary, it could indicate formation close to the chemocline, where Fe could be oxidised by photochemical reactions, iron oxidising bacteria, or free O_2 generated by cyanobacteria. Our Ce/Ce* values do not preclude this scenario, as intermediate redox conditions may have been sufficient to oxidise Fe, but insufficient to initiate the oxidation of Mn and Ce. However, experiments

that generated greenalite in the presence of Fe^{3+} produced a mineral assemblage containing magnetite and hematite, which differs from the greenalite-chert-minnesotaite-siderite assemblage in our samples (Hinz et al., 2021). Similarly, when Fe(II)-silicates are generated via in situ Fe oxidation, they co-precipitate with ferrihydrite, which was not observed in our mineral assemblage (Hinz et al., 2023).

Given the sixth order dependency of greenalite precipitation on H^+, pH exerts a major control on the precipitation rate of greenalite. The pH range required for greenalite nucleation is similar to the pH range of the modern ocean (Tosca et al., 2016). However, atmospheric CO_2 is thought to have been higher in the Precambrian to maintain a clement climate under a faint young Sun (Sheldon, 2006). All else being equal, this would have contributed to a lower oceanic pH. Geochemical estimates based on the presence or absence of sulfate evaporites would place seawater at pH 8 or less (Grotzinger & Kasting, 1993). Independent constraints derived from calcium isotope ratios in sedimentary carbonate rocks, assuming a marine Ca^{2+} concentration of 10 – 135 $mmol.kg^{-1}$, place an upper limit on marine pH of <7.8 when pCO_2 is constrained by a paleosol estimate, and <7.1 when pCO_2 is modelled based on the faint young Sun hypothesis (Blättler et al., 2017). Statistical models suggest pH generally increased over geological time and give a 95% chance that pH was <8 at 2.5 Ga (Halevy & Bachan, 2017). Using these constraints, conditions in most of the ocean would not have been conducive to rapid greenalite nucleation. Constraints from carbon cycle models suggest ocean pH was 7.0 at the Archean-Proterozoic boundary, which would have suppressed greenalite precipitation altogether (Krissansen-Totton et al., 2018). The calculated pH range for early seawater is highly dependent on the proportion of CO_2 versus methane in the early atmosphere, and so a methane-rich greenhouse could allow for a seawater pH that was higher than current models suggest. In addition, elevated pH levels in localized environments, driven by upwelling alkaline water masses or anaerobic respiration of organic carbon, may not be accurately represented in global ocean models (Bergmann et al., 2013; Higgins et al., 2009).

Alternatively, warmer average temperatures in early oceans may have facilitated Fe(II)-silicate precipitation at lower pH. Oxygen isotope records in marine iron oxides and mineral pairs indicate that $\boldsymbol{\delta}^{18}O_{H2O}$ has increased over time, while seawater temperatures in the Archean Eon and Paleoproterozoic Era reached well above 70˚C (Galili et al., 2019; Isson and Rauzi, 2024), similar to modern temperatures. Given the temperature dependence of the solubility product of Fe(II)-silicate, this could facilitate precipitation at lower pH (Tostevin & Ahmed, 2023). I use a numerical model to explore this, assuming an Fe^{2+} concentration of 0.1 to 1 $mmol.kg^{-1}$ (Jiang & Tosca, 2019) and a dissolved

Si concentration of 2 mmol.kg^{-1} . Under these conditions, pH as low as >6.2 to >6.7 could facilitate rapid precipitation of Fe(II)-silicate minerals at 70˚C (Fig. 4.5). This suggests that seawater would have been sufficiently alkaline to support widespread Fe(II)-silicate precipitation, particularly in low latitude surface waters.

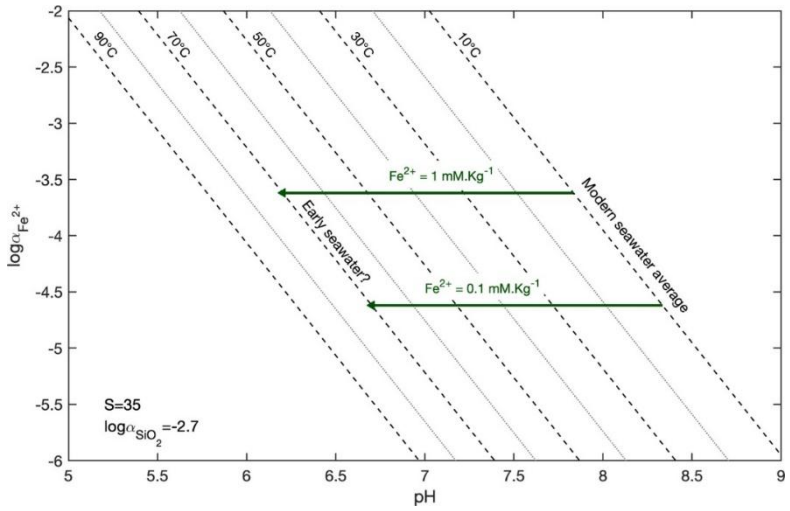

Figure 4. 5 | Modelled relationship between Fe^{2+} activity and pH at which Fe(II) silicate nucleation will occur for a given temperature (dashed lines), based on experimental constraints on the solubility product at a range of temperatures (Tostevin & Ahmed, 2023). The system has a salinity (S) of 35 g.kg^{-1} and dissolved silica concentrations are set by the saturation of amorphous SiO_2. An estimated Fe^{2+} concentration for Precambrian seawater of 0.1–1 mmol.kg^{-1} (Jiang & Tosca, 2019), suggests that at 70˚C, Fe(II)-silicate minerals could precipitate at pH of 6.2 to 6.7.

4.4. Conclusion

Well-preserved greenalite in Paleoproterozoic chert precipitated from seawater in shelf environments, potentially triggered by small changes in pH. The similarity between the data from this study and greenalite-chert data from the Colonial Chert Member of the Mt McRae shale in Western Australia suggests that a shelf origin for greenalite preserved in chert was widespread. However, this does not preclude the formation of greenalite in other settings. It is possible that large quantities of greenalite precipitated around hydrothermal vent systems but were rarely transported to the shelf and preserved in the geological record. This would be analogous to many minerals today, such as pyrite, which have diverse origins and precipitate both at hydrothermal vents and in shelf sediments. The preservation of primary REY patterns in chert-hosted greenalite, potentially safeguarded by early silicification, makes this archive a promising candidate to capture other primary geochemical signatures, such as metal contents and isotopes.

Chapter 5

Metal Concentrations in Paleoproterozoic Seawater

5.1. Introduction

Metals are essential micronutrients and are required by all forms of life to build metalloproteins (Mertz, 1998; Nordberg & Nordberg, 2016). Some metalloproteins are cambialistic, and can adapt to use metals that are environmentally abundant. Therefore, changes in marine metal availability would have influenced patterns of metal utilisation by evolving metabolisms. For example, manganese (Mn) was preferred by early evolving microbes, whereas later evolving microbes, such as eukaryotes, favored zinc (Zn) (Isson et al., 2018; Saito et al., 2003). Some proteins can only function with a specific metal, and in such cases, associated metabolisms may have been suppressed when those metals were scarce. The resulting dominance of different metabolic processes could in turn have impacted ocean-atmosphere chemistry and the climate (Buick, 1992; Konhauser et al., 2011).

Geochemical records, thermodynamic models, and proteomics suggest that metal availability in seawater has changed dramatically over geological time (Anbar & Knoll, 2002; Konhauser et al., 2009; Robbins et al., 2016; Saito et al., 2003; Scott et al., 2013; Swanner et al., 2014; Tostevin & Ahmed, 2023). These changes reflect major geological events, such as the cooling of the mantle and the emergence of stable subaerial continents, as well as biological and chemical changes in seawater. In the Archean Eon (4.0–2.5 billion years ago), the oceans were dominantly anoxic and rich in ferrous iron (Fe^{2+}), which could have resulted in complexation, sorption and co-precipitation of metals onto Fe(II)-bearing phases, Fe(III)-bearing phases, or iron sulfide minerals (Konhauser et al., 2018; Saito et al., 2003; Tostevin & Ahmed, 2023).

Attempts to corroborate these predictions using the rock record have focussed on changes in the average abundance of a particular metal in either shales, pyrite, or IF over long timespans (Konhauser et al., 2018; Large et al., 2014; Robbins et al., 2016; Scott et al., 2013; Swanner et al., 2014). While these records present a broad view of large shifts over time, they present several limitations. Firstly, some of these records only provide qualitative constraints, because the exact location of the metal and the partitioning behaviour during precipitation of that phase is unknown. Secondly, mobilisation of metals during diagenesis and metamorphism could skew records. Current data from the rock record present several inconsistencies with biological and thermodynamic constraints. For example, Zn records from shales and banded IF suggest that Zn levels remained stable over geological time, yet thermodynamic models and proteomics suggest Zn availability was low in early marine systems.

Recent work on Archean rocks has highlighted the role of Fe(II)-silicate minerals, such as greenalite, as abundant, primary precipitates in Archean sedimentary rocks (Rasmussen et al., 2021). Sorption of

dissolved silica to greenalite nanoparticles as they are transported through the water column, followed by early lithification in chert protected primary geochemical signals from diagenetic and late-stage alteration (Rasmussen & Muhling, 2021). Furthermore, experimental work demonstrated that several key metals enter Fe(II)-silicates, thought to be a precursor to crystalline greenalite, during precipitation and the partition coefficients are well constrained (Tostevin & Ahmed, 2023). Furthermore, most metals are largely retained in the structure during heating and crystallisation, suggesting that greenalite could represent a robust archive of the metal content of early oceans (Tostevin & Ahmed, 2023). Here, I present mineral-specific metal contents for natural greenalite from ~2.46 Ga chert beds from the Kuruman Formation, Transvaal Supergroup, South Africa (see chapter 3) and place these into a quantitative framework to calculate the concentration of five key metals in Archean seawater. See chapter 3 for sample description and characterization, and the detailed methodology used for data collection.

The interpretations presented in this chapter build upon foundational work by Rasmussen et al. (2013, 2014, 2019), which provided compelling evidence through high-resolution microscopy that greenalite is a primary precipitate in iron formations. This chapter is focused specifically on using the chemical properties of greenalite to determine its precipitation environment, operating on the assumptions that greenalite is indeed a primary phase, and there is an absence of REY fractionation between sweater and greenalite. However, if the greenalite analyzed here were instead a diagenetic phase, several key implications would arise. For example, the greenalite in this study may exhibit trace metal concentrations from a diagenetic environment that could influence the interpretations of early ocean chemistry and the environmental conditions inferred from these iron formations. These considerations are acknowledged and would warrant a re-evaluation of certain conclusions if further evidence were to indicate a diagenetic origin for greenalite in these samples.

5.2. Calculating the trace metal concentration in seawater

Trace metal concentrations derived from LA ICP-MS spot analyses (see chapter 3) underestimate the metal content in the mineral phase because of the dilution effect from the chert matrix. The metal concentrations are recalculated from each spot analysis using the estimated proportion of greenalite within each spot to project the metal content to 100% greenalite (Table 5.1), and then converted to molkg^{-1} by dividing by the atomic mass of each element. Subsequently, the proportion of each metal (X_{metal}) was calculated by dividing its individual concentration (M_{conc} in molkg^{-1}) by the total metal concentration in the mineral (M^{T}_{conc}) (i.e., $X_{metal} = M_{conc} / M^{T}_{conc}$). This was followed by determining the metal to iron ratio within the solid phase (R_{solid}) (i.e., $R_{solid} = X_{metal} / X_{Fe}$). Next, the partition

coefficient for each metal (K'_{Dmetal}) (Tostevin & Ahmed, 2023) was used to calculate the metal to iron ratio in the fluid from which greenalite precipitated (R_{fluid}) (i.e., $R_{fluid} = R_{solid} / K'_{Dmetal}$). The last step involved multiplying R_{fluid} by the estimated Fe content in the Archean ocean, providing us with the estimated value of each metal in the ocean (Table 5.2). To obtain a comprehensive range of metal content in the Paleoproterozoic Era, a reasonable range of Fe^{2+} concentration estimates (0.1 and 1 $mmol.kg^{-1}$; Jiang & Tosca, 2019) was considered. Comparison with modern seawater concentrations was used to explore how seawater chemistry has evolved through time.

Table 5. 1 | Raw LA ICP-MS trace metal concentration from natural greenalite from the Kuruman Formation, Transvaal Supergroup, along with the calculated % greenalite (% Gre), and the recalculated metal concentrations from each laser spot analysis.

Analysis no.	% Gre	Metal concentration (ppm)						Metal concentration (in 100% greenalite) (ppm)					
		V	Zn	Co	Ni	Mn	Fe	V	Zn	Co	Ni	Mn	Fe
349-59A-55/23	99	25.5	43.4	2.68	12.0	959	546000	25.8	43.8	2.71	12.1	969	551515
349-59A-56/23	99	20.6	39.2	2.44	12.6	730	487000	20.8	39.6	2.46	12.7	737	491919
349-59A-58/23	61	8.3	23.8	1.52	7.0	503	318900	13.6	39.0	2.49	11.4	825	522787
349-59A-59/23	58	6.6	21.3	1.24	5.9	552	302400	11.4	36.7	2.13	10.2	952	521379
349-59A-62/23	97	33.8	51.3	3.30	16.9	943	645000	34.8	52.9	3.40	17.4	972	664948
349-59A-63/23	98	27.2	44.9	2.93	13.9	901	576000	27.8	45.8	2.99	14.2	919	587755
349-59A-64/23	62	12.4	30.0	1.86	8.6	606	390000	20.0	48.4	3.00	13.9	977	629032
349-59A-65/23	61	9.7	26.7	1.64	7.3	799	372000	15.9	43.8	2.69	12.0	1310	609836
349-59A-66/23	61	7.5	23.4	1.31	6.7	631	328400	12.2	38.4	2.15	10.9	1034	538361
349-59A-69/23	97	19.7	37.1	2.18	10.7	757	464000	20.3	38.2	2.25	11.0	780	478351
349-59A-70/23	65	14.4	31.4	1.98	9.2	621	407000	22.1	48.3	3.04	14.2	955	626154
349-59A-71/23	57	8.4	23.5	1.40	7.1	645	329900	14.8	41.2	2.45	12.5	1132	578772
349-59A-72/23	58	8.4	23.9	1.46	6.7	671	326300	14.4	41.2	2.51	11.5	1157	562586
349-59A-73/23	61	9.9	25.6	1.57	7.0	546	332400	16.2	42.0	2.57	11.5	895	544918
349-59A-76/23	64	10.2	26.5	1.63	7.3	587	349000	15.9	41.4	2.55	11.5	917	545313
349-59A-77/23	60	8.9	25.0	1.54	6.2	624	342000	14.8	41.6	2.56	10.4	1040	570000
349-59A-78/23	57	8.1	23.0	1.40	6.3	555	318200	14.2	40.3	2.46	11.0	974	558246
349-59A-79/23	57	8.3	24.6	1.51	6.7	1220	379000	14.5	43.2	2.64	11.7	2140	664912
349-59A-80/23	58	6.7	23.3	1.27	5.9	1230	366000	11.6	40.2	2.18	10.2	2121	631034
349-59B-26/23	61	23.5	27.1	0.84	5.1	534	345700	38.6	44.4	1.37	8.4	875	566721
349-59B-28/23	67	20.6	25.3	0.74	5.3	519	314000	30.7	37.8	1.10	7.9	775	468657
349-59B-29/23	27	8.5	10.6	0.27	2.9	226	147200	31.6	39.2	1.01	10.6	837	545185
349-59B-30/23	37	14.3	17.0	0.40	4.1	327	211600	38.6	45.9	1.08	11.2	884	571892
349-59B-33/23	48	11.5	13.9	0.38	3.3	278	175600	23.9	28.9	0.79	6.9	579	365833
349-59B-34/23	42	12.7	15.6	0.47	3.4	308	195300	30.3	37.1	1.13	8.2	733	465000
349-59B-35/23	62	13.9	16.3	0.48	3.8	331	209400	22.4	26.2	0.78	6.1	534	337742
349-59B-36/23	33	13.2	15.4	0.43	3.7	309	194200	40.0	46.7	1.30	11.1	936	588485
349-59B-37/23	17	11.6	13.9	0.35	4.4	270	169800	68.2	81.6	2.07	25.9	1588	998824
349-59B-38/23	34	7.7	10.5	0.33	2.9	200	128900	22.5	30.8	0.97	8.5	588	379118
349-59B-40/23	72	28.1	29.9	1.00	5.9	640	387000	39.0	41.5	1.39	8.2	889	537500

Table 5. 1 (continued)

Analysis	% Gre	Metal concentration (ppm)						Metal concentration (in 100% greenalite) (ppm)					
		V	Zn	Co	Ni	Mn	Fe	V	Zn	Co	Ni	Mn	Fe
349-59B-41/23	69	30.4	33.0	1.09	6.3	701	419000	44.1	47.8	1.59	9.1	1016	607246
349-59B-42/23	70	23.6	26.0	0.84	5.6	540	330000	33.6	37.1	1.21	8.0	771	471429
349-59B-43/23	70	26.6	30.0	0.90	5.9	611	373000	38.0	42.9	1.29	8.4	873	532857
349-59B-44/23	63	28.4	31.0	1.15	6.1	642	393100	45.1	49.2	1.83	9.7	1019	623968
349-59B-47/23	37	8.8	10.6	0.26	2.6	217	138600	23.8	28.8	0.70	7.1	587	374595
349-59B-48/23	41	22.1	24.5	0.76	5.2	490	306300	53.8	59.8	1.84	12.7	1195	747073
349-59B-49/23	48	15.7	17.1	0.61	4.0	389	227000	32.7	35.6	1.28	8.3	810	472917
349-59B-50/23	43	14.5	16.1	0.50	3.4	329	208000	33.7	37.4	1.16	7.8	765	483721
349-59B-51/23	68	25.0	26.9	0.92	5.8	564	354000	36.8	39.6	1.35	8.5	829	520588
351-66-5/23	60	21.2	14.2	0.81	15.0	1410	272300	35.3	23.7	1.35	25.0	2350	453833
351-66-6/23	74	33.9	19.8	1.14	20.9	1716	389200	45.8	26.8	1.55	28.2	2319	525946
351-66-7/23	22	22.4	14.8	0.81	16.0	1068	269000	101.8	67.1	3.69	72.7	4855	1222727
351-66-8/23	63	20.0	14.0	0.88	14.3	2010	299000	31.7	22.3	1.39	22.8	3190	474603
351-66-9/23	73	39.1	24.9	1.54	26.7	2050	456000	53.6	34.1	2.11	36.6	2808	624658
351-66-12/23	70	36.4	22.5	1.36	24.7	1472	391600	52.0	32.2	1.94	35.3	2103	559429
351-66-13/23	49	26.0	17.4	1.04	17.7	1690	330100	53.1	35.4	2.13	36.0	3449	673673
351-66-14/23	51	23.5	15.0	0.95	16.1	814	259300	46.2	29.4	1.86	31.5	1596	508431
351-66-15/23	61	29.0	18.5	1.11	19.8	1500	339800	47.5	30.2	1.82	32.4	2459	557049
351-66-16/23	52	26.9	17.2	1.03	18.8	1273	314200	51.8	33.0	1.98	36.2	2448	604231
351-66-19/23	54	22.1	15.0	0.90	16.4	2070	327300	40.9	27.7	1.67	30.4	3833	606111
351-66-20/23	62	24.8	15.9	1.00	18.2	1169	298000	40.0	25.6	1.61	29.4	1885	480645
351-66-21/23	61	34.4	20.5	1.25	24.0	1836	413800	56.4	33.6	2.05	39.3	3010	678361
351-66-22/23	50	28.1	18.0	1.09	20.7	1236	341000	56.2	36.0	2.18	41.4	2472	682000
351-66-23/23	58	34.1	21.1	1.26	24.1	1324	396500	58.8	36.3	2.16	41.6	2283	683621

Table 5. 2 | Trace metal concentrations in Paleoproterozoic seawater calculated from metal concentrations in natural greenalite. Concentrations were calculated using experimentally determined partition coefficients (Tostevin & Ahmed, 2023) and an Fe concentration of 0.1 mmol.kg^{-1}. Values are based on individual spot analyses, reported in molkg^{-1}, excluding samples with siderite contamination.

Analysis	V	Zn	Co	Ni	Mn
349-59A-55/23	3.8 X 10^{-13}	1.2 X 10^{-12}	6.4 X 10^{-10}	5.6 X 10^{-09}	4.0 X 10^{-03}
349-59A-56/23	3.1 X 10^{-13}	1.2 X 10^{-12}	6.6 X 10^{-10}	6.6 X 10^{-09}	3.4 X 10^{-03}
349-59A-58/23	2.0 X 10^{-13}	1.1 X 10^{-12}	6.2 X 10^{-10}	5.6 X 10^{-09}	3.6 X 10^{-03}
349-59A-59/23	1.7 X 10^{-13}	1.1 X 10^{-12}	5.3 X 10^{-10}	5.0 X 10^{-09}	4.1 X 10^{-03}
349-59A-62/23	5.2 X 10^{-13}	1.2 X 10^{-12}	6.7 X 10^{-10}	6.7 X 10^{-09}	3.3 X 10^{-03}
349-59A-63/23	4.1 X 10^{-13}	1.2 X 10^{-12}	6.7 X 10^{-10}	6.2 X 10^{-09}	3.6 X 10^{-03}
349-59A-64/23	3.0 X 10^{-13}	1.2 X 10^{-12}	6.2 X 10^{-10}	5.7 X 10^{-09}	3.5 X 10^{-03}
349-59A-65/23	2.4 X 10^{-13}	1.1 X 10^{-12}	5.8 X 10^{-10}	5.0 X 10^{-09}	4.9 X 10^{-03}
349-59A-66/23	1.8 X 10^{-13}	1.1 X 10^{-12}	5.2 X 10^{-10}	5.2 X 10^{-09}	4.4 X 10^{-03}
349-59A-69/23	3.0 X 10-^{13}	1.2 X 10^{-12}	6.1 X 10^{-10}	5.9 X 10^{-09}	3.7 X 10^{-03}
349-59A-70/23	3.3 X 10^{-13}	1.2 X 10^{-12}	6.4 X 10^{-10}	5.8 X 10^{-09}	3.5 X 10^{-03}
349-59A-71/23	2.2 X 10^{-13}	1.1 X 10^{-12}	5.6 X 10^{-10}	5.5 X 10^{-09}	4.4 X 10^{-03}
349-59A-72/23	2.1 X 10^{-13}	1.1 X 10^{-12}	5.8 X 10^{-10}	5.2 X 10^{-09}	4.7 X 10^{-03}
349-59A-73/23	2.4 X 10^{-13}	1.2 X 10^{-12}	6.2 X 10^{-10}	5.4 X 10^{-09}	3.7 X 10^{-03}
349-59A-76/23	2.4 X 10^{-13}	1.2 X 10^{-12}	6.1 X 10^{-10}	5.4 X 10^{-09}	3.8 X 10^{-03}
349-59A-77/23	2.2 X 10^{-13}	1.1 X 10^{-12}	5.9 X 10^{-10}	4.7 X 10^{-09}	4.1 X 10^{-03}
349-59A-78/23	2.1 X 10^{-13}	1.1 X 10^{-12}	5.8 X 10^{-10}	5.1 X 10^{-09}	4.0 X 10^{-03}
349-59A-79/23	2.2 X 10^{-13}	9.9 X 10^{-13}	5.2 X 10^{-10}	4.5 X 10^{-09}	7.3 X 10^{-03}
349-59A-80/23	1.7 X 10^{-13}	9.7 X 10^{-13}	4.5 X 10^{-10}	4.2 X 10^{-09}	7.6 X 10^{-03}
349-59B-26/23	5.8 X 10^{-13}	1.2 X 10^{-12}	3.2 X 10^{-10}	3.8 X 10^{-09}	3.5 X 10^{-03}
349-59B-28/23	4.6 X 10^{-13}	1.2 X 10^{-12}	3.1 X 10^{-10}	4.3 X 10^{-09}	3.8 X 10^{-03}
349-59B-29/23	4.7 X 10^{-13}	1.1 X 10^{-12}	2.4 X 10^{-10}	5.0 X 10^{-09}	3.5 X 10^{-03}
349-59B-30/23	5.8 X 10^{-13}	1.2 X 10^{-12}	2.5 X 10^{-10}	5.0 X 10^{-09}	3.5 X 10^{-03}
349-59B-33/23	3.6 X 10^{-13}	1.2 X 10^{-12}	2.8 X 10^{-10}	4.8 X 10^{-09}	3.6 X 10^{-03}
349-59B-34/23	4.5 X 10^{-13}	1.2 X 10^{-12}	3.2 X 10^{-10}	4.5 X 10^{-09}	3.6 X 10^{-03}
349-59B-35/23	3.3 X 10^{-13}	1.2 X 10^{-12}	3.0 X 10-^{10}	4.6 X 10^{-09}	3.6 X 10^{-03}
349-59B-36/23	6.0 X 10^{-13}	1.2 X 10^{-12}	2.9 X 10^{-10}	4.8 X 10^{-09}	3.6 X 10^{-03}
349-59B-37/23	1.0 X 10^{-12}	1.2 X 10^{-12}	2.7 X 10^{-10}	6.7 X 10^{-09}	3.6 X 10^{-03}
349-59B-38/23	3.4 X 10^{-13}	1.2 X 10^{-12}	3.3 X 10^{-10}	5.8 X 10^{-09}	3.5 X 10^{-03}
349-59B-40/23	5.8 X 10^{-13}	1.2 X 10^{-12}	3.4 X 10^{-10}	3.9 X 10^{-09}	3.8 X 10^{-03}
349-59B-41/23	6.6 X 10^{-13}	1.2 X 10^{-12}	3.4 X 10^{-10}	3.9 X 10^{-09}	3.8 X 10^{-03}
349-59B-42/23	5.0 X 10^{-13}	1.2 X 10^{-12}	3.3 X 10^{-10}	4.4 X 10^{-09}	3.7 X 10^{-03}
349-59B-43/23	5.7 X 10^{-13}	1.2 X 10^{-12}	3.2 X 10^{-10}	4.1 X 10^{-09}	3.7 X 10^{-03}
349-59B-44/23	6.7 X 10^{-13}	1.2 X 10^{-12}	3.8 X 10^{-10}	4.0 X 10^{-09}	3.7 X 10^{-03}
349-59B-47/23	3.6 X 10^{-13}	1.2 X 10^{-12}	2.5 X 10^{-10}	4.9 X 10^{-09}	3.6 X 10^{-03}
349-59B-48/23	8.0 X 10^{-13}	1.2 X 10^{-12}	3.2 X 10^{-10}	4.3 X 10^{-09}	3.6 X 10^{-03}
349-59B-49/23	4.9 X 10^{-13}	1.1 X 10^{-12}	3.5 X 10^{-10}	4.5 X 10^{-09}	3.9 X 10^{-03}
349-59B-50/23	5.0 X 10^{-13}	1.2 X 10^{-12}	3.1 X 10^{-10}	4.2 X 10^{-09}	3.6 X 10^{-03}
349-59B-51/23	5.5 X 10^{-13}	1.2 X 10^{-12}	3.4 X 10^{-10}	4.2 X 10^{-09}	3.6 X 10^{-03}

5.3. Metal abundance in Paleoproterozoic greenalite

Data for five metals from 54 independent laser ablation spot analyses across three samples are presented, encompassing variable proportions of greenalite laths and chert (Fig. 5.1; Table 5.3). The data suggest that Zn and V were substantially lower in Paleoproterozoic seawater compared to today (by 3 and 4 orders of magnitude, respectively). While Ni levels were similar to today, Co and Mn were more abundant (by 3 and 6 orders of magnitude, respectively) (Table 5.3; Figs. 2B & C).

Table 5. 3 | Summary of trace metal content in ~2.46 Ga greenalite (Transvaal Supergroup), calculated metal concentrations for Paleoproterozoic seawater, and data from modern seawater. Paleoproterozoic seawater concentrations are based on experimentally determined partition coefficients for each metal (Tostevin & Ahmed, 2023) and an Fe concentration of 0.1 mmol.kg^{-1}.

Metal	Content in natural greenalite (molkg^{-1})	Calc. concentration in Archean seawater (molkg^{-1})	Concentration in modern seawater (molkg^{-1})	Modern seawater reference
V	0.224–1.338	0.17–1.02 x 10^{-12}	1.3–2.2 x 10^{-8}	Whitmore et al. (2019)
Zn	0.400–1.250	0.97–1.24 x 10^{-12}	0.1–2.5 x 10^{-9}	Ikhsani et al. (2023)
Co	0.012–0.058	0.24–0.67 x 10^{-9}	0.097–1.0 x 10^{-12}	Bown et al. (2011)
Ni	0.104–0.441	3.79–6.73 x 10^{-9}	1.9–3.9 x 10^{-9}	Middag et al. (2020)
Mn	9.710–38.96	3.32–7.64 x 10^{-3}	0.1–3.8 x 10^{-9}	Ikhsani et al. (2023)

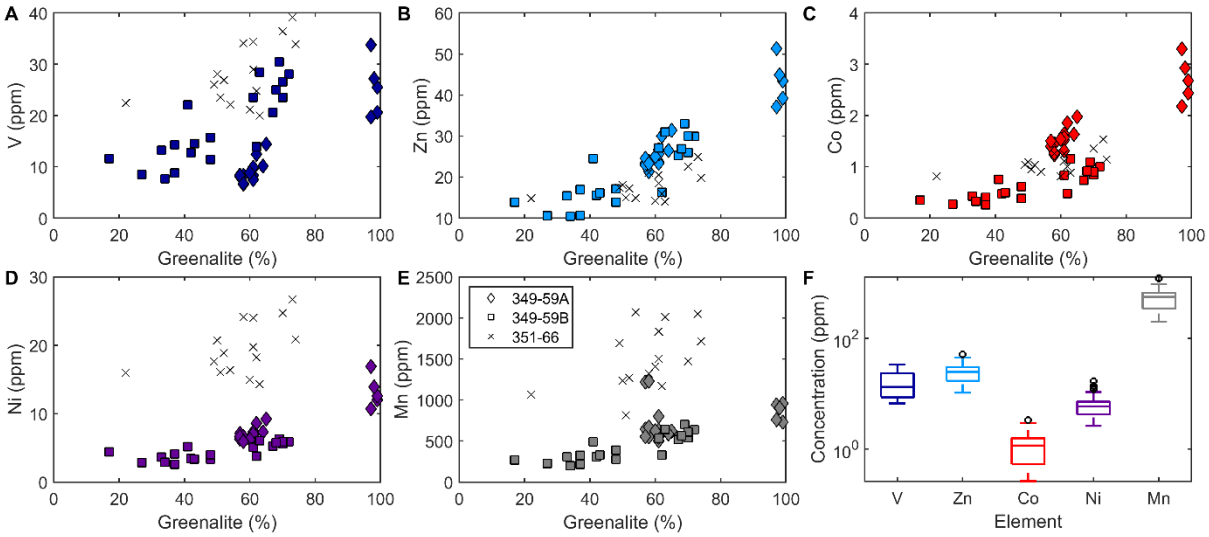

Figure 5. 1 | (A–E). Cross plots of unadjusted metal abundance in Paleoproterozoic greenalite from this study; **(F)**. Boxplot showing the relationship between the various metal concentrations in natural greenalite.

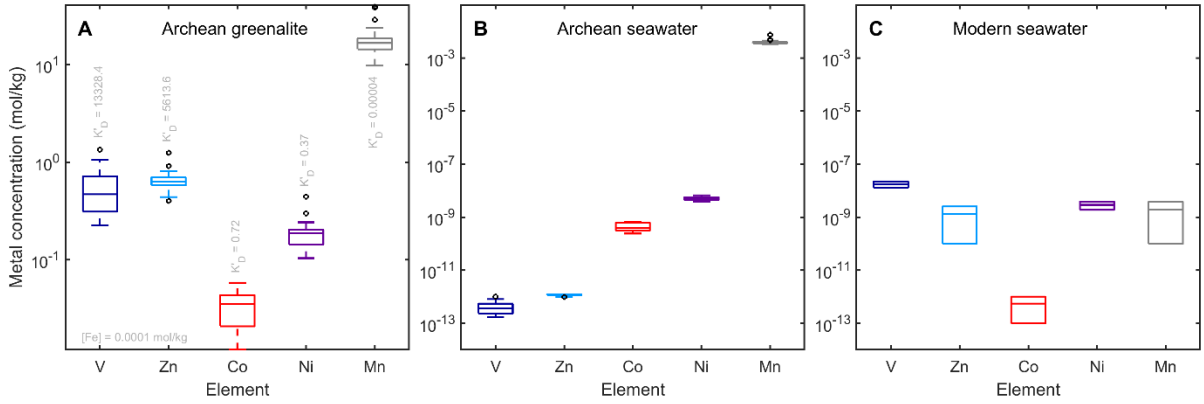

Figure 5. 2 | (A). Metal concentrations in Paleoproterozoic greenalite along with partition coefficients (K'_D) of each metal from Tostevin and Ahmed (2023); **(B)**. Calculated metal concentration in Paleoproterozoic seawater; **(C)**. A representation of metal concentrations in modern seawater, from the literature, for comparison with those of Paleoproterozoic seawater. Modern seawater sources as follows: Co from Bown et al. (2011); Mn and Zn from Ikhsani et al. (2023); Ni from Middag et al. (2020); V from Whitmore et al. (2019).

5.4. An archive of shallow marine conditions

Since the data in this study are tied to individual minerals, they reflect metal abundance in the local environment, which raises the question, where did these minerals precipitate (see section 4.3)? Rare earth element patterns were analysed alongside metals, and the patterns are similar to those of carbonate rocks from the same successions, and overall, are consistent with formation from seawater (see chapter 4). While greenalite may have been an abundant precipitate at hydrothermal vents, the greenalite preserved in chert beds in the Transvaal Supergroup, South Africa appear to have formed on the shallow shelf. The data therefore represent an archive of ambient seawater in a setting where most ecosystems are located. While metal abundances will have varied both spatially and temporally, perhaps by 1–2 orders of magnitude, the metals data in this study provide a quantitative snapshot into Paleoproterozoic seawater chemistry in a typical shelf environment. When compared to modern seawater, the data reveal significant changes in some elements, up to six orders of magnitude outside of the modern range.

5.5. An emerging picture from geology and biology

5.5.1. Nickel, cobalt, and vanadium in the Early Proterozoic Eon

Ni plays an important role in methanogenesis, the byproducts of which play an important role in climate regulation, as well as hydrolyzing ammonia to yield urea, a critical step in the nitrogen cycle (Ragsdale, 2009). Long term records of Ni/Fe ratios in hematite and magnetite suggest dissolved Ni concentrations were high in the Archean Eon, reaching hundreds of $nmolkg^{-1}$, but dropped dramatically around the Archean–Paleoproterozoic boundary (Konhauser et al., 2009). In contrast,

thermodynamic models suggest Archean Ni concentration were up to ten times lower than the present day (Saito et al., 2003), and phylogenomic data indicate that Ni utilisation was low before 1.8 Ga (David & Alm, 2011). The data from this study suggest that Ni concentrations were only moderately higher than modern seawater in the Late Archean Eon (4–7 $nmolkg^{-1}$), and this overlaps with the lower end of the range of estimates from bulk IF from the Transvaal Supergroup, which constrain Ni concentrations to 2.3–146 $nmolkg^{-1}$ (at $SiO_2(aq)$ = 0.67 $mmol.kg^{-1}$; Konhauser et al., 2009) (Fig. 3). While anoxic sinks, including greenalite precipitation, could have attenuated Ni concentrations, the weathering of Ni-rich ultramafic rocks may have compensated for this.

My data indicate that Co concentrations were considerably higher in the Early Proterozoic Eon compared to the present day (0.2–0.7 $nmolkg^{-1}$), and this is consistent with available geological and biological data. Co/Ti and Co/Al ratios in Late Archean pyrite, IF, and shales are all elevated compared to modern sediments (Swanner et al., 2014). Genome utilisation of Co was also elevated between ~3.0–1.3 Ga (David & Alm, 2011), and Co plays an important role in many of the anaerobic metabolisms that emerged in the Archean Eon, including fermentation, dehalogenation, and electron transfers (Banerjee & Ragsdale, 2003). While greenalite precipitation may have removed modest amounts of Co, the capacity for Co burial in Paleoproterozoic oceans was likely insufficient to compensate for the increased flux from alteration of Co-rich ultramafic rocks, leading to Co-rich oceans.

The calculated concentrations suggest that V was scarce in Early Proterozoic seawater, with a concentration four orders of magnitude lower than today (0.2–1 $pmolkg^{-1}$). This is consistent with thermodynamic modelling, which predicts V concentrations of 1 $pmolkg^{-1}$ under anoxic, sulfidic conditions (Williams & Da Silva, 2003) (Fig. 3). Analysis of V-bearing minerals also shows an increase in oxidised V-minerals over time (Moore et al., 2020). Nitrogen isotope data suggest that Mo-nitrogenase was preferred for N-fixation over V-based nitrogenase in the mid-Archean Eon (Stüeken et al., 2015), consistent with low environmental V. Vanadium levels may have been supressed by low levels of oxidative weathering, combined with pervasive sinks under anoxic, ferruginous conditions, including scavenging by clay minerals and co-precipitation with Fe(II)-silicate minerals.

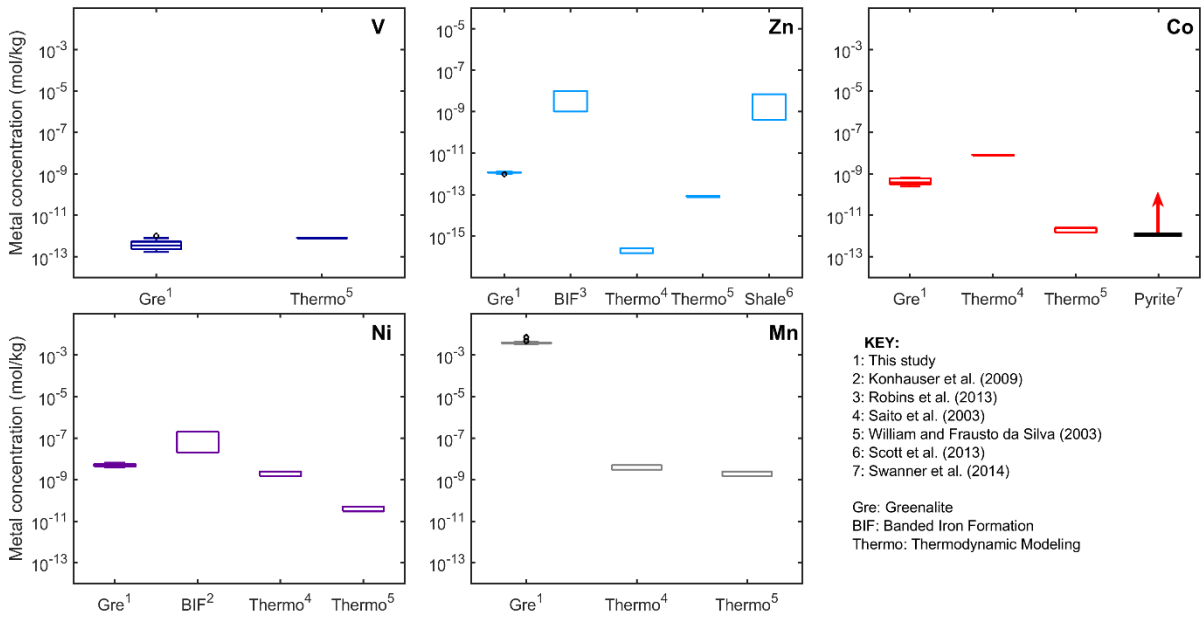

Figure 5. 3 | Comparison of my estimate for the metal concentration in Paleoproterozoic seawater with quantitative estimates from other geological archives or models.

5.5.2. Zinc availability in the late archean

Data from this study indicate that Zn concentrations in the Paleoproterozoic Era were three orders of magnitude lower than in modern seawater (1–1.2 pmolkg^{-1}; Fig. 5.2B, C). This is consistent with thermodynamic modelling, which predicts low Zn concentrations under anoxic conditions, as well as mineral precipitation experiments that show greenalite precipitation would have stripped Zn from hydrothermal fluids, drastically limiting the input flux. The Zn content of pyrite minerals also supports a depleted Zn reservoir in the Archean Eon (Large et al., 2014). Phylogenomic data show that most Zn-binding proteins evolved relatively late in Earth history, which could be consistent with Zn limitation in early seawater (Dupont et al., 2010). However, a significant discrepancy arises between the data from this study and the Zn record from shales and hematite (Robbins et al., 2013; Scott et al., 2013), which both show a large range of Zn content, but with no trend in the range or average over geological time. These records have been used to infer than marine Zn reservoir has remained stable at concentrations close to 10 nmolkg^{-1} since the Archean Eon. Bulk rock records utilise large datasets spanning billions of years, and integrate large spatial and temporal variability. While shale records have the advantage that they can be calibrated against modern sediments, potential variation in the partition coefficient with other parameters (e.g., pH, SiO_2) is poorly constrained, and incorporation of other phases may skew records towards higher values (Slotznick et al., 2022). Hematite records are tied to experimental constraints on partitioning behaviour, but recent work has shown that at least some of the natural hematite in the rock record is a product of late-stage oxidation (Rasmussen et al., 2014). While different archives present a conflicting picture, low Zn concentrations, as indicated by

the data from this study, could have presented a barrier to the development of Zn-metalloproteins, which are critical to eukaryotic cellular function, although Co-substitution may have relieved this stress (Price & Morel, 1990; Sunda & Huntsman, 1995).

5.5.3. Manganese was abundant in Archean seawater

Data from this study indicate that Mn was abundant in Paleoproterozoic seawater, more so than any other metal (Fig. 5.2B). In the modern ocean, Mn is a trace element with a concentration of ~4 nmolkg^{-1} (Ikhsani et al., 2023), yet my data imply concentrations reached 7 mmol.kg^{-1} in the Early Proterozoic Eon, making Mn the most abundant cation in seawater. Quantitative estimates of Mn concentrations in the past oceans are limited, with the only available constraints based on thermodynamic modelling (Saito et al., 2003; Williams & Da Silva, 2003). High marine Mn concentrations are consistent with widespread deposition of Mn minerals around the Late Archean Eon, suggesting fundamental differences in Mn cycle sources and sinks (e.g., Tsikos et al., 2003).

Archean hydrothermal fluxes were ten times higher than today due to a higher mantle heat flux (Kump et al., 2001). Under anoxic conditions, the concentration of reducing elements in hydrothermal fluids is predicted to have been substantially higher. For example, Fe concentrations are estimated to have been up to 10–100 mmol.kg^{-1} (Kump & Seyfried Jr, 2005). The ratio of Fe/Mn in modern hydrothermal fluids is ~10 (Lough et al., 2019), with Mn being the second most abundant metal. Assuming a similar relationship in the Proterozoic Eon, the hydrothermal flux of Mn could have been 1–10 mmol.kg^{-1}. Output fluxes of Mn may have been less pervasive in Archean-Paleoproterozoic seawater, as the formation of Mn(IV) oxide minerals under anoxic conditions would have been limited to light driven reactions. The ceiling for dissolved Mn may have been set by the solubility of Mn(II)-carbonate or Mn(II)-silicate minerals, or removal as a trace constituent of carbonates. My data suggest that the critical supersaturation required to nucleate these phases must have been high, placing a high ceiling on dissolved Mn^{2+}. This new estimate for marine Mn should be factored into experimental seawater solutions and thermodynamic calculations relating to early seawater. Such high concentrations could have presented a challenge for early microbial life, and may explain the high fraction of genes that bound Mn 2.5 Ga (1.28x higher than today; David & Alm, 2011) and the preferential selection of Mn by early evolving life (Dupont et al., 2010).

5.6. Conclusion

The data from this study provide high resolution, reliable and quantitative constraints on marine metal concentrations from a shelf environment ~2.46 Ga. Patterns of metal availability are radically different

to today: Zn and V were scarce, Ni was similar, Co was enriched, and Mn was one of the most abundant cations. The data are largely consistent with predictions based on thermodynamic models, and in places, overlap with predictions from other geological archives. These radically different patterns of metal availability would have had a profound impact on the evolution of early microbial life and are consistent with some phylogenomic and proteomic data which indicate that Mn and Co were selected over Zn by early microbes. The approach used here demonstrates the utility of greenalite as a paleo-archive and raises the possibility of exploring the Archean and Proterozoic Eons record to reconstruct metal concentrations in different settings and over geological time.

Chapter 6

Conclusions and Outlook

6.1. Introduction

The study of ancient marine biogeochemistry through the lens of seawater precipitates, such as iron formations and carbonate rocks, offers insights into early Earth's environmental and biological evolution. This research embarked on a journey to decode the chemistry of Archean-Paleoproterozoic oceans, focusing on the Transvaal Supergroup in South Africa. By employing novel methodologies and cutting-edge analytical techniques, this work has advanced our understanding of the mineralogical and geochemical characteristics of these ancient deposits and provided new perspectives on the conditions that prevailed during a critical period of Earth's history.

6.2. Integrative synthesis of findings

The findings from this study now provide answers to the following key questions that shaped this research.

What were the predominant chemical and redox conditions in the Archean and Paleoproterozoic oceans during the formation of microbial carbonates, and what does this tell us about the onset of oxygenic photosynthesis?

Microbial carbonates from the Transvaal Supergroup exhibit seawater-like REY patterns, characterized by HREE enrichment over LREE, Y/Ho > 36, positive Eu and La anomalies, and low total REE content, implying this archive preserves primary seawater REE patterns. However, the patterns lack any Ce anomalies, indicating that conditions were anoxic. These features are similar to other carbonate and iron formation data from the Transvaal Supergroup, implying that the Archean-Paleoproterozoic marine environments were largely anoxic. However, an absence of evidence is not necessarily evidence for absence. While the Ce anomaly should capture the presence of oxygen on water column scales (tens of meters), if oxygen levels exceeded 10 $\mu molkg^{-1}$, it may not capture more muted occurrences of oxygenation. Therefore, localized oxygen oases cannot be entirely ruled out. Indeed, there is Fe speciation evidence for local oxygen build up in the Transvaal Supergroup – a proxy that responds to very low oxygen levels, so perhaps oxygen was present but only at very low concentrations. However, my approach was designed to target chemical precipitates closely linked to microbial communities, to maximise the potential for O_2 build-up to levels able to trigger Ce cycling. For example, oxygen levels as high as 50 $\mu molkg^{-1}$ have been recorded within modern microbial mats at the bottom of anoxic lakes in Antarctica (Sumner et al., 2015). So, if cyanobacteria were present at this time, we'd expect to see signals in these facies. However, it is possible that the oxygen was rapidly consumed by other metabolisms or not detectable due to the fine-scale nature of environmental

conditions. Overall, the scarcity of geochemical data supporting significant oxygenation, even in shallow facies with clear evidence for microbial mats, supports hypotheses that oxygenic photosynthesis evolved relatively late, coinciding with the GOE. This, in turn, supports hypothesis for the generation of iron formation that involve only ferrous minerals, with ferric minerals forming through post-depositional alteration after the GOE.

What are the primary minerals in the iron formations of the Transvaal Supergroup, and can their geochemical characteristics be extracted?

Greenalite has been identified as a primary mineral precipitate in the iron formation of the Hamersley Basin, Western Australia, and the Transvaal Supergroup, South Africa in large body of recent work (Rasmussen et al., 2013, 2015, 2017, 2021). This thesis investigated new cores from the Transvaal Supergroup, South Africa, using high-resolution imagine techniques. Similar to previous work, petrographic evidence suggests that greenalite was an early forming phase that was preserved in early diagenetic chert.

BIF are typically made up of fine-grained phases, including primary greenalite, which complicates the targeting of individual grains. To address this complexity, I cut samples parallel to the banding, thereby exposing a large surface area of greenalite needles suspended and preserved in chert. This approach not only maximized the visibility of these elusive grains but also made room for targeted analyses. Laser ablation techniques were used to collect REY data from the exposed greenalite laths, and further isolated from the enclosing chert using a custom MATLAB script. This method allowed accurate extraction of the REY contents of primary greenalite.

Where did the primary minerals in the iron formations precipitate?

These novel data suggest greenalite in the Kuruman Formation may have precipitated in a shelf environment, rather than around hydrothermal vents. This could have been triggered by elevated pH, indicating that models of early pH are missing a component or do not accurately capture global average conditions. Alternatively, greenalite precipitation at low pH could have been facilitated by warmer ocean temperatures. This interpretation aligns with oxygen isotope records from iron oxides and mineral pairs, which suggest that $\delta^{18}O_{H2O}$ has increased over time while temperatures in the early Earth exceeded 70˚C, similar to temperatures in the modern ocean. If this is the case, then the

temperature-dependence of the solubility product of all minerals should be factored into experiments and models that emulate early sedimentary environments.

The preservation of primary REY patterns in chert-hosted greenalite suggests that these minerals captured primary geochemical signatures. This may have been aided by early silicification (Rasmussen & Muhling, 2021). This makes greenalite a promising archive for capturing primary geochemical signals, including metal contents and isotopic compositions.

How did metal availability in the Paleoproterozoic ocean influence the evolution and metabolic pathways of early microbial life?

The trace metal content of greenalite was used to determine metal availability in the Paleoproterozoic oceans. The data indicate that Zn and V were scarce, Ni was present in similar concentrations to modern oceans, Co was enriched, and Mn was abundant. These patterns of metal availability are consistent with some other geological archives and model predictions. Specifically, the patterns match predictions based on greenalite itself (Tostevin & Ahmed, 2023), suggesting widespread precipitation of greenalite played a role in controlling metal availability in early oceans. However, the Zn data produce a very different result compared with estimates from bulk iron formation and shale. This discrepancy may indicate an issue with Zn, as it is prone to contamination, or the limitations of using bulk rocks with complex mineralogy for geochemical analysis. Alternatively, the data here may provide a localised snapshot of conditions which were not representative of average marine conditions over longer timescales.

The data suggest that Mn and Co were more readily available and utilized by early microbes, while Zn was less available. This is in line with the metal preferences of early microbial life, suggesting the distinct metal availability patterns likely shaped early microbial evolution as supported by phylogenomic and proteomic data. This highlights the ongoing strong links between the environment and ecosystems over Earth history.

How can the study of iron formations and microbial carbonates from the Transvaal Supergroup enhance our understanding of the broader geological and biological context of early Earth?

The study of iron formations and microbial carbonates from the Transvaal Supergroup provides valuable insights into early Earth's ocean chemistry and biosphere evolution. The preservation of

primary REY patterns and trace metal contents in these formations allows for reliable reconstructions of ancient marine conditions. The findings suggest that early oceans were predominantly anoxic and that metal availability played a crucial role in shaping microbial evolution and metabolic pathways. These insights contribute to our understanding of the timing and mechanisms of oxygenation events, the evolution of early life, and the geochemical processes governing ancient marine environments. By establishing greenalite as a robust archive for paleoceanographic studies, this research opens avenues for exploring the Archean and Proterozoic records to reconstruct metal concentrations and environmental conditions across different settings and geological timescales.

6.3. Broader geological context

Placing these findings in a broader geological context, this research underscores the complexity and dynamism of early Earth systems. The Proterozoic Eon, a time of significant geological, chemical, and biological transitions, set the stage for the subsequent evolution of the biosphere and the atmosphere. The absence of substantial oxygen oases, implies that the rise of atmospheric oxygen was a rapid process, which occurred soon after the development of oxygen-producing cyanobacteria.

The Paleoproterozoic world was a landscape of profound transitions, where the chemistry of the oceans played a crucial role in shaping the trajectory of life on Earth. This era, characterized by predominantly anoxic marine environments, harbored early microbial communities that thrived in conditions starkly different from today. Iron formations and microbial carbonates tell a story of an ocean rich in iron and manganese but scarce in zinc and vanadium, reflecting a world where early life had to adapt to the metals that were available. The presence of greenalite, a primary precipitate in iron formation, indicates that sedimentation processes were influenced by subtle shifts in pH, temperature, and localized redox conditions. Cyanobacteria, possibly present and producing oxygen, hinted at the dawn of oxygenic photosynthesis, yet their impact was muted, with oxygen either being rapidly consumed by aerobic processes or remaining undetectable in the geochemical record. Alternatively, recent work suggests the ancestors of cyanobacteria were present in the Archean, but their metabolism shifted to start producing oxygen later in their lineage (Sanchez-Baracaldo, 2024). If so, this could reconcile biological data that indicate an early origin for cyanobacteria and some geochemical data that suggest oxygen was not present until the GOE, although it could not explain other isolated geochemical data that have been interpreted to indicate pre-GOE oxygen. This complex interplay of chemistry and biology set the stage for the Great Oxidation Event, marking a pivotal shift in Earth's history. The Paleoproterozoic oceans were thus a crucible of evolutionary experimentation, where early life forms navigated the challenges of metal availability and redox variability, laying down

the biochemical foundations that would eventually lead to the oxygen-rich atmosphere we know today.

6.4. Future directions and implications

This study not only enhances our understanding of Proterozoic ocean chemistry but also demonstrates the utility of greenalite as a robust archive for reconstructing ancient marine environments. The methodological advancements developed in this research, including the innovative sampling techniques and the application of MATLAB code to isolate greenalite data, pave the way for future studies to explore other periods and settings in Earth's history. By extending these approaches, we can build a more detailed and nuanced picture of how marine chemistry and microbial life co-evolved through deep time. There is room for this application to be expanded to the contemporary, well-preserved Hamersley Group, Pilbara Craton, Western Australia, to cross-check the results from this study. It could also be expanded into earlier Archean and later Proterozoic deposits to see how greenalite formation mechanisms or metal availability changed over time. Additionally, the partition coefficient of REE into greenalite could be confirmed through experimental work.

In a broader sense, this research contributes to the ongoing discourse on the co-evolution of life and the environment. It reminds us that the history of our planet is a tapestry woven from countless interactions between the lithosphere, hydrosphere, atmosphere, and biosphere. The findings presented here are a testament to the intricate and often subtle ways in which these spheres have influenced each other over billions of years.

6.5. Concluding thoughts

As I reflect on the journey undertaken in this research, it is clear that the study of ancient marine biogeochemistry is not just about deciphering the past but also about understanding the foundations upon which our present environment and life are built. This work contributes a vital chapter to the story of Earth, one that highlights the resilience and adaptability of life in the face of a constantly changing planet. It also serves as a reminder of the importance of scientific curiosity and innovation in uncovering the secrets of our world's deep history.

In conclusion, this research has provided significant new insights into the chemistry of Proterozoic oceans, the depositional environments of iron formation and carbonate rocks, and the early conditions that shaped microbial evolution. By advancing our understanding of these ancient systems, we move closer to comprehending the complex and intertwined narrative of Earth's geological and

biological evolution. This study stands as a testament to the power of interdisciplinary research in unlocking the mysteries of our planet's past and lays a solid foundation for future explorations into the ancient archives of Earth's history.

References

Alibert, C. (2016). Rare earth elements in Hamersley BIF minerals. *Geochimica et Cosmochimica Acta*, *184*, 311-328.

Alibo, D. S., & Nozaki, Y. (1999). Rare earth elements in seawater: particle association, shale-normalization, and Ce oxidation. *Geochimica et Cosmochimica Acta*, *63*(3-4), 363-372.

Altermann, W., & Nelson, D. R. (1998). Sedimentation rates, basin analysis and regional correlations of three Neoarchaean and Palaeoproterozoic sub-basins of the Kaapvaal craton as inferred from precise U–Pb zircon ages from volcaniclastic sediments. *Sedimentary Geology*, *120*(1-4), 225-256.

Anbar, A. D. (2008). Elements and evolution. *Science*, *322*(5907), 1481-1483.

Anbar, A. D., Buick, R., Gordon, G. W., Johnson, A. C., Kendall, B., Lyons, T. W., Ostrander, C. M., Planavsky, N. J., Reinhard, C. T., & Stüeken, E. E. (2023). Technical comment on "Reexamination of 2.5-Ga 'whiff'of oxygen interval points to anoxic ocean before GOE". *Science advances*, *9*(14), eabq3736.

Anbar, A. D., Duan, Y., Lyons, T. W., Arnold, G. L., Kendall, B., Creaser, R. A., Kaufman, A. J., Gordon, G. W., Scott, C., & Garvin, J. (2007). A whiff of oxygen before the great oxidation event? *Science*, *317*(5846), 1903-1906.

Anbar, A. D., & Knoll, A. H. (2002). Proterozoic ocean chemistry and evolution: a bioinorganic bridge? *Science*, *297*(5584), 1137-1142.

Anbar, A. D., & Rouxel, O. (2007). Metal stable isotopes in paleoceanography. *Annu. Rev. Earth Planet. Sci.*, *35*(1), 717-746.

Arnold, G. L., Anbar, A., Barling, J., & Lyons, T. (2004). Molybdenum isotope evidence for widespread anoxia in mid-Proterozoic oceans. *Science*, *304*(5667), 87-90.

Baldwin, G. J., Thurston, P. C., & Kamber, B. S. (2011). High-precision rare earth element, nickel, and chromium chemistry of chert microbands pre-screened with in-situ analysis. *Chemical Geology*, *285*(1-4), 133-143.

Banerjee, R., & Ragsdale, S. W. (2003). The many faces of vitamin B12: catalysis by cobalamin-dependent enzymes. *Annual review of biochemistry*, *72*(1), 209-247.

Banner, J. L., Hanson, G., & Meyers, W. (1988). Water-rock interaction history of regionally extensive dolomites of the Burlington-Keokuk Formation (Mississippian): isotopic evidence.

Barton, E., Altermann, W., Williams, I., & Smith, C. (1994). U-Pb zircon age for a tuff in the Campbell Group, Griqualand West Sequence, South Africa: implications for Early Proterozoic rock accumulation rates. *Geology*, *22*(4), 343-346.

Bau, M. (1999). Scavenging of dissolved yttrium and rare earths by precipitating iron oxyhydroxide: experimental evidence for Ce oxidation, Y-Ho fractionation, and lanthanide tetrad effect. *Geochimica et Cosmochimica Acta*, *63*(1), 67-77.

Bau, M., & Dulski, P. (1996). Distribution of yttrium and rare-earth elements in the Penge and Kuruman iron-formations, Transvaal Supergroup, South Africa. *Precambrian Research*, *79*(1-2), 37-55.

Bau, M., & Dulski, P. (1999). Comparing yttrium and rare earths in hydrothermal fluids from the Mid-Atlantic Ridge: implications for Y and REE behaviour during near-vent mixing and for the Y/Ho ratio of Proterozoic seawater. *Chemical Geology*, *155*(1-2), 77-90.

Bau, M., Dulski, P., & Möller, P. (1995). Yttrium and holmium in South Pacific seawater: vertical distribution and possible fractionation mechanisms. *Chem. Erde*, *55*(1), 1-15.

Bau, M., & Koschinsky, A. (2009). Oxidative scavenging of cerium on hydrous Fe oxide: evidence from the distribution of rare earth elements and yttrium between Fe oxides and Mn oxides in hydrogenetic ferromanganese crusts. *Geochemical Journal*, *43*(1), 37-47.

Bau, M., Romer, R. L., Lüders, V., & Beukes, N. J. (1999). Pb, O, and C isotopes in silicified Mooidraai dolomite (Transvaal Supergroup, South Africa): implications for the composition of

Paleoproterozoic seawater and 'dating'the increase of oxygen in the Precambrian atmosphere. *Earth and Planetary Science Letters*, *174*(1-2), 43-57.

Baumgartner, L. K., Reid, R. P., Dupraz, C., Decho, A. W., Buckley, D., Spear, J., Przekop, K. M., & Visscher, P. T. (2006). Sulfate reducing bacteria in microbial mats: changing paradigms, new discoveries. *Sedimentary Geology*, *185*(3-4), 131-145.

Beard, B. L., & Johnson, C. M. (2004). Fe isotope variations in the modern and ancient earth and other planetary bodies. *Reviews in Mineralogy and Geochemistry*, *55*(1), 319-357.

Bekker, A., Holland, H., Wang, P.-L., Rumble Iii, D., Stein, H., Hannah, J., Coetzee, L., & Beukes, N. (2004). Dating the rise of atmospheric oxygen. *Nature*, *427*(6970), 117-120.

Bekker, A., Kaufman, A. J., Karhu, J. A., Beukes, N. J., Swart, Q. D., Coetzee, L. L., & Eriksson, K. A. (2001). Chemostratigraphy of the Paleoproterozoic Duitschland Formation, South Africa: implications for coupled climate change and carbon cycling. *American Journal of Science*, *301*(3), 261-285.

Bekker, A., Planavsky, N., Rasmussen, B., Krapez, B., Hofmann, A., Slack, J., Rouxel, O., & Konhauser, K. (2014). Iron formations: Their origins and implications for ancient seawater chemistry. In *Treatise on geochemistry* (Vol. 12, pp. 561-628). Elsevier.

Bekker, A., Slack, J. F., Planavsky, N., Krapez, B., Hofmann, A., Konhauser, K. O., & Rouxel, O. J. (2010). Iron formation: the sedimentary product of a complex interplay among mantle, tectonic, oceanic, and biospheric processes. *Economic Geology*, *105*(3), 467-508.

Bergmann, K. D., Grotzinger, J. P., & Fischer, W. W. (2013). Biological influences on seafloor carbonate precipitation. *Palaios*, *28*(2), 99-115.

Berner, R. A. (1980). *Early diagenesis: a theoretical approach*. Princeton University Press.

Beukes, N. (1980). Stratigrafie en litofasies van die Campbellrand-subgroep van die Proterofitiese Ghaap-groep, noord-Kaapland. *South African Journal of Geology*, *83*(2), 141-170.

Beukes, N. (1983). Palaeoenvironmental setting of iron-formations in the depositional basin of the Transvaal Supergroup, South Africa. In *Developments in Precambrian Geology* (Vol. 6, pp. 131-198). Elsevier.

Beukes, N. (1984). Sedimentology of the Kuruman and Griquatown iron-formations, transvaal supergroup, Griqualand West, South Africa. *Precambrian Research*, *24*(1), 47-84.

Beukes, N. (1986). The Transvaal sequence in Griqualand west. Mineral deposits of southern Africa,

Beukes, N. (1992). Models for iron formation deposition. *Proterozoic Biosphere*.

Beukes, N., De Kock, M., Vorster, C., Ravhura, L., Frei, D., Gumsley, A., & Harris, C. (2019). The age and country rock provenance of the Molopo Farms Complex: implications for Transvaal Supergroup correlation in southern Africa. *South African Journal of Geology 2019*, *122*(1), 39-56.

Beukes, N. J. (1987). Facies relations, depositional environments and diagenesis in a major early Proterozoic stromatolitic carbonate platform to basinal sequence, Campbellrand Subgroup, Transvaal Supergroup, Southern Africa. *Sedimentary Geology*, *54*(1-2), 1-46.

Beukes, N. J., & Gutzmer, J. (2008). Origin and paleoenvironmental significance of major iron formations at the Archean-Paleoproterozoic boundary.

Beukes, N. J., & Klein, C. (1990). Geochemistry and sedimentology of a facies transition—from microbanded to granular iron-formation—in the early Proterozoic Transvaal Supergroup, South Africa. *Precambrian Research*, *47*(1-2), 99-139.

Beukes, N. J., Swindell, E. P., & Wabo, H. (2016). Manganese deposits of Africa. *Episodes Journal of International Geoscience*, *39*(2), 285-317.

Bjerrum, C. J., & Canfield, D. E. (2002). Ocean productivity before about 1.9 Gyr ago limited by phosphorus adsorption onto iron oxides. *Nature*, *417*(6885), 159-162.

Blatt, H., Tracy, R., & Owens, B. (2006). *Petrology: igneous, sedimentary, and metamorphic*. Macmillan.

Blättler, C., Kump, L., Fischer, W., Paris, G., Kasbohm, J., & Higgins, J. (2017). Constraints on ocean carbonate chemistry and p CO2 in the Archaean and Palaeoproterozoic. *Nature Geoscience*, *10*(1), 41-45.

Bolhar, R., Kamber, B. S., Moorbath, S., Fedo, C. M., & Whitehouse, M. J. (2004). Characterisation of early Archaean chemical sediments by trace element signatures. *Earth and Planetary Science Letters*, *222*(1), 43-60.

Bolhar, R., & Van Kranendonk, M. J. (2007). A non-marine depositional setting for the northern Fortescue Group, Pilbara Craton, inferred from trace element geochemistry of stromatolitic carbonates. *Precambrian Research*, *155*(3-4), 229-250.

Bolhar, R., Van Kranendonk, M. J., & Kamber, B. S. (2005). A trace element study of siderite–jasper banded iron formation in the 3.45 Ga Warrawoona Group, Pilbara Craton—formation from hydrothermal fluids and shallow seawater. *Precambrian Research*, *137*(1-2), 93-114.

Bown, J., Boye, M., Baker, A., Duvieilbourg, E., Lacan, F., Le Moigne, F., Planchon, F., Speich, S., & Nelson, D. M. (2011). The biogeochemical cycle of dissolved cobalt in the Atlantic and the Southern Ocean south off the coast of South Africa. *Marine chemistry*, *126*(1-4), 193-206.

Boyle, R., Clark, J., Poulton, S. W., Shields-Zhou, G., Canfield, D. E., & Lenton, T. (2013). Nitrogen cycle feedbacks as a control on euxinia in the mid-Proterozoic ocean. *Nature communications*, *4*(1), 1533.

Brady, M. P., Tostevin, R., & Tosca, N. J. (2022). Marine phosphate availability and the chemical origins of life on Earth. *Nature communications*, *13*(1), 5162.

Buick, R. (1992). The antiquity of oxygenic photosynthesis: evidence from stromatolites in sulphate-deficient Archaean lakes. *Science*, *255*(5040), 74-77.

Butterfield, N. J. (2015). Proterozoic photosynthesis–a critical review. *Palaeontology*, *58*(6), 953-972.

Byrne, R., & Sholkovitz, E. (1996). In Handbook on the Physics and Chemistry of Rare Earths; Gschneidner, KA, Eyring, L. In: Elsevier Science: Amsterdam, NE.

Byrne, R. H., & Kim, K.-H. (1990). Rare earth element scavenging in seawater. *Geochimica et Cosmochimica Acta*, *54*(10), 2645-2656.

Byrne, R. H., & Lee, J. H. (1993). Comparative yttrium and rare earth element chemistries in seawater. *Marine chemistry*, *44*(2-4), 121-130.

Canfield, D. E. (1998). A new model for Proterozoic ocean chemistry. *Nature*, *396*(6710), 450-453.

Canfield, D. E. (2005). The early history of atmospheric oxygen: homage to Robert M. Garrels. *Annu. Rev. Earth Planet. Sci.*, *33*(1), 1-36.

Canfield, D. E., Poulton, S. W., Knoll, A. H., Narbonne, G. M., Ross, G., Goldberg, T., & Strauss, H. (2008). Ferruginous conditions dominated later Neoproterozoic deep-water chemistry. *Science*, *321*(5891), 949-952.

Cantrell, K. J., & Byrne, R. H. (1987). Rare earth element complexation by carbonate and oxalate ions. *Geochimica et Cosmochimica Acta*, *51*(3), 597-605.

Catling, D. C., Zahnle, K. J., & McKay, C. P. (2001). Biogenic methane, hydrogen escape, and the irreversible oxidation of early Earth. *Science*, *293*(5531), 839-843.

Chen, D., Qing, H., Yan, X., & Li, H. (2006). Hydrothermal venting and basin evolution (Devonian, South China): constraints from rare earth element geochemistry of chert. *Sedimentary Geology*, *183*(3-4), 203-216.

Chen, J., Algeo, T. J., Zhao, L., Chen, Z.-Q., Cao, L., Zhang, L., & Li, Y. (2015). Diagenetic uptake of rare earth elements by bioapatite, with an example from Lower Triassic conodonts of South China. *Earth-Science Reviews*, *149*, 181-202.

Claire, M. W., Catling, D. C., & Zahnle, K. J. (2006). Biogeochemical modelling of the rise in atmospheric oxygen. *Geobiology*, *4*(4), 239-269.

Claypool, G. E., & Kaplan, I. R. (1974). The origin and distribution of methane in marine sediments. *Natural gases in marine sediments*, 99-139.

Cornell, D., & Schütte, S. (1995). A volcanic-exhalative origin for the world's largest (Kalahari) manganese field. *Mineralium Deposita*, *30*, 146-151.

Cornell, D., Schütte, S., & Eglington, B. (1996). The Ongeluk basaltic andesite formation in Griqualand West, South Africa: submarine alteration in a 2222 Ma Proterozoic sea. *Precambrian Research*, *79*(1-2), 101-123.

Crowe, S. A., Døssing, L. N., Beukes, N. J., Bau, M., Kruger, S. J., Frei, R., & Canfield, D. E. (2013). Atmospheric oxygenation three billion years ago. *Nature*, *501*(7468), 535-538.

Crowe, S. A., Jones, C., Katsev, S., Magen, C., O'Neill, A. H., Sturm, A., Canfield, D. E., Haffner, G. D., Mucci, A., & Sundby, B. (2008). Photoferrotrophs thrive in an Archean Ocean analogue. *Proceedings of the National Academy of Sciences*, *105*(41), 15938-15943.

Czaja, A. D., Johnson, C. M., Roden, E. E., Beard, B. L., Voegelin, A. R., Nägler, T. F., Beukes, N. J., & Wille, M. (2012). Evidence for free oxygen in the Neoarchean ocean based on coupled iron–molybdenum isotope fractionation. *Geochimica et Cosmochimica Acta*, *86*, 118-137.

Dauphas, N., van Zuilen, M., Busigny, V., Lepland, A., Wadhwa, M., & Janney, P. E. (2007). Iron isotope, major and trace element characterization of early Archean supracrustal rocks from SW Greenland: protolith identification and metamorphic overprint. *Geochimica et Cosmochimica Acta*, *71*(19), 4745-4770.

Dauphas, N., Van Zuilen, M., Wadhwa, M., Davis, A. M., Marty, B., & Janney, P. E. (2004). Clues from Fe isotope variations on the origin of early Archean BIFs from Greenland. *Science*, *306*(5704), 2077-2080.

David, L. A., & Alm, E. J. (2011). Rapid evolutionary innovation during an Archaean genetic expansion. *Nature*, *469*(7328), 93-96.

De Baar, H., Schijf, J., & Byrne, R. (1991). Solution chemistry of the rare earth elements in seawater. *European Journal of Solid State Inorganic Chemistry*, *28*.

De Baar, H. J., Bacon, M. P., Brewer, P. G., & Bruland, K. W. (1985b). Rare earth elements in the Pacific and Atlantic Oceans. *Geochimica et Cosmochimica Acta*, *49*(9), 1943-1959.

De Baar, H. J., Brewer, P. G., & Bacon, M. P. (1985a). Anomalies in rare earth distributions in seawater: Gd and Tb. *Geochimica et Cosmochimica Acta*, *49*(9), 1961-1969.

De Muynck, W., Verbeken, K., De Belie, N., & Verstraete, W. (2013). Influence of temperature on the effectiveness of a biogenic carbonate surface treatment for limestone conservation. *Applied microbiology and biotechnology*, *97*, 1335-1347.

DeJong, J. T., Mortensen, B. M., Martinez, B. C., & Nelson, D. C. (2010). Bio-mediated soil improvement. *Ecological engineering*, *36*(2), 197-210.

Derry, L. A. (2015). Causes and consequences of mid-Proterozoic anoxia. *Geophysical Research Letters*, *42*(20), 8538-8546.

Dodd, M. S., Wang, H., Li, C., Towner, M., Thomson, A. R., Slack, J. F., Wan, Y.-s., Pirajno, F., Manikyamba, C., & Wang, Q. (2022). Abiotic anoxic iron oxidation, formation of Archean banded iron formations, and the oxidation of early Earth. *Earth and Planetary Science Letters*, *584*, 117469.

Douville, E., Bienvenu, P., Charlou, J. L., Donval, J. P., Fouquet, Y., Appriou, P., & Gamo, T. (1999). Yttrium and rare earth elements in fluids from various deep-sea hydrothermal systems. *Geochimica et Cosmochimica Acta*, *63*(5), 627-643.

Dubinin, A. (2004). Geochemistry of rare earth elements in the ocean. *Lithology and mineral resources*, *39*, 289-307.

Dunlea, A., Scudder, R., & Murray, R. (2018). Marine sediment. *Encyclopedia of Earth Sciences Series*, 878-892.

Dupont, C. L., Butcher, A., Valas, R. E., Bourne, P. E., & Caetano-Anollés, G. (2010). History of biological metal utilization inferred through phylogenomic analysis of protein structures. *Proceedings of the National Academy of Sciences*, *107*(23), 10567-10572.

Elderfield, H. (1988). The oceanic chemistry of the rare-earth elements. *Philosophical Transactions of the Royal Society of London. Series A, Mathematical and Physical Sciences*, *325*(1583), 105-126.

Elderfield, H., & Greaves, M. J. (1982). The rare earth elements in seawater. *Nature*, *296*(5854), 214-219.

Eriksson, K., Krapez, B., & Fralick, P. (1994). Sedimentology of Archean greenstone belts: signatures of tectonic evolution. *Earth-Science Reviews*, *37*(1-2), 1-88.

Eriksson, K. A. (1995). Crustal growth, surface processes, and atmospheric evolution on the early Earth. *Geological Society, London, Special Publications*, *95*(1), 11-25.

Eriksson, P., Altermann, W., Hartzer, F., Johnson, M., Anhaeusser, C., & Thomas, R. (2006). The Transvaal Supergroup and its precursors. *The Geology of South Africa*, 237-260.

Eriksson, P., Hattingh, P., & Altermann, W. (1995). An overview of the geology of the Transvaal Sequence and Bushveld Complex, South Africa. *Mineralium Deposita*, *30*, 98-111.

Eriksson, P. G., Condie, K. C., Tirsgaard, H., Mueller, W., Altermann, W., Miall, A. D., Aspler, L. B., Catuneanu, O., & Chiarenzelli, J. R. (1998). Precambrian clastic sedimentation systems. *Sedimentary Geology*, *120*(1-4), 5-53.

Eroglu, S., Schoenberg, R., Wille, M., Beukes, N., & Taubald, H. (2015). Geochemical stratigraphy, sedimentology, and Mo isotope systematics of the ca. 2.58–2.50 Ga-old Transvaal Supergroup carbonate platform, South Africa. *Precambrian Research*, *266*, 27-46.

Eroglu, S., van Zuilen, M. A., Taubald, H., Drost, K., Wille, M., Swanner, E. D., Beukes, N. J., & Schoenberg, R. (2017). Depth-dependent δ13C trends in platform and slope settings of the Campbellrand-Malmani carbonate platform and possible implications for Early Earth oxygenation. *Precambrian Research*, *302*, 122-139.

Evans, D., Beukes, N. J., & Kirschvink, J. L. (1997). Low-latitude glaciation in the Palaeoproterozoic era. *Nature*, *386*(6622), 262-266.

Fairey, B., Tsikos, H., Corfu, F., & Polteau, S. (2013). U–Pb systematics in carbonates of the Postmasburg Group, Transvaal Supergroup, South Africa: primary versus metasomatic controls. *Precambrian Research*, *231*, 194-205.

Farquhar, J., Bao, H., & Thiemens, M. (2000). Atmospheric influence of Earth's earliest sulfur cycle. *Science*, *289*(5480), 756-758.

Farquhar, J., Peters, M., Johnston, D. T., Strauss, H., Masterson, A., Wiechert, U., & Kaufman, A. J. (2007). Isotopic evidence for Mesoarchaean anoxia and changing atmospheric sulphur chemistry. *Nature*, *449*(7163), 706-709.

Feely, R. A., Doney, S. C., & Cooley, S. R. (2009). Ocean acidification: Present conditions and future changes in a high-CO_2 world. *Oceanography*, *22*(4), 36-47.

Fischer, W. W., & Knoll, A. H. (2009). An iron shuttle for deepwater silica in Late Archean and early Paleoproterozoic iron formation. *Geological Society of America Bulletin*, *121*(1-2), 222-235.

Fischer, W. W., Schroeder, S., Lacassie, J. P., Beukes, N. J., Goldberg, T., Strauss, H., Horstmann, U. E., Schrag, D. P., & Knoll, A. (2009). Isotopic constraints on the Late Archean carbon cycle from the Transvaal Supergroup along the western margin of the Kaapvaal Craton, South Africa. *Precambrian Research*, *169*(1-4), 15-27.

Frei, R., Gaucher, C., Poulton, S. W., & Canfield, D. E. (2009). Fluctuations in Precambrian atmospheric oxygenation recorded by chromium isotopes. *Nature*, *461*(7261), 250-253.

French, K. L., Hallmann, C., Hope, J. M., Schoon, P. L., Zumberge, J. A., Hoshino, Y., Peters, C. A., George, S. C., Love, G. D., & Brocks, J. J. (2015). Reappraisal of hydrocarbon biomarkers in Archean rocks. *Proceedings of the National Academy of Sciences*, *112*(19), 5915-5920.

Frimmel, H. E. (2010). On the reliability of stable carbon isotopes for Neoproterozoic chemostratigraphic correlation. *Precambrian Research*, *182*(4), 239-253.

Galili, N., Shemesh, A., Yam, R., Brailovsky, I., Sela-Adler, M., Schuster, E.M., Collom, C., Bekker, A., Planavsky, N., Macdonald, F.A. , & Préat, A. (2019). The geologic history of seawater oxygen isotopes from marine iron oxides. *Science*, *365*(6452), pp.469-473.

Gandin, A., & Wright, D. (2007). Evidence of vanished evaporites in Neoarchaean carbonates of South Africa. *Geological Society, London, Special Publications*, *285*(1), 285-308.

Gandin, A., Wright, D. T., & Melezhik, V. (2005). Vanished evaporites and carbonate formation in the Neoarchaean Kogelbeen and Gamohaan formations of the Campbellrand Subgroup, South Africa. *Journal of African Earth Sciences*, *41*(1-2), 1-23.

German, C. R., & Elderfield, H. (1990). Application of the Ce anomaly as a paleoredox indicator: the ground rules. *Paleoceanography*, *5*(5), 823-833.

Gole, M. (1980). Mineralogy and petrology of very-low-metamorphic grade Archaean banded iron-formations, Weld Range, Western Australia. *American Mineralogist*, *65*(1-2), 8-25.

Gole, M. J., & Klein, C. (1981). Banded iron-formations through much of Precambrian time. *The Journal of Geology*, *89*(2), 169-183.

Gourcerol, B., Thurston, P., Kontak, D., & Côté-Mantha, O. (2015). Interpretations and implications of LA ICP-MS analysis of chert for the origin of geochemical signatures in banded iron formations (BIFs) from the Meadowbank gold deposit, Western Churchill Province, Nunavut. *Chemical Geology*, *410*, 89-107.

Grassineau, N., Nisbet, E., Fowler, C., Bickle, M., Lowry, D., Chapman, H., Mattey, D., Abell, P., Yong, J., & Martin, A. (2002). Stable isotopes in the Archaean Belingwe belt, Zimbabwe: evidence for a diverse microbial mat ecology. *Geological Society, London, Special Publications*, *199*(1), 309-328.

Gross, G. A. (1980). A classification of iron formations based on depositional environments. *The Canadian Mineralogist*, *18*(2), 215-222.

Grotzinger, J. P., & Kasting, J. F. (1993). New constraints on Precambrian ocean composition. *The Journal of Geology*, *101*(2), 235-243.

Grotzinger, J. P., & Knoll, A. H. (1999). Stromatolites in Precambrian carbonates: evolutionary mileposts or environmental dipsticks? *Annual review of earth and planetary sciences*, *27*(1), 313-358.

Guggenheim, S., Bailey, S. W., Eggleton, R. A., & Wilkes, P. (1982). Structural aspects of greenalite and related minerals. *The Canadian Mineralogist*, *20*(1), 1-18.

Gumsley, A. P., Chamberlain, K. R., Bleeker, W., Söderlund, U., De Kock, M. O., Larsson, E. R., & Bekker, A. (2017). Timing and tempo of the Great Oxidation Event. *Proceedings of the National Academy of Sciences*, *114*(8), 1811-1816.

Guo, Q., Shields, G. A., Liu, C., Strauss, H., Zhu, M., Pi, D., Goldberg, T., & Yang, X. (2007). Trace element chemostratigraphy of two Ediacaran–Cambrian successions in South China: implications for organosedimentary metal enrichment and silicification in the early Cambrian. *Palaeogeography, Palaeoclimatology, Palaeoecology*, *254*(1-2), 194-216.

Guo, Q., Strauss, H., Kaufman, A. J., Schröder, S., Gutzmer, J., Wing, B., Baker, M. A., Bekker, A., Jin, Q., & Kim, S.-T. (2009). Reconstructing Earth's surface oxidation across the Archean-Proterozoic transition. *Geology*, *37*(5), 399-402.

Gutzmer, J., & Beukes, N. (1998). High-grade manganese ores in the Kalahari Manganese Field: Characterisation and dating of ore-forming events. *Unpublished Report. Rand Afrikaans University, Johannesburg*.

Gutzmer, J., & Beukes, N. J. (1996a). Mineral paragenesis of the Kalahari managanese field, South Africa. *Ore Geology Reviews*, *11*(6), 405-428.

Habicht, K. S., Gade, M., Thamdrup, B., Berg, P., & Canfield, D. E. (2002). Calibration of sulfate levels in the Archean ocean. *Science*, *298*(5602), 2372-2374.

Halevy, I., Alesker, M., Schuster, E., Popovitz-Biro, R., & Feldman, Y. (2017). A key role for green rust in the Precambrian oceans and the genesis of iron formations. *Nature Geoscience*, *10*(2), 135-139.

Halevy, I., & Bachan, A. (2017). The geologic history of seawater pH. *Science*, *355*(6329), 1069-1071.

Haynes, W. M. (2016). *CRC handbook of chemistry and physics*. CRC press.

Hein, J. R., Koschinsky, A., Halbach, P., Manheim, F. T., Bau, M., Kang, J.-K., & Lubick, N. (1997). Iron and manganese oxide mineralization in the Pacific. *Geological Society, London, Special Publications*, *119*(1), 123-138.

Hickman-Lewis, K., Gourcerol, B., Westall, F., Manzini, D., & Cavalazzi, B. (2020). Reconstructing Palaeoarchaean microbial biomes flourishing in the presence of emergent landmasses using trace and rare earth element systematics. *Precambrian Research*, *342*, 105689.

Higgins, J. A., Fischer, W., & Schrag, D. (2009). Oxygenation of the ocean and sediments: consequences for the seafloor carbonate factory. *Earth and Planetary Science Letters*, *284*(1-2), 25-33.

Himmler, T., Bach, W., Bohrmann, G., & Peckmann, J. (2010). Rare earth elements in authigenic methane-seep carbonates as tracers for fluid composition during early diagenesis. *Chemical Geology*, *277*(1-2), 126-136.

Hinz, I. L., Nims, C., Theuer, S., Templeton, A. S., & Johnson, J. E. (2021). Ferric iron triggers greenalite formation in simulated Archean seawater. *Geology*, *49*(8), 905-910.

Hinz, I. L., Rossi, L., Ma, C., & Johnson, J. E. (2023). Simulated diagenesis of the iron-silica precipitates in banded iron formations. *American Mineralogist*, *108*(9), 1732-1753.

Hofmann, A., Bolhar, R., Dirks, P., & Jelsma, H. (2003). The geochemistry of Archaean shales derived from a mafic volcanic sequence, Belingwe greenstone belt, Zimbabwe: provenance, source area unroofing and submarine versus subaerial weathering. *Geochimica et Cosmochimica Acta*, *67*(3), 421-440.

Høgdahl, O. T., Melsom, S., & BOWEN, V. T. (1968). Neutron activation analysis of lanthanide elements in sea water. In. ACS Publications.

Holland, H. D. (2002). Volcanic gases, black smokers, and the Great Oxidation Event. *Geochimica et Cosmochimica Acta*, *66*(21), 3811-3826.

Holland, H. D. (2006). The oxygenation of the atmosphere and oceans. *Philosophical Transactions of the Royal Society B: Biological Sciences*, *361*(1470), 903-915.

Ikhsani, I. Y., Wong, K. H., Ogawa, H., & Obata, H. (2023). Dissolved trace metals (Fe, Mn, Pb, Cd, Cu, and Zn) in the eastern Indian Ocean. *Marine chemistry*, *248*, 104208.

Isley, A. E. (1995). Hydrothermal plumes and the delivery of iron to banded iron formation. *The Journal of Geology*, *103*(2), 169-185.

Isson, T. , & Rauzi, S. (2024). Oxygen isotope ensemble reveals Earth's seawater, temperature, and carbon cycle history. *Science*, *383*(6683), pp.666-670.

Isson, T.T., Love, G.D., Dupont, C.L., Reinhard, C.T., Zumberge, A.J., Asael, D., Gueguen, B., McCrow, J., Gill, B.C., Owens, J., & Rainbird, R.H. (2018). Tracking the rise of eukaryotes to ecological dominance with zinc isotopes. *Geobiology*, *16*(4), pp.341-352.

James, H. L. (1954). Sedimentary facies of iron-formation. *Economic Geology*, *49*(3), 235-293.

Jamieson, J., Wing, B., Farquhar, J., & Hannington, M. (2013). Neoarchaean seawater sulphate concentrations from sulphur isotopes in massive sulphide ore. *Nature Geoscience*, *6*(1), 61-64.

Jiang, C. Z., Halevy, I., & Tosca, N. J. (2022). Kinetic isotope effect in siderite growth: Implications for the origin of banded iron formation siderite. *Geochimica et Cosmochimica Acta*, *322*, 260-273.

Jiang, C. Z., & Tosca, N. J. (2019). Fe (II)-carbonate precipitation kinetics and the chemistry of anoxic ferruginous seawater. *Earth and Planetary Science Letters*, *506*, 231-242.

Jochum, K. P., Nohl, U., Herwig, K., Lammel, E., Stoll, B., & Hofmann, A. W. (2005). GeoReM: a new geochemical database for reference materials and isotopic standards. *Geostandards and Geoanalytical Research*, *29*(3), 333-338.

Johnson, C. M., & Beard, B. L. (2006). Fe isotopes: An emerging technique for understanding modern and ancient biogeochemical cycles. *GSA today*, *16*(11), 4.

Johnson, C. M., Beard, B. L., Klein, C., Beukes, N. J., & Roden, E. E. (2008a). Iron isotopes constrain biologic and abiologic processes in banded iron formation genesis. *Geochimica et Cosmochimica Acta*, *72*(1), 151-169.

Johnson, C. M., Beard, B. L., & Roden, E. E. (2008b). The iron isotope fingerprints of redox and biogeochemical cycling in modern and ancient Earth. *Annu. Rev. Earth Planet. Sci.*, *36*(1), 457-493.

Johnson, J. E., Muhling, J. R., Cosmidis, J., Rasmussen, B., & Templeton, A. S. (2018). Low-Fe (III) greenalite was a primary mineral from Neoarchean Oceans. *Geophysical Research Letters*, *45*(7), 3182-3192.

Johnson, J. E., Webb, S. M., Thomas, K., Ono, S., Kirschvink, J. L., & Fischer, W. W. (2013). Manganese-oxidizing photosynthesis before the rise of cyanobacteria. *Proceedings of the National Academy of Sciences*, *110*(28), 11238-11243.

Johnston, D. T., Poulton, S. W., Dehler, C., Porter, S., Husson, J., Canfield, D. E., & Knoll, A. H. (2010). An emerging picture of Neoproterozoic ocean chemistry: Insights from the Chuar Group, Grand Canyon, USA. *Earth and Planetary Science Letters*, *290*(1-2), 64-73.

Jolliffe, F. (1935). A study of greenalite. *American Mineralogist: Journal of Earth and Planetary Materials*, *20*(6), 405-425.

Jones, C., Nomosatryo, S., Crowe, S. A., Bjerrum, C. J., & Canfield, D. E. (2015). Iron oxides, divalent cations, silica, and the early earth phosphorus crisis. *Geology*, *43*(2), 135-138.

Kamber, B. S., & Webb, G. E. (2001). The geochemistry of late Archaean microbial carbonate: implications for ocean chemistry and continental erosion history. *Geochimica et Cosmochimica Acta*, *65*(15), 2509-2525.

Kamber, B. S., Webb, G. E., & Gallagher, M. (2014). The rare earth element signal in Archaean microbial carbonate: information on ocean redox and biogenicity. *Journal of the Geological Society*, *171*(6), 745-763.

Kastner, M. (1999). Oceanic minerals: Their origin, nature of their environment, and significance. *Proceedings of the National Academy of Sciences*, *96*(7), 3380-3387.

Kempe, S., & Degens, E. T. (1985). An early soda ocean? *Chemical Geology*, *53*(1-2), 95-108.

Kendall, B., Reinhard, C. T., Lyons, T. W., Kaufman, A. J., Poulton, S. W., & Anbar, A. D. (2010). Pervasive oxygenation along late Archaean ocean margins. *Nature Geoscience*, *3*(9), 647-652.

Kim, K.-H., Byrne, R. H., & Lee, J. H. (1991). Gadolinium behavior in seawater: a molecular basis for gadolinium anomalies. *Marine chemistry*, *36*(1-4), 107-120.

Kirschvink, J. L., Gaidos, E. J., Bertani, L. E., Beukes, N. J., Gutzmer, J., Maepa, L. N., & Steinberger, R. E. (2000). Paleoproterozoic snowball Earth: Extreme climatic and geochemical global change and its biological consequences. *Proceedings of the National Academy of Sciences*, *97*(4), 1400-1405.

Kirschvink, J. L., & Kopp, R. E. (2008). Palaeoproterozoic ice houses and the evolution of oxygen-mediating enzymes: the case for a late origin of photosystem II. *Philosophical Transactions of the Royal Society B: Biological Sciences*, *363*(1504), 2755-2765.

Klein, C. (2005). Some Precambrian banded iron-formations (BIFs) from around the world: Their age, geologic setting, mineralogy, metamorphism, geochemistry, and origins. *American Mineralogist*, *90*(10), 1473-1499.

Klein, C., & Beukes, N. J. (1989). Geochemistry and sedimentology of a facies transition from limestone to iron-formation deposition in the early Proterozoic Transvaal Supergroup, South Africa. *Economic Geology*, *84*(7), 1733-1774.

Klein, C., & Beukes, N. J. (1993). Sedimentology and geochemistry of the glaciogenic late Proterozoic Rapitan iron-formation in Canada. *Economic Geology*, *88*(3), 542-565.

Knoll, A. H. (2003). Biomineralization and evolutionary history. *Reviews in Mineralogy and Geochemistry*, *54*(1), 329-356.

Knoll, A. H., & Beukes, N. J. (2009). Introduction: Initial investigations of a Neoarchean shelf margin-basin transition (Transvaal Supergroup, South Africa). *Precambrian Research*, *169*(1-4), 1-14.

Konhauser, K. O., Hamade, T., Raiswell, R., Morris, R. C., Ferris, F. G., Southam, G., & Canfield, D. E. (2002). Could bacteria have formed the Precambrian banded iron formations? *Geology*, *30*(12), 1079-1082.

Konhauser, K. O., Kappler, A., & Roden, E. E. (2011). Iron in microbial metabolisms. *Elements*, *7*(2), 89-93.

Konhauser, K. O., Pecoits, E., Lalonde, S. V., Papineau, D., Nisbet, E. G., Barley, M. E., Arndt, N. T., Zahnle, K., & Kamber, B. S. (2009). Oceanic nickel depletion and a methanogen famine before the Great Oxidation Event. *Nature*, *458*(7239), 750-753.

Konhauser, K. O., Planavsky, N., Hardisty, D., Robbins, L., Warchola, T., Haugaard, R., Lalonde, S., Partin, C., Oonk, P., & Tsikos, H. (2017). Iron formations: A global record of Neoarchaean to Palaeoproterozoic environmental history. *Earth-Science Reviews*, *172*, 140-177.

Konhauser, K. O., Robbins, L. J., Alessi, D. S., Flynn, S. L., Gingras, M. K., Martinez, R. E., Kappler, A., Swanner, E. D., Li, Y.-L., & Crowe, S. A. (2018). Phytoplankton contributions to the trace-element composition of Precambrian banded iron formations. *GSA Bulletin*, *130*(5-6), 941-951.

Krapež, B., Barley, M. E., & Pickard, A. L. (2003). Hydrothermal and resedimented origins of the precursor sediments to banded iron formation: sedimentological evidence from the Early Palaeoproterozoic Brockman Supersequence of Western Australia. *Sedimentology*, *50*(5), 979-1011.

Krause, A. J., Mills, B. J., Zhang, S., Planavsky, N. J., Lenton, T. M., & Poulton, S. W. (2018). Stepwise oxygenation of the Paleozoic atmosphere. *Nature communications*, *9*(1), 4081.

Krissansen-Totton, J., Arney, G. N., & Catling, D. C. (2018). Constraining the climate and ocean pH of the early Earth with a geological carbon cycle model. *Proceedings of the National Academy of Sciences*, *115*(16), 4105-4110.

Kump, L. R., Kasting, J. F., & Barley, M. E. (2001). Rise of atmospheric oxygen and the "upside-down" Archean mantle. *Geochemistry, Geophysics, Geosystems*, *2*(1).

Kump, L. R., & Seyfried Jr, W. E. (2005). Hydrothermal Fe fluxes during the Precambrian: Effect of low oceanic sulfate concentrations and low hydrostatic pressure on the composition of black smokers. *Earth and Planetary Science Letters*, *235*(3-4), 654-662.

Kunzmann, M., Gutzmer, J., Beukes, N., & Halverson, G. (2014). Depositional environment and lithostratigraphy of the Paleoproterozoic Mooidraai Formation, Kalahari manganese field, South Africa. *South African Journal of Geology*, *117*(2), 173-192.

Lantink, M., Davies, J., Mason, P., Schaltegger, U., & Hilgen, F. (2019). Milankovitch cyclicity in Paleoproterozoic BIF of the Kuruman Iron Formation in South Africa. Geophysical Research Abstracts,

Large, R. R., Halpin, J. A., Danyushevsky, L. V., Maslennikov, V. V., Bull, S. W., Long, J. A., Gregory, D. D., Lounejeva, E., Lyons, T. W., & Sack, P. J. (2014). Trace element content of sedimentary pyrite as a new proxy for deep-time ocean–atmosphere evolution. *Earth and Planetary Science Letters*, *389*, 209-220.

Lawrence, M. G., Greig, A., Collerson, K. D., & Kamber, B. S. (2006). Rare earth element and yttrium variability in South East Queensland waterways. *Aquatic Geochemistry*, *12*, 39-72.

Lechte, M., & Wallace, M. (2016). Sub–ice shelf ironstone deposition during the Neoproterozoic Sturtian glaciation. *Geology*, *44*(11), 891-894.

Lechte, M. A., Wallace, M. W., van Smeerdijk Hood, A., & Planavsky, N. (2018). Cryogenian iron formations in the glaciogenic Kingston Peak Formation, California. *Precambrian Research*, *310*, 443-462.

Lee, J. H., & Byrne, R. H. (1993). Complexation of trivalent rare earth elements (Ce, Eu, Gd, Tb, Yb) by carbonate ions. *Geochimica et Cosmochimica Acta*, *57*(2), 295-302.

Li, C., Love, G. D., Lyons, T. W., Fike, D. A., Sessions, A. L., & Chu, X. (2010). A stratified redox model for the Ediacaran ocean. *Science*, *328*(5974), 80-83.

Ling, H.-F., Chen, X., Li, D., Wang, D., Shields-Zhou, G. A., & Zhu, M. (2013). Cerium anomaly variations in Ediacaran–earliest Cambrian carbonates from the Yangtze Gorges area, South China: implications for oxygenation of coeval shallow seawater. *Precambrian Research*, *225*, 110-127.

Loges, A., Wagner, T., Barth, M., Bau, M., Göb, S., & Markl, G. (2012). Negative Ce anomalies in Mn oxides: the role of Ce4+ mobility during water–mineral interaction. *Geochimica et Cosmochimica Acta*, *86*, 296-317.

Lough, A., Homoky, W., Connelly, D., Comer-Warner, S., Nakamura, K., Abyaneh, M., Kaulich, B., & Mills, R. (2019). Soluble iron conservation and colloidal iron dynamics in a hydrothermal plume. *Chemical Geology*, *511*, 225-237.

Lowe, D. R. (1994). Archean greenstone-related sedimentary rocks. In *Developments in precambrian geology* (Vol. 11, pp. 121-169). Elsevier.

Luo, G., Ono, S., Beukes, N. J., Wang, D. T., Xie, S., & Summons, R. E. (2016). Rapid oxygenation of Earth's atmosphere 2.33 billion years ago. *Science advances*, *2*(5), e1600134.

Lyons, T. W., Reinhard, C. T., & Planavsky, N. J. (2014). The rise of oxygen in Earth's early ocean and atmosphere. *Nature*, *506*(7488), 307-315.

Macleod, G., McKeown, C., Hall, A. J., & Russell, M. J. (1994). Hydrothermal and oceanic pH conditions of possible relevance to the origin of life. *Origins of Life and Evolution of the Biosphere*, *24*, 19-41.

Maynard, J. B. (2010). The chemistry of manganese ores through time: a signal of increasing diversity of earth-surface environments. *Economic Geology*, *105*(3), 535-552.

McLennan, S., & Taylor, S. (1991). Sedimentary rocks and crustal evolution: tectonic setting and secular trends. *The Journal of Geology*, *99*(1), 1-21.

Mertz, W. (1998). Review of the scientific basis for establishing the essentiality of trace elements. *Biological trace element research*, *66*, 185-191.

Meyer, E. E., Quicksall, A. N., Landis, J. D., Link, P. K., & Bostick, B. C. (2012). Trace and rare earth elemental investigation of a Sturtian cap carbonate, Pocatello, Idaho: evidence for ocean redox conditions before and during carbonate deposition. *Precambrian Research*, *192*, 89-106.

Mhlanga, X., Tsikos, H., Lee, B., Rouxel, O., Boyce, A., Harris, C., & Lyons, T. (2023). The Palaeoproterozoic Hotazel BIF-Mn Formation as an archive of Earth's earliest oxygenation. *Earth-Science Reviews*, *240*, 104389.

Middag, R., De Baar, H. J., Bruland, K. W., & Van Heuven, S. M. (2020). The distribution of nickel in the west-Atlantic Ocean, its relationship with phosphate and a comparison to cadmium and zinc. *Frontiers in Marine Science*, *7*, 105.

Miyano, T., & Beukes, N. (1984). Phase relations of stilpnomelane, ferri-annite, and riebeckite in very low-grade metamorphosed iron-formations. *South African Journal of Geology*, *87*(2), 111-124.

Moorbath, S., O'nions, R., & Pankhurst, R. (1973). Early Archaean age for the Isua iron formation, West Greenland. *Nature*, *245*(5421), 138-139.

Moore, E. K., Hao, J., Spielman, S. J., & Yee, N. (2020). The evolving redox chemistry and bioavailability of vanadium in deep time. *Geobiology*, *18*(2), 127-138.

Moore, J. M., Polteau, S., Armstrong, R., Corfu, F., & Tsikos, H. (2012). The age and correlation of the Postmasburg Group, southern Africa: Constraints from detrital zircon grains. *Journal of African Earth Sciences*, *64*, 9-19.

Morris, R. (1993). Genetic modelling for banded iron-formation of the Hamersley Group, Pilbara Craton, Western Australia. *Precambrian Research*, *60*(1-4), 243-286.

Muhling, J. R., Gilbert, S. E., & Rasmussen, B. (2023). Rare earth element and yttrium (REY) geochemistry of 3.46–2.45 Ga greenalite-bearing banded iron formations: New insights into iron deposition and ancient ocean chemistry. *Chemical Geology*, *641*, 121789.

Nealson, K. H., & Myers, C. R. (1992). Microbial reduction of manganese and iron: new approaches to carbon cycling. *Applied and Environmental Microbiology*, *58*(2), 439-443.

Nel, B. P. (2013). *Petrography and geochemistry of iron formations of the Paleoproterozoic Koegas Subgroup, Transvaal Supergroup, Griqualand West, South Africa*. University of Johannesburg (South Africa).

Nicholson, K. (1992). Contrasting mineralogical-geochemical signatures of manganese oxides; guides to metallogenesis. *Economic Geology*, *87*(5), 1253-1264.

Noffke, N., Beukes, N., Bower, D., Hazen, R., & Swift, D. (2008). An actualistic perspective into Archean worlds–(cyano-) bacterially induced sedimentary structures in the siliciclastic Nhlazatse Section, 2.9 Ga Pongola Supergroup, South Africa. *Geobiology*, *6*(1), 5-20.

Nordberg, M., & Nordberg, G. F. (2016). Trace element research-historical and future aspects. *Journal of Trace Elements in Medicine and Biology*, *38*, 46-52.

Nothdurft, L. D., Webb, G. E., & Kamber, B. S. (2004). Rare earth element geochemistry of Late Devonian reefal carbonates, Canning Basin, Western Australia: confirmation of a seawater REE proxy in ancient limestones. *Geochimica et Cosmochimica Acta*, *68*(2), 263-283.

Nozaki, Y., Zhang, J., & Amakawa, H. (1997). The fractionation between Y and Ho in the marine environment. *Earth and Planetary Science Letters*, *148*(1-2), 329-340.

Och, L. M., & Shields-Zhou, G. A. (2012). The Neoproterozoic oxygenation event: Environmental perturbations and biogeochemical cycling. *Earth-Science Reviews*, *110*(1-4), 26-57.

Olson, S. L., Kump, L. R., & Kasting, J. F. (2013). Quantifying the areal extent and dissolved oxygen concentrations of Archean oxygen oases. *Chemical Geology*, *362*, 35-43.

Oonk, P., Mason, P., Tsikos, H., & Bau, M. (2018). Fraction-specific rare earth elements enable the reconstruction of primary seawater signatures from iron formations. *Geochimica et Cosmochimica Acta*, *238*, 102-122.

Ossa, F. O., Hofmann, A., Wille, M., Spangenberg, J. E., Bekker, A., Poulton, S. W., Eickmann, B., & Schoenberg, R. (2018). Aerobic iron and manganese cycling in a redox-stratified Mesoarchean epicontinental sea. *Earth and Planetary Science Letters*, *500*, 28-40.

Palandri, J. L., & Kharaka, Y. K. (2004). *A compilation of rate parameters of water-mineral interaction kinetics for application to geochemical modeling* (2331-1258).

Partin, C. A., Bekker, A., Planavsky, N. J., Scott, C., Gill, B. C., Li, C., Podkovyrov, V., Maslov, A., Konhauser, K. O., & Lalonde, S. V. (2013). Large-scale fluctuations in Precambrian atmospheric and oceanic oxygen levels from the record of U in shales. *Earth and Planetary Science Letters*, *369*, 284-293.

Paton, C., Hellstrom, J., Paul, B., Woodhead, J., & Hergt, J. (2011). Iolite: Freeware for the visualisation and processing of mass spectrometric data. *Journal of Analytical Atomic Spectrometry*, *26*(12), 2508-2518.

Pattan, J. N., Pearce, N., & Mislankar, P. (2005). Constraints in using Cerium-anomaly of bulk sediments as an indicator of paleo bottom water redox environment: A case study from the Central Indian Ocean Basin. *Chemical Geology*, *221*(3-4), 260-278.

Pavlov, A., & Kasting, J. (2002). Mass-independent fractionation of sulfur isotopes in Archean sediments: strong evidence for an anoxic Archean atmosphere. *Astrobiology*, *2*(1), 27-41.

Pickard, A. (2003). SHRIMP U–Pb zircon ages for the Palaeoproterozoic Kuruman Iron Formation, northern Cape Province, South Africa: evidence for simultaneous BIF deposition on Kaapvaal and Pilbara cratons. *Precambrian Research*, *125*(3-4), 275-315.

Piper, D., & Heath, G. (1989). Hydrogenous sediment.

Piper, D. Z., & Bau, M. (2013). Normalized rare earth elements in water, sediments, and wine: identifying sources and environmental redox conditions. *American Journal of Analytical Chemistry*, *2013*.

Planavsky, N., Bekker, A., Rouxel, O. J., Kamber, B., Hofmann, A., Knudsen, A., & Lyons, T. W. (2010). Rare earth element and yttrium compositions of Archean and Paleoproterozoic Fe formations revisited: new perspectives on the significance and mechanisms of deposition. *Geochimica et Cosmochimica Acta*, *74*(22), 6387-6405.

Planavsky, N. J., Asael, D., Hofmann, A., Reinhard, C. T., Lalonde, S. V., Knudsen, A., Wang, X., Ossa Ossa, F., Pecoits, E., & Smith, A. J. (2014). Evidence for oxygenic photosynthesis half a billion years before the Great Oxidation Event. *Nature Geoscience*, *7*(4), 283-286.

Planavsky, N. J., Bekker, A., Hofmann, A., Owens, J. D., & Lyons, T. W. (2012). Sulfur record of rising and falling marine oxygen and sulfate levels during the Lomagundi event. *Proceedings of the National Academy of Sciences*, *109*(45), 18300-18305.

Planavsky, N. J., McGoldrick, P., Scott, C. T., Li, C., Reinhard, C. T., Kelly, A. E., Chu, X., Bekker, A., Love, G. D., & Lyons, T. W. (2011). Widespread iron-rich conditions in the mid-Proterozoic ocean. *Nature*, *477*(7365), 448-451.

Polteau, S., Moore, J. M., & Tsikos, H. (2006). The geology and geochemistry of the Palaeoproterozoic Makganyene diamictite. *Precambrian Research*, *148*(3-4), 257-274.

Poulton, S. W., & Canfield, D. E. (2011). Ferruginous conditions: a dominant feature of the ocean through Earth's history. *Elements*, *7*(2), 107-112.

Poulton, S. W., Fralick, P. W., & Canfield, D. E. (2010). Spatial variability in oceanic redox structure 1.8 billion years ago. *Nature Geoscience*, *3*(7), 486-490.

Pourmand, A., Dauphas, N., & Ireland, T. J. (2012). A novel extraction chromatography and MC-ICP-MS technique for rapid analysis of REE, Sc and Y: Revising CI-chondrite and Post-Archean Australian Shale (PAAS) abundances. *Chemical Geology*, *291*, 38-54.

Power, I. M., Wilson, S., Small, D. P., Dipple, G. M., Wan, W., & Southam, G. (2011). Microbially mediated mineral carbonation: roles of phototrophy and heterotrophy. *Environmental Science & Technology*, *45*(20), 9061-9068.

Price, N., & Morel, F. (1990). Cadmium and cobalt substitution for zinc in a marine diatom. *Nature*, *344*(6267), 658-660.

Pufahl, P., & Hiatt, E. (2012). Oxygenation of the Earth's atmosphere–ocean system: a review of physical and chemical sedimentologic responses. *Marine and Petroleum Geology*, *32*(1), 1-20.

Ragsdale, S. W. (2009). Nickel-based enzyme systems. *Journal of Biological Chemistry*, *284*(28), 18571-18575.

Rasmussen, B., Buick, R., & Taylor, W. R. (1998). Removal of oceanic REE by authigenic precipitation of phosphatic minerals. *Earth and Planetary Science Letters*, *164*(1-2), 135-149.

Rasmussen, B., Fletcher, I. R., Brocks, J. J., & Kilburn, M. R. (2008). Reassessing the first appearance of eukaryotes and cyanobacteria. *Nature*, *455*(7216), 1101-1104.

Rasmussen, B., Krapež, B., & Muhling, J. R. (2014). Hematite replacement of iron-bearing precursor sediments in the 3.46-by-old Marble Bar Chert, Pilbara craton, Australia. *Bulletin*, *126*(9-10), 1245-1258.

Rasmussen, B., Krapež, B., Muhling, J. R., & Suvorova, A. (2015). Precipitation of iron silicate nanoparticles in early Precambrian oceans marks Earth's first iron age. *Geology*, *43*(4), 303-306.

Rasmussen, B., Meier, D. B., Krapež, B., & Muhling, J. R. (2013). Iron silicate microgranules as precursor sediments to 2.5-billion-year-old banded iron formations. *Geology*, *41*(4), 435-438.

Rasmussen, B., Muhling, J., & Krapež, B. (2021). Greenalite and its role in the genesis of early Precambrian iron formations–A review. *Earth-Science Reviews*, *217*, 103613.

Rasmussen, B., Muhling, J.R. & Tosca, N.J. (2024). Nanoparticulate apatite and greenalite in oldest, well-preserved hydrothermal vent precipitates. *Science Advances*, *10*(4), p.eadj4789.

Rasmussen, B., & Muhling, J. R. (2021). Development of a greenalite-silica shuttle during incursions of hydrothermal vent plumes onto Neoarchean shelf, Hamersley region, Australia. *Precambrian Research*, *353*, 106003.

Rasmussen, B., Muhling, J. R., Suvorova, A., & Krapež, B. (2017). Greenalite precipitation linked to the deposition of banded iron formations downslope from a late Archean carbonate platform. *Precambrian Research*, *290*, 49-62.

Reinhard, C. T., Planavsky, N. J., Robbins, L. J., Partin, C. A., Gill, B. C., Lalonde, S. V., Bekker, A., Konhauser, K. O., & Lyons, T. W. (2013). Proterozoic ocean redox and biogeochemical stasis. *Proceedings of the National Academy of Sciences*, *110*(14), 5357-5362.

Reinhard, C. T., Raiswell, R., Scott, C., Anbar, A. D., & Lyons, T. W. (2009). A late Archean sulfidic sea stimulated by early oxidative weathering of the continents. *Science*, *326*(5953), 713-716.

Riding, R., Fralick, P., & Liang, L. (2014). Identification of an Archean marine oxygen oasis. *Precambrian Research*, *251*, 232-237.

Ritger, S., Carson, B., & Suess, E. (1987). Methane-derived authigenic carbonates formed by subduction-induced pore-water expulsion along the Oregon/Washington margin. *Geological Society of America Bulletin*, *98*(2), 147-156.

Robbins, L., Lalonde, S., Saito, M. A., Planavsky, N., Mloszewska, A., Pecoits, E., Scott, C., Dupont, C., Kappler, A., & Konhauser, K. (2013). Authigenic iron oxide proxies for marine zinc over

geological time and implications for eukaryotic metallome evolution. *Geobiology*, *11*(4), 295-306.

Robbins, L. J., Lalonde, S. V., Planavsky, N. J., Partin, C. A., Reinhard, C. T., Kendall, B., Scott, C., Hardisty, D. S., Gill, B. C., & Alessi, D. S. (2016). Trace elements at the intersection of marine biological and geochemical evolution. *Earth-Science Reviews*, *163*, 323-348.

Rooney, A. D., Strauss, J. V., Brandon, A. D., & Macdonald, F. A. (2015). A Cryogenian chronology: Two long-lasting synchronous Neoproterozoic glaciations. *Geology*, *43*(5), 459-462.

Rosing, M. T., & Frei, R. (2004). U-rich Archaean sea-floor sediments from Greenland–indications of> 3700 Ma oxygenic photosynthesis. *Earth and Planetary Science Letters*, *217*(3-4), 237-244.

Roy, S. (1992). Environments and processes of manganese deposition. *Economic Geology*, *87*(5), 1218-1236.

Roy, S. (2000). Late Archean initiation of manganese metallogenesis: its significance and environmental controls. *Ore Geology Reviews*, *17*(3), 179-198.

Sahoo, S. K., Planavsky, N., Jiang, G., Kendall, B., Owens, J., Wang, X., Shi, X., Anbar, A., & Lyons, T. (2016). Oceanic oxygenation events in the anoxic Ediacaran ocean. *Geobiology*, *14*(5), 457-468.

Saito, M. A., Sigman, D. M., & Morel, F. M. (2003). The bioinorganic chemistry of the ancient ocean: the co-evolution of cyanobacterial metal requirements and biogeochemical cycles at the Archean–Proterozoic boundary? *Inorganica Chimica Acta*, *356*, 308-318.

Sanchez-Baracaldo, P. (2024). *Primary producers during the early Earth*.

Schier, K., Bau, M., Muenker, C., Beukes, N., & Viehmann, S. (2018). Trace element and Nd isotope composition of shallow seawater prior to the Great Oxidation Event: Evidence from stromatolitic bioherms in the Paleoproterozoic Rooinekke and Nelani Formations, South Africa. *Precambrian Research*, *315*, 92-102.

Schier, K., Bau, M., Smith, A., Beukes, N., Coetzee, L., & Viehmann, S. (2020). Chemical evolution of seawater in the Transvaal Ocean between 2426 Ma (Ongeluk Large Igneous Province) and 2413 Ma ago (Kalahari Manganese Field). *Gondwana Research*, *88*, 373-388.

Schirrmeister, B. E., Sanchez-Baracaldo, P., & Wacey, D. (2016). Cyanobacterial evolution during the Precambrian. *International Journal of Astrobiology*, *15*(3), 187-204.

Schneiderhan, E., Gutzmer, J., Strauss, H., Mezger, K., & Beukes, N. J. (2006). The chemostratigraphy of a Paleoproterozoic MnF-BIF succession–the Voëlwater Subgroup of the Transvaal Supergroup in Griqualand West, South Africa. *South African Journal of Geology*, *109*(1-2), 63-80.

Schobben, M., Foster, W. J., Sleveland, A. R., Zuchuat, V., Svensen, H. H., Planke, S., Bond, D. P., Marcelis, F., Newton, R. J., & Wignall, P. B. (2020). A nutrient control on marine anoxia during the end-Permian mass extinction. *Nature Geoscience*, *13*(9), 640-646.

Schopf, J., Hayes, J., & Walter, M. (1983). Evolution of earth's earliest ecosystems- Recent progress and unsolved problems. *Earth's earliest biosphere: Its origin and evolution(A 84-43051 21-51). Princeton, NJ, Princeton University Press, 1983*, 361-384.

Schopf, J. W., & Klein, C. (1992). *The Proterozoic biosphere: a multidisciplinary study*. Cambridge University Press.

Schröder, S., Bedorf, D., Beukes, N., & Gutzmer, J. (2011). From BIF to red beds: Sedimentology and sequence stratigraphy of the Paleoproterozoic Koegas Subgroup (South Africa). *Sedimentary Geology*, *236*(1-2), 25-44.

Schröder, S., Lacassie, J. P., & Beukes, N. J. (2006). Stratigraphic and geochemical framework of the Agouron drill cores, Transvaal Supergroup (Neoarchean–Paleoproterozoic, South Africa). *South African Journal of Geology*, *109*(1-2), 23-54.

Scott, C., Lyons, T., Bekker, A., Shen, Y.-a., Poulton, S., Chu, X.-l., & Anbar, A. (2008). Tracing the stepwise oxygenation of the Proterozoic ocean. *Nature*, *452*(7186), 456-459.

Scott, C., Planavsky, N. J., Dupont, C. L., Kendall, B., Gill, B. C., Robbins, L. J., Husband, K. F., Arnold, G. L., Wing, B. A., & Poulton, S. W. (2013). Bioavailability of zinc in marine systems through time. *Nature Geoscience*, *6*(2), 125-128.

Scott, C. T., Bekker, A., Reinhard, C. T., Schnetger, B., Krapež, B., Rumble III, D., & Lyons, T. W. (2011). Late Archean euxinic conditions before the rise of atmospheric oxygen. *Geology*, *39*(2), 119-122.

Senger, M., Davies, J., Ovtcharova, M., Beukes, N., Gumsley, A., Gaynor, S., Ulianov, A., Ngobeli, R., & Schaltegger, U. (2023). Improving the chronostratigraphic framework of the Transvaal Supergroup (South Africa) through in-situ and high-precision U-Pb geochronology. *Precambrian Research*, *392*, 107070.

Severmann, S., & Anbar, A. D. (2009). Reconstructing paleoredox conditions through a multitracer approach: the key to the past is the present. *Elements*, *5*(6), 359-364.

Shannon, R. D. (1976). Revised effective ionic radii and systematic studies of interatomic distances in halides and chalcogenides. *Foundations of Crystallography*, *32*(5), 751-767.

Sheldon, N. D. (2006). Precambrian paleosols and atmospheric CO2 levels. *Precambrian Research*, *147*(1-2), 148-155.

Shields, G., & Stille, P. (2001). Diagenetic constraints on the use of cerium anomalies as palaeoseawater redox proxies: an isotopic and REE study of Cambrian phosphorites. *Chemical Geology*, *175*(1-2), 29-48.

Shields, G. A., & Webb, G. E. (2004). Has the REE composition of seawater changed over geological time?

Sholkovitz, E. R., Landing, W. M., & Lewis, B. L. (1994). Ocean particle chemistry: the fractionation of rare earth elements between suspended particles and seawater. *Geochimica et Cosmochimica Acta*, *58*(6), 1567-1579.

Simonson, B. M., Chan, M., & Archer, A. (2003). Origin and evolution of large Precambrian iron formations. *Special Papers-Geological Society of America*, 231-244.

Sleep, N. H., & Zahnle, K. (2001). Carbon dioxide cycling and implications for climate on ancient Earth. *Journal of Geophysical Research: Planets*, *106*(E1), 1373-1399.

Slotznick, S. P., Johnson, J. E., Rasmussen, B., Raub, T. D., Webb, S. M., Zi, J.-W., Kirschvink, J. L., & Fischer, W. W. (2022). Reexamination of 2.5-Ga "whiff" of oxygen interval points to anoxic ocean before GOE. *Science advances*, *8*(1), eabj7190.

Strnad, L., Ettler, V., Mihaljevic, M., Hladil, J., & Chrastny, V. (2009). Determination of trace elements in calcite using solution and laser ablation ICP-MS: Calibration to NIST SRM glass and USGS MACS carbonate, and application to real landfill calcite. *Geostandards and Geoanalytical Research*, *33*(3), 347-355.

Stüeken, E. E., Buick, R., Guy, B. M., & Koehler, M. C. (2015). Isotopic evidence for biological nitrogen fixation by molybdenum-nitrogenase from 3.2 Gyr. *Nature*, *520*(7549), 666-669.

Sumner, D. Y. (1997). Carbonate precipitation and oxygen stratification in late Archean seawater as deduced from facies and stratigraphy of the Gamohaan and Frisco formations, Transvaal Supergroup, South Africa. *American Journal of Science*, *297*(5), 455-487.

Sumner, D. Y., & Bowring, S. A. (1996). U· Pb geochronologic constraints on deposition of the Campbellrand Subgroup, Transvaal Supergroup, South Africa. *Precambrian Research*, *79*(1-2), 25-35.

Sumner, D. Y., & Grotzinger, J. P. (2004). Implications for Neoarchaean ocean chemistry from primary carbonate mineralogy of the Campbellrand-Malmani Platform, South Africa. *Sedimentology*, *51*(6), 1273-1299.

Sumner, D. Y., Hawes, I., Mackey, T. J., Jungblut, A. D., & Doran, P. T. (2015). Antarctic microbial mats: A modern analog for Archean lacustrine oxygen oases. *Geology*, *43*(10), 887-890.

Sun, S., Konhauser, K. O., Kappler, A., & Li, Y.-L. (2015). Primary hematite in Neoarchean to Paleoproterozoic oceans. *Bulletin*, *127*(5-6), 850-861.

Sunda, W. G., & Huntsman, S. A. (1995). Cobalt and zinc interreplacement in marine phytoplankton: Biological and geochemical implications. *Limnology and Oceanography*, *40*(8), 1404-1417.

Swanner, E. D., Planavsky, N. J., Lalonde, S. V., Robbins, L. J., Bekker, A., Rouxel, O. J., Saito, M. A., Kappler, A., Mojzsis, S. J., & Konhauser, K. O. (2014). Cobalt and marine redox evolution. *Earth and Planetary Science Letters*, *390*, 253-263.

Swanson-Hysell, N. L., Rose, C. V., Calmet, C. C., Halverson, G. P., Hurtgen, M. T., & Maloof, A. C. (2010). Cryogenian glaciation and the onset of carbon-isotope decoupling. *Science*, *328*(5978), 608-611.

Syverson, D.D., Reinhard, C.T., Isson, T.T., Holstege, C.J., Katchinoff, J.A.R., Tutolo, B.M., Etschmann, B., Brugger, J. & Planavsky, N.J. (2021). Nutrient supply to planetary biospheres from anoxic weathering of mafic oceanic crust. *Geophysical Research Letters*, *48*(19), p.e2021GL094442.

Takahashi, Y., Sakami, H., & Nomura, M. (2002). Determination of the oxidation state of cerium in rocks by Ce LIII-edge X-ray absorption near-edge structure spectroscopy. *Analytica Chimica Acta*, *468*(2), 345-354.

Taylor, S. R., & McLennan, S. M. (1985). The continental crust: its composition and evolution.

Tice, M. M., & Lowe, D. R. (2004). Photosynthetic microbial mats in the 3,416-Myr-old ocean. *Nature*, *431*(7008), 549-552.

Tivey, M. K. (2007). Generation of seafloor hydrothermal vent fluids and associated mineral deposits. *Oceanography*, *20*(1), 50-65.

Tosca, N. J., Guggenheim, S., & Pufahl, P. K. (2016). An authigenic origin for Precambrian greenalite: Implications for iron formation and the chemistry of ancient seawater. *Bulletin*, *128*(3-4), 511-530.

Tosca, N. J., & Tutolo, B. M. (2023). Hydrothermal vent fluid-seawater mixing and the origins of Archean iron formation. *Geochimica et Cosmochimica Acta*, *352*, 51-68.

Tostevin, R., & Ahmed, I. A. (2023). Micronutrient availability in Precambrian oceans controlled by greenalite formation. *Nature Geoscience*, *16*(12), 1188-1193.

Tostevin, R., Shields, G. A., Tarbuck, G. M., He, T., Clarkson, M. O., & Wood, R. A. (2016). Effective use of cerium anomalies as a redox proxy in carbonate-dominated marine settings. *Chemical Geology*, *438*, 146-162.

Trendall, A. (2002). The significance of iron-formation in the Precambrian stratigraphic record. *Precambrian sedimentary environments: A modern approach to ancient depositional systems*, 33-66.

Trichet, J., & Defarge, C. (1995). Non-biologically supported organomineralization. *BULLETIN-INSTITUT OCEANOGRAPHIQUE MONACO-NUMERO SPECIAL-*, 203-236.

Tsikos, H., Beukes, N. J., Moore, J. M., & Harris, C. (2003). Deposition, diagenesis, and secondary enrichment of metals in the Paleoproterozoic Hotazel Iron Formation, Kalahari manganese field, South Africa. *Economic Geology*, *98*(7), 1449-1462.

Tsikos, H., Matthews, A., Erel, Y., & Moore, J. M. (2010). Iron isotopes constrain biogeochemical redox cycling of iron and manganese in a Palaeoproterozoic stratified basin. *Earth and Planetary Science Letters*, *298*(1-2), 125-134.

Tsikos, H., Moore, J., & Harris, C. (2001). Geochemistry of the Palaeoproterozoic Mooidraai formation: Fe-rich limestone as end member of iron formation deposition, Kalahari manganese field, Transvaal Supergroup, South Africa. *Journal of African Earth Sciences*, *32*(1), 19-27.

Tsikos, H., & Moore, J. M. (1997). Petrography and geochemistry of the Paleoproterozoic Hotazel Iron-Formation, Kalahari manganese field, South Africa; implications for Precambrian manganese metallogenesis. *Economic Geology*, *92*(1), 87-97.

Veizer, J., Compston, W., Hoefs, J., & Nielsen, H. (1982). Mantle buffering of the early oceans. *Naturwissenschaften*, *69*, 173-180.

Voegelin, A. R., Nägler, T. F., Beukes, N. J., & Lacassie, J. P. (2010). Molybdenum isotopes in late Archean carbonate rocks: implications for early Earth oxygenation. *Precambrian Research*, *182*(1-2), 70-82.

Walker, J. C. (1983). Possible limits on the composition of the Archaean ocean. *Nature*, *302*(5908), 518-520.

Wallace, M. W., Shuster, A., Greig, A., Planavsky, N. J., & Reed, C. P. (2017). Oxygenation history of the Neoproterozoic to early Phanerozoic and the rise of land plants. *Earth and Planetary Science Letters*, *466*, 12-19.

Walter, L. M., & Burton, E. A. (1990). Dissolution of recent platform carbonate sediments in marine pore fluids. *American Journal of Science*, *290*(6), 601-643.

Walton, C. R., Ewens, S., Coates, J. D., Blake, R. E., Planavsky, N. J., Reinhard, C., Ju, P., Hao, J., & Pasek, M. A. (2023). Phosphorus availability on the early Earth and the impacts of life. *Nature Geoscience*, *16*(5), 399-409.

Ward, L. M., Kirschvink, J. L., & Fischer, W. W. (2016). Timescales of oxygenation following the evolution of oxygenic photosynthesis. *Origins of Life and Evolution of Biospheres*, *46*, 51-65.

Warke, M. R. (2017). *Stratigraphic and geochemical framework of the Palaeoproterozoic rise in atmospheric oxygen: Transvaal supergroup (South Africa) [Doctoral dissertation]*. University of Manchester (United Kingdom).

Warke, M. R., Edwards, N. P., Wogelius, R. A., Manning, P. L., Bergmann, U., Egerton, V. M., Kimball, K. C., Garwood, R. J., Beukes, N. J., & Schröder, S. (2019). Decimeter-scale mapping of carbonate-controlled trace element distribution in Neoarchean cuspate stromatolites. *Geochimica et Cosmochimica Acta*, *261*, 56-75.

Warke, M. R., Schröder, S., & Strauss, H. (2018). Testing models of pre-GOE environmental oxidation: a Paleoproterozoic marine signal in platform dolomites of the Tongwane Formation (South Africa). *Precambrian Research*, *313*, 205-220.

Warke, M. R., Strauss, H., & Schröder, S. (2020). Positive cerium anomalies imply pre-GOE redox stratification and manganese oxidation in Paleoproterozoic shallow marine environments. *Precambrian Research*, *344*, 105767.

Webb, G. E., & Kamber, B. S. (2000). Rare earth elements in Holocene reefal microbialites: a new shallow seawater proxy. *Geochimica et Cosmochimica Acta*, *64*(9), 1557-1565.

Webb, G. E., Nothdurft, L. D., Kamber, B. S., Kloprogge, J., & ZHAO, J. X. (2009). Rare earth element geochemistry of scleractinian coral skeleton during meteoric diagenesis: a sequence through neomorphism of aragonite to calcite. *Sedimentology*, *56*(5), 1433-1463.

Whitmore, L. M., Morton, P. L., Twining, B. S., & Shiller, A. M. (2019). Vanadium cycling in the Western Arctic Ocean is influenced by shelf-basin connectivity. *Marine chemistry*, *216*, 103701.

Widdel, F., Schnell, S., Heising, S., Ehrenreich, A., Assmus, B., & Schink, B. (1993). Ferrous iron oxidation by anoxygenic phototrophic bacteria. *Nature*, *362*(6423), 834-836.

Wilks, M., & Nisbet, E. (1988). Stratigraphy of the Steep Rock Group, northwest Ontario: a major Archaean unconformity and Archaean stromatolites. *Canadian Journal of Earth Sciences*, *25*(3), 370-391.

Wille, M., Kramers, J. D., Nägler, T. F., Beukes, N., Schröder, S., Meisel, T., Lacassie, J., & Voegelin, A. (2007). Evidence for a gradual rise of oxygen between 2.6 and 2.5 Ga from Mo isotopes and Re-PGE signatures in shales. *Geochimica et Cosmochimica Acta*, *71*(10), 2417-2435.

Williams, R. P., & Da Silva, J. F. (2003). Evolution was chemically constrained. *Journal of Theoretical Biology*, *220*(3), 323-343.

Wilmeth, D., Corsetti, F., Beukes, N., Awramik, S., Petryshyn, V., Spear, J., & Celestian, A. (2019). Neoarchean (2.7 Ga) lacustrine stromatolite deposits in the Hartbeesfontein Basin, Ventersdorp Supergroup, South Africa: implications for oxygen oases. *Precambrian Research*, *320*, 291-302.

Wright, D. T., & Altermann, W. (2000). Microfacies development in Late Archaean stromatolites and oolites of the Ghaap Group of South Africa. *Geological Society, London, Special Publications*, *178*(1), 51-70.

Zahnle, K. J., Catling, D. C., & Claire, M. W. (2013). The rise of oxygen and the hydrogen hourglass. *Chemical Geology*, *362*, 26-34.

Zeh, A., Wilson, A. H., & Gerdes, A. (2020). Zircon U-Pb-Hf isotope systematics of Transvaal Supergroup–Constraints for the geodynamic evolution of the Kaapvaal Craton and its hinterland between 2.65 and 2.06 Ga. *Precambrian Research*, *345*, 105760.

Zerkle, A. L., Claire, M. W., Domagal-Goldman, S. D., Farquhar, J., & Poulton, S. W. (2012). A bistable organic-rich atmosphere on the Neoarchaean Earth. *Nature Geoscience*, *5*(5), 359-363.

Zhang, J., Amakawa, H., & Nozaki, Y. (1994). The comparative behaviors of yttrium and lanthanides in the seawater of the North Pacific. *Geophysical Research Letters*, *21*(24), 2677-2680.

Zhang, W., Hu, Z., Yang, L., Liu, Y., Zong, K., Xu, H., Chen, H., Gao, S., & Xu, L. (2015). Improved inter-calibration of faraday cup and ion counting for in situ Pb isotope measurements using LA-MC-ICP-MS: Application to the study of the origin of the Fangshan pluton, North China. *Geostandards and Geoanalytical Research*, *39*(4), 467-487.

Zhao, H., & Jones, B. (2013). Distribution and interpretation of rare earth elements and yttrium in Cenozoic dolostones and limestones on Cayman Brac, British West Indies. *Sedimentary Geology*, *284*, 26-38.

Zhao, M.-Y., & Zheng, Y.-F. (2017). A geochemical framework for retrieving the linked depositional and diagenetic histories of marine carbonates. *Earth and Planetary Science Letters*, *460*, 213-221.

Zhao, Y.-Y., Jiang, S.-Y., Li, D., & Yang, J.-H. (2016). A petrographic and geochemical study of carbonate and silica phases from the Ediacaran Doushantuo Formation in the Three Gorges area of South China: Implications for diagenetic conditions. *Palaeogeography, Palaeoclimatology, Palaeoecology*, *463*, 150-167.

Supplementary Data

The supplementary tables, which include the ICP-MS data for samples and standards, are available here.

Acknowledgments

My PhD journey has been everything I could have hoped for, thanks to the incredible support from friends, colleagues, and mentors. Jess Von Der Meden, McDonald Mtonda, Aidan Wilton, Wendy Khumalo, and Loyce Mpangala made the work office a lively and enjoyable place. Chad Peel and Sinelethu Hashibi, whom I can honestly call friends, were there for me during tough times. The staff at the Department of Geological Sciences and the Department of Chemical Engineering at UCT, as well as the Geological Science department at Utrecht University, all contributed to making my PhD experience much smoother.

I am deeply grateful to my family—Afumbom Nke, Ankinimbom Nke, Rosemary Awoh, and Valentine Nke—for their constant support and encouragement.

I have had the pleasure of working with some brilliant minds in my field, including Prof. Paul Mason at Utrecht University, Prof. Harilaos Tsikos at the University of Patras, and Dr. Xholahne Mpangala at the University of Mpumalanga. I am immensely grateful to all of you for the opportunities to learn from you.

Finally, I cannot thank my PhD supervisor, Dr. Rosalie Tostevin, enough. Anyone who knows me knows I can't stop singing your praises. You have been the perfect supervisor for my PhD journey—smart, kind, thoughtful, and always exceeding my expectations. From our first Zoom interview to the final day, working with you has been a joy. It's a pity more students won't get the pleasure of working with you as you transition to industry. Glen and Matt are lucky to have you. Always stay true to yourself. I could not have achieved this dream of earning a PhD without you. A big THANK YOU!

I would also like to acknowledge South 32 for providing drill cores and the South African National Research Foundation's Centre of Excellence (CIMERA & GENUS) and the Biogeochemistry Research Infrastructure Platform for funding this work.

Finally, thank you, UCT, for the opportunity to be part of this great university! Shalom!